TECHNISCHE UNIVERSITÄT WIEN

DISSERTATION

Giomo: A robust modeling approach of ionospheric delays for GNSS real-time positioning applications

Ausgeführt zum Zwecke der Erlangung des akademischen Grades einer Doktorin der technischen Wissenschaften unter der Leitung von

Ao. Univ.-Prof. Dipl.-Ing. Dr.techn. Robert Weber
E 120-4
Department für Geodäsie und Geoinformation

eingereicht an der Technischen Universität Wien
Fakultät für Mathematik und Geoinformation

von

Dipl.-Ing. Nina Magnet

Matr.-Nr.: 00426635
Lavaterstraße 6/2/12
1220 Wien

Wien, März 2019

TECHNISCHE UNIVERSITÄT WIEN

DISSERTATION

Giomo: A robust modeling approach of ionospheric delays for GNSS real-time positioning applications

carried out in order to obtain the academic degree "“doctor of technical sciences"” under the supervision of

Ao. Univ.-Prof. Dipl.-Ing. Dr.techn. Robert Weber

E 120-4

Department of Geodesy and Geoinformation

submitted to Technische Universität Wien

Fakultät für Mathematik und Geoinformation

by

Dipl.-Ing. Nina Magnet

Matr.-Nr.: 00426635

Lavaterstraße 6/2/12

1220 Wien

Vienna, March 2019

Author's Statement
Erklärung zur Verfassung der Arbeit

I hereby declare, that I independently drafted this manuscript, that all sources and references used are correctly cited and that the respective parts of this manuscript including tables, maps and figures – which were included from other manuscripts or the internet, either semantically or syntactically –, are made clearly evident in the text and all respective sources are correctly cited.

Hiermit erkläre ich, dass ich diese Arbeit selbstständig verfasst habe, dass ich die verwendeten Quellen und Hilfsmittel vollständig angegeben habe und dass ich die Stellen der Arbeit – einschließlich Tabellen, Karten und Abbildungen –, die anderen Werken oder dem Internet im Wortlaut oder dem Sinn nach entnommen sind, auf jeden Fall unter Angabe der Quelle als Entlehnung kenntlich gemacht habe.

Dipl.-Ing. Nina Magnet

Lavaterstraße 6/2/12
1220 Wien
Österreich

Acknowledgments

Writing my thesis took me much longer than expected in the beginning, as I had the joy of having my daughter Mia born, who was a great enrichment to my life. I am so glad I finally finished this work, so thanks to all the people, no matter if family or friends, who helped me in their own special way to succeed.

I want to thank you, Robert, for always supporting me and motivating me to continue this thesis, even over this long time. I also want to thank you for giving me the opportunity to work in such a great team at our research group, I would never want to miss that experience!

Thank you to all my colleagues, especially to Janina, who investigated the ionosphere at TU Wien with me, and my former office mate Gregor, who knew the answer to almost every GNSS related problem.

Matthias, a really big part of my gratitude goes to you! Without all our discussions and your never ending support I am not sure if I had ever finished this work.

Mia, thank you for coming to my life and showing me, that also high goals can be achieved.

Abstract

The upper part of the atmosphere, which affects electromagnetic waves by its concentration of electrons is called ionosphere. It extends from about 50 km up to 1500 km height above the Earth's surface and is divided up into several layers (D, E and F). The ionization mainly depends on the activity of the Sun and the electromagnetic field, yielding a maximum ionization around noon and a lower ionization during night time.

For navigation and positioning applications, the introduced ionospheric delay of the satellite signals depicts an error source which has to be corrected. The effect can be eliminated using dual-frequency receivers due to the dispersive behavior of microwaves within the ionosphere by building the ionosphere-free linear combination. In case of single-frequency measurements, models of the ionospheric delay are mandatory.

The topic of this thesis deals with the use of such models in the application of positioning using satellite navigation. A new and simple model is developed for the correction of the ionospheric delay of satellite signals. The model consists of only five parameters compared to state-of-the-art established models which estimate the ionospheric delay at discrete, gridded locations on the Earth. This simple model serves professional needs like, in this case, of the Austrian reference station provider EPOSA. This company will use these ionospheric data corrections also in their operational applications.

The parameters of the newly developed model Giomo are the coordinates of the ionospheric maximum, the amplitude of the ionospheric maximum ($VTEC_{max}$) and two weighting functions in longitude and latitude directions, respectively. These parameters are estimated in an iterative least-squares adjustment based on phase-smoothed code measurements of a network of globally distributed GNSS reference stations. The five parameters are estimated every hour due to the rapid changes of the ionospheric corrections.

Due to non-linearity of the equation system, the parameter estimation system needs a priori values within a certain quality of ±30 %. This thesis shows that these requirements can be mostly satisfied using the presented methods.

A statistical analysis of the model estimates shows a mean formal error of 0.33 TECU ±0.93 TECU (median 0.27 TECU) of $VTEC_{max}$. The mean formal errors of the weighting factors are in the range of 1 % of the total values, and the coordinates of the ionospheric maximum indicate an accuracy of ±0.24° in latitude and ±0.63° in longitude direction. Statistical significant correlations around -0.6 are found for $VTEC_{max}$ and each of the weighting factors and, however

smaller, for the weighting factor in latitude direction and the latitude coordinate of the maximum.

An external validation is performed by comparing the Giomo Model to established ionospheric correction models. The Giomo Model shows a good agreement to both the CODE (0.8 TECU mean difference) and the IGS (0.1 TECU mean difference) models. The actual variation seems, however, to be larger, as indicated by the standard deviations (CODE: ±2.8 TECU, IGS: ±2.8 TECU). The models CODE and IGS show an agreement below 1 TECU (mean difference -0.9 TECU ±0.52 TECU). The Klobuchar Model shows the largest discrepancies to all other models, indicating a less accurate prediction of the ionospheric electron content.

Another validation procedure is performed by converting the models' TEC values to pseudorange corrections. The corrected L1 pseudoranges are then compared to ranges obtained by the ionosphere-free linear combination. Although the models of IGS and CODE perform better, the close to real-time Giomo Model can compete (corrections within a difference of ±1 m: 79.9 % for CODE, 80.1 % for IGS and 75.5 % for Giomo).

For real-time applications, like PPP, the model also needs to predict the ionospheric corrections. Several prediction methods for the five parameters are tested. The best results are found for using a weighted average of the last three (five for the parameter longitude coordinate) days at the same hour of the value to be predicted.

Kurzfassung

Der obere Teil der Atmosphäre, der durch seine Elektronenkonzentration elektromagnetische Wellen beeinflusst, wird Ionosphäre genannt. Sie erstreckt sich von etwa 50 km bis zu 1500 km Höhe über der Erdoberfläche und wird von der Wissenschaft in mehrere Schichten unterteilt (D, E und F). Die Stärke der Ionisation hängt hauptsächlich mit der Sonnenaktivität und dem elektromagnetischen Feld zusammen. Die maximale Ionisierung wird somit um die Mittagszeit erreicht, während der Nacht wird nur eine sehr geringe Ionisierung festgestellt.

Für Navigations- und Positionierungsanwendungen gilt die Verzögerungen von Signalen durch die Ionosphäre als Fehlerquelle, die es zu korrigieren gilt. Aufgrund der Dispersivität von Mikrowellen in der Ionosphäre kann der Effekt mit Zweifrequenzempfängern und unter Verwendung der ionsphärenfreien Linearkombination eliminiert werden. Bei Einfrequenzmessungen sind demnach Ionosphärenmodelle unumgänglich.

Diese Arbeit beschäftigt sich mit der Entwicklung und Verwendung solcher Ionosphärenmodelle für die Positionierungsbestimmung mittels Satellitennavigation. Ein neues und einfaches Modell zur Korrektur der Ionosphärenverzögerung wird vorgestellt, das im Gegensatz zu etablierten Modellen nur aus fünf Parametern besteht. Die Verzögerung durch die Ionosphäre wird zusätzlich für verschiedene Anwendungen an diskreten, gitterförmig angeordneten Punkten verteilt über die gesamte Erde angegeben. Ein solch einfaches Modell erfüllt professionelle Anforderungen, wie in diesem Fall die des österreichischen Referenzstations-Anbieters EPOSA. Diese Firma beabsichtigt, diese Ionosphärenkorrekturdaten in ihren Anwendungen zu integrieren und den Nutzern von Einfrequenz-Geräten zur Verfügung zu stellen.

Die Parameter des neu entwickelten Modells Giomo sind die Koordinaten und die Amplitude ($VTEC_{max}$) des ionosphärischen Maximums und zwei Gewichtungsfunktionen in Länge und Breite. Diese Parameter werden in einer iterativen Kleinste-Quadrate-Ausgleichung basierend auf phasengeglätteten Codemessungen eines Netzwerks von global verteilten GNSS-Referenzstationen geschätzt. Die fünf Parameter werden wegen der schnellen Änderungen der ionosphärischen Korrekturen jede Stunde berechnet.

Aufgrund der Nichtlinearität des Gleichungssystems benötigt die Ausgleichung a priori Werte innerhalb eines bestimmten Bereichs von ±30 % Differenz zum wahren Wert. Diese Arbeit zeigt, dass diese Genauigkeitsanforderungen mit den vorgestellten Methoden ausreichend erfüllt werden können.

Eine statistische Analyse der mit dem Modell berechneten Daten zeigt einen mittleren for-

malen Fehler von 0.33 TECU ±0.93 TECU (Median 0.27 TECU) von $VTEC_{max}$. Die mittleren formalen Fehler der Gewichtungsfaktoren sind im Bereich von rund 1 % der Gesamtwerte und die Koordinaten des ionosphärischen Maximums ergeben eine Genauigkeit von ±0.24° in Breite und ±0.63° in Länge. Statistisch signifikante Korrelationen von -0.6 finden sich für $VTEC_{max}$ mit jedem der Gewichtungsfaktoren und, wenn auch kleiner, für den Gewichtungsfaktor in Breite und die Breite des Maximums.

Eine externe Validierung wird durchgeführt, indem das Giomo-Modell mit etablierten Ionosphären-Korrekturmodellen verglichen wird. Das Giomo-Modell zeigt eine gute Übereinstimmung sowohl mit dem CODE (0.8 TECU mittlere Differenz) als auch mit dem IGS Modell (0.1 TECU mittlere Differenz). Die tatsächliche Variation scheint jedoch größer zu sein, wie durch die Standardabweichungen angezeigt (CODE: ±2,8 TECU, IGS: ±2,8 TECU). Die Modelle von CODE und IGS zeigen untereinander eine Übereinstimmung unter 1 TECU (mittlere Differenz -0.9 TECU ±0.52 TECU). Das Klobuchar Modell weist die größten Unterschiede zu allen anderen Modellen auf, was auf eine weniger genaue Vorhersage des Elektronengehaltes in der Ionosphäre hinweist.

In einem weiteren Testverfahren werden die von den Modellen berechneten Verzögerungen in Pseudorange-Korrekturen umgewandelt, die anschließend an L1-Messungen angebracht werden. Als Referenzgröße dienen die Ergebnisse der ionosphärenfreien Linearkombination. Obwohl die Modelle von IGS und CODE besser abschneiden, liefert das in nahe Echtzeit verfügbare Giomo Modell vergleichbare Werte (Korrekturen innerhalb einer Differenz von ±1 m: 79.9 % für CODE, 80.1 % für IGS und 75.5 % für Giomo).

Für Echtzeitanwendungen wie PPP muss das Modell auch prädiziert werden. Dazu werden mehrere Prädiktionsverfahren für die fünf Parameter getestet. Die besten Ergebnisse liefert ein gewichteter Durchschnitt der letzten drei Tage (bzw. fünf für den Parameter Länge des Maximums) zur gleichen Stunde des zu prognostizierenden Wertes.

Acronyms

ARPL	Aeronomy and Radiopropagation Laboratory
BIMF	Barcelona Ionospheric Mapping Function
BOC	Binary Offset Carrier
CAS	Commercial Authentication Service
CDDIS	Crustal Dynamics Data Information System
CDMA	Code Division Multiple Access
CODE	Center for Orbit Determination in Europe
COSPAR	Committee on Space Research
CS	Commercial Service
DCB	Differential Code Bias
DGFI-TUM	Deutsches Geodätisches Forschungsinstitut
DLR	Deutsches Zentrum für Luft- und Raumfahrt
DOY	day of year
EC	European Commission
EGNOS	European Geostationary Navigation Overlay Service
EPOSA	Echtzeit Positionierung Austria
ESA	European Space Agency
ESM	Extended Slab Model
ESOC	European Space Operations Center
F/NAV	Freely Accessible Navigation Message
FDMA	Frequency Division Multiple Access
FFG	Austrian Research Promotion Agency
FOC	Full Operational Capability
FTP	File Transfer Protocol
GEO	Geostationary Orbit
GIM	Global Ionosphere Map
GLONASS	Globalnaja Nawigazionnaja Sputnikowaja Sistema

GNSS	Global Navigation Satellite System
GPS	Global Positioning System
HAS	High Accuracy Service
I/NAV	Integrity Navigation Message
IAAC	Ionospheric Associate Analysis Centers
IGS	International GNSS Service
IGSO	Inclined Geosynchronous Orbit
IONEX	Ionosphere Map Exchange Format
IOV	In Orbit Validation
IPP	Ionospheric Pierce Point
IRI	International Reference Ionosphere
ITU-R	International Telecommunication Union, Radiocommunication Sector
JPL	Jet Propulsion Laboratory
JPO	Joint Program Office
MEO	Medium Earth Orbit
MGEX	Multi-GNSS Experiment
MSLM	Modified Single-Layer Model Mapping Function
NAVSTAR GPS	Navigational Satellite Timing and Ranging Global Positioning System
NRCan	Natural Resources Canada
nT	Nanotesla
OS	Open Service
PPP	Precise Point Positioning
PPS	Precise Positioning Service
PRN	Pseudorandom Noise
PRS	Public Regulated Service
RINEX	Receiver Independent Exchange Format
SAR	Search and Rescue Service
SID	Sudden Ionospheric Disturbances
SLM MF	Single-Layer Model Mapping Function
SPS	Standard Positioning Service
STEC	Slant Total Electron Content
TEC	Total Electron Content
TECU	TEC Units
TGD	Total Group Delay

TSM Thin-Shell Model
UPC Technical University of Catalonia
URSI International Union of Radio Science
UT Universal Time
UTC Universal Time Coordinated
VTEC Vertical Total Electron Content

Contents

Chapter 1

Introduction

Depending on the temperature the atmosphere consists of several layers called troposphere, stratosphere, mesosphere, thermosphere and exosphere (with rising altitude). The lower layers belong to the neutral atmosphere, whereas the upper layers are ionized by solar radiation. This part is called the ionosphere, extending from about 50 km to 1 500 km height above the Earth's surface. Formally, the ionosphere also gets divided up into several layers (D, E and F), depending on their ionization, height and other characteristics. The ionization mainly depends on the activity of the Sun and the electromagnetic field.

The ionosphere affects electromagnetic waves by its concentration of electrons. This is the reason why Global Navigation Satellite System (GNSS) observations have to be corrected by the ionospheric delay. The ionosphere is a dispersive medium, so electromagnetic waves with diverse frequencies get influenced in different ways. Because of this effect the ionospheric delay can be calculated from dual-frequency GNSS measurements.

From there data models of the ionization described by the Total Electron Content (TEC) can be obtained. In case of single-frequency measurements these models can be introduced to increase the positioning accuracy. But the models are also used in multi-signal GNSS data processing e.g. in Precise Point Positioning (PPP) mode in order to solve for ambiguities without forming the ionosphere-free linear combination.

On the other hand GNSS based ionospheric information can be used for monitoring and studying space weather. Ionosphere models are also required in radio science and of course for navigation of vehicles, air traffic and shipping. Forecasting e.g. ionospheric storms is very important especially for safety-of-life applications, because they can cause huge errors in GNSS positioning or lead to a total shutdown of electronic systems.

1.1 Motivation

Various ionosphere models from different institutions are available for download via the internet, e.g. the TEC Maps from the International GNSS Service (IGS). In fact most of them are only available with a few days delay, even the rapid products can be downloaded next morning

at the earliest.

The parameters of the common, empirical Klobuchar Model are broadcasted via the Global Positioning System (GPS) navigation message, which makes it available in real-time. However, it corrects only about 50 % of the range error caused by the ionosphere.

Because of these two facts the aim of this thesis is the development of a new ionosphere model which on the one hand is easy to predict in order to use it for real-time applications, on the other hand it should be more accurate than the Klobuchar Model.

Within two scientific projects funded by the Austrian Research Promotion Agency (FFG) called GIOMO (Next Generation Near Real-Time Ionospheric Models) and Regiomontan (Regional Ionosphere Modeling for Single-Frequency Users) two ionosphere models were developed. They made use of an Austrian reference station network maintained by "“Echtzeit Positionierung Austria"” (EPOSA) in order to achieve higher resolution and accuracy of the TEC data over Austria. The regional model originally labeled Multilayer Model, which was designated for the GIOMO project, was then adapted and modified to derive a global model. Therefore this global model, finally called Giomo Model, became subject of the present thesis and described and evaluated in this work.

The title of this thesis is "“Giomo: A robust modeling approach of ionospheric delays for GNSS real-time positioning applications"”. In this context the term "“robust"” stands for delivering robust/reliable Vertical Total Electron Content (VTEC) data, it should not refer to statistically established robust estimation methods.

1.2 Outline

Following the table of contents,

Chapter 2 – The Ionosphere gives an overview of the structure and the variations of the ionosphere. Furthermore some principles of the propagation of electromagnetic waves and ionospheric refraction are explained. These form the theoretical basis for the subsequent chapters.

Chapter 3 – Global Navigation Satellite Systems summarizes the characteristics of the different GNSS (Galileo, GPS, GLONASS and BeiDou) together with their signal structure. Afterwards, the GNSS observation equations for code and phase measurements and possible error sources are described. In the end of the chapter various methods for eliminating and minimizing those errors are specified, including double- and triple differences and the most common linear combinations.

Chapter 4 – Ionospheric propagation delay derived from GNSS defines in the beginning some terms essential for ionosphere modeling like the used coordinate system, the single-layer and mapping functions. Then the geometry-free linear combination is explained in more detail compared to Chapter 3, before Differential Code Biases (DCBs) and their handling in GNSS processing are introduced. Finally a selection of existing empirical and mathematical ionospheric models is presented.

Chapter 5 – Giomo Model: Algorithm introduces the new Giomo Model and defines all parame-

ters and calculation strategies developed within the work for this dissertation. Besides the GNSS station network utilized for the processing, also a description of the least-squares adjustment including a section on the a priori values for the model parameters is available. Here also the spatial and temporal resolution of the Giomo Model is specified.
Chapter 6 – Giomo Model: Results focuses on the results gained from the processing of the Giomo Model. First all model parameters are analyzed and then the computed TEC Maps are compared to those from established models. Subsequently a quality analysis is carried out. The last part of the chapter is dedicated to the prediction of the TEC with the Giomo Model.
Chapter 7 – Summary and Conclusions summarizes all major developments of the thesis and draws conclusions out of the gained results.

Acronyms used in this thesis are defined at the beginning of the document.
The **bibliography** can be found at the end.

Chapter 2

The Ionosphere

The ionosphere is part of the upper atmosphere which affects electromagnetic waves by its ionization. The ionization mainly depends on the activity of the Sun, the electromagnetic field (e.g. ultraviolet and X-radiation) and particle radiation.

The ionosphere is a dispersive medium, so electromagnetic waves with diverse frequencies get influenced in different ways. For this reason, the resulting propagation delay can be calculated out of dual-frequency GNSS measurements. Using these measurements, also the structure and composition of the ionosphere can be determined. Contrary, accurate ionospheric model information is mandatory to correct single-frequency measurements (Brunini, 1997). Today, due to the availability of multiple-frequency GNSS measurements, combinations of different frequencies can be applied to cancel out the ionospheric refraction.

2.1 Ionosphere structure

The ionosphere extends from about 50 km to 1500 km height above the Earth's surface and is part of the thermosphere and exosphere. The electron density maximum is located at about 350 km, also called the F_2-peak. Below the ionosphere the neutral atmosphere is located, including the troposphere. The layer above 1000 km height is called plasmasphere. Figure 2.1 illustrates the atmosphere up to 1000 km height. The black curve gives the average temperature in the specific regions.

The ionosphere is divided up into several layers called D, E, F_1 and F_2 with increasing height. The layers are a result of the four electron maxima in different heights, which are typical for various processes of electron generation.

The F layer gets split up into two layers F_1 and F_2 at daytime and also the D layer exists only during the day (Table 2.1) (Hargreaves, J. K., 1992). Figure 2.2 shows the variation of electron density with height. The values are derived from the IRI model (Bilitza *et al.*, 2014) and evaluated for a station in Central Europe (Vienna). January and July are selected because they show the typical behavior of a winter and summer month, respectively.

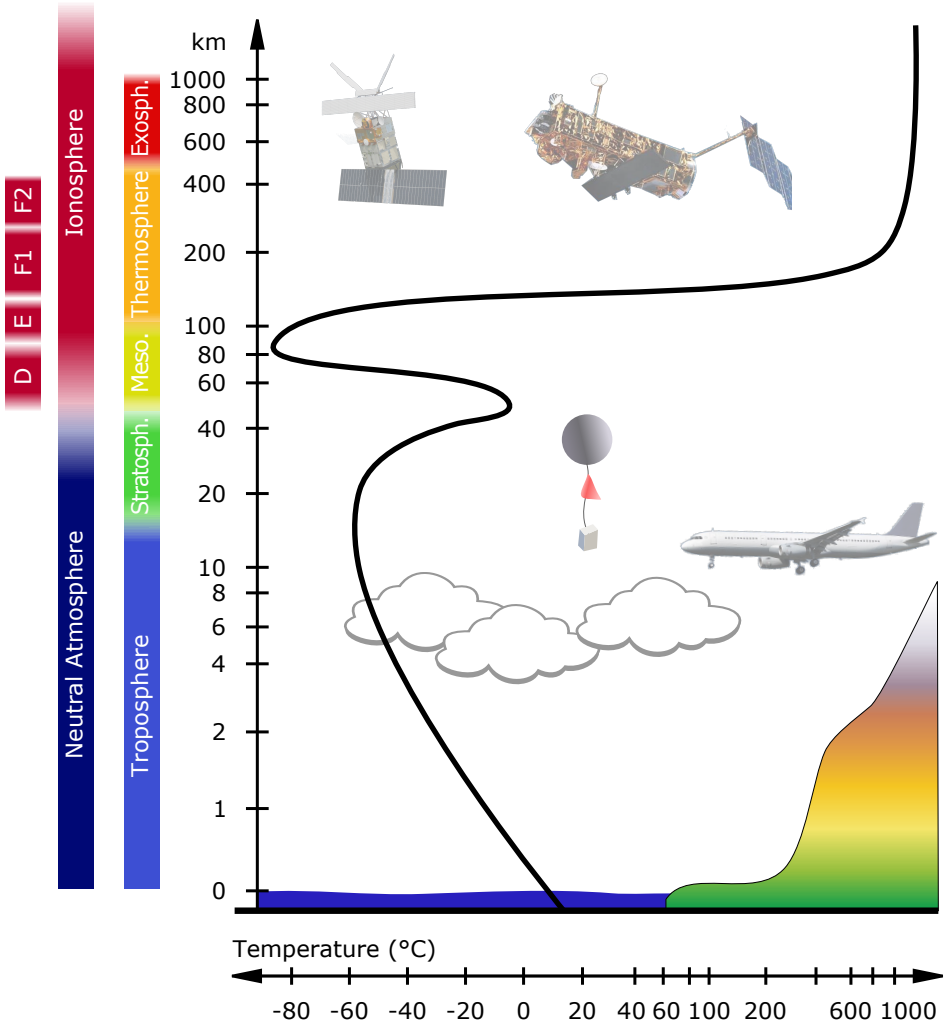

Figure 2.1: Illustration of atmospheric layers

2.1.1 D layer

The D layer is the lowermost layer of the ionosphere in a height from 50 to 90 km and with a low electron density of about 10^8–10^{10} m^{-3}. It is mainly caused by solar radiation but also by cosmic rays traveling through the Earth's magnetic field to the polar regions.

The extent of ionization is primarily dependent on photoionization. This effect can only take place at daytime, when the solar radiation is high. This means that the maximum is found around midday, whereas there is hardly any ionization at nighttime. Most electrons are bound because of the high concentration of particles in this region. For this reason the D layer disappears during night.

Besides the day and night variations other periodic fluctuations are taking place, like an annual and an 11-year cycle. In addition there exists an anomaly in winter for the southern hemisphere, which results in a higher ionization. Furthermore sunspots affect the electron content in the D layer (Zolesi & Cander, 2014).

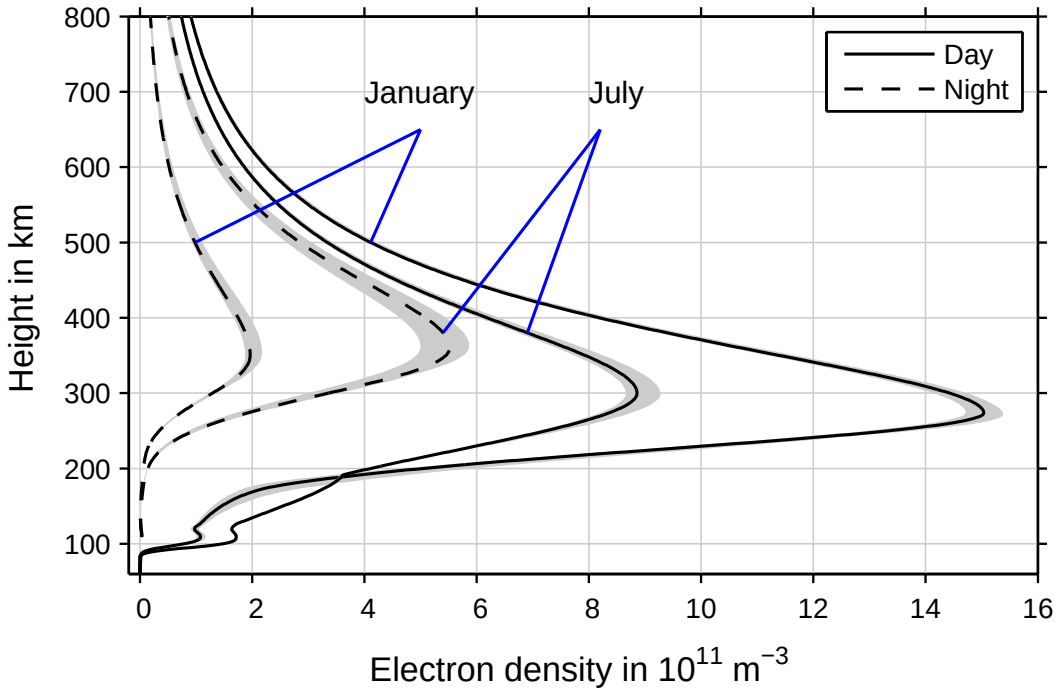

Figure 2.2: Ionospheric profile computed from International Reference Ionosphere (IRI) model for Vienna in 2017

Table 2.1: Ionospheric layers (Hargreaves, J. K., 1992)

Layer	**Height**	**Electron density N_e [m^{-3}]**
D	60–90 km	10^8–10^{10} m^{-3}
E	105–160 km	several 10^{11} m^{-3}
F_1	160–180-km	several 10^{11}–10^{12} m^{-3}
F_2	180–1000 km	up to several 10^{12} m^{-3}

2.1.2 E layer

The E layer, also labeled Kenelly-Heaviside layer, extends from 90 to 150 km height above the Earth's surface. During daytime it is induced by ultraviolet and X-radiation, during nighttime by cosmic rays.

This layer is dominated by temporal and spatial variations. Because of the magnetic field the electron density depends on the geographic latitude. Only the polar regions are exempted where very high electron densities can be measured.

In addition to the E layer there is also the sporadic E_s layer. This layer exists only for several minutes to a few hours and concentrates on mid-latitudes, summer months and at daytime. Near the equator it can be an almost regular phenomenon. The E_s layer characterizes an abnormal behavior of the E layer and has a thickness of only a few kilometers. As the name implies the

electron density increases sporadically by several percent up to the 25-fold (Hobiger, 2006).

2.1.3 F layer

The F layer, also known as Appleton layer, is divided into two layers F_1 and F_2 at daytime. The F_1 layer intensifies in the summer months and also during a period with a low number of sunspots and disappears during night. The F_2 layer is highly variable and for this difficult to predict. A lot of anomalies reaching time spans from a few seconds up to 11 years caused by the solar cycle affect this layer, e.g. a diurnal, a seasonal, a semiannual and an annual anomaly. The daily maximum is reached at midday in winter and shortly before or after midday in summer. Because of the seasonal anomaly the electron density is usually higher in winter than in summer. During the equinoxes the electron density exceeds normal values, which is caused by the semiannual anomaly. When the Earth passes perihelion (the closest point to the Sun) the solar radiation is 6 % higher than at aphelion (the farthest point to the Sun). Due to this effect and the annual anomaly the difference in the electron density between the northern and southern hemisphere is in December 20 % larger than in July.

In the equatorial regions two more variations can be found, the geomagnetic and the equatorial which are caused by tidal oscillations. Because of this anomalies the maximum of free electrons is not placed around the equator but in a northern and southern latitude of about 20°. Then it decreases again towards the poles (Zolesi & Cander, 2014).

2.2 Variations of the electron density

The changing electron density in the ionosphere is subject to many different conditions. The most important one is the Sun, but also the Earth's magnetic field is causing variations. Besides the 11-year solar cycle there are two other main effects caused by the Sun, a diurnal and a seasonal. During daytime, when the solar radiation is high, the electron density is increasing. At night the electron density comes to its minimum. The seasonal effect is induced due to the fact that the two hemispheres are exposed to more sunlight in their summer months and less in their winter months. But also the activity of the Sun is responsible for changes in the electron density.

2.2.1 Activity of the Sun

Solar flares and the number of sunspots are regarded as indications for the activity of the Sun.

Sunspots

The reason for sunspots are strong magnetic fields, which can produce dramatic changes in the ultraviolet and x-ray emissions. The sunspot's temperature is reduced compared to the rest of the surface. For this they do not emit as much light, so they appear as dark spots in the photosphere

of the Sun. Most of the time they appear in groups. Their number and dimension are the most common quantity to measure the activity of the Sun (Friedli, Th. K., 2016).

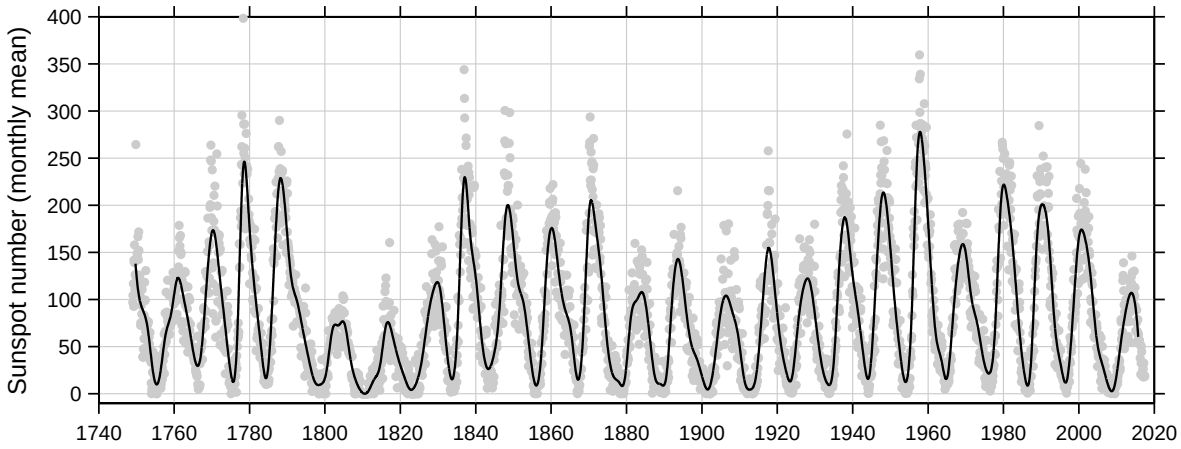

Figure 2.3: Visualization of the solar cycle: Monthly mean sunspot numbers from 1749–2018. The black line indicates a smoothing average. Source: WDC-SILSO, Royal Observatory of Belgium, Brussels.

The number and size of sunspots is represented by the Wolf number R (Rudolf Wolfer, 1848).

$$R = k\,(f + 10g) \tag{2.1}$$

In Equation (2.1) f is the total amount of visible sunspots, g is the number of groups of sunspots (also single sunspots count as group) and k is a correction value individual for each observatory, which is close to 1.

The observed frequency of sunspots underlies a period of eleven years known as solar cycle or sunspot cycle. Figure 2.3 shows that the cycles are not symmetrical. The period between a certain minimum and the subsequent maximum is about 4.3 years, whereas vice versa it is about 6.6 years. Also the length of one period is varying, it can last between 9 to 14 years, but the average is 11 years (Friedli, Th. K., 2016).

Sudden Ionospheric Disturbance (SID)

Sudden Ionospheric Disturbances (SID) are caused by solar flares and/or coronal mass ejections. At these events there are much more particles like protons, electrons or alpha-particles and a higher amount of ultraviolet and x-radiation emitted than normally. These phenomenons mainly affect the D layer of the ionosphere and reach the Earth about eight minutes past the flare (Liu *et al.*, 2011).

Geomagnetic storm

Geomagnetic storms are caused by an increase of the solar wind due to coronal mass ejections. They interact with the Earth's magnetic field and cause an increase of the electron content in the ionosphere. The occurrence of geomagnetic storms is adapted to the sunspot cycle (Kintner Jr. *et al.*, 2013).

2.2.2 Earth's magnetic field

The magnetic field near the Earth is close to a dipole field generated by a strong bar magnet (Figure 2.4). The axis of the geomagnetic field is currently about 11° inclined to the rotation axis of the Earth. The geomagnetic equator is the intersection between the Earth's surface and the plane normal to the dipole axis. The current (March 2019) geographic coordinates of the geomagnetic south pole are $\varphi_0 = 80.33°$ N and $\lambda_0 = -72.67°$ E. The geomagnetic poles realize a model represented by a bar magnet and do not match the true magnetic poles (= points at which the field lines are perpendicular to the surface). The real magnetic pole has been changing its position very quickly and is currently at $\varphi_0 = 86.4°$ N and $\lambda_0 = 175.3°$ E.

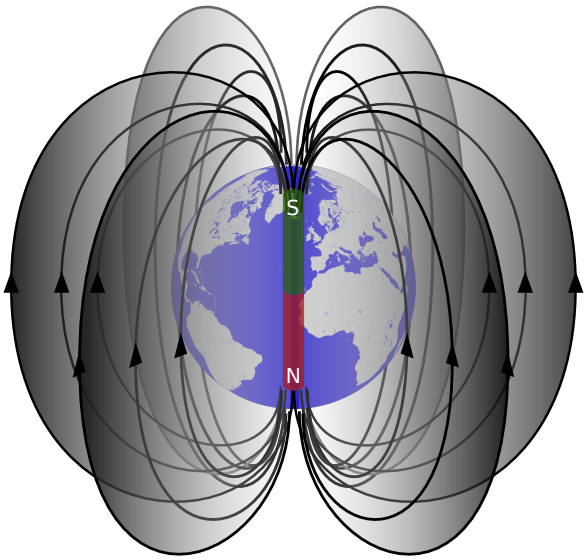

Figure 2.4: Illustration of the Earth's magnetic field

In order to obtain geomagnetic coordinates φ_m and λ_m from geographic coordinates φ_g and λ_g the Equations (4.2) can be used.

Figure 2.5 shows the Earth's magnetosphere, which is defined as the region where charged particles are affected by the Earth's magnetic field. Its boundary to space is defined by the magnetopause, where the magnetic field is equal to the pressure of the solar wind. Below the magnetosphere there is another layer called plasmasphere. It can be seen as the top level of the ionosphere starting above 1000 km in altitude and is shaped like a torus around the Earth (Zolesi & Cander, 2014). Its outer boundary is called plasmapause, located at about 26 000 km height (about 4

Earth radii). It can extend up to 7 Earth radii under quiet solar conditions, while at disturbed conditions it shrinks to 3 Earth radii.

Solar wind is defined as mass ejection producing multiple million tons of particles per second, such as alpha particles (He^{++}) and protons (H^{+}). Due to the solar wind the magnetic field lines get deformed, causing a deformation of the magnetic field. On the side facing the Sun the field lines get compressed whereas on the reverse side they are deformed to a tail.

The magnetizing field strength of the Earth is measured using a global distributed network of observatories. On the equator it is about 25 000 Nanotesla (nT), whereas on the poles it reaches up to 75 000 nT. During strong disturbances of the Earth's magnetic field the measured values can vary by 300 nT at the equator, 500 nT in mid latitudes and 2 000 nT around the poles (Zolesi & Cander, 2014).

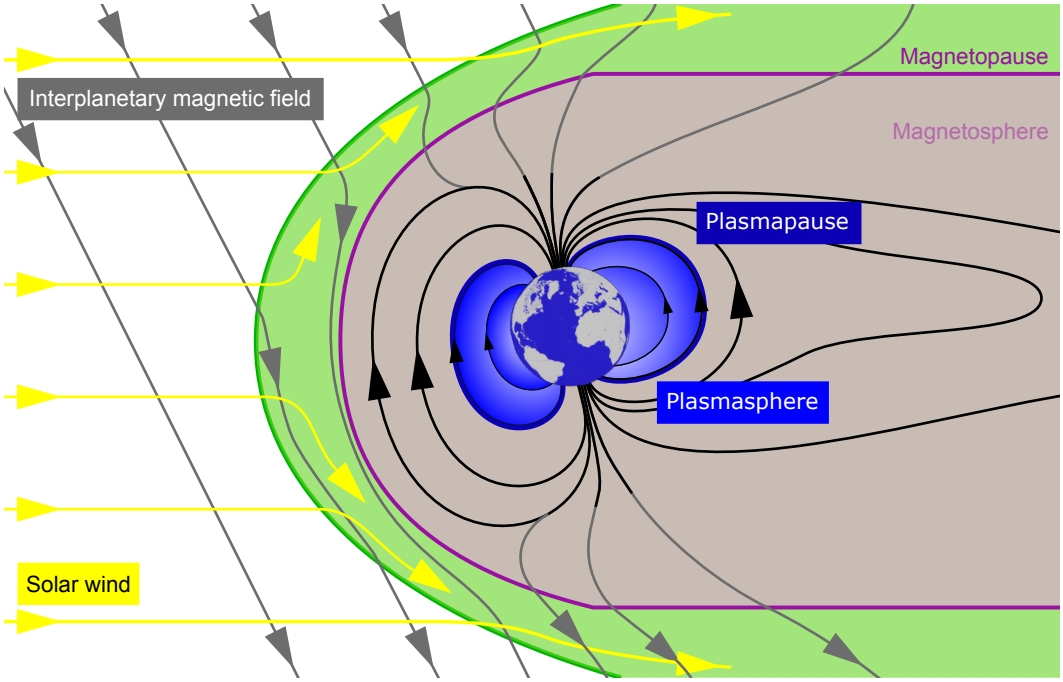

Figure 2.5: Illustration of the magnetosphere

2.2.3 Latitude dependent variations

Because of the distinct behavior of the ionosphere above different geographic parts, Earth gets divided in three regions, the equatorial zone, the mid-latitudes and the auroral zone (Figure 2.6). The regions change dependent on the time of day and the activity of the Sun (Zolesi & Cander, 2014).

Equatorial zone

In the equatorial zone electron density reaches the highest values. Due to the equatorial anomaly (Chapter 2.1.3) the maximum of free electrons is not placed directly at the equator but

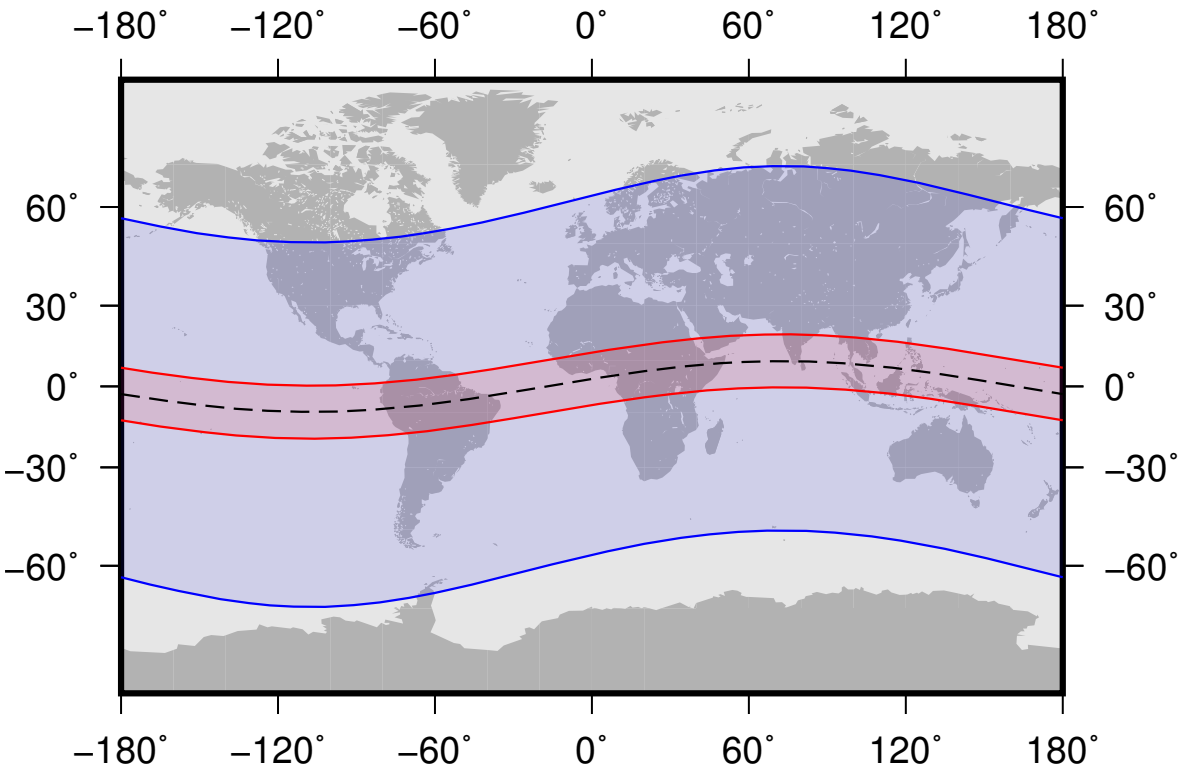

Figure 2.6: Red: equatorial zone; Blue: mid-latitudes; Grey: auroral zone

in a northern and southern latitude of about 20°.

Mid-latitudes

The mid-latitudes are regions without high variations of the electron content. Therefore they can be described more easily with ionospheric models. Nevertheless magnetic storms can also cause variations of 20–30 %. Austria is located in this usually quiet ionospheric region.

Auroral zone

Near the poles and at high latitudes the ionosphere cannot be predicted due to the heavy disturbances caused by the magnetic field. Charged particles move along the magnetic field lines towards the poles which is the reason for aurorae borealis occurring in this region.

2.3 Electromagnetic waves

Satellite Navigation Systems are based on the transmission of electromagnetic waves. These waves can be described with four parameters: amplitude, frequency, phase and polarization. In order to broadcast information with electromagnetic waves one of these parameters has to be modulated. The most common way is phase modulation, but amplitude modulation or frequency modulation are also possible.

2.3.1 Electromagnetic spectrum

Figure 2.7 shows the electromagnetic spectrum. The International Telecommunication Union (ITU) is responsible for the allocation of different frequency bands to different services. It is forbidden to interfere with services of neighboring frequencies, so their use is strictly regulated. Satellite navigation uses L-, S- and C-band frequencies, which belong to the microwave frequency window (Hofmann-Wellenhof *et al.*, 2008).

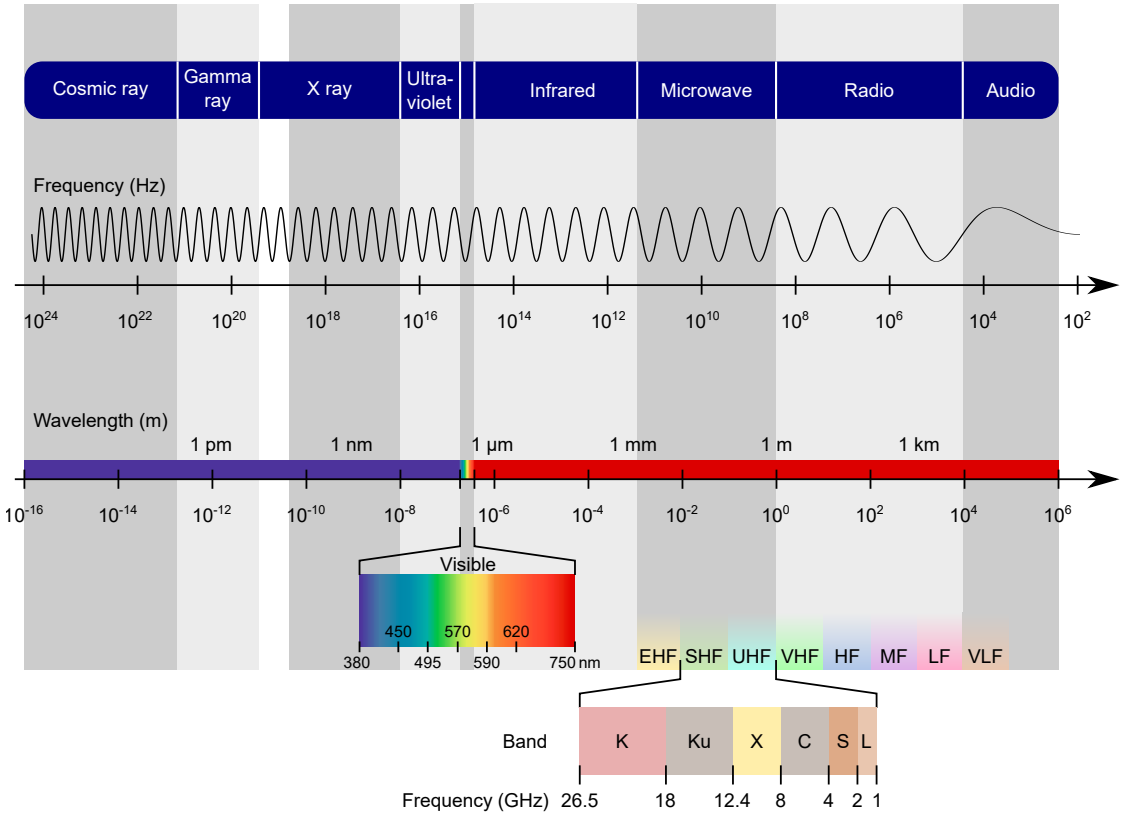

Figure 2.7: Electromagnetic spectrum

2.3.2 Wave propagation

Electromagnetic waves consist of two field components, an electric and a magnetic component. The magnetic field is induced by the oscillating electric field.

Wave propagation in vacuum

Maxwell's electromagnetic wave equations describe the behavior of electromagnetic waves in vacuum. They lead to the two differential equations (2.2) and (2.3) (Winkler, 2006).

$$\nabla^2 \mathbf{E} + \epsilon_0 \mu_0 \omega^2 \mathbf{E} = 0 \tag{2.2}$$

$$\nabla^2 \mathbf{B} + \epsilon_0 \mu_0 \omega^2 \mathbf{B} = 0 \tag{2.3}$$

E denotes the electric and **B** the magnetic field vector. ϵ_0 is the dielectric permittivity in vacuum (2.5), μ_0 the magnetic permeability in vacuum (2.4) and ω the angular frequency (Teunissen & Montenbruck, 2017). Denoting N = Newton $\left[\frac{\mathrm{m} \cdot \mathrm{kg}}{\mathrm{s}^2}\right]$, F = Farad $\left[\frac{\mathrm{s}^4 \cdot \mathrm{A}^2}{\mathrm{m}^2 \cdot \mathrm{kg}}\right]$ and A = Ampere, μ_0 and ϵ_0 can be expressed as

$$\mu_0 = 4\pi \cdot 10^{-7}\ \mathrm{NA}^{-2} = 12.566370614 \cdot 10^{-7}\ \mathrm{NA}^{-2} \tag{2.4}$$

$$\epsilon_0 = \frac{1}{\mu_0 c^2} = 8.854187817 \cdot 10^{-12}\ \mathrm{Fm}^{-1} \tag{2.5}$$

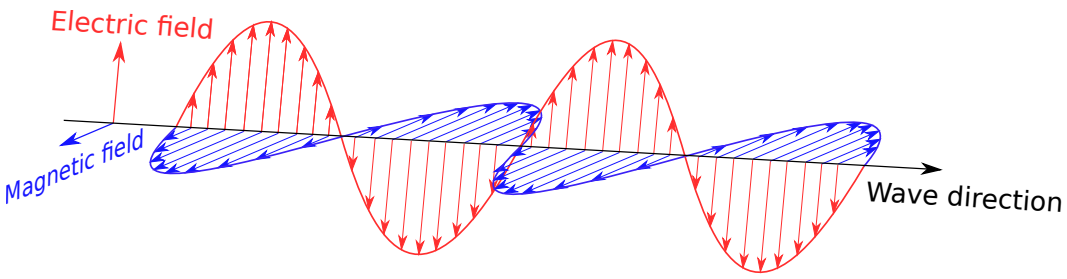

Figure 2.8: Electromagnetic wave

The solution of the differential equations are plane and spherical waves. They propagate with a constant velocity $c = 1/\sqrt{\epsilon_0 \mu_0}$ equal to the speed of light in vacuum. Equation (2.6) shows the solution for the electric field vector **E**, the formula for the magnetic field vector **B** is analog (Wilson *et al.*, 2014).

$$\mathbf{E}(\mathbf{x}, t) = \mathbf{E}_0 \cdot \mathrm{e}^{i(\boldsymbol{\omega} t - \boldsymbol{k}\mathbf{x} + \phi)} \tag{2.6}$$

$\boldsymbol{k} = \boldsymbol{\omega}/c$ is the wave vector, ϕ is an arbitrary and constant phase factor.

In a homogeneous, isotropic and static medium, which is constant in time and space, the electric and magnetic field are perpendicular (Figure 2.8). The direction of propagation **n** is orthogonal to the plane built by the field vectors **E** and **B**.

If the x-axis is set to **E** direction and the y axis points in **B** direction, the z axis points to the wave propagation direction **n**. There are no fields in the z-direction because the divergences of **E** and **B** are zero. The solutions in (2.6) can be split into x and y components. If the axes are set as described above, the real parts can be written as (Wilson *et al.*, 2014)

$$\mathbf{E}_x = \mathbf{E}_0 \cos(\omega t - k\boldsymbol{x} + \phi_x) \qquad \mathbf{E}_y = 0 \tag{2.7}$$

$$\mathbf{B}_x = 0 \qquad \mathbf{B}_y = \mathbf{B}_0 \cos(\omega t - k\boldsymbol{x} + \phi_y). \tag{2.8}$$

The polarization of the electromagnetic wave depends on the phase shift $\Delta\phi$ of ϕ_x and ϕ_y (Figure 2.9). Satellite navigation uses right-handed circular polarization (RHCP). If a signal gets reflected (e.g. multipath) it can change to left-handed circular polarization (LHCP).

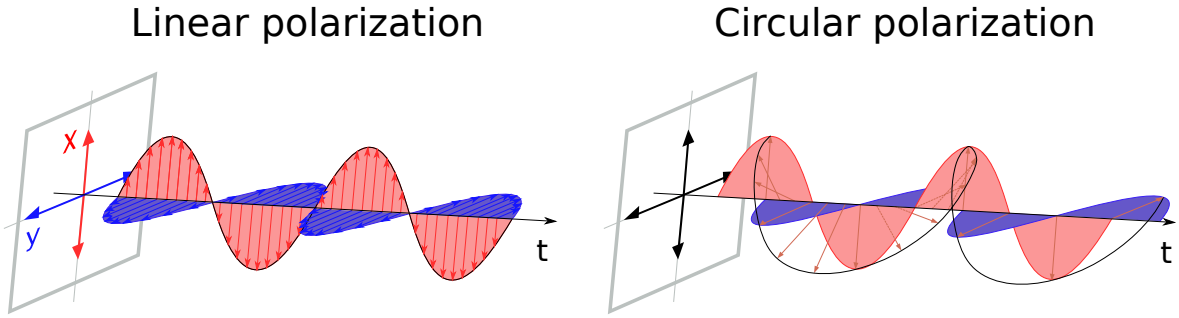

Figure 2.9: Linear and circular polarization

Wave propagation in medium

The propagation characteristics in space are very similar to those in vacuum. Passing the Earth's atmosphere, electromagnetic waves get refracted. Instead of speed of light it is now traveling with the frequency dependent velocity v which makes the ionosphere a dispersive medium (Teunissen & Montenbruck, 2017).

Electromagnetic waves propagating with the frequency f and the wave length λ have the phase velocity v_{ph}:

$$v_{\text{ph}} = \lambda f \tag{2.9}$$

In order to broadcast information electromagnetic waves get modulated. This is done by superimposing multiple sinusoidal waves with different frequencies. Due to the fact that the ionosphere is dispersive, the waves travel with different velocities.

The group velocity v_g is given by

$$v_{\text{gr}} = -\frac{df}{d\lambda}\lambda^2. \tag{2.10}$$

In order to find a relation between phase and group velocity the total differential of Equation (2.9) is built.

$$dv_{\text{ph}} = f\ d\lambda + \lambda\ df \tag{2.11}$$

This equation is converted to

$$\frac{df}{d\lambda} = \frac{dv_{\text{ph}}}{\lambda\, d\lambda} - \frac{f}{\lambda} \tag{2.12}$$

and substituted in Equation (2.10)

$$v_{\text{gr}} = -\lambda \frac{dv_{\text{ph}}}{d\lambda} + f\lambda. \tag{2.13}$$

Finally one gets the Rayleigh Equation.

$$v_{\text{gr}} = v_{\text{ph}} - \lambda \frac{dv_{\text{ph}}}{d\lambda} \tag{2.14}$$

In vacuum group and phase velocity are identical and equal to the speed of light.

The refractive index describes the ratio between the velocity of a wave in vacuum c with respect to the velocity in medium v.

$$n = \frac{c}{v} \tag{2.15}$$

Substituting for the phase and group velocity Equation (2.15) gives a modified version of Equation (2.14).

$$n_{\text{gr}} = n_{\text{ph}} - \lambda \frac{dn_{\text{ph}}}{d\lambda} \tag{2.16}$$

2.4 Ionospheric refraction

The refraction index for the phase can be approximated with Equation (2.17) (Blewitt, 2007).

$$n_{\text{ph}} = 1 + \frac{c_2}{f^2} + \frac{c_3}{f^3} + \frac{c_4}{f^4} + \cdots \tag{2.17}$$

The coefficients c_i are the product of a constant and the electron density N_e, which is the number of electrons per cubic meter.

If the series expansion is truncated after the second term, a more simple equation for the phase refraction index (2.18) is found. After differentiation of (2.18) and substitution in (2.16) a formula for the group refraction index can be obtained (2.19). The two equations only differ by their opposite sign in front of the second term (Hofmann-Wellenhof *et al.*, 2008).

$$n_{\text{ph}} = 1 + \frac{c_2}{f^2} \tag{2.18}$$

$$n_{\text{gr}} = 1 - \frac{c_2}{f^2} \tag{2.19}$$

with

$$c_2 = -\frac{e^2}{8\pi\epsilon_0 m_e} N_e = -40.309\ N_e\ [\mathrm{Hz}^2] \tag{2.20}$$

In Equation (2.20) e is the electron charge, ϵ_0 is the permittivity of free space and m_e is the electron mass (Böhm & Schuh, 2013).

Because N_e is always a non-negative number, the group refraction index is larger than the phase refraction index and for this the phase velocity is larger than the group velocity. Consequently distances obtained from code measurements are too long and distances obtained with phase measurements are too short.

The measured distance s is the integral along the signal path (Seeber, 2003):

$$s = \int n\ ds \tag{2.21}$$

The geometrical distance s_0, which means the straight connection between satellite and receiver, is obtained with $n = 1$.

$$s_0 = \int ds_0 \tag{2.22}$$

The ionospheric refraction Δ^{Ion} is the difference between the measured and the geometrical distance.

$$\Delta^{\mathrm{Ion}} = \int n\ ds - \int ds_0 \tag{2.23}$$

Inserting the phase refraction index n_{ph} (2.18) and the group refraction index n_{gr} respectively (2.19) one gets the following equations:

$$\Delta^{\mathrm{Ion}}_{\mathrm{ph}} = \int \left(1 + \frac{c_2}{f^2}\right) ds - \int ds_0 \tag{2.24}$$

$$\Delta^{\mathrm{Ion}}_{\mathrm{gr}} = \int \left(1 - \frac{c_2}{f^2}\right) ds - \int ds_0 \tag{2.25}$$

In order to simplify the equations, the first term is approximated by the integration along the geometrical distance and ds is replaced by ds_0.

$$\Delta^{\mathrm{Ion}}_{\mathrm{ph}} = \int \frac{c_2}{f^2} ds_0 \qquad \Delta^{\mathrm{Ion}}_{\mathrm{gr}} = -\int \frac{c_2}{f^2} ds_0 \tag{2.26}$$

Substituting the Equation (2.20) for c_2 the equation reads:

$$\Delta_{\text{ph}}^{\text{Ion}} = -\frac{40.309}{f^2} \int N_e \, ds_0 \qquad \Delta_{\text{gr}}^{\text{Ion}} = \frac{40.309}{f^2} \int N_e \, ds_0 \tag{2.27}$$

The TEC is defined as (Blewitt, 2007)

$$\text{TEC} = \int N_e \, ds_0 \tag{2.28}$$

Introducing the TEC in Equations (2.27) results in the distance error caused by the ionosphere in meters.

$$\Delta_{\text{ph}}^{\text{Ion}} = -\frac{40.309}{f^2}\text{TEC} \qquad \Delta_{\text{gr}}^{\text{Ion}} = \frac{40.309}{f^2}\text{TEC} \tag{2.29}$$

The TEC is defined as the number of free electrons integrated between the satellite and the receiver along a tube with a base area of one square meter. The TEC is given in TEC Units (TECU).

$$1 \text{ TECU} = 10^{16} \text{ electrons/m}^2 \tag{2.30}$$

It should be noted that the total ionospheric effect on GNSS signals also contains a curvature or bending of the ray path. This excess of the signal path yields an additional correction to the ionospheric delay up to a few millimeters for low elevations. So if these two effects are split in Equation (2.29), the ionospheric phase delay reads

$$\Delta_{\text{ph}}^{\text{Ion}} = -\frac{40.309}{f^2}(\text{TEC}_{\text{LoS}} + \Delta\text{TEC}_{\text{bend}}) \tag{2.31}$$

where TEC_{LoS} denotes the TEC along the straight line between satellite and receiver and $\Delta\text{TEC}_{\text{bend}}$ is the TEC difference between the bent and the straight signal paths (Hoque & Jakowski, 2011).

For an arbitrary ray path between a satellite and a receiver the Slant Total Electron Content (STEC) can be obtained (cf. Equation (2.28)). With a Mapping Function M (see chapter 4.1.3) the STEC can be projected to the VTEC dependent on the zenith angle.

$$\text{VTEC} = \frac{1}{M} \cdot \text{STEC} \tag{2.32}$$

Data centers like the IGS or CODE provide VTEC values covering the whole globe with a time resolution of one or two hours (see Figure 2.10 as a snapshot).

2.4.1 Chapman profile

Chapman profiles are used to describe the electron density of the ionosphere dependent on latitude, longitude and height.

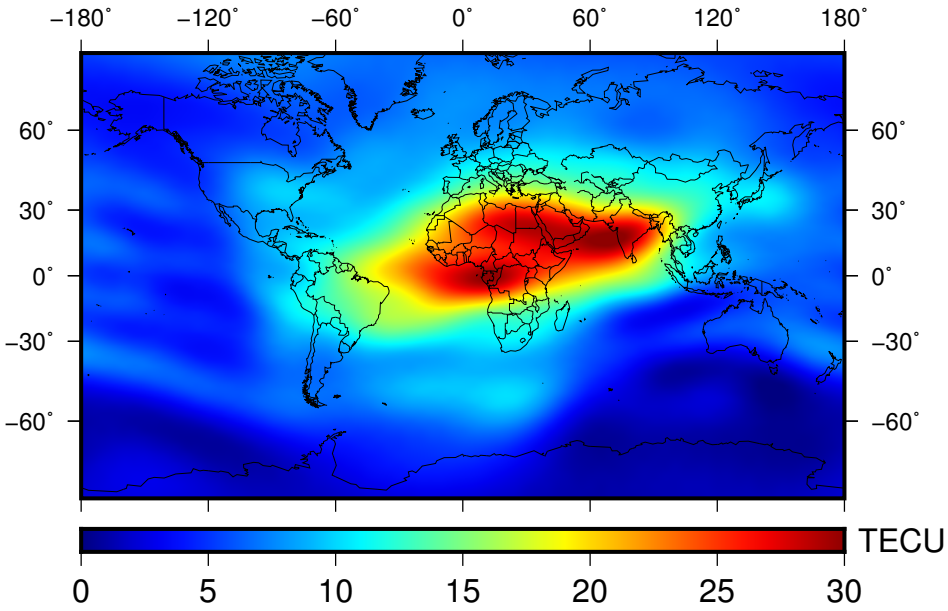

Figure 2.10: Ionospheric TEC Map from Center for Orbit Determination in Europe (CODE) for DOY 121 in 2018, 14:00

The production rate of ion pairs in the ionosphere is given by the Chapman function (Davies, 1990):

$$q(h,\chi) = q_0\, e^{1-z-\sec\chi\; e^{-z}} \quad \text{with} \quad z = \frac{h-h_0}{\Delta h} \tag{2.33}$$

where $q(h,\chi)$ is the ion production rate, h is the height, χ is the zenith angle with respect to the Sun, q_0 is the ion production rate at $z = 0$, z is the scaled altitude, h_0 is the reference height of maximum ion production when the Sun is in zenith direction ($\chi = 0$) and Δh is the scale height (Schaer, 1999).

The ion production rate q_0 can be determined via

$$q_0 = \frac{\phi(\infty)\,\eta}{\Delta h\; e} \tag{2.34}$$

where $\phi(\infty)$ is the solar flux density outside the atmosphere in units of photons per unit area and η is the number of ion pairs produced per photon.

By differentiating Equation (2.33) the height of the maximum ion production $h_{\max}$ is obtained:

$$h_{\max} = h_0 + \Delta h\; z_{\max} \quad \text{with} \quad z_{\max} = \ln\sec\chi \tag{2.35}$$

The ion production peak is reached at

$$q_{\max} = q_0\;\cos\chi \tag{2.36}$$

In the lower layers ions recombine with electrons according to:

$$\frac{\partial N_e}{\partial t} = q - a\, N_e^{\frac{1}{\alpha}} \tag{2.37}$$

where a is the mean recombination coefficient for ions and α is a constant depending on the altitude. In higher layers the recombination rate depends linearly on N_e.

The distribution of electrons named simple Chapman layer is reached at photochemical equilibrium (when $dN_e/dt = 0$) (Rishbeth & Garriott, 1969):

$$N_e(z,\chi) = N_{e,0}\; e^{\alpha\,(1-z-\sec\chi\; e^{-z})} \quad \text{with} \quad N_{e,0} = \left(\frac{q_0}{a}\right)^{\alpha} \tag{2.38}$$

where $N_{e,0}$ is the electron density at $z = 0$. The height of the maximum electron density can again be calculated with Equation (2.35), so the maximum electron density is (Schaer, 1999):

$$N_{e,\max}(\chi) = N_{e,0}\; \cos^{\alpha}\chi \tag{2.39}$$

As Equation (2.39) shows, both $N_{e,\max}$ and $h_{\max}$ depend on the zenith angle with respect to the Sun. At midday, when the Sun is approximately in zenith and therefore $\chi = 0$, maximum N_e is reached. The maximum value for h can be observed at sunrise and sunset, where N_e comes to its minimum.

Figure 2.11 shows the vertical electron density profile of the simple Chapman layer for zenith angles with respect to the Sun from 0° to 80°. The reference height of maximum ion production h_0 was set to 450 km and the scale height Δh to 100 km. The figure shows again that at noon the maximum electron density is reached.

As mentioned before the constant α introduced in Equation (2.37) is dependent on the altitude. Ezquer *et al.* (1996) defined different constants representing the bottom-side (below the F_2-peak) and topside (above the F_2-peak) of the ionosphere, also called α- and β-layers (Limberger, 2015). So for the bottom-side ionosphere a linear behavior of Equation (2.37) is assumed, which means $\alpha = 1$. For the topside ionosphere $\alpha = 1/2 = \beta$ is chosen because the loss rate is assumed to be proportional to the square of the electron density (Alizadeh, 2013).

Chapman profiles are not applied to the Giomo Model as it is based on a single-layer approach (see Chapter 4.1.2).

2.4.2 Important parameters

In this chapter some important parameters for ionosphere modeling are introduced. They are used in the scientific community to entitle quantities more precise.

Figure 2.12 illustrates the electron density of the different ionospheric layers. The maximum electron density is typically located in the F_2-layer at an altitude of about 250–350 km in mid-latitude regions and up to 500 km at equatorial regions (Limberger *et al.*, 2013). Consequently this highest concentration of electrons is also called F_2-peak. The following three parameters are

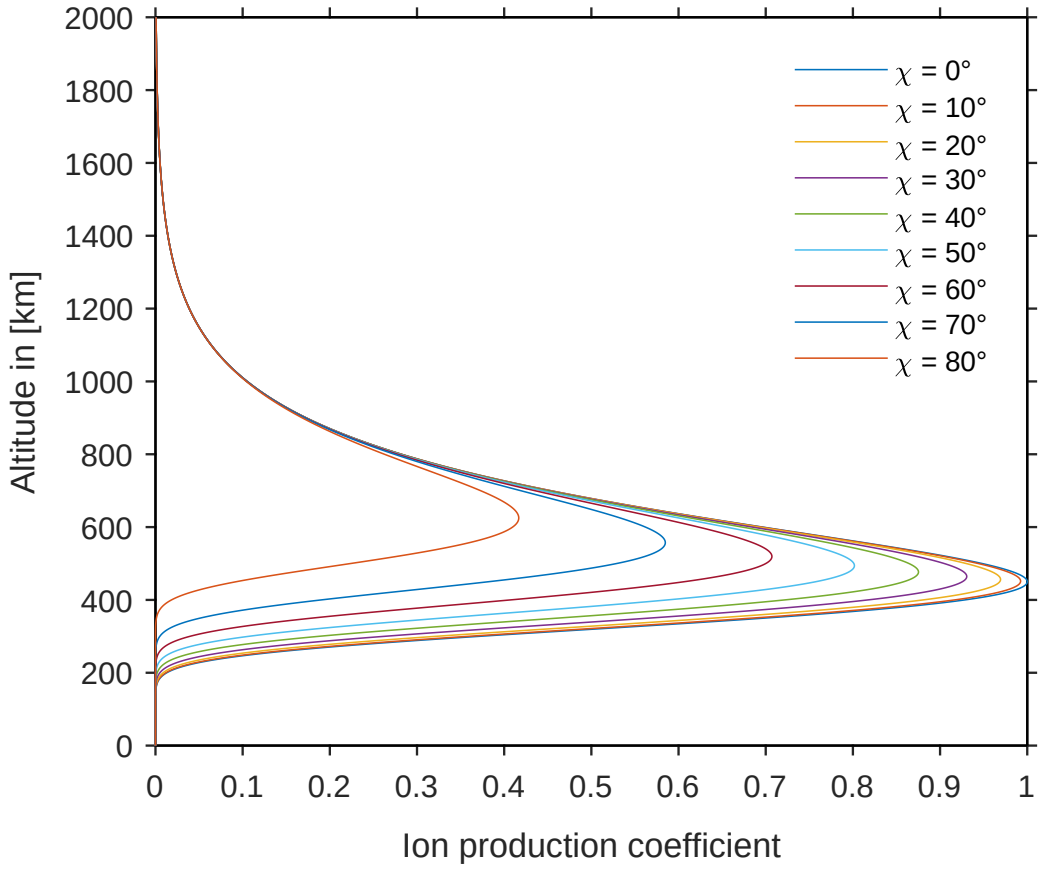

Figure 2.11: Chapman layer: Vertical electron density distribution

defined describing the F_2-peak:

- N_mF_2: Maximum electron density of the F_2 layer
- h_mF_2: altitude of the F_2-peak
- HF_2: scale height of the F_2-peak

Figure 2.13 shows a time series of the two parameters h_mF_2 and N_mF_2 computed with IRI (Version 2016) (Bilitza *et al.*, 2017) for five days in the beginning of the year 2018. The location, for which the quantities are calculated is $\varphi = 50°$ N and $\lambda = 40°$ E. h_mF_2 varies between 230 and 350 km, the maximums are reached during night. N_mF_2 shows an opposite behavior, it has its maximum during daytime, when the ionization is high because of the solar radiation.

Correspondent parameters are defined for the electron density peak located in the E layer

- N_mE: Maximum electron density of the E layer
- h_mE: altitude of the peak height

as well as for the F_1 and the D layer.

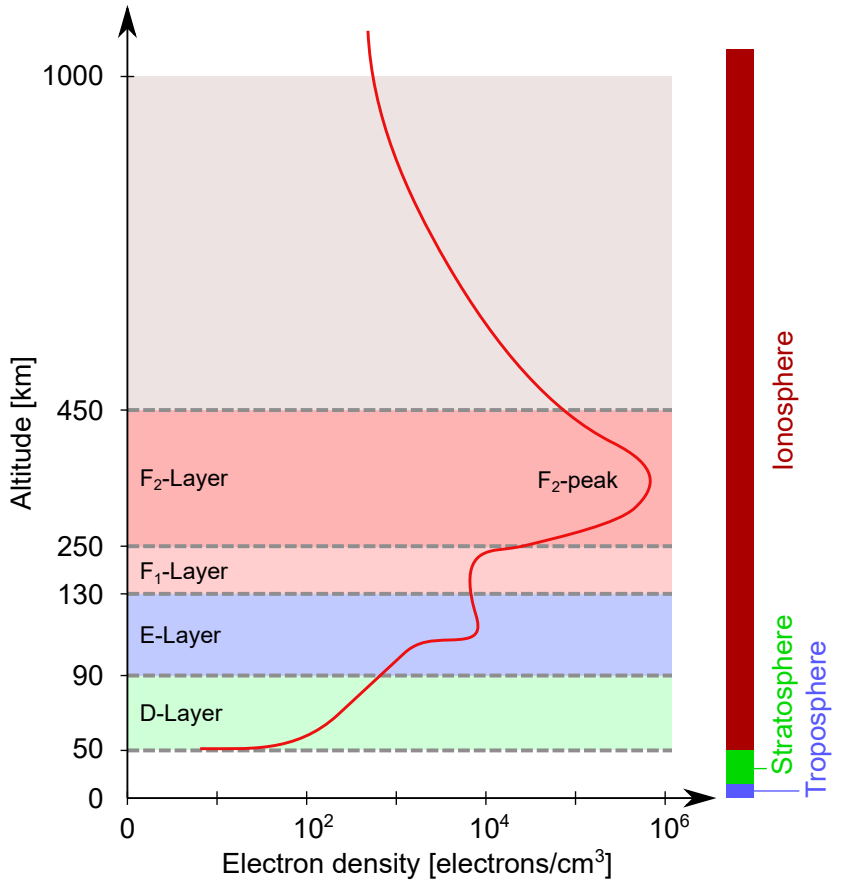

Figure 2.12: Vertical electron density distribution of the ionospheric layers

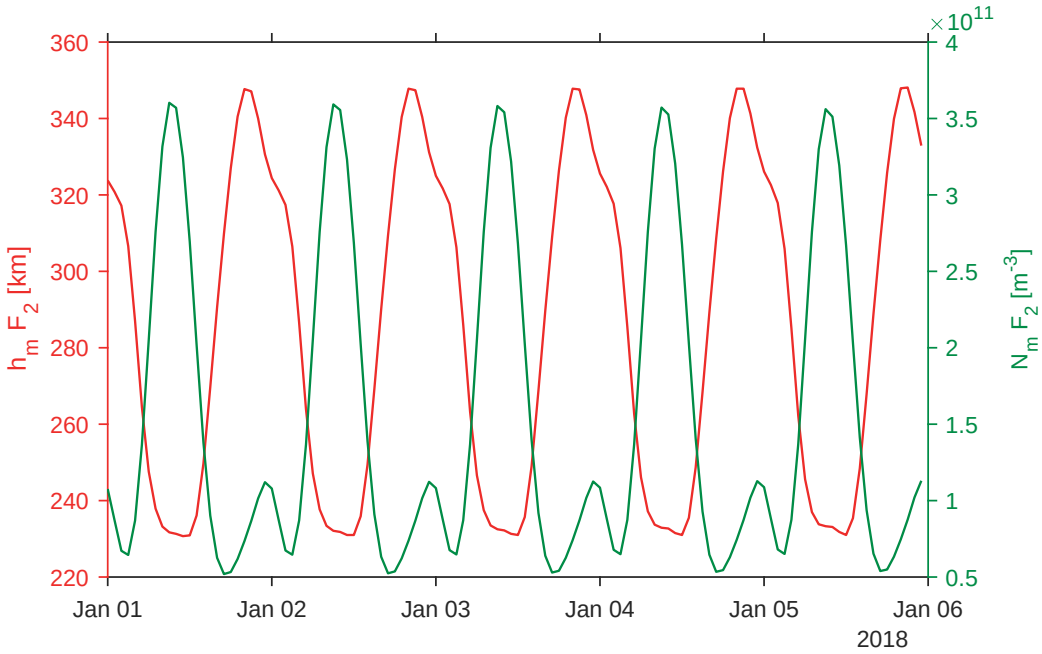

Figure 2.13: Vertical electron density distribution of the ionospheric layers

Chapter 3

Global Navigation Satellite Systems

GNSS is an umbrella term for all existing global navigation satellite systems designed for worldwide positioning and navigation. Currently GNSS consist of the systems GPS, GLONASS, Galileo and BeiDou. Major application areas are the positioning of vehicles in air traffic or shipping, navigation systems in cars and route guidance systems integrated in smartphones.

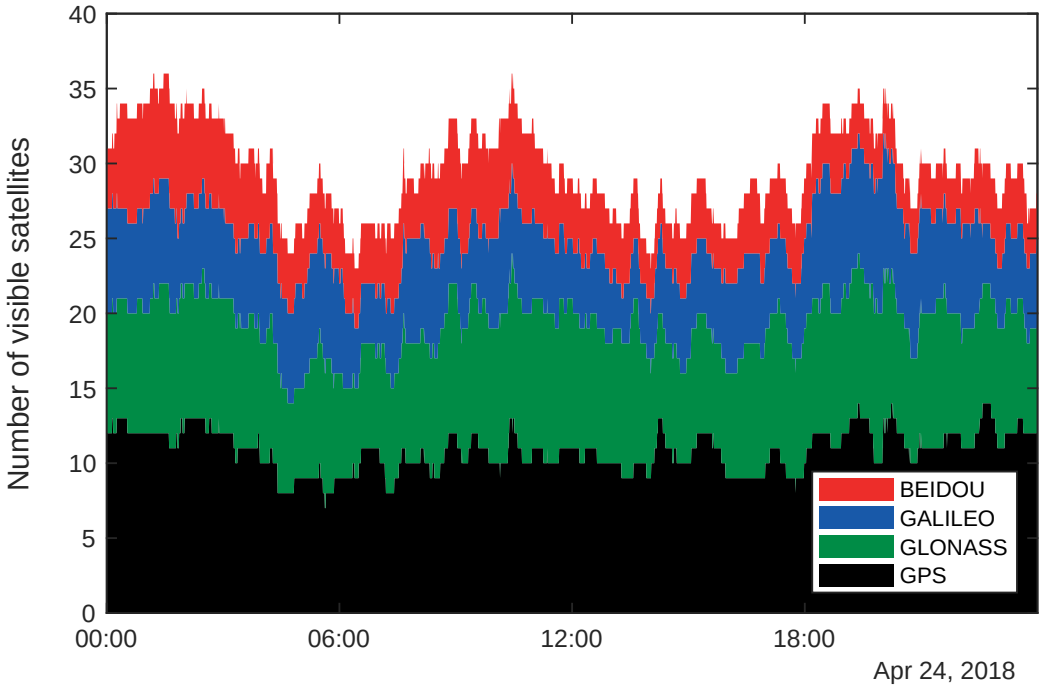

Figure 3.1: Satellite visibility for the EPOSA reference station in Linz, Austria, over a whole day

Because of the compatibility of the systems, a large number of satellites are available for users, which makes it much easier to cope with signal loss in urban canyons. Figure 3.1 shows the satellite visibility of the four systems GPS, Galileo, GLONASS and BeiDou for April 24, 2018 at a reference station in Linz, Austria. There are always 23 or more satellites visible. In 2020 there will be more than 100 GNSS satellites in orbit.

Each system consists of a space segment and a ground segment, realized by control stations. These are shortly described in the next chapters. For the realization of the Giomo Model, only GPS measurements were taken into account. For further details regarding the GNSS, please refer to the literature (Hofmann-Wellenhof *et al.*, 2008; Teunissen & Montenbruck, 2017).

3.1 Overview

3.1.1 Global Positioning System

The Global Positioning System (GPS), officially Navigational Satellite Timing and Ranging Global Positioning System (NAVSTAR GPS), was established in 1973 by the US Department of Defense and is now operated by the Joint Program Office (JPO). Originally it was designed for military purposes, to offer an accurate position, velocity and time for objects on land, sea, air and space. Since the 1980s it is open for civil use (Hofmann-Wellenhof *et al.*, 2008). Selective availability, an artificial signal degradation for civil users, was turned off in 2000.

The constellation is planned for 24 operational satellites in six orbital planes with an inclination of 55°, although there are usually about 30 satellites in orbit. The almost circular orbits have an altitude of about 20 200 km with a period of 11 hours and 58 minutes. Due to resonance with the rotation of the Earth GPS satellites need correcting pulses from time to time in order to keep the nominal orbits (Parkinson & Spilker Jr., 1996).

Since 2005 modernized satellites with a second (Block IIR-M) and a third (Block IIF) civil signal were launched. The first launch of a GPS III/IIIF satellite with a fourth civil signal has taken place on December 23, 2018.

Two services are provided by GPS, the Standard Positioning Service (SPS) and the Precise Positioning Service (PPS). SPS is freely available to all users and is transmitted on GPS L1 (GPS NAVSTAR Global Positioning System, 2008). PPS is provided on GPS L1 and L2, but admission is restricted (GPS NAVSTAR Global Positioning System, 2007).

3.1.1.1 GPS signal structure

GPS atomic clocks operate with a fundamental frequency of 10.23 MHz. This frequency is used to generate the signals.

Older satellites (Block IIA and IIR) only transmit the so called *legacy* signals L1 and L2 with the carrier frequencies of 1575.42 MHz and 1227.6 MHz, respectively. L1 is modulated with the coarse/acquisition (C/A) code and both L1 and L2 broadcast the precision (P(Y)) code, which is usually encrypted and used for military purposes.

Recent satellites transmit new *modernized* navigation signals. They include a new military (M) code on L1 and L2, a new civil signal L2C and the L5 code on the new carrier frequency at 1176.45 MHz. With the GPS III satellites another new civil signal L1C will be transmitted (Teunissen & Montenbruck, 2017). All GNSS signals are illustrated in Figure 3.2.

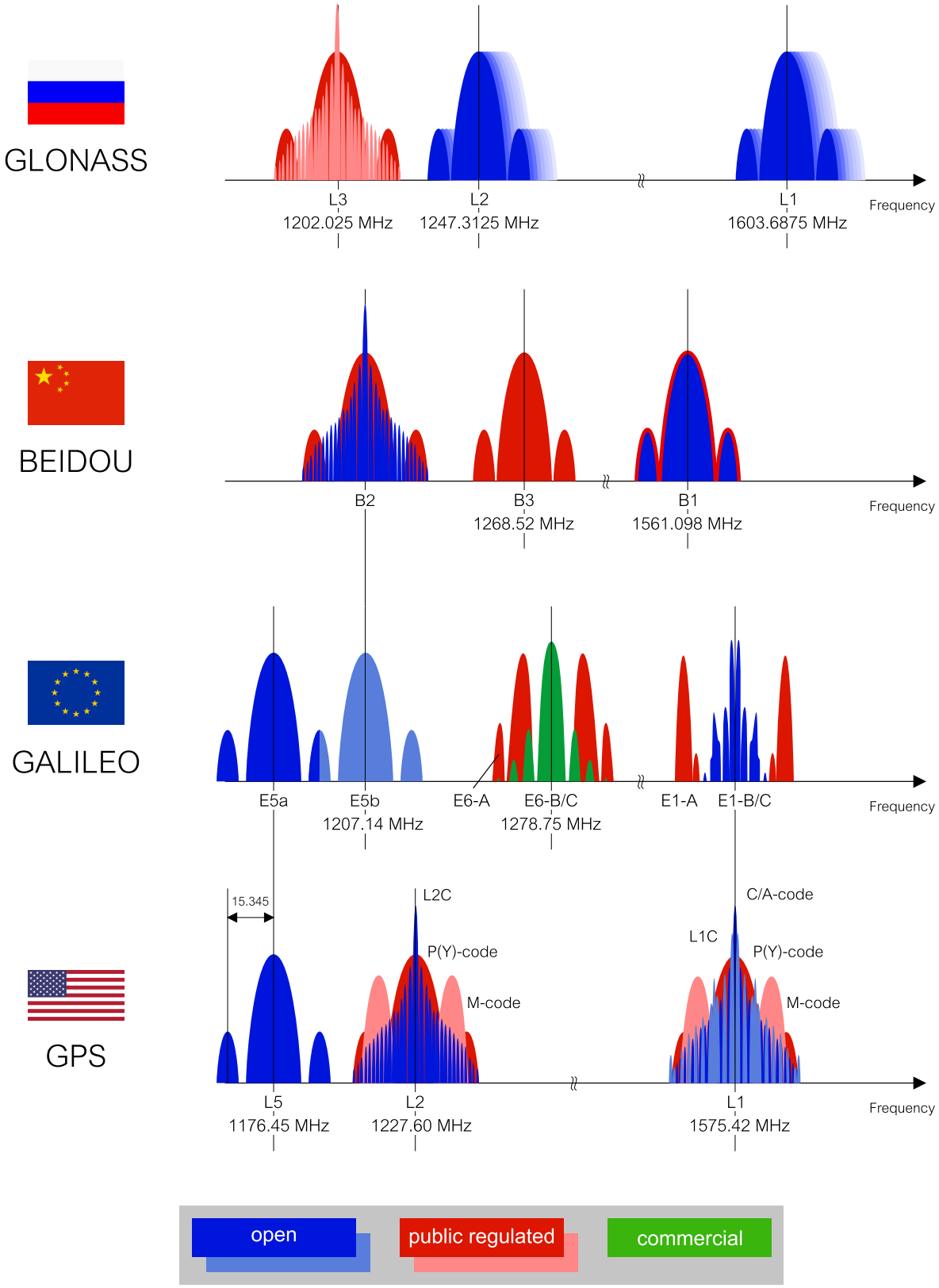

Figure 3.2: GNSS signal structure

3.1.2 GLONASS

Globalnaja Nawigazionnaja Sputnikowaja Sistema (GLONASS) is operated by the Russian Federation and similar to GPS nominally consists of 24 satellites. They orbit in an altitude of about 19 100 km in three circular planes (Walker 24/3/1 constellation) with an inclination of 64.8°, which secures visibility and improved geometry for positioning even in higher latitudes. The satellites' revolution period is 11 hours 15 minutes and 44 seconds, so after eight days the satellites pass over the same point on Earth again (Hofmann-Wellenhof *et al.*, 2008).

The system has been developed since 1972 and in 1982 first satellites were launched. 1995 there were already 24 satellites in orbit, but the financial crisis in the nineties resulted in a dramatic reduction. Full Operational Capability (FOC) was only reached again in the end of 2011 (Teunissen & Montenbruck, 2017).

GLONASS satellites are identified by their slot number, where the numbers 1–8 are assigned to satellites in the orbital plane I, 9–16 to plane II and 17–24 to plane III.

Like GPS, GLONASS provides an open service on three frequencies (L1, L2, L3) and a service for authorized users with encrypted signals on L1 and L2 (Teunissen & Montenbruck, 2017).

3.1.2.1 GLONASS signal structure

The first generation GLONASS I/II satellites (launched 1982–2005) and most of the second generation GLONASS-M satellites (launched 2003–2016) only provide Frequency Division Multiple Access (FDMA) signals. The third generation GLONASS-K (launched 2011–2018) and GLONASS-K2 satellites (from 2018 onwards) provide both, FDMA and Code Division Multiple Access (CDMA), in order to increase interoperability to GPS (Teunissen & Montenbruck, 2017).

With FDMA modulation the two antipodal GLONASS satellites of each orbital plane transmit on the same frequency, because they are not visible at the same time for terrestrial users. Different channels ($k = -7, -6, ..., 6$) define the frequencies on L1 and L2 (Seeber, 2003):

$$f_{\mathrm{L1}}(k) = 1602\ \mathrm{MHz} + k \cdot 0.5625\ \mathrm{MHz} \tag{3.1}$$

$$f_{\mathrm{L2}}(k) = 1246\ \mathrm{MHz} + k \cdot 0.4375\ \mathrm{MHz} \tag{3.2}$$

Due to improved accuracy, improved interference liability and enhanced possibilities to separate open and authorized service GLONASS decided to add CDMA signals to their constellation.

GLONASS-M satellites transmit a C/A-code and a P-code on the frequencies L1 and L2, GLONASS-K satellites additionally transmit a C/A-code on L3 in CDMA mode. GLONASS-K2 satellites will provide all of the prior signals plus C/A- and P-codes on L1 and L2 in CDMA modulation. Table 3.1 shows an overview of the transmitted signals for each satellite type (Teunissen & Montenbruck, 2017). They are also displayed in Figure 3.2.

Satellites	L1	L2	L3
GLONASS I/II	L1OF		
	L1SF	L2SF	
GLONASS-M	L1OF	L2OF	
	L1SF	L2SF	
			(L3OC)
GLONASS-K	L1OF	L2OF	
	L1SF	L2SF	
			L3OC
GLONASS-K2	L1OF	L2OF	
	L1SF	L2SF	
	L1OC	L2OC	L3OC
	L1SC	L2SC	

Table 3.1: GLONASS signal overview: Service type O (open) or S (authorized special), modulation type F (FDMA) or C (CDMA)

3.1.3 Galileo

The Global Navigation Satellite System Galileo was built up in cooperation of the European Space Agency (ESA) and the European Commission (EC). Galileo consists of nominally 24 satellites with 6 spare satellites (Teunissen & Montenbruck, 2017). According to plan they orbit in a Walker constellation (24/3/1) with an inclination of 56° in an altitude of 23 260 km. After 17 orbits (10 days) the satellites' ground track is repeated, so their revolution period is 14 hours, 4 minutes and 42 seconds.

In 2011 and 2012 four In Orbit Validation (IOV) satellites were launched followed by the first FOC satellites in 2014. Unfortunately these were released into the wrong orbits due to problems with the carrier rocket.

Up to now (July 2018) 26 (4 IOV/ 22 FOC) satellites were brought into orbit, the last four on July 25, 2018. There are no more launches scheduled until 2020.

Galileo provides four services, the Open Service (OS), the Public Regulated Service (PRS), the Commercial Service (CS) and the Search and Rescue Service (SAR). As the name tells OS is open for public use, PRS is reserved for authorized users (Teunissen & Montenbruck, 2017). Contrary to the CS Commercial Authentication Service (CAS), the CS High Accuracy Service (HAS) is not encrypted.

3.1.3.1 Galileo signal structure

Galileo transmits on three frequencies: E1 (1575.420 MHz), which corresponds to GPS L1, E5 (1191.795 MHz) and E6 (1278.750 MHz). E5 offers two subbands E5a (1176.450 MHz) and E5b (1207.140 MHz) with a difference of ±15.345 MHz to the central carrier frequency. E5a is then aligned with GPS L5. The overall signal E5 is also used as an alternative Binary Offset Carrier (BOC) (AltBOC) signal with a very large signal bandwidth (European Union, December

2016). The signals are illustrated in Figure 3.2.

All Galileo signals provide a pair of pilot and data components. The pilot component is used for pseudorange determination whereas the data component carries mainly the navigation message. They are transmitted at the same time at the same frequency and have the same noise characteristics (Borio & Lo Presti, 2008).

3.1.4 BeiDou

The Chinese Global Navigation Satellite System BeiDou is named after the asterism *the Big Dipper* (US) or *the Plough* (UK), in Chinese BeiDou.

BeiDou consists nominally of 27 Medium Earth Orbit (MEO) satellites, five Geostationary Orbit (GEO) satellites and three Inclined Geosynchronous Orbit (IGSO) satellites. The GEO satellites are positioned at 58.75°E, 80°E, 110.5°E, 140°E and 160°E. The IGSO satellites operate in three different planes in an altitude of 36 000 km. MEO and IGSO orbits have an inclination of 55°, the MEO satellites have an altitude of 21 500 km.

The global system BeiDou-3 is the third generation of BeiDou, following the regional BeiDou-2 or COMPASS system. So the constellation of BeiDou-2 will also be part of BeiDou-3. Until now (July 2018) 29 satellites are in orbit, but almost half of them are undergoing testing or commissioning. The satellite constellation should be completed by 2020.

3.1.4.1 BeiDou signal structure

BeiDou will offer an open service and an authorized service transmitting on four frequencies. They are called B1, B2, B3 and Bs with their center frequencies at 1575.42 MHz, 1191.795 MHz, 1268.52 MHz and 2492.028 MHz. B1 has two signals B1-A, which is authorized, and B1-C, which is open. B2, which matches the Galileo E5b signal, is also modulated with two open signals B2a and B2b. Also B3 consists of two authorized signals B3 and B3-A as well as Bs of Bs-D and Bs-P (Teunissen & Montenbruck, 2017). Currently (December 2018) there is a lack of B3 observations. The signals are visualized in Figure 3.2.

3.2 Observation equations

In case of synchronized clocks positioning using GNSS is based on trilateration, i.e., the determination of the position by measurements of (at least) three distances. These distances are measured ranges between a satellite (superscript s in subsequent equations) and the receiver (subscript r).

The observables of GNSS positioning are, thus, code and phase measurements between satellites and receivers. As GNSS is a passive or one-way system, biases due to receiver and satellite clocks are introduced and have to be corrected for. The following chapter summarizes the observations equations of both code and phase measurements.

3.2.1 Code Measurements

GNSS receivers do not measure ranges directly, but determine pseudoranges (P) being the time difference between the receiver's and satellite's clocks, multiplied by the speed of light c:

$$P_r^s = c(t_r(r) - t^s(s)) \tag{3.3}$$

where P_r^s is the code observable (pseudorange) [m], c is the speed of light in vacuum [m/s], $t_r(r)$ is the receiving time in the receiver's time frame in [s], and $t^s(s)$ is the transmitting time in the satellite's time frame in [s].

In order to describe both clock readings in Equation (3.3) in a common time frame, the pseudorange observation can be written as (Seeber, 2003)

$$P_r^s = c\,[(t_r + \delta t_r) - (t^s + \delta t^s)] = c(\Delta t + \Delta\delta t) \tag{3.4}$$

where t_r and t^s (and also their difference $\Delta t = t_r - t^s$) refer to the same time frame. δt_r and δt^s denote time-dependent clock biases of receiver and satellite, respectively.

The product $c\Delta t$ calculated from the code travel time Δt corresponds to the distance between the satellite at t^s and the receiver at t_r. Due to multipath, measurement noise and systematic effects like atmospheric and instrumental delays, $c\Delta t$ is not equal to the geometric distance between the two points. More details on error sources of GNSS measurements are given in Section 3.3 or in the literature (Hofmann-Wellenhof *et al.*, 2008; Parkinson & Spilker Jr., 1996; Teunissen & Montenbruck, 2017).

The observation equation for code measurements including the major error sources reads (Limberger, 2015, Equation (3.7))

$$P_r^s = c(t_r - t^s) + c(\delta t_r - \delta t^s) + \xi_r^s + c(d_r - d^s) + c\delta t_{\text{rel}} + I_r^s + T_r^s + \text{MP}_r + \varepsilon_r^s \tag{3.5}$$

where ξ_r^s contains the phase center offsets of the receiver and satellite antennas; d_r and d^s denote hardware delays; δt_{rel} is the summarized effect of the relativistic clock correction and the relativistic delay; I_r^s denotes the (frequency-dependent) ionospheric delay; T_r^s describes the tropospheric delay; MP_r are multipath effects; and ε_r^s summarizes remaining errors and noise.

3.2.2 Phase Measurements

The carrier phase measurement is the difference between the received, Doppler-shifted signal and a reference signal generated by the receiver. This observable can be multiplied by the wavelength of the carrier (e.g. ≈19 cm for GPS L1) to obtain a range to the satellite. Such a phase measurement can be ≈100 times more precise than a code measurement (Blewitt, 2007, p. 367).

The simplified phase equation reads (Hofmann-Wellenhof *et al.*, 2008)

$$\begin{aligned}\varphi_r^s(t) &= \varphi_r(t) - \varphi^s(t) \\ &= f^s \frac{\rho}{c} - f^s \delta t^s + f_r \delta t_r - (f^s - f_r)t\end{aligned} \tag{3.6}$$

where φ^s is the phase of the received signal in [cycles] with frequency f^s, φ_r is the phase of the receiver-generated signal in [cycles] with frequency f_r, ρ is the range between satellite and receiver, c is the speed of light, and δt^s and δt_r denote clock biases of the satellite and the receiver, respectively. The epoch parameter t denotes the time passed since an initial epoch t_0 at which the initial phases are given by

$$\begin{aligned}\varphi_0^s &= -f^s \delta t^s \\ \varphi_{0r} &= -f_r \delta t_r.\end{aligned} \tag{3.7}$$

However, as the observable only measures the fractional phase within one full cycle, the main challenge is to derive the integer number of full wavelengths, usually referred to as ambiguity (Seeber, 2003; Teunissen & Montenbruck, 2017). This is required when a range is to be derived from phase measurements. If the number of full cycles at t_0 is N, the phase pseudorange is given by (Limberger, 2015, Equation (3.8))

$$\phi_r^s = c(t_r - t^s) + c(\delta t_r - \delta t^s) + \xi_r^s + c\delta t_{\text{rel}} - I_r^s + T_r^s + \text{MP}_r + \varepsilon_r^s + \lambda N \tag{3.8}$$

where ϕ_r^s is the carrier phase observable [m] and λ is the wavelength [m]. In several textbooks the sign of λN in the phase observation equation differs from Equation (3.8). This is due to the arbitrary chosen number of N depending on the receiver firmware.

3.3 Error sources

The measured time difference between the transmitter and the receiver multiplied by the speed of light is not equal to the geometric distance between the two. In addition to measurement noise, systematic biases affect both code and phase pseudorange measurements. Hofmann-Wellenhof *et al.* (2008) identifies three groups of errors: (1) Satellite-related errors, (2) signal propagation-related errors, and (3) receiver-related errors. The main errors of these groups are listed in Table 3.2.

Different errors (error groups) are dealt with using different approaches. Internal antenna and radome errors such as antenna phase center variations usually require calibration which can, however, be difficult. Other effects, such as satellite orbit errors can be strongly reduced by using more precise products such as final satellite orbits.

Other systematic errors of Table 3.2 can be modeled and are added to the observation equations (Equations (3.4) and (3.8)). These effects include signal propagation effects, i.e., tropo-

Table 3.2: Error sources of zero-difference GNSS pseudorange observations

Source	Effect	Order of magnitude
Satellite-related	Satellite clock error	0.02–1.5 m RMS[a]
	Satellite orbit errors	0.025–1 m RMS[a]
	Satellite hardware delay	0–3 m
	Satellite phase center variations	mm–cm
	Satellite phase center offset	1 m
Signal propagation	Ionospheric delay	<15 m (35 m at solar maximum)
	Tropospheric delay	<3 m (zenith direction) – 30 m (5° elevation)[b]
Receiver-related	Antenna phase center variation	mm–cm
	Receiver clock error	km
	Receiver hardware delay	m
	Multipath	m (Code), mm–cm (Phase)

[a] IGS http://www.igs.org/products, accessed: 2018-07-14
[b] IERS Conventions (2010), Böhm & Schuh (2006)

spheric and ionospheric delays, which are the major topic of this thesis, or relativistic corrections. Another possibility of treating errors is the estimation of these effects as part of the parameter adjustment (usually a Kalman filter or a least-squares adjustment). The receiver clock clearly requires this procedure. Tropospheric delays, on the other hand, are typically modeled using blind or measurement-demanding models or get estimated in the analysis. A very common parameter to be derived in the analysis of GNSS observations is the tropospheric zenith or slant delay.

Another state-of-the-art approach dealing with errors is the elimination using appropriate linear combinations of the measurements. This important procedure in the analysis of GNSS observations is presented in Section 3.4.

3.4 Combinations of observations

Building appropriate differences between receivers, satellites and/or epochs or combinations of the GNSS observables allows the elimination or heavy decrease of some of the systematic effects (Section 3.3).

3.4.1 GNSS Single, Double and Triple Differences

Following groups of differences can be identified (Seeber, 2003, p. 258):

- Between two receivers (r_1,r_2)
- Between two satellites (s_1,s_2)

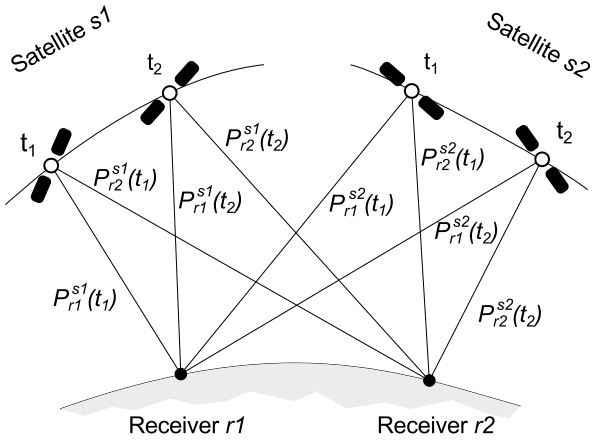

Figure 3.3: Scheme of GNSS differences

- Between two epochs (t_1, t_2),

The most common combinations are differences between stations and satellites, respectively. A scheme for GNSS differences is shown in Figure 3.3. The one-way observations $P_r^s(t)$ in Figure 3.3 denote zero-difference code (or phase) measurements. These can be differenced with respect to station, receiver or epoch, yielding single differences.

Typically, single differences between to two receivers (r_1,r_2) are formed (i.e., to the same satellite s),

$$P_{r12}^s = P_{r1}^s - P_{r2}^s. \tag{3.9}$$

This eliminates the satellite clock offset and the satellite hardware delay. As this single difference is contaminated with the receiver clock errors, it is well suited for time and frequency transfer (Schaer, 1999). Furthermore, the signal propagation error as well as the satellite orbit error only contains the differential effect, meaning that for nearby receivers these error sources are considerably decreased. On the other hand, when single differences between two satellites s_1 and s_2 are formed,

$$P_r^{s12} = P_r^{s1} - P_r^{s2}, \tag{3.10}$$

the receiver clock errors as well as the receiver biases are eliminated. The third possibility for single differences is to difference two epochs,

$$P_r^s(t_{12}) = P_r^s(t_1) - P_r^s(t_2). \tag{3.11}$$

In this case, the ambiguity term N in Equation (3.8) vanishes because the phase ambiguities at t_1 and t_2 are equal if there are no cycle slips (Seeber, 2003).

Differences between two single differences to satellites s_1 and s_2 of the form in Equation (3.9),

denote double differences

$$P_{r12}^{s12} = P_{r12}^{s1} - P_{r12}^{s2} \tag{3.12}$$

The receiver clock errors are eliminated in these measurements, which is the main reason why double differences are used (Hofmann-Wellenhof *et al.*, 2008, p. 175). The scheme shown in Figure 3.3 allows one double difference at time t_1 and one double difference at time t_2.

These two double differences can be differenced as well, resulting in a triple difference. Similar to single differences at two epochs (Equation (3.11)), triple differences do not contain ambiguities. The difficult task to determine the number of full cycles is, thus, obsolete. Triple differences are used for initial processing and data screening in GNSS analysis, but the disadvantages are a high noise level and high correlations between the observations (Schaer, 1999).

3.4.2 Common Linear Combinations

The previous section discusses combinations with respect to receiver, satellite, and epoch. Observations of the same type can also be combined by forming differences between carrier phases or code measurements, respectively. It should be noted, however, that all advantages come in turn with a disadvantage. For several common combinations the noise level is seriously increased. The number of possible linear combinations is unlimited, however, only some of them are useful for navigation and positioning purposes.

Urquhart (2009) identifies three main benefits linear combinations can fulfill: (1) The combined signal has a larger wavelength, which has advantages for solving ambiguities; (2) The ionospheric error is reduced compared to standard signals; or (3) The combined signal has a lower noise or multipath effect.

A linear combination of two carrier-phase observations in cycles is given by (Wübbena, 1989)

$$\Phi_{\kappa_1,\kappa_2} = \kappa_1\Phi_1 + \kappa_2\Phi_2 = \kappa_1 f_1 t + \kappa_2 f_2 t = f\,t \tag{3.13}$$

where κ_1 and κ_2 are the coefficients, $f = \kappa_1 f_1 + \kappa_2 f_2$ is the frequency and $\lambda = c/f$ is the wavelength of the combined signal.

Of course linear combinations can also comprise three or more signals, but this chapter concentrates on linear combinations with only two frequencies.

For units of meters, Equation (3.13) is given by

$$P_{\alpha_1,\alpha_2} = \alpha_1 P_1 + \alpha_2 P_2 \tag{3.14}$$

with the coefficients α_1 and α_2, being related to κ_1 and κ_2 by

$$\begin{aligned} \alpha_1 &= \frac{\lambda}{\kappa_1 \lambda_1} \\ \alpha_2 &= \frac{\lambda}{\kappa_2 \lambda_2} \end{aligned} \tag{3.15}$$

Increasing the frequency, e.g. $\kappa_1 = \kappa_2 = 1$ for L1 and L2 GNSS frequencies, decreases the wavelength. Decreasing the frequency, e.g. using $\kappa_1 = 1$ and $\kappa_2 = -1$, increases the wavelength. The former is, thus, called narrow-lane, the latter wide-lane. Both are important for solving ambiguities.

In case the two signals are uncorrelated, the noise level of the combination is

$$\sigma_{\Phi_{\kappa_1,\kappa_2}} = \sqrt{\kappa_1^2 \sigma_{f_1}^2 + \kappa_2^2 \sigma_{f_2}^2} \tag{3.16}$$

If the noise level is equal for both original phases ($\sigma_{f_1} = \sigma_{f_2}$), the noise level changes by $\sqrt{\kappa_1^2 + \kappa_2^2}$. For units of meters the noise level can be computed by

$$\sigma_{P_{\alpha_1,\alpha_2}} = \lambda \sigma_{\Phi_{\kappa_1,\kappa_2}} \tag{3.17}$$

The most common linear combinations are listed in Table 3.3. They are given for carrier-phase measurements but of course every linear combination can also be formed with pseudorange measurements.

The so-called **Melbourne-Wübbena linear combination L_{MW}** is a mixture of both. It consists of wide-lane carrier-phase observations and narrow-lane pseudorange observations. The combination is used for solving wide-lane ambiguities and to detect cycle slips. Equation (3.18) in [m] is an example for this linear combination with GPS L1 and L2 (Teunissen & Montenbruck, 2017).

$$\begin{aligned} L_{MW} &= \varphi_{WL} - P_{NL} \\ &= \frac{f_1}{f_1 - f_2}\varphi_1 - \frac{f_2}{f_1 - f_2}\varphi_2 - \frac{f_1}{f_1 + f_2}P_1 - \frac{f_2}{f_1 + f_2}P_2 \end{aligned} \tag{3.18}$$

The **ionosphere-free linear combination L_{IF}** is used to eliminate the first order ionospheric effect. As the ionosphere is an dispersive medium, different frequencies are affected in a different way. If two frequencies are available L_{IF} is built with (in [m]):

$$L_{IF} = \frac{f_1^2}{f_1^2 - f_2^2}L_1 - \frac{f_2^2}{f_1^2 - f_2^2}L_2 \tag{3.19}$$

A kind of ionosphere-free linear combination can also be applied for single-frequency measurements. It is then called GRAPHIC (group and phase ionospheric calibration) combination L_{GPH} and makes use of the opposite sign of the ionospheric error in carrier-phase and pseudorange

measurements. But the resulting combination suffers from the higher measurement noise of the pseudorange (Teunissen & Montenbruck, 2017).

$$L_{GPH} = \frac{1}{2}(\varphi_1 - P_1) \tag{3.20}$$

The **geometry-free or ionosphere linear combination L_{GF}** eliminates all non-dispersive elements of the observations. Consequently only the ionospheric part and satellite and receiver dependent hardware delays remain. Therefore this linear combination is perfect for estimating the ionospheric delay or to detect cycle slips (Glaner, 2017). Due to the fact that the ionosphere affects phase and code measurements with opposite signs, also the geometry-free combination is built in an opposite way. The equation is given in [m].

$$\begin{aligned} \varphi_{GF} &= \varphi_2 - \varphi_1 \\ P_{GF} &= P_1 - P_2 \end{aligned} \tag{3.21}$$

A more detailed description of the geometry-free linear combination, which is used for the computation of the Giomo Model, is provided in Chapter 4.2.

Table 3.3: Common linear combinations of GNSS observations (numbers refer to GPS, $f_0 = 10.230$ MHz). Coefficients $\kappa_{1,2}$ given in units of cycles (Teunissen & Montenbruck, 2017).

Name	λ	Signals		κ_1	κ_2	α_1	α_2	Purpose
L_1 ($f_1 = 1575.42$ MHz)	≈ 190 mm	L_1		1		1		GPS L1 signal
L_2 ($f_2 = 1227.60$ MHz)	≈ 244 mm	L_2		1		1		GPS L2 signal
L_5 ($f_5 = 1176.45$ MHz)	≈ 255 mm	L_5		1		1		GPS L5 signal
Narrow-Lane L_{NL}	≈ 107 mm	L_1	L_2	1	1	$\frac{f_1}{f_1+f_2}$	$\frac{f_2}{f_1+f_2}$	geometry-preserving, used for ambiguity resolution
Medium-Lane L_{ML}	≈ 751 mm	L_1	L_5	1	-1	$\frac{f_1}{f_1-f_5}$	$-\frac{f_5}{f_1-f_5}$	used for ambiguity resolution
Wide-Lane L_{WL}	≈ 862 mm	L_1	L_2	1	-1	$\frac{f_1}{f_1-f_2}$	$-\frac{f_2}{f_1-f_2}$	geometry-preserving, used for ambiguity resolution
Extra Wide-Lane L_{EWL}	≈ 5861 mm	L_2	L_5	1	-1	$\frac{f_2}{f_2-f_5}$	$-\frac{f_5}{f_2-f_5}$	used for ambiguity resolution
Ionosphere-free L_{IF}	≈ 107 mm	L_1	L_2			$\frac{f_1^2}{f_1^2-f_2^2}$	$-\frac{f_2^2}{f_1^2-f_2^2}$	eliminates ionospheric refraction
Geometry-free L_{GF}	∞	L_1	L_2			1	-1	eliminates all non-dispersive parts of the observations, used for computation of the TEC

Chapter 4

Ionospheric propagation delay derived from GNSS

The main purpose of all GNSS is to deliver accurate positions all over the world at any time for military and civil purposes. But GNSS signals can also be used for a wide range of other applications, for example for monitoring and modeling the ionosphere.

With dual-frequency receivers the ionospheric range error can be eliminated because it is frequency dependent. On the other hand lots of single-frequency receivers nowadays are used because they are much cheaper. They are also integrated in each smartphone. With only one frequency the user cannot eliminate the ionospheric range error, so it has to be corrected by a ionospheric model. These models can be obtained from measurement data from global or regional distributed GNSS reference stations.

4.1 Definitions

4.1.1 Solar-fixed/geomagnetic coordinates

The behavior of the ionosphere depends on two main processes: the geomagnetic field and the solar activity (see Chapter 2.2). To account for these processes in modeling the ionosphere, convenient coordinate systems are introduced.

The **solar-fixed system** rotates with respect to the Sun, resulting in a low variation of the electron density for the coordinates. This allows to average the TEC over a short period, e.g. for 1 – 2 hours (Böhm & Schuh, 2013). The origin of the system is the Earth's center of mass and the rotation axis is defined as Z-axis. For the X-axis the mean solar meridian is chosen and the Y-axis is the completion to a right-handed system, which can be seen on Figure 4.1. Geographic coordinates (φ_g,λ_g) can be transformed to the solar-fixed system (φ_s,s) with the following equation:

$$\begin{aligned} \varphi_s &= \varphi_g \\ \lambda_s = s &= \lambda_g + \mathrm{UT} - \pi = \lambda_g + a \cdot (\mathrm{UT} - 12)^{\mathrm{hours}} \end{aligned} \tag{4.1}$$

where φ and λ are in degrees and UT stands for the Universal Time in hours, so the term $(\mathrm{UT} - 12)^{\mathrm{hours}}$ has to be multiplied by $a = 15°/\mathrm{hour}$. It can be seen that the latitude stays the same while the solar-fixed longitude s is equal to the hour angle of the mean Sun.

Due to the nonuniform motion of the Sun the apparent solar time is not equal to the mean solar time. This means that the true length of a day varies over the year, adding up to seasonal deviations from about -14 to +16 minutes compared to the mean solar time (McCarthy & Seidelmann, 2018). Because of this reason the solar-fixed system does not reflect the real position of the Sun, which should be kept in mind for the Chapters 5 and 6.

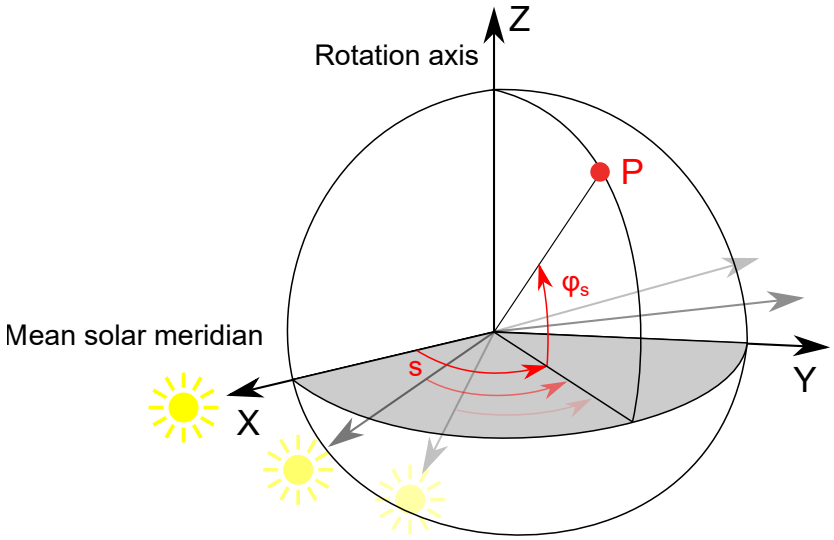

Figure 4.1: Solar-fixed coordinate system

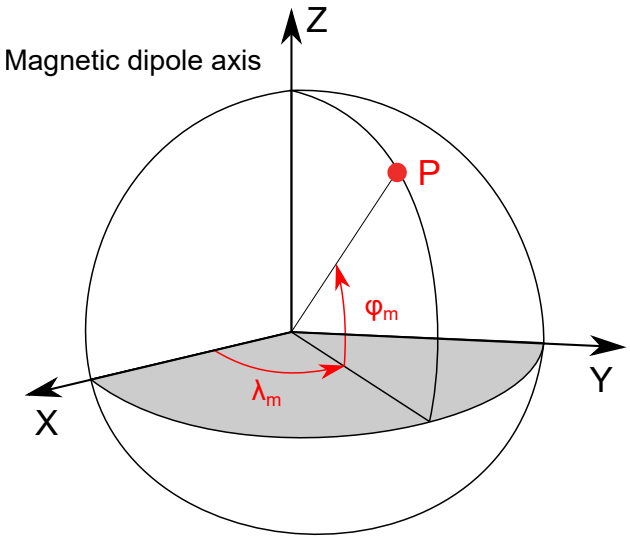

Figure 4.2: Geomagnetic coordinate system

The Z-axis of the **geomagnetic system** (see Figure 4.2) is parallel to the axis of the magnetic dipole and the Y-axis is perpendicular to the Z-axis and to the Earth's rotation axis. This means,

that if **D** is the direction of the dipole axis and **S** is the axis of the geographic poles pointing towards the South Pole, it results in $\mathbf{Y} = \mathbf{D} \times \mathbf{S}$. The X-axis completes the right-handed system. The following equations show the relation between geographic coordinates (φ_g,λ_g) and geomagnetic coordinates (φ_m,λ_m) (Böhm & Schuh, 2013):

$$\begin{aligned} \sin\varphi_m &= \sin\varphi_g \sin\varphi_0 + \cos\varphi_g \cos\varphi_0 \cos(\lambda_g - \lambda_0) \\ \sin\lambda_m &= \frac{\cos\varphi_g \sin(\lambda_g - \lambda_0)}{\cos\varphi_m} \end{aligned} \tag{4.2}$$

with the geographic coordinates of the geomagnetic South Pole φ_0 and λ_0. Currently (July 2018) the coordinates of the geomagnetic South Pole are $\varphi_0 = 80.33°$ N, $\lambda_0 = -72.67°$ E.

4.1.2 Single-layer model

For simplification in most ionosphere models the electrons of the ionosphere are assumed to be in an infinitesimal thin layer in a constant height h above the Earth's surface (Montenbruck *et al.*, 2014a). The intersection point of the signal path between the receiver and the satellite and the single-layer is called Ionospheric Pierce Point (IPP). The IPP's projection to the Earth's surface is defined as sub-ionospheric point (Hernández-Pajares *et al.*, 2009).

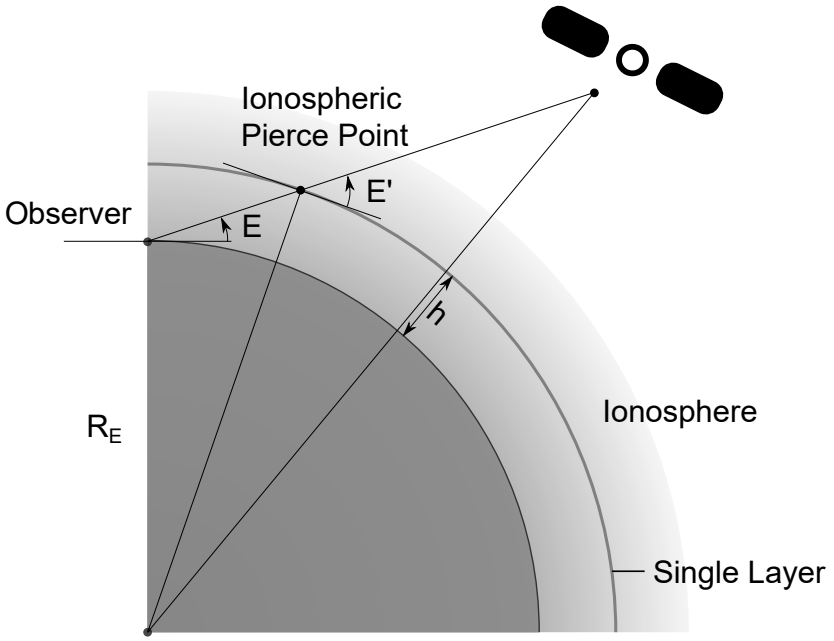

Figure 4.3: Single-layer model for the ionosphere

Figure 4.3 shows a sketch of a single-layer model for the ionosphere. The elevation angle of the satellite seen from the observer on the Earth's surface is denoted with E, while E' stands for the elevation of the satellite at the IPP. The corresponding zenith angles (in radians) can be calculated via $z = \pi/2 - E$ and $z' = \pi/2 - E'$. The relation between the two zenith angles is given by:

$$\sin z' = \frac{R_E}{R_E + h} \sin z \tag{4.3}$$

The height h of the single-layer is typically chosen between 350 km and 550 km, which is slightly above the height of the electron maximum at the F_2-peak (Böhm & Schuh, 2013). $R_E = 6371$ km is the mean Earth radius.

4.1.3 Mapping functions

In ionosphere products gained from GNSS measurements usually the VTEC is considered. As GNSS signal paths deliver STEC values instead, the ratio between STEC and VTEC is indicated by a zenith angle dependent mapping function M, also called **Single-Layer Model Mapping Function (SLM MF)**:

$$M(z) = \frac{STEC}{VTEC} \cong \frac{1}{\cos z'} = \frac{1}{\sqrt{1 - \sin^2 z'}} \tag{4.4}$$

By applying Equation (4.3) the mapping function results in:

$$M(z) = \frac{1}{\sqrt{1 - \left(\frac{R_E}{R_E + h} \sin z\right)^2}} \tag{4.5}$$

where typically the height $h = 450$ km is chosen and $R_E = 6371$ km is the mean Earth radius. VTEC and STEC and their relation can be seen in Figure 4.4. The vertical TEC is measured in zenith direction whereas the slant TEC is the TEC in direction of the satellite under the zenith angle z.

A modernized version of the SLM MF was developed at the Center for Orbit Determination in Europe (CODE), named **Modified Single-Layer Model Mapping Function (MSLM)** (Dach *et al.*, 1998, p. 317), which fits best the Extended Slab Model (ESM) mapping function from Jet Propulsion Laboratory (JPL) (Coster *et al.*, 1992).

$$M(z) = \frac{1}{\sqrt{1 - \left(\frac{R_E}{R_E + h} \sin \alpha z\right)^2}} \tag{4.6}$$

For the added factor $\alpha = 0.9782$ and for the height $h = 506.7$ km is chosen.

Lyu *et al.* (2018) propose the **Barcelona Ionospheric Mapping Function (BIMF)**. It represents the ionosphere in a more realistic way than a single-layer mapping function, as it is based on an estimation of the topside electron content fraction of VTEC ($= \mu_2$). A two-layer model is used, where the first layer is defined between 110 and 790 km and the second one from 790 to

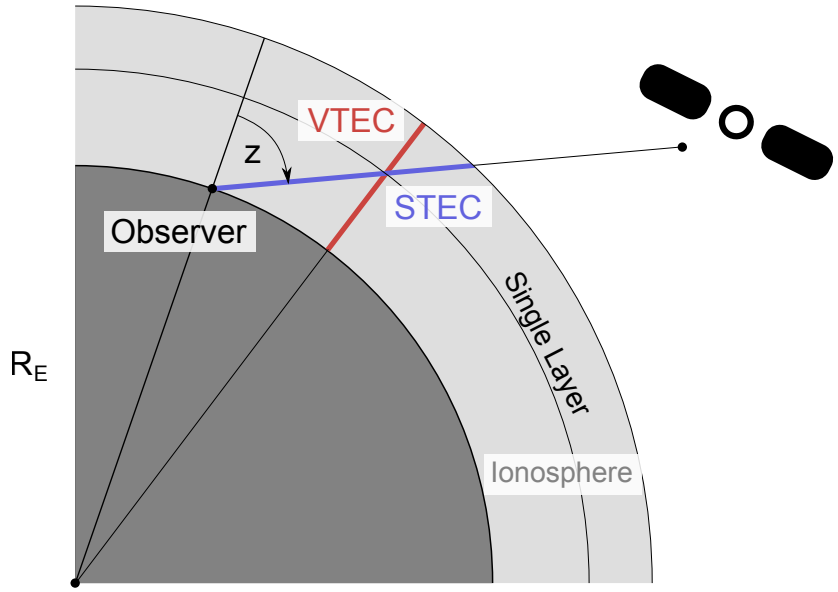

Figure 4.4: Relation between VTEC (TEC in zenith direction) and STEC (TEC in arbitrary direction)

1470 km, with the two central heights 450 km and 1130 km (= IPP_1 and IPP_2).

Two ratio values μ_1 and μ_2 are defined:

$$\begin{aligned} \mu_1 &= \frac{N_1}{N_1+N_2} = \frac{P_1}{P_1+P_2} = \frac{P_1}{V} \\ \mu_2 &= \frac{N_2}{N_1+N_2} = \frac{P_2}{P_1+P_2} = \frac{P_2}{V} \end{aligned} \tag{4.7}$$

where N_1 and N_2 represent the mean electron densities of both layers, V characterizes the VTEC of the whole ionosphere and P_1 and P_2 are the partial vertical electron contents of both layers.

The STEC is then computed with the following equation:

$$\begin{aligned} \text{STEC} &= P_1 \cdot M_1 + P_2 \cdot M_2 \\ &= M_1 \cdot \mu_1 V + M_2 \cdot \mu_2 V \\ &= (1-\mu_2) M_1 V + \mu_2 M_2 V \end{aligned} \tag{4.8}$$

where M_1 and M_2 are standard mapping functions (cf. Equation (4.4)). The key parameter of the function is μ_2, which corresponds to the shape function of the second layer. The Universitat Politècnica de Catalunya (UPC) forecasts and provides μ_2 as a function of space, time and latitude. Further details can be obtained in Lyu *et al.* (2018).

4.2 Geometry-free Linear Combination

The geometry-free linear combination allows to extract the signal delay caused by the ionosphere. By building the difference between two signals or carriers of the same epoch, e.g. GPS L1 and GPS L2, the geometric term and all frequency independent effects of the observation equation get eliminated. These include for example the clock biases and the tropospheric delay (Todorova, 2009).

Following the denotation in Chapter 3.2, the observation equations for **carrier-phases** at the frequencies L1 and L2 read

$$\begin{aligned} \mathrm{L}_1 &= \rho + c(\delta t_r - \delta t^s) - I^s_{r,\mathrm{L1}} + T^s_r + \varepsilon^s_{r,L1} + \lambda_{\mathrm{L1}} B_{\mathrm{L1}} \\ \mathrm{L}_2 &= \rho + c(\delta t_r - \delta t^s) - I^s_{r,\mathrm{L2}} + T^s_r + \varepsilon^s_{r,L2} + \lambda_{\mathrm{L2}} B_{\mathrm{L2}} \end{aligned} \tag{4.9}$$

where B contains the integer carrier-phase ambiguity N and the frequency-dependent hardware delays of the satellite and the receiver, which cannot be separated (Schaer, 1999).

The geometry-free linear combination for carrier-phase measurements in [m] is then built with

$$\mathrm{L}_{\mathrm{GF}} = \alpha_{1,\mathrm{GF}}\, \mathrm{L}_1 + \alpha_{2,\mathrm{GF}}\, \mathrm{L}_2 \tag{4.10}$$

Assigning

$$\alpha_{1,\mathrm{GF}} = -1 \;\text{ and }\; \alpha_{2,\mathrm{GF}} = 1 \tag{4.11}$$

results in

$$\mathrm{L}_{\mathrm{GF}} = \mathrm{L}_2 - \mathrm{L}_1 = -\xi_{\mathrm{GF}}\, I + B_{\mathrm{GF}} + \varepsilon_{L_{\mathrm{GF}}} \tag{4.12}$$

where $B_{\mathrm{GF}} = \lambda_{\mathrm{L1}} B_{\mathrm{L1}} - \lambda_{\mathrm{L2}} B_{\mathrm{L2}}$. The factor $\xi_{\mathrm{GF}} = 1 - f^2_{L1}/f^2_{L2}$ relates the ionospheric refraction on L_{GF} to L_1.

The observation equations for **pseudorange measurements $\mathbf{P}_1$, $\mathbf{P}_2$** on the frequencies L1 and L2 can be expressed by

$$\begin{aligned} \mathrm{P}_1 &= \rho + c(\delta t_r - \delta t^s) + I^s_{r,\mathrm{P1}} + T^s_r + c(d_r - d^s)_{\mathrm{P1}} + \varepsilon^s_{r,P1} \\ \mathrm{P}_2 &= \rho + c(\delta t_r - \delta t^s) + I^s_{r,\mathrm{P2}} + T^s_r + c(d_r - d^s)_{\mathrm{P2}} + \varepsilon^s_{r,P2} \end{aligned} \tag{4.13}$$

where d_r and d^s denote the frequency-dependent hardware delays of the satellite (s) and the receiver (r).

The geometry-free linear combination for code measurements in [m] is then built with

$$\mathrm{P}_{\mathrm{GF}} = \beta_{1,\mathrm{GF}}\, \mathrm{P}_1 + \beta_{2,\mathrm{GF}}\, \mathrm{P}_2 \tag{4.14}$$

and

$$\beta_{1,\mathrm{GF}} = 1 \quad \text{and} \quad \beta_{2,\mathrm{GF}} = -1 \tag{4.15}$$

and results in

$$\mathrm{P}_{\mathrm{GF}} = \mathrm{P}_1 - \mathrm{P}_2 = \xi_{\mathrm{GF}}\, I + c(\mathrm{DCB}_r - \mathrm{DCB}^s) + \varepsilon_{P_{\mathrm{GF}}} \tag{4.16}$$

In Equation (4.16) $\mathrm{DCB}_r = d_{r,\mathrm{P1}} - d_{r,\mathrm{P2}}$ and $\mathrm{DCB}^s = d^s_{\mathrm{P1}} - d^s_{\mathrm{P2}}$ denote the differential inter-frequency hardware delays of the receiver (r) and the satellite (s), also called Differential Code Biases (DCBs), which are described in Chapter 4.3 (Jin *et al.*, 2012) in more detail.

The ionospheric refraction I can be expressed via

$$I = \vartheta\ \mathrm{STEC}(\beta, s) = \vartheta\ M(z)\ \mathrm{VTEC}(\beta, s) \tag{4.17}$$

where $M(z)$ is the mapping function (see Equation (4.5)) and β and s are the geomagnetic latitude and the solar-fixed longitude (see Chapter 4.1.1). For the GPS frequency f_1 the factor $\vartheta = \dfrac{40.309 \cdot 10^{16}}{f_1^2}$ (see Equation (2.20)) gives approximately 0.162 m/TECU.

Finally, by substituting Equation (4.17) in the Equations (4.16) and (4.12) the geometry-free linear combination results in

$$\mathrm{L}_{\mathrm{GF}} = -\xi_{\mathrm{GF}}\ \vartheta\ M(z)\ \mathrm{VTEC}(\beta, s) + B_{\mathrm{GF}} + \varepsilon_{L_{\mathrm{GF}}} \tag{4.18}$$

$$\mathrm{P}_{\mathrm{GF}} = \xi_{\mathrm{GF}}\ \vartheta\ M(z)\ \mathrm{VTEC}(\beta, s) + c(\mathrm{DCB}_r - \mathrm{DCB}^s) + \varepsilon_{P_{\mathrm{GF}}} \tag{4.19}$$

4.3 Differential Code Biases (DCBs)

Differential Code Biases (DCBs) have to be considered when dealing with ionosphere calculations based on GNSS code measurements. DCBs are a result of hardware delays in satellites and receivers. As stated in Chapter 4.2 the DCBs are frequency dependent, but also differ dependent on the tracked signal type, the kind of GNSS and the tracking technology (Dach *et al.*, 1998).

4.3.1 Origin of DCBs

DCBs are small time delays induced by the hardware of the satellite or the receiver. So the emission time given by the satellite clock differs from the real emission time of the signal and the reception time given by the receiver clock differs from the real reception time (see Figure 4.5).

The clock terms as well as the hardware delays are part of the Equations (4.13). By building double-differences it is assumed that the clock terms drop out, but the DCBs remain in the equation as long as they are not identical for the two satellites or receivers.

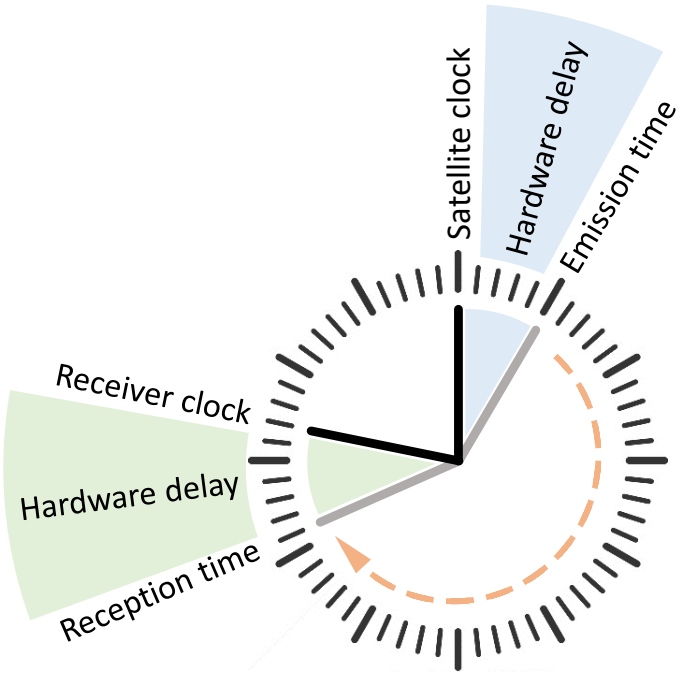

Figure 4.5: Definition of satellite and receiver hardware delays

For example if a receiver tracks the signals P1 and P2 (GPS) and the geometry-free linear combination is built, the difference between the two hardware delays (= DCB) should be considered. This can be done via the two equations:

$$\begin{aligned} d_{\mathrm{P1}} &= d_{\mathrm{P2}} + \mathrm{DCB}_{\mathrm{P1,P2}} \\ \mathrm{DCB}_{\mathrm{P2,P1}} + d_{\mathrm{P1}} &= d_{\mathrm{P2}} \end{aligned} \tag{4.20}$$

They are equivalent as $\mathrm{DCB}_{\mathrm{P1,P2}} = -\mathrm{DCB}_{\mathrm{P2,P1}}$. Of course DCBs exist for all signal differences, e.g. $\mathrm{DCB}_{\mathrm{P1,P2}}$, $\mathrm{DCB}_{\mathrm{P1,C2}}$ or $\mathrm{DCB}_{\mathrm{P2,C2}}$.

Because of the assumption that all DCBs can be shifted by a common bias and for that only relative DCBs have to be taken into account, a zero-mean condition is applied (Schaer, 1999):

$$\frac{1}{n}\sum_{i=1}^{n}\mathrm{DCB}^{i} = 0 \tag{4.21}$$

where n represents the total number of satellites.

DCBs are stable over a long time and do not jump rapidly. Figure 4.6 shows the monthly average of the GPS P1-P2 satellite DCBs calculated by CODE. The different satellites can be identified by their Pseudorandom Noise (PRN) number. In March 2018 PRN18 retired, which can be seen in the jump of the DCB. PRN32 was replaced by another satellite in February 2016 (`https://en.wikipedia.org/wiki/List_of_GPS_satellites#cite_note-NANU2018015-45`, accessed: 18.07.2018, 19:15). PRN04 is used for test transmissions for reserve satellites, so the DCB

value changes continuously (`http://gpsworld.com/the-almanac/`, accessed: 18.07.2018, 19:19). All other satellites have very stable DCBs with a day-to-day reproducibility RMS of about 0.05 ns (Dach *et al.*, 1998).

Satellite $DCB_{P1,P2}$s are in the range of about -10 to 10 ns for GPS. This causes a delay of up to 30 TECU (1 ns ≅ 2.86 TECU at L4 frequency (∼ 1958.677 MHz, LC_{GF}) and 1 TECU ≅ 0.162 m delay on frequency L1) (Li *et al.*, 2012). Compared to $DCB_{P1,P2}$ the order of magnitude of DCBs on the same frequency, like $DCB_{P1,C1}$ or $DCB_{P2,C2}$, is three times smaller (Dach *et al.*, 1998).

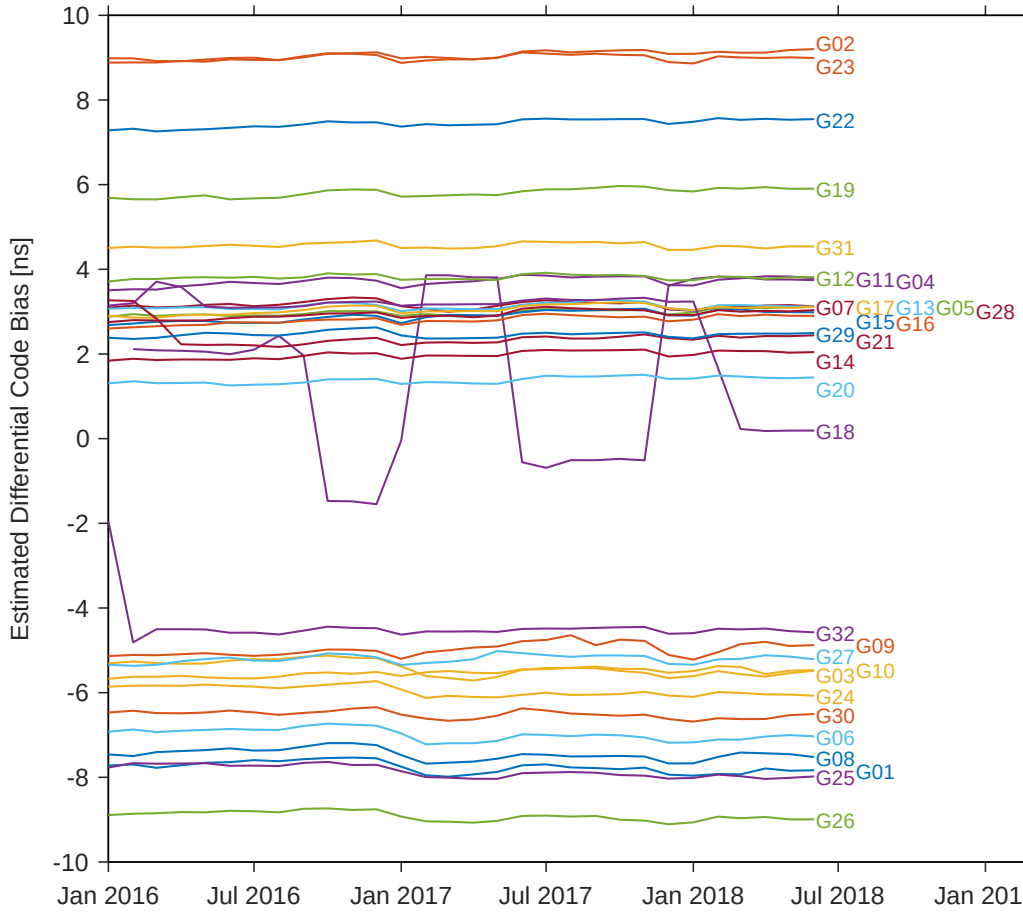

Figure 4.6: GPS P1-P2 satellite DCBs monthly average in [ns] for January 2016 to June 2018, satellites are identified by their PRN number, data source: CODE

Figure 4.7 displays the monthly average of the GPS P1-P2 station DCBs calculated by CODE. The different IGS stations can be identified via their 4-character site name. The major jumps are due to receiver changes at the particular stations, e.g. at ALBH (Victoria, Canada) and DRAO (Penticton, Canada) in June 2016 (`ftp://ftp.igs.org/pub/station/log/albh_20180411.log` and `ftp://ftp.igs.org/pub/station/log/drao_20180504.log`, accessed: 18.07.2018, 19:41) or DUBO (Lac du Bonnet, Canada) in February and June 2017 (`ftp://ftp.igs.org/pub/station/log/dubo_20170626.log`, accessed: 18.07.2018, 19:48). It can be seen that the station DCBs are not as stable as the satellite DCBs.

They are also slightly larger, in the range of about -13 to 17 ns for GPS.

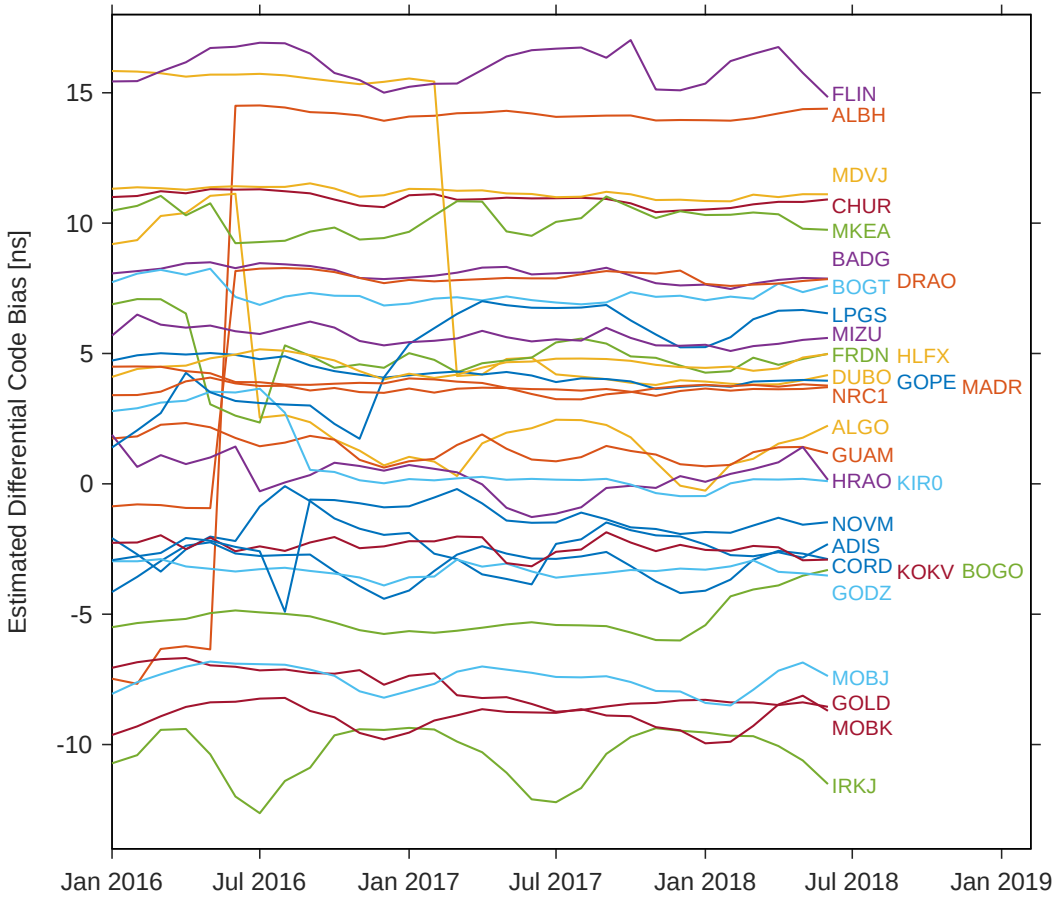

Figure 4.7: GPS P1-P2 IGS station DCBs monthly average in [ns] for January 2016 to June 2018, stations are identified by their IGS 4-character site name, data source: CODE

Also receiver DCBs for GLONASS stations are provided by CODE, they are visualized in Figure 4.8. It can be observed that the jumps in the time series belong to the same receiver changes as with GPS (Figure 4.7).

Besides for ionosphere analysis, DCBs are significant for positions derived by code measurements only, and if different receiver models are part of a solution, e.g. in precise clock estimation or ambiguity resolution using the Melbourne-Wübbena linear combination (Dach *et al.*, 1998).

4.3.2 Correlation between DCBs and TGDs

The Total Group Delay (TGD) is broadcasted with the GPS navigation message and is proportional to the DCBs (Sanz Subirana *et al.*, 2013):

$$\mathrm{TGD}_{\mathrm{P1}} = -\hat{\vartheta}_1 \, \mathrm{DCB}_{\mathrm{P2,P1}} \tag{4.22}$$

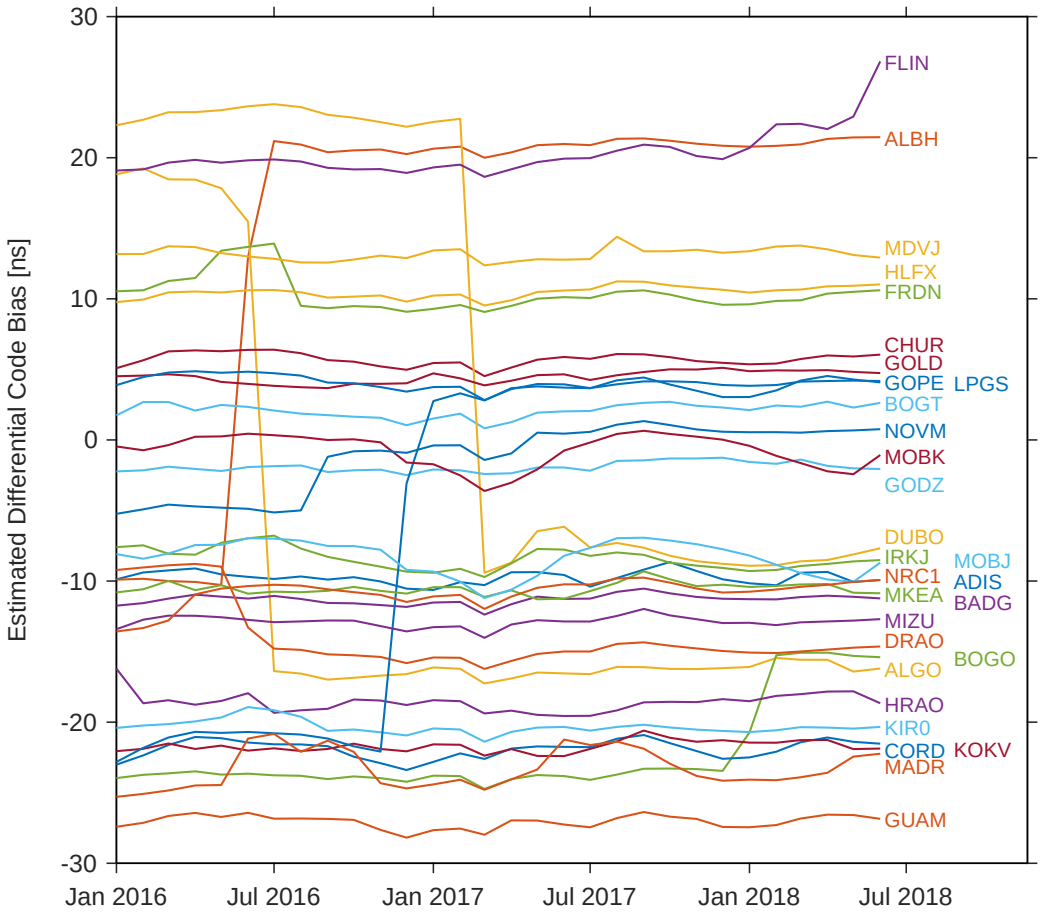

Figure 4.8: GLONASS P1-P2 IGS station DCBs monthly average in [ns] for January 2016 to June 2018, stations are identified by their IGS 4-character site name, data source: CODE

with

$$\hat{\vartheta}_i = \frac{\vartheta_i}{\vartheta_2 - \vartheta_1} \quad (i = 1, 2) \quad \text{and} \quad \vartheta_i = \frac{40.309 \cdot 10^{16}}{f_i^2} \text{ m/TECU} \tag{4.23}$$

The two TGDs referring to $DCB_{P1,P1}$ and $DCB_{P2,P1}$ are related by:

$$TGD_{P2} = \frac{f_1^2}{f_2^2} TGD_{P1} \tag{4.24}$$

Also Galileo broadcasts TGDs in the Freely Accessible Navigation Message (F/NAV) and the Integrity Navigation Message (I/NAV). There are no TGDs broadcasted for GLONASS.

4.3.3 Estimation of DCBs

In case of GPS L1 and L2 observations the $DCB_{P1,P2}$ can be obtained using the geometry-free linear combination P_{GF} following Equation (4.19). The DCBs are gained as a side product of the

ionosphere analysis.

4.3.4 DCB Download

With the start of the ionosphere working group of the IGS in June 1998 one aim was the estimation of DCBs (Feltens, 2003). The following Ionospheric Associate Analysis Centers (IAAC) take part in the actions and provide monthly mean DCB values in [ns]:

- Center for Orbit Determination in Europe (CODE), University of Bern, Switzerland: `ftp://ftp.aiub.unibe.ch/CODE/`
- Jet Propulsion Laboratory (JPL) via Crustal Dynamics Data Information System (CDDIS), Pasadena, CA, USA: `ftp://cddis.nasa.gov/gnss/products/bias/`
- European Space Operations Center (ESOC), Darmstadt, Germany
- Technical University of Catalonia (UPC), Barcelona, Spain
- Natural Resources Canada (NRCan), Canada
- Wuhan University, Wuhan, China

The IGS calculates a weighted combined solution out of the individual solutions of the IAACs (Hernández-Pajares *et al.*, 2009):

- International GNSS Service (IGS): `ftp://igs.ign.fr/pub/igs/products/mgex/dcb`

The IAACs calculate DCBs for GPS, GLONASS, Galileo and/or BeiDou.

Two analysis groups provide DCBs under the umbrella of the Multi-GNSS Experiment (MGEX) for GPS, GLONASS, Galileo and BeiDou (see Montenbruck *et al.* (2017) and Montenbruck *et al.* (2014b)):

- Institute of Geodesy and Geophysics (IGG), Chinese Academy of Sciences (CAS), Wuhan, China
- Deutsches Zentrum für Luft- und Raumfahrt (DLR), Cologne, Germany

The data can be retrieved via `ftp://cddis.nasa.gov/gnss/products/bias/` or `ftp://igs.ign.fr/pub/igs/products/mgex/dcb`. The products of IGG are delivered daily in BSX format (Wang *et al.*, 2016) whereas the products of DLR are generated for three months also in BSX format and include weekly averages of the satellite DCBs. Additionally also daily biases are provided as a reference (Montenbruck *et al.*, 2014a).

4.3.5 Other biases

4.3.5.1 GLONASS inter-frequency biases

The FDMA used by GLONASS causes inter-frequency biases (IFB) for carrier-phase measurements in the receiver, which makes it difficult or impossible to fix ambiguities. In addition, these biases assume different values for receivers from different manufacturers but are similar for receivers of the same type and also for L1 and L2 (Wanninger, 2012). The Equations (4.25) show the difference between GPS and GLONASS single-difference observations, where k indicates the channel number:

$$\begin{aligned} 2\phi_{r_{12}}^{\mathrm{GPS},s} &= \Delta\rho_{r_{12}}^{s} + c\cdot\Delta\delta t_{r_{12}}^{\mathrm{GPS}} + \lambda\cdot\Delta N_{r_{12}}^{s} + \epsilon_{\Delta\phi} \\ \phi_{r_{12}}^{\mathrm{GLO},s} &= \Delta\rho_{r_{12}}^{s} + c\cdot(\Delta\delta t_{r_{12}}^{\mathrm{GLO}} + k^{s}\cdot\Delta\delta h_{r_{12}}^{\mathrm{GLO}}) + \lambda\cdot\Delta N_{r_{12}}^{s} + \epsilon_{\Delta\phi} \end{aligned} \quad 2 \tag{4.25}$$

$\Delta\rho$ denotes the single-difference of the ranges between the satellite and the receivers, $\Delta\delta t$ is the difference of the receiver clocks and $\Delta\delta h$ is the difference between the inter-frequency biases of the two receivers. It can be seen that the carrier-phase IFBs are linearly dependent on the frequency.

Usually IFBs remain constant over time, only for some receivers a restart results in small changes. For consecutive frequencies the IFBs can reach values of up to 0.2 ns ($\sim$ 5 cm), which cause errors of about 2.4 ns ($\sim$ 73 cm) for the complete frequency bands (Wanninger, 2012).

4.3.5.2 BeiDou elevation-dependent code pseudorange variations

Code pseudorange measurements of BeiDou 2 satellites show divergences of more than 1 m, dependent on the elevation of the observed satellite (Wanninger & Beer, 2015). The cause of the effect is unknown, although some authors speculate that it is the result of spacecraft internal multipath (Hauschild *et al.*, 2012; Montenbruck *et al.*, 2013). BeiDou 3 satellite observations do not show such an effect any more.

4.4 Existing ionospheric models

The delay or advance of GNSS signals caused by the TEC can be calculated by models, which allow the derivation of signal delays along arbitrary ray paths. The most common models used for GNSS analysis are described in this following chapter.

4.4.1 Empirical Models

4.4.1.1 Klobuchar Model

The Klobuchar model was established in 1986 in order to approximate the ionospheric refraction. During daytime it corrects at least 50 % of the range error caused by the ionosphere, at

nighttime, where the variation of the ionosphere is low, it gives a constant value. The model is from particular interest because it uses the eight ionospheric coefficients broadcasted within the GPS navigation message. These coefficients are updated daily and cover the ionospheric behavior for 24 hours worldwide (Alizadeh, 2013).

The time delay caused by the ionosphere ΔT_v^{Iono} derived from the Klobuchar model is calculated with

$$\Delta T_v^{Iono} = A_1 + A_2 \cos\left(\frac{2\pi(t - A_3)}{A_4}\right) \tag{4.26}$$

where

$$\begin{aligned} A_1 &= 5 \cdot 10^{-9}\ \text{s} = 5\ \text{ns}, \\ A_2 &= \alpha_1 + \alpha_2\ \varphi_{\text{IPP}}^m + \alpha_3\ \varphi_{\text{IPP}}^{m\ 2} + \alpha_4\ \varphi_{\text{IPP}}^{m\ 3}, \\ A_3 &= 14^{\text{h}}\ \text{local time}, \\ A_4 &= \beta_1 + \beta_2\ \varphi_{\text{IPP}}^m + \beta_3\ \varphi_{\text{IPP}}^{m\ 2} + \beta_4\ \varphi_{\text{IPP}}^{m\ 3}, \end{aligned} \tag{4.27}$$

$$t = \frac{\lambda_{\text{IPP}}}{15} + t_{\text{UT}} \tag{4.28}$$

and

$$\varphi_{\text{IPP}}^m = \sin\varphi_{\text{IPP}} \sin\varphi_0 + \cos\varphi_{\text{IPP}} \cos\varphi_0 \cos(\lambda_{\text{IPP}} - \lambda_0). \tag{4.29}$$

As it can be seen from the formula, A_1 and A_3 are fixed numbers whereas A_2 and A_4 are calculated from the coefficients α_i, β_i, $i = 1, \ldots, 4$ of the navigation message and the spherical distance φ_{IPP}^m between the geomagnetic pole and the IPP. The local time t of the IPP can be derived from (4.28), where t_{UT} denotes the observation epoch in Universal Time (UT). The values φ_{IPP} and λ_{IPP} represent the coordinates of the IPP and φ_0 and λ_0 those of the geomagnetic pole, which can be downloaded for example from the CODE webpage (Hofmann-Wellenhof *et al.*, 2008). Current values are given at the end of Chapter 4.1.1.

4.4.1.2 NeQuick Model

The NeQuick model is based on the DGR model (named after the initial letters of their names) introduced by Di Giovanni & Radicella (1990) and was developed by the Aeronomy and Radiopropagation Laboratory (ARPL) of the Abdus Salam International Centre for Theoretical Physics in Trieste (Italy) and the Institute for Geophysics, Astrophysics and Meteorology of the University of Graz (Austria). This ionospheric electron density model is three-dimensional and time dependent, which means that the electron content at any given location (latitude, longitude and height) in the ionosphere can be obtained. The input parameters are position, time and solar flux, which is expressed by either the sunspot number R_{12} or the average 10.7 cm solar radio flux

$F_{10.7}$ (Hofmann-Wellenhof *et al.*, 2008).

$$R_{12} = \frac{(F_{10.7} - 57)}{0.93} \tag{4.30}$$

Furthermore the NeQuick model allows the calculation of an electron density profile for an arbitrary path between satellite and receiver (Nava *et al.*, 2006). The NeQuick source code in Fortran77 is freely available at the website of the International Telecommunication Union, Radiocommunication Sector (ITU-R).

European Geostationary Navigation Overlay Service (EGNOS) uses NeQuick for system assessment analysis in order to simulate realistic ionospheric conditions under disturbed conditions (Radicella, 2009). The most important user is the Galileo satellite navigation system, which corrects the ionospheric effects in single frequency operations with the so-called NeQuick-GAL model (Arbesser-Rastburg, 2006). For Galileo the solar flux is replaced by an effective ionization level *Az*

$$Az = a_0 + a_1\mu + a_2\mu^2 \tag{4.31}$$

where the coefficients a_0, a_1 and a_2 are broadcast to the users in the GALILEO navigation message and μ is the modified magnetic dip.

$$\tan\mu = \frac{I}{\sqrt{\cos\varphi}} \tag{4.32}$$

In (4.32) I is the magnetic dip or true magnetic inclination and φ is the geographic latitude of the receiver (Rawer, 1963).

The TEC is calculated by integration of the electron density along the satellite–receiver ray path. The model defines a bottomside and topside electron density, computed with the ionospheric parameters $N_m\mathrm{F}_2$, $h_m\mathrm{F}_2$, $h_m\mathrm{F}_1$ and $h_m\mathrm{E}$ (cf. Chapter 2.4.2) (European GNSS (Galileo) Open Service, 2016).

$$\mathrm{TEC} = \int_{h_1}^{h_2} N(h)\, dh \tag{4.33}$$

with

$$N(h) = \begin{cases} \text{bottomside } N & \text{if } h \leq h_m\mathrm{F}_2 \\ \text{topside } N & \text{if } h > h_m\mathrm{F}_2 \end{cases} \tag{4.34}$$

4.4.1.3 International Reference Ionosphere (IRI)

The IRI is an international cooperation sponsored by Committee on Space Research (COSPAR) and International Union of Radio Science (URSI) since 1969 and stands for an empirical standard

model for ionospheric parameters. For example a user can obtain monthly averages of the electron density and temperature, ion temperature and composition, the TEC, the occurrence probability for Spread-F and also the F1-region, and the equatorial vertical ion drift. A worldwide network of ionosondes, incoherent scatter radars, topside sounders and in situ instruments on several satellites and rockets provides data for the calculation of the parameters (Bilitza *et al.*, 2014).

Because of the fact that IRI is an empirical model based on sensors it is not influenced by mathematical simplifications of the ionospheric structure. But with this it comes along that the accuracy decreases in areas or time periods which are not covered sufficiently by observations (Bilitza *et al.*, 2011).

The latest release is IRI2016, which can be obtained via web (`https://ccmc.gsfc.nasa.gov/modelweb/models/iri2016_vitmo.php`) or via a software package. This package includes FORTRAN subroutines, model coefficients, and documentation files. For a description or more information see Bilitza (1990).

4.4.2 Mathematical models

By using mathematical models the VTEC is represented as a function of latitude, longitude or alternatively as function of the geomagnetic latitude β and the sun-fixed longitude s.

4.4.2.1 Taylor Series Expansion Model

The Taylor Series Expansion Model is used for regional VTEC calculations. It is represented by a function of the spherical distance to the origin of the expansion located in the center of the area of interest. The degree of development depends on the distribution of available data and local rates of change of the VTEC. In practice the processing is mostly truncated at a very low degree.

The VTEC can be estimated with (Kumar *et al.*, 2012):

$$\mathrm{VTEC}(\beta_{\mathrm{IPP}}, s_{\mathrm{IPP}}) = \sum_{n=0}^{n_{\max}} \sum_{m=0}^{m_{\max}} C_{nm} (\beta_{\mathrm{IPP}} - \beta_0)^n (s_{\mathrm{IPP}} - s_0)^m \tag{4.35}$$

where β_{IPP} and s_{IPP} are the geomagnetic latitude and sun-fixed longitude of the IPP and β_0 and s_0 are the coordinates of the origin of the expansion.The C_{nm} represent the unknown coefficients of the Taylor Series and $n_{\max}$ and $m_{\max}$ are the maximum orders of the expansion in latitude and longitude.

4.4.2.2 Spherical Harmonics Expansion Model

With a Spherical Harmonics Expansion the VTEC can be obtained with the following equation (Schaer, 1999):

$$\mathrm{VTEC}(\beta,s) = \sum_{n=0}^{n_{\max}} \sum_{m=0}^{n} \widetilde{P}_{nm}(\sin\beta)(a_{nm}\cos(ms) + b_{nm}\sin(ms)) \tag{4.36}$$

where $VTEC(\beta,s)$ is the VTEC dependent on the geomagnetic latitude β and the sun-fixed longitude s, $\widetilde{P}_{nm}$ are the normalized Legendre functions of degree n and order m and a_{nm} and b_{nm} are the spherical harmonics coefficients to be estimated.

The normalized Legendre functions $\widetilde{P}_{nm} = N_{nm}P_{nm}$ are built with:

$$N_{nm} = \sqrt{\frac{(n-m)!(2n+1)(2-\delta_{0m})}{(n+m)!}} \tag{4.37}$$

where δ_{0m} is the Kronecker delta.

Concerning numerical applications the equation has to be truncated at the degree N, resulting in $(N+1)^2$ terms in the double sum (Schmidt *et al.*, 2011). Typically $N = 15$ is chosen. Subsequently the resolution in latitude r_β and sun-fixed longitude r_s of the expansion results in:

$$r_\beta = \frac{2\pi}{n_{\max}} \qquad\qquad r_s = \frac{2\pi}{m_{\max}} \tag{4.38}$$

where $n_{\max}$ and $m_{\max}$ define the maximum degree and order of the expansion.

For example the Center for Orbit Determination in Europe (CODE) uses a Spherical Harmonics Expansion for computing their TEC maps.

4.4.2.3 B-Spline Model

The German Geodetic Research Institute (Deutsches Geodätisches Forschungsinstitut, DGFI-TUM) developed an approach for calculating the VTEC based on tensor products of B-spline functions (Schmidt *et al.*, 2011). Since B-splines are localizing functions the approach copes with data of heterogeneous density and quality. For global modeling the approach reads

$$\mathrm{VTEC}_{\mathrm{global}}(\varphi,\lambda,t_i) = \sum_{k_1=0}^{K_1-1} \sum_{k_2=0}^{K_2-1} d_{k_1,k_2}^{J_1,J_2}(t_i)\, N_{k_1}^{J_1}(\varphi)\, T_{k_2}^{J_2}(\lambda) \tag{4.39}$$

where φ, λ and t denote the horizontal position and time. $N_{k_1}^{J_1}(\varphi)$ and $T_{k_2}^{J_2}(\lambda)$ are polynomial and trigonometric B-splines, respectively; the time-dependent unknown B-spline coefficients $d_{k_1,k_2}^{J_1,J_2}$ are located on the sphere depending on the position parameters k_1 and k_2. The numbers $K_1 = 2^{J_1}+2$ and $K_2 = 3\cdot 2^{J_2}$ of B-spline functions depend on the resolution levels level J_1 and J_2

(Dettmering *et al.*, 2011; Limberger, 2015; Schmidt *et al.*, 2013).

A regional VTEC modeling approach

$$\mathrm{VTEC}_{\mathrm{regional}}(\varphi,\lambda,t_i) = \mathrm{VTEC}_{\mathrm{global}}(\varphi,\lambda,t_i) + \Delta\mathrm{VTEC}_{\mathrm{regional}}(\varphi,\lambda,t_i) \tag{4.40}$$

can be set up as the sum of the global model part (4.39) and the regional correction part

$$\Delta\mathrm{VTEC}_{\mathrm{regional}}(\varphi,\lambda,t_i) = \sum_{k_3=0}^{K_{J_3}-1}\sum_{k_4=0}^{K_{J_4}-1} d_{k_3,k_4}^{J_3,J_4}(t_i)\, N_{k_3}^{J_3}(\varphi)\, N_{k_4}^{J_4}(\lambda) \tag{4.41}$$

where $N_{k_3}^{J_3}(\varphi)$ and $N_{k_4}^{J_4}(\lambda)$ are polynomial B-spline functions of resolution levels J_3 and J_4 defined within the regional area of investigation (Goss *et al.* (2017)). The approach (4.40) can be used for near real-time and real-time applications. In the latter case a forecast global model was established (Goss *et al.*, 2017).

4.4.2.4 Regiomontan Model

The Regiomontan Model was established at Technische Universität Wien in the framework of the FFG project Regiomontan (Regional Ionosphere Modeling for Single-Frequency Users). It is a regional model using integer-leveled phase measurements of permanent stations in Austria and neighboring countries. The aim was to obtain precise ionospheric GNSS signal delays provided to single-frequency users (Boisits *et al.*, 2016).

Thin-shell model

The Regiomontan Model is based on a Thin-Shell Model (TSM) (Mitch & Psiaki, 2010). The Thin-Shell Layer, for which this model has a constant height of 350 km, is approximated regionally using a second-order Taylor Series Expansion:

$$\begin{aligned}\mathrm{VTEC}(\varphi_{\mathrm{IPP}},\lambda_{\mathrm{IPP}}) = \mathrm{VTEC}_0 &+ \frac{\partial\mathrm{VTEC}}{\partial\varphi}\Delta\varphi_{\mathrm{IPP}} + \frac{\partial\mathrm{VTEC}}{\partial\lambda}\Delta\lambda_{\mathrm{IPP}} + \\ &+ \frac{1}{2}\frac{\partial^2\mathrm{VTEC}}{\partial\varphi^2}\Delta\varphi_{\mathrm{IPP}}^2 + \frac{1}{2}\frac{\partial^2\mathrm{VTEC}}{\partial\lambda^2}\Delta\lambda_{\mathrm{IPP}}^2 + \frac{\partial^2\mathrm{VTEC}}{\partial\varphi\,\partial\lambda}\Delta\varphi_{\mathrm{IPP}}\lambda_{\mathrm{IPP}}\end{aligned} \tag{4.42}$$

with

$$\begin{aligned}\Delta\varphi_{\mathrm{IPP}} &= \varphi_{\mathrm{IPP}} - \varphi_0 \\ \Delta\lambda_{\mathrm{IPP}} &= \lambda_{\mathrm{IPP}} - \lambda_0\end{aligned} \tag{4.43}$$

where φ_{IPP} and λ_{IPP} denote the coordinates of the IPP and φ_0 and λ_0 the coordinates of the origin of the expansion. As the model should mainly serve for Austrian applications, the origin was set

to $\varphi_0 = 48°$ N and $\lambda_0 = 14°$ E (Boisits & Weber, 2016).

All unknown parameters (VTEC_0, $\frac{\partial \text{VTEC}}{\partial \varphi}$, $\frac{\partial \text{VTEC}}{\partial \lambda}$, $\frac{\partial^2 \text{VTEC}}{\partial \varphi^2}$, $\frac{\partial^2 \text{VTEC}}{\partial \lambda^2}$, $\frac{\partial^2 \text{VTEC}}{\partial \varphi \partial \lambda}$) are estimated in a least-squares adjustment.

Station network

The station network consists of 22 reference stations in Austria and nearby operated by the Austrian reference station provider EPOSA. Hourly Receiver Independent Exchange Format (RINEX) files with a time resolution of one second are provided. Figure 4.9 illustrates the station network used to setup the Regiomontan Model including the origin of the Taylor Series Expansion.

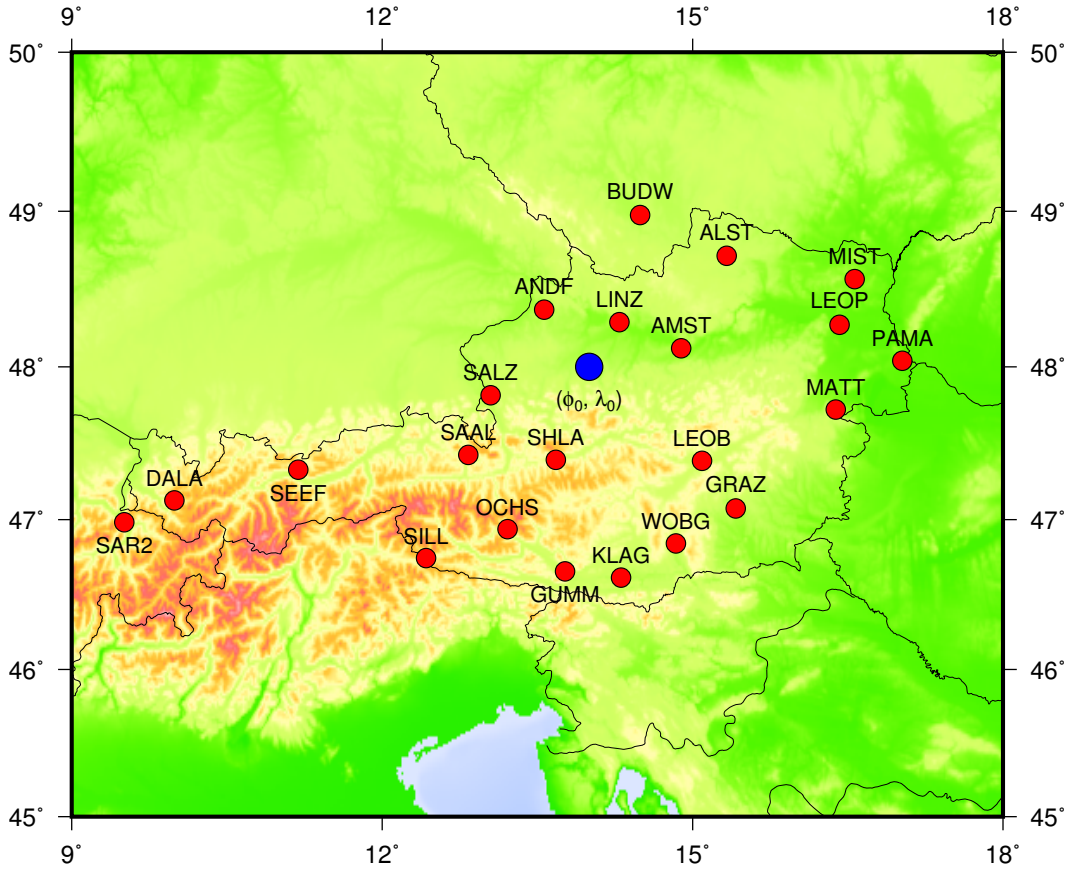

Figure 4.9: Chosen EPOSA stations (red) in Austria and nearby for Regiomontan Model, origin of the expansion (blue)

Leveling approach

VTEC values calculated with the Regiomontan Model are derived out of the geometry-free linear combination for phase L_{GF} and code measurements P_{GF} (see Equations (4.12) and (4.16)). In case of carrier-phases the non-integer ambiguity term B (consisting of the ambiguity and the hardware delays, which cannot be separated) remains in the equation, whereas with pseudoranges

the DCBs for satellites and receivers remain. In order to solve for the non-integer ambiguity term B a leveling approach is utilized (Boisits *et al.*, 2016). In addition to the geometry-free linear combination the range bias $\bar{A}^j_{\mathrm{GF}}$ is calculated for every satellite arc, which can be expressed by (Banville *et al.*, 2013):

$$\bar{A}^j_{\mathrm{GF}} = \langle P^j_{\mathrm{GF}} - L^j_{\mathrm{GF}} \rangle \tag{4.44}$$

By adding this range bias to the phase geometry-free linear combination VTEC values can be calculated.

Unknown Station DCBs

Differently to the satellite DCBs, which are obtained from CODE (see Chapter 4.3.4), the DCBs for the EPOSA stations remain unknown and have to be estimated for building the pseudorange geometry-free linear combination P_{GF}. Within the Regiomontan Model this is done via a least-squares adjustment by building the difference to the IGS VTEC values. The station DCBs are calculated once a week. To ensure their stability over a whole week, they were calculated for test purposes three times a week. An example is displayed in Figure 4.10.

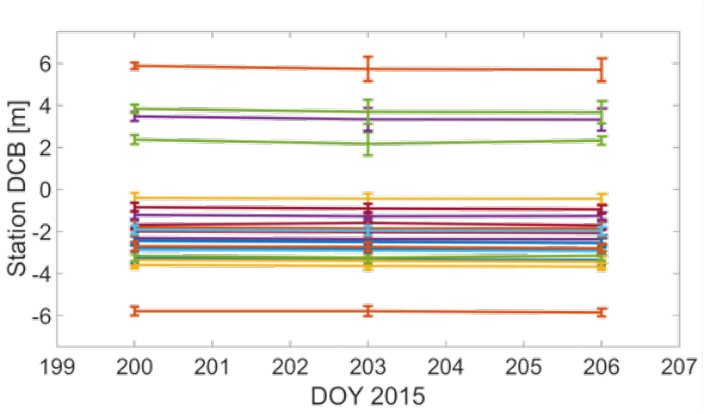

Figure 4.10: Stability of the EPOSA station DCBs calculated for Regiomontan Model (Boisits *et al.*, 2016)

Resolution

All parameters are calculated with a temporal resolution of one hour and distributed via Ionosphere Map Exchange Format (IONEX) file in a $1° \times 1°$ grid over Europe, which extends from $\varphi = 30° - 70°$ N and $\lambda = -20° - 45°$ E. The grid covers the whole field of view for a user location within Austria (Boisits *et al.*, 2016).

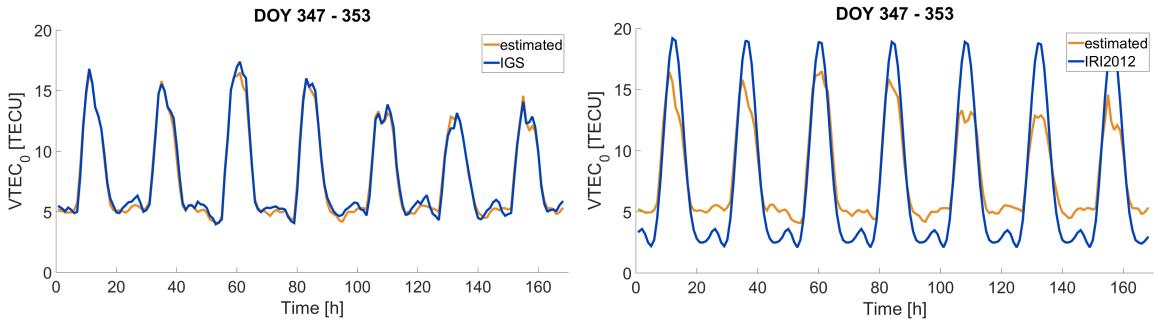

(a) (b)

Figure 4.11: VTEC values of the Regiomontan Model (orange) compared to those from (a) IGS (blue) and (b) IRI (blue) at the origin of the expansion, December 13–19, 2015 (Boisits *et al.*, 2016)

Model validation

In order to investigate the quality of the model it was compared to the results of the IGS TEC Maps (see Chapter 4.4.2.2) and IRI2012 (see Chapter 4.4.1.3). Figure 4.11 shows a time series of the VTEC calculated at the origin of the expansion, which corresponds to the parameter $VTEC_0$ of the Taylor Series Expansion. The differences related to IGS are below 1.5 TECU, which corresponds to the accuracy of the IGS TEC Maps. Compared to the Regiomontan Model IRI is overestimating the VTEC at daytime and underestimating the VTEC at nighttime.

On the other hand STEC values calculated with Regiomontan, NeQuick-GAL (see Chapter 4.4.1.2) and Klobuchar (see Chapter 4.4.1.1) models are converted to range corrections and applied to phase-smoothed L1 pseudoranges. Those are compared to the ionosphere-free linear combination derived out of phase-smoothed code observations, which serve as true values for the ranges (see Figure 4.12). Only observations with an elevation angle larger than 5° were considered. For better visibility the results were plotted with a time-resolution of one hour. For the Regiomontan Model most of the differences lie within ±0.5 m. The other two models, especially the Klobuchar Model, show considerably larger range differences.

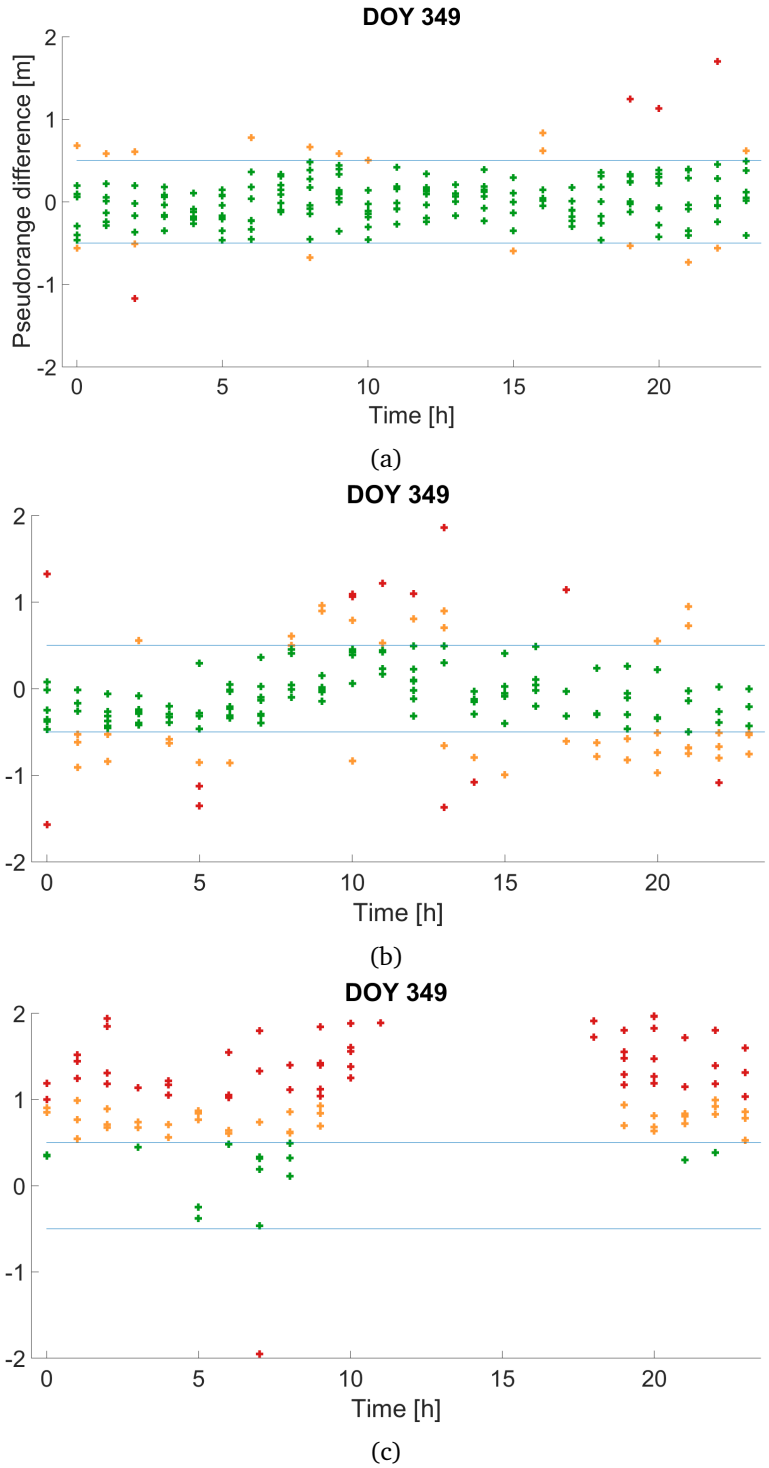

Figure 4.12: Pseudoranges corrected with (a) Regiomontan Model (b) NeQuick-GAL Model (c) Klobuchar Model compared to the ionosphere-free linear combination (reference), December 15, 2015 (Boisits *et al.*, 2016)

Chapter 5

Giomo Model: Algorithm

A new ionospheric model, labeled Giomo Model, was developed at the Research Group Advanced Geodesy (Department of Geodesy and Geoinformation, Vienna University of Technology). The model is based on a single-layer and describes the TEC by only five parameters: The current maximum VTEC plus its geodetic coordinates and two weighting functions in latitude and longitude to account for the spherical distance between the maximum VTEC and the Ionospheric Pierce Point (IPP) of interest.

The Giomo Model was originally developed under the name Multilayer Model (Magnet & Weber, 2012a,b, 2013) in the FFG project GIOMO (Next Generation Near Real-Time Ionospheric Models). The model consisted formally of nine vertically distributed equidistant electron layers within the height range of the F2-layer instead of a single-layer. The Multilayer Model was developed to serve for regional applications and to increase the accuracy of the TEC modeling over Austria. But the requirements changed, so also global distributed reference stations were included. To establish an easy predictable model it was more practicable and adequate to reduce the number of layers because the model should depend only on few parameters. In the course of those changes the label Multilayer Model was no longer appropriate, so it was changed to Giomo Model.

5.1 Definition

The Giomo Model uses a single-layer model, where all electrons are assumed to be in an infinitesimal layer in a height of 450 km above the Earth's surface. The VTEC at any IPP of interest is obtained from the location and magnitude of the current global electron maximum multiplied by two distance dependent weighting functions, which account for the spherical distance to the IPP.

Numerous examples derived from CODE and IGS VTEC maps were investigated to search for the best algorithm. The parametrization now available has proven to be a good and simple (for prediction purposes) approximation. The model is not primarily aimed at high spatial resolution.

All parameters are calculated with an hourly time resolution from a combination of global

GNSS observation data. Because of its small and easy predictable set of parameters the Giomo Model focuses on rapid availability.

5.2 Parameters

With the new model the global electron maximum (= amplitude) and its location in latitude and longitude (Figure 5.1) are characterized. Two weighting functions describing the decrease of the electron density with increasing distance to this point both in latitude and longitude are introduced. In case of a double electron maxima, the Giomo Model estimates the mean coordinates of both. The figure shows the schematic definition of the model: The VTEC at the position of the user is calculated with respect to the current maximum VTEC and the weighting function.

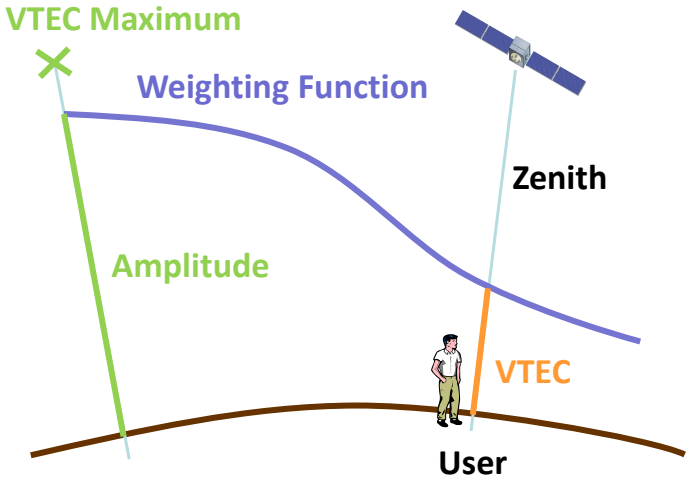

Figure 5.1: Schematic Definition of the Giomo Model

Figure 5.2 shows the calculation of the VTEC at the position (β,s). The front view (Figure 5.2a) describes that the VTEC at the position (β,s) decreases with increasing distance to the maximum VTEC by applying the weighting function. The plan view (Figure 5.2b) displays the maximum VTEC and the two weighting functions in latitude and longitude. The distance in longitude is abbreviated with d_s, the distance in latitude with d_β. Depending on the position of the user the VTEC(β,s) is calculated.

Equation (5.1) shows the corresponding mathematical model:

$$\mathrm{VTEC}(\beta_{\mathrm{IPP}}, s_{\mathrm{IPP}}) = \mathrm{VTEC}_{\mathrm{max}} \cdot \frac{1}{1+\frac{d_\beta^2}{w_\beta^2}} \cdot \frac{1}{1+\frac{d_s^2}{w_s^2}} \tag{5.1}$$

where VTEC($\beta_{\mathrm{IPP}}, s_{\mathrm{IPP}}$) denotes the VTEC in [TECU] at the IPP with the coordinates (β_{IPP}, s_{IPP}),

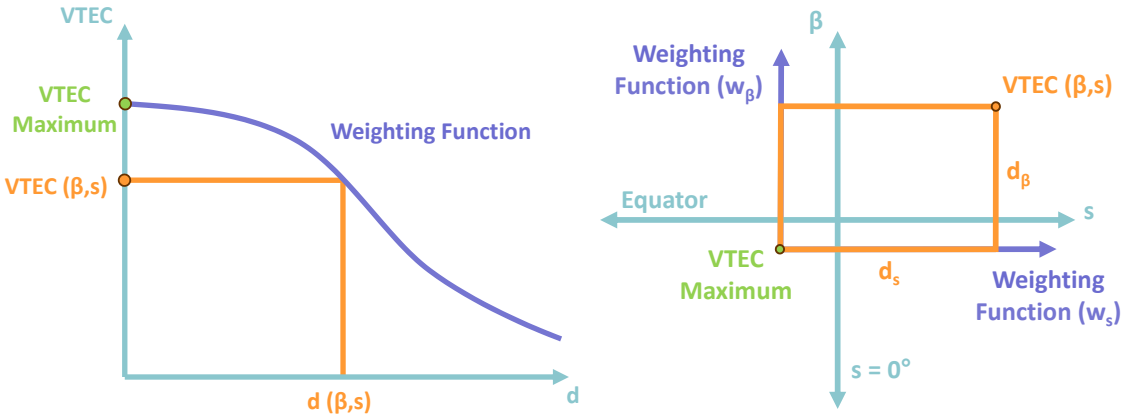

(a) front view (b) plan view

Figure 5.2: Calculation of VTEC at the position (β,s)

VTEC_{max} in [TECU] is the current maximum VTEC, w_β and w_s in [m] are the parameters of the weighting functions in latitude and longitude and d_β and d_s are the spherical differences converted to [m] between the maximum VTEC and the IPP. They are calculated with equations (5.2) and (5.3):

$$d_\beta = R \cdot (\beta_{\text{IPP}} - \beta_{\text{max}}) \tag{5.2}$$

$$d_s = R \cdot (s_{\text{IPP}} - s_{\text{max}}) \cdot \cos\beta_{\text{IPP}} \tag{5.3}$$

where R denotes the Earth's radius in [m], β_{IPP} and β_{max} the geomagnetic latitudes of the IPP and the maximum VTEC in [rad] and s_{IPP} and s_{max} the solar-fixed longitudes of the IPP and the maximum VTEC in [rad]. For the coordinate transformation from ϕ, λ to β, s see Chapter 4.1.1.

If only the component in longitude is considered, Equation 5.1 reads:

$$\text{VTEC}(\beta_{\text{IPP}}, s_{\text{IPP}}) = \text{VTEC}_{\text{max}} \cdot \frac{1}{1 + \frac{d_s^2}{w_s^2}} \tag{5.4}$$

This means, if the IPP is located in a distance equivalent to w_s, such that $d_s = w_s$, the VTEC at this point is $\text{VTEC} = 1/2 \cdot \text{VTEC}_{\text{max}}$. A similar function is also used for plane covariance functions.

The Figures 5.3 and 5.4 show the VTEC profiles through the VTEC maximum of the CODE TEC Maps compared to the weighting functions in latitude and longitude. They both agree well with the reference data, although of course some smaller variations of the TEC cannot be modeled. For reasons of simplification in this case the geographical coordinates were taken instead of the solar-fixed coordinates.

This type of weighting function allows to approximate any profiles of the ionospheric buldge within a few TEC Units (TECU), at least up to $\mathrm{VTEC}_{\mathrm{max}}/2$.

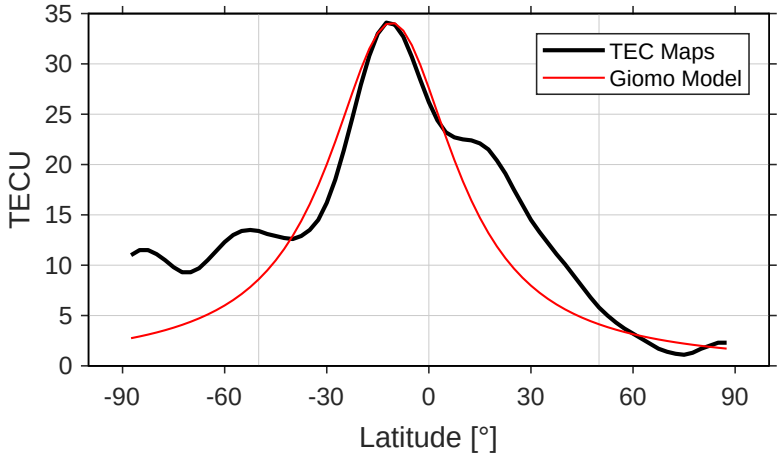

Figure 5.3: Comparison of the Giomo Model and the CODE TEC Maps for January 15, 2017, 14:00 UTC. Profile in latitude with $w_\phi = 2.52 \cdot 10^6$ m, $\mathrm{VTEC}_{\mathrm{max}} = 34.10$ TECU.

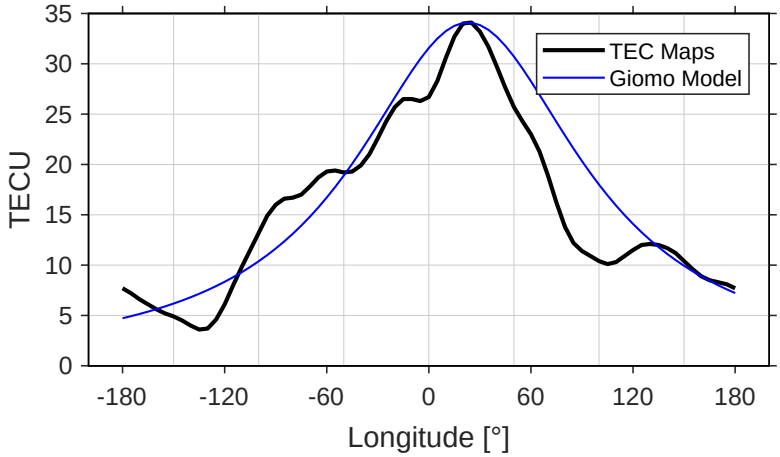

Figure 5.4: Comparison of the Giomo Model and the CODE TEC Maps for January 15, 2017, 14:00 UTC. Profile in longitude with $w_\lambda = 8.84 \cdot 10^6$ m, $\mathrm{VTEC}_{\mathrm{max}} = 34.10$ TECU.

5.2.1 Examples of the parameters

The Figures 5.5 – 5.7 show some examples of the magnitude of the different parameters. One has to be aware that the solar-fixed coordinate system described in Chapter 4.1.1 was used to calculate the parameters, so e.g. the value of s_{max} does not correspond to the distance to the real position of the Sun, but to the position of the mean Sun.

Almost always the parameter w_β is smaller than w_s. This is because due to the rotation of the Earth the ionospheric buldge has a larger extension in east-west direction.

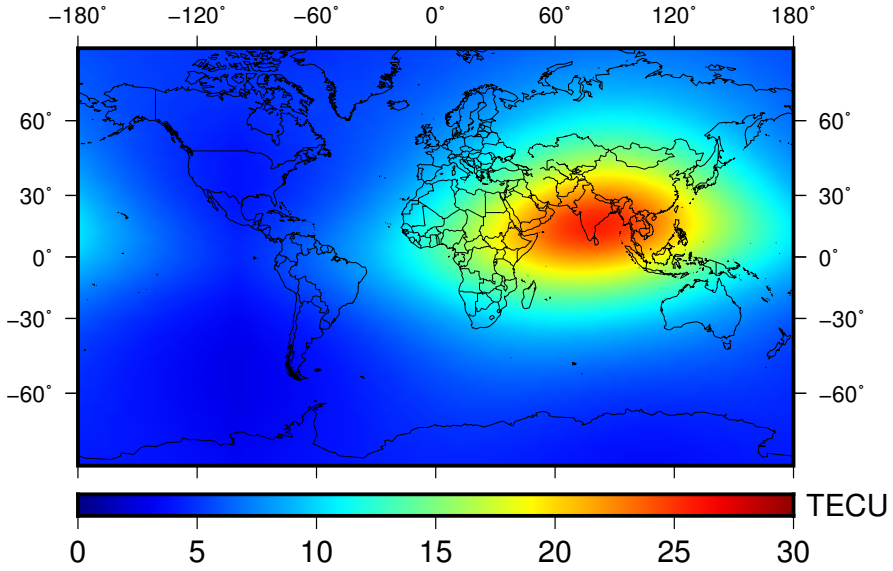

Figure 5.5: Giomo Model, DOY 139, 2018, 10:00 UTC, $\mathrm{VTEC}_{\max} = 23.47$ TECU, $w_\beta = 4.66 \cdot 10^6$ m, $w_s = 9.79 \cdot 10^6$ m, $\beta_{\max} = 10.076°$, $s_{\max} = 38.924°$

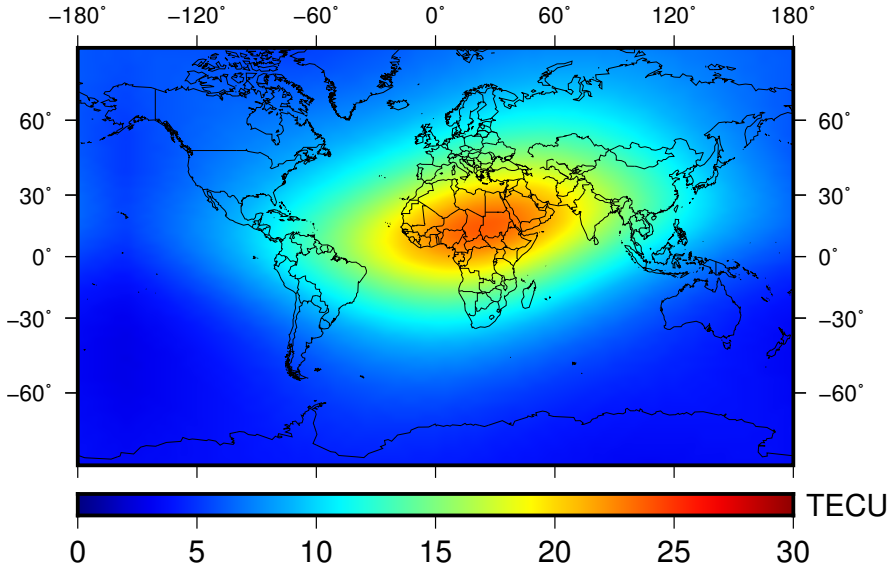

Figure 5.6: Giomo Model, DOY 121, 2018, 14:00 UTC, $\mathrm{VTEC}_{\max} = 22.29$ TECU, $w_\beta = 4.52 \cdot 10^6$ m, $w_s = 1.01 \cdot 10^7$ m, $\beta_{\max} = 14.043°$, $s_{\max} = 37.115°$

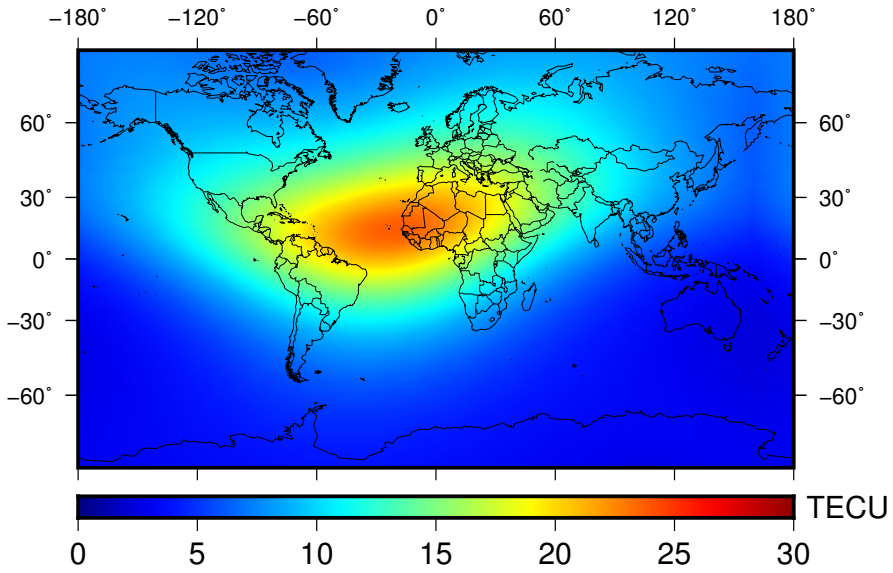

Figure 5.7: Giomo Model, DOY 154, 2018, 16:00 UTC, $\mathrm{VTEC}_{\max} = 24.15$ TECU, $w_\beta = 4.35 \cdot 10^6$ m, $w_s = 1.07 \cdot 10^7$ m, $\beta_{\max} = 22.381°$, $s_{\max} = 24.139°$

5.3 IGS reference station network

Since 1994 the International GNSS Service (IGS) provides open access to GNSS data and products. The base of the organization is a network of approximately 500 stations located worldwide, which track GNSS signals continuously and offer their data to the community. Standards and regulations for the contributing stations are defined by the IGS Site Guidelines (Teunissen & Montenbruck, 2017). Figure 5.8 illustrates the IGS sites used to calculate the parameters of the Giomo Model. Hourly RINEX data is downloaded and processed on a regular basis. The selection which of the IGS sites should be part of the calculation was made due to which station provides L_1, L_2, P_1 and P_2 observables, which are used for the Giomo processing.

A well known problem is the distribution of the sites. Most of them are located in the northern hemisphere in Europe and North America. As the VTEC maximum travels with the Sun along the equatorial region, the parameters of the Giomo Model are predicted with larger uncertainties - especially when the VTEC maximum is located in the Pacific region, where hardly sites exist (cf. 6.5).

5.4 Pseudorange observations with phase smoothing

For the computation of the Giomo Model, the pseudorange measurements P_1 and P_2 are used. To reduce the noise of the code measurements they are smoothed with the carrier-phase measurements L_1 and L_2. For the smoothing, the Hatch filter is used by building time differences of phase observations ϕ (Teunissen & Montenbruck, 2017). By building those time differences, the carrier

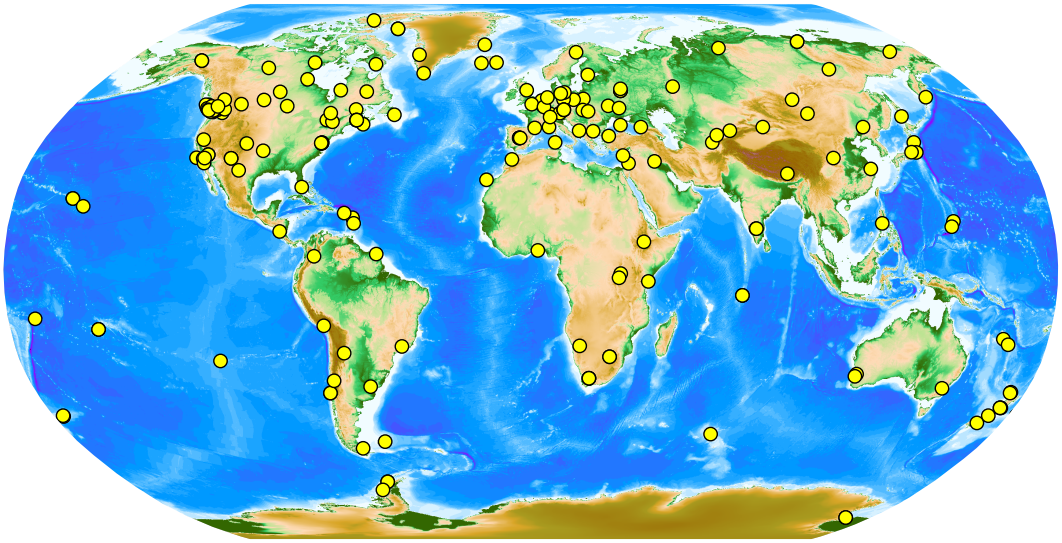

Figure 5.8: IGS station network used for Giomo Model

phase ambiguities are eliminated.

$$\hat{P}_k^s = \frac{1}{k} P_k^s + \frac{k-1}{k} [\hat{P}_{k-1}^s + (\phi_k^s - \phi_{k-1}^s)] \tag{5.5}$$

where $\hat{P}_k^s$ is the smoothed pseudorange for satellite s at epoch k. In principle it can be seen that $\hat{P}_k^s$ is a linear combination of the $1/k$ weighted pseudorange and the $(k-1)/k$ weighted predicted pseudorange. The filter is initialized by:

$$\hat{P}_1^s = P_1^s \tag{5.6}$$

If cycle slips occur, the prediction cannot be used any more and the filter has to be initialized again. The effect of the smoothing on the noise behavior can be seen in the Figures 5.9a and 5.9b.

5.5 Differential Code Biases (DCBs)

The theory behind DCBs is described in Chapter 4.3. In this chapter only data sources of the DCB files used for computing the Giomo Model are given.

5.5.1 Satellite DCBs

Satellite DCBs for P1 - P2 are downloaded via File Transfer Protocol (FTP) from CODE: `ftp://ftp.aiub.unibe.ch/CODE/`. If available, monthly solutions are retrieved and taken into account:

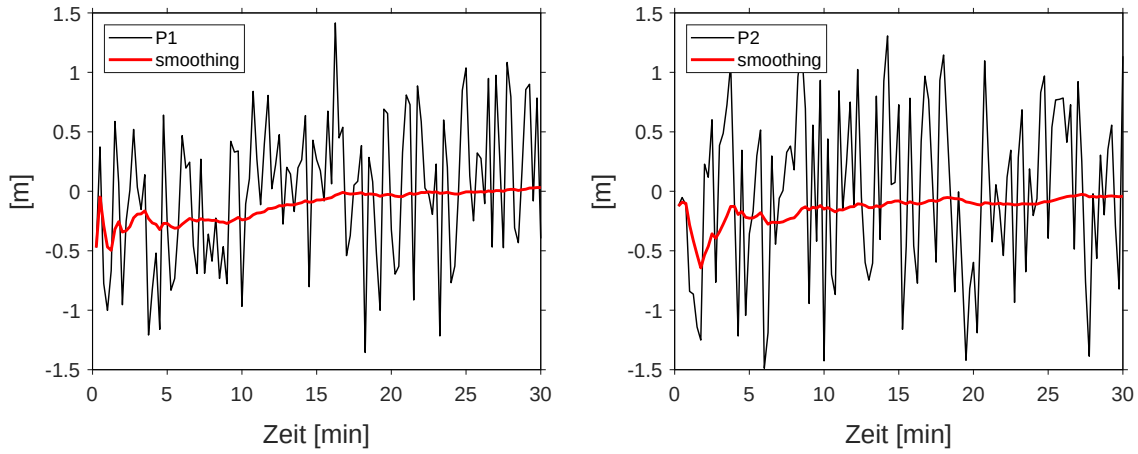

(a) For P1 code (b) For P2 code

Figure 5.9: Pseudorange measurements (black) vs. smoothed pseudorange measurements (red)

```
\yyyy\P1P2yymm.DCB.Z
```

where `yyyy` stands for the 4-digit year, `yy` for the 2-digit year and `mm` for the month. Monthly solutions are uploaded a few days (around 4 – 8 days) after the end of the relevant month.

If there is no monthly solution available, especially for near real-time applications, the file

```
P1P2.DCB
```

is downloaded, taking into account the last 30 daily solutions for the DCBs.

5.5.2 Station DCBs

The same holds for the receiver\station DCBs. When there is a monthly solution available, this file is taken from `ftp://ftp.aiub.unibe.ch/CODE/`:

```
\yyyy\P1P2yymm_all.DCB.Z
```

Otherwise the 30-day average is downloaded:

```
P1P2_all.DCB
```

The ending `_all` denotes that satellite DCBs as well as receiver DCBs are included.

5.6 Least-squares adjustment

To obtain the Giomo Model parameters a least-squares adjustment is carried out according to the functional relation $\phi(\mathbf{x})$ of the measured observations $\mathbf{L}$ ($[n \times 1]$), where n denotes the number of observations, and the error vector $\mathbf{v}$ (Hofmann-Wellenhof *et al.*, 2008):

$$\mathbf{L} + \mathbf{v} = \phi(\mathbf{x}) \tag{5.7}$$

where $\mathbf{x} = \mathbf{x}_0 + \mathbf{dx}$ denotes the unknowns. The parameter $\mathbf{x}_0$ indicates the approximate values for the unknowns and $\mathbf{dx}$ the differences to their true value.

By linearizing Equation (5.7) the formula results in:

$$\mathbf{L} + \mathbf{v} = \phi(\mathbf{x}_0) + \mathbf{A}\mathbf{x} \tag{5.8}$$

where $\mathbf{A}$ is called design matrix and contains all partial derivatives of the unknowns $\mathbf{A} = \left(\frac{\partial \phi(\mathbf{x})}{\partial \mathbf{x}}\right)$.

Solving Equation (5.8) for $\mathbf{v}$ gives:

$$\mathbf{v} = \mathbf{A}\mathbf{x} - (\mathbf{L} - \phi(\mathbf{x}_0)) = \mathbf{A}\mathbf{x} - \mathbf{l} \tag{5.9}$$

where $\mathbf{l} = \mathbf{L} - \phi(\mathbf{x}_0)$ denotes the difference between the measured and computed observations.

The stochastic model is described by:

$$\mathbf{P} = \mathbf{Q}_{ll}^{-1} = \sigma_0^2 \Sigma_{ll}^{-1} \tag{5.10}$$

where $\mathbf{P}$ stands for the matrix of weights for each observation, $\mathbf{Q}_{ll}$ is the matrix of cofactors, σ_0 gives the variance factor and Σ_{ll} is the so-called observation covariance matrix (or variance-covariance matrix).

For uncorrelated observations the matrix of weights $\mathbf{P}$ simply contains diagonal elements σ_0^2/σ_l^2, where σ_l^2 is the a priori variance of the l-th observation. If all observations have the same accuracy, $\mathbf{P}$ results in the unit matrix $\mathbf{I}$. If the observations are correlated, $\mathbf{P}$ becomes a dense matrix.

Following the method of least-squares adjustment Equation (5.9) gets solved by minimizing the term $\mathbf{v}^T\mathbf{P}\mathbf{v}$ (Todorova, 2009).

$$\begin{aligned} \mathbf{v}^T\mathbf{P}\mathbf{v} &= (\mathbf{x}^T\mathbf{A}^T - \mathbf{l}^T)\mathbf{P}(\mathbf{A}\mathbf{x} - \mathbf{l}) \\ &= \mathbf{x}^T\mathbf{A}^T\mathbf{P}\mathbf{A}\mathbf{x} - \mathbf{x}^T\mathbf{A}^T\mathbf{P}\mathbf{l} - \mathbf{l}^T\mathbf{P}\mathbf{A}\mathbf{x} + \mathbf{l}^T\mathbf{P}\mathbf{l} \end{aligned} \tag{5.11}$$

To achieve a minimum, the first derivative with respect to $\mathbf{x}$ has to be set to zero.

$$\frac{\partial \mathbf{v}^T\mathbf{P}\mathbf{v}}{\partial \mathbf{x}} = 2\mathbf{A}^T\mathbf{P}\mathbf{A}\mathbf{x} - 2\mathbf{A}^T\mathbf{P}\mathbf{l} = 0 \tag{5.12}$$

This results in the normal equation:

$$(\mathbf{A}^T\mathbf{PA})\mathbf{x} - \mathbf{A}^T\mathbf{Pl} = \mathbf{Nx} - \mathbf{b} \tag{5.13}$$

with $\mathbf{N} = \mathbf{A}^T\mathbf{PA}$ and $\mathbf{b} = \mathbf{A}^T\mathbf{Pl}$. $\mathbf{N}$ is called normal equation matrix.

Finally the unknowns can be calculated, if $\mathbf{N}$ is regular:

$$\mathbf{x} = (\mathbf{A}^T\mathbf{PA})^{-1}\mathbf{A}^T\mathbf{Pl} = \mathbf{N}^{-1}\mathbf{b} \tag{5.14}$$

The accuracy of the estimated parameters can be derived from the variance-covariance matrix $\boldsymbol{Q}_{\hat{x}\hat{x}} = \boldsymbol{N}^{-1}$ which contains the variances of the parameters in the main diagonal. More details about the post-adjustment accuracy assessment is presented in Section 6.4.1.

5.6.1 Partial derivatives with respect to the unknowns

The five parameters of the Giomo Model are gained by a least-squares adjustment of the measurements of a global observation network. In order to set up the $\mathbf{A}$ matrix the derivations with respect to the unknowns have to be calculated (Equations (5.15 - 5.19)), from the Equations (5.1) to (5.3).

$$\frac{\partial \mathrm{VTEC}}{\partial \mathrm{VTEC}_{\max}} = \left(\frac{1}{1 + \dfrac{d_\beta^2}{w_\beta^2}} \cdot \frac{1}{1 + \dfrac{d_s^2}{w_s^2}} \right) \tag{5.15}$$

$$\frac{\partial \mathrm{VTEC}}{\partial w_\beta} = \mathrm{VTEC}_{\max} \cdot \left(\frac{2\, w_\beta\, w_s^2\, d_\beta^2}{(w_\beta^2 + d_\beta^2)^2 \cdot (w_s^2 + d_s^2)} \right) \tag{5.16}$$

$$\frac{\partial \mathrm{VTEC}}{\partial w_s} = \mathrm{VTEC}_{\max} \cdot \left(\frac{2\, w_s\, w_\beta^2\, d_s^2}{(w_\beta^2 + d_\beta^2) \cdot (w_s^2 + d_s^2)^2} \right) \tag{5.17}$$

$$\frac{\partial \mathrm{VTEC}}{\partial s_{\max}} = \mathrm{VTEC}_{\max} \cdot \frac{2\, R^2 \cdot \cos^2 \beta_{\mathrm{IPP}} \cdot (s_{\mathrm{IPP}} - s_{\max})}{w_s^2 \cdot \left(1 + \dfrac{d_\beta^2}{w_\beta^2}\right) \cdot \left(1 + \dfrac{d_s^2}{w_s^2}\right)^2} \tag{5.18}$$

$$\frac{\partial \mathrm{VTEC}}{\partial \beta_{\max}} = \mathrm{VTEC}_{\max} \cdot \frac{2\,R^2 \cdot (\beta_{\mathrm{IPP}} - \beta_{\max})}{w_\beta^2 \cdot \left(1 + \frac{d_\beta^2}{w_\beta^2}\right)^2 \cdot \left(1 + \frac{d_s^2}{w_s^2}\right)} \tag{5.19}$$

5.6.2 Approximate values

For a robust convergence of the estimates, approximate values of the Giomo parameters are requested. The following section deals with test calculations in order to get accuracy requirements for the a priori values. Afterwards the calculation strategies to obtain these requirements are presented.

Accuracy of the approximate values

All subsequent calculations are performed for Epoch June 2, 2018, 05:00 UTC. The values that are used for these tests are shown in Table 5.1.

For the first tests, only one of the five parameters was selected to vary from the true value (the a priori values of the remaining four parameters are set to the true value). This depicts an extremely optimistic assumption yielding accuracy requirements that have to be met in any case. The results indicate that in this setting, the estimated parameters (except for $\beta_{\max}$) are not sensitive to wrong a priori values in the tested range (see Table 5.1). This means that the iterative parameter estimation process yields the correct values for all parameters even if one of the parameters $\mathrm{VTEC}_{\max}$, w_β, w_s, or $s_{\max}$ has wrong a priori values in the range of ±50 % or ±50° (see Figure 5.10). This is, however, not the case for $\beta_{\max}$, where results deteriorate if the a priori value is wrong by more than approximately 35°. The errors in the estimated parameters instantly increase significantly. These results are shown in Figure 5.11.

A second set of tests has been performed, yielding presumably more realistic accuracy requirements for a priori values. For these tests the a prioris of all parameters are modified at the same time.
This test yields to a very pessimistic (too strict) accuracy requirement for the parameters, because all parameters are assumed to be similarly wrong.
The range for the a priori test values is again presented in Table 5.1. The resultant errors of the estimated parameters are shown in Figure 5.12. Estimates with relative errors $<10^{-5}$ % are assumed to be correct and, for better visibility, set to 10^{-5} %. The results show a degradation of derived parameters if all a priori values are approximately 22 % (or 22° for the coordinates of the ionospheric maximum, $\beta_{\max}$ and $s_{\max}$) too small or 34 % (34°) too large.

Based on the above tests, the discovered accuracy requirements of a priori values for the parameter estimation procedure are the following: If – in an optimistic scenario – only one parameter has significantly wrong a priori values, these can be corrected for the parameters $\mathrm{VTEC}_{\max}$, w_β and w_s within a range of ±50 % or ±50° for $s_{\max}$. $\beta_{\max}$ must be known in advance within ±35°,

Table 5.1: Settings for the a priori accuracy requirements tests

Parameter	True value (June 2, 05:00 UTC)	Test range	Test range (June 2, 05:00 UTC)
$VTEC_{max}$	29.4 TECU	±50 %	14.7 TECU–44.1 TECU
w_β	4153195 m	±50 %	2076597 m–6229793 m
w_s	10461654 m	±50 %	5230827 m–15692481 m
β_{max}	7.2°	±50° [a]	-42.8°–57.2° [a]
s_{max}	34.0°	±50°	-16.0°–84.0°

[a] The maximal/minimal declination of the Sun is reached at ±23.44°. As β_{max} is approximately equal to the declination of the Sun, the test range is larger than any possible error.

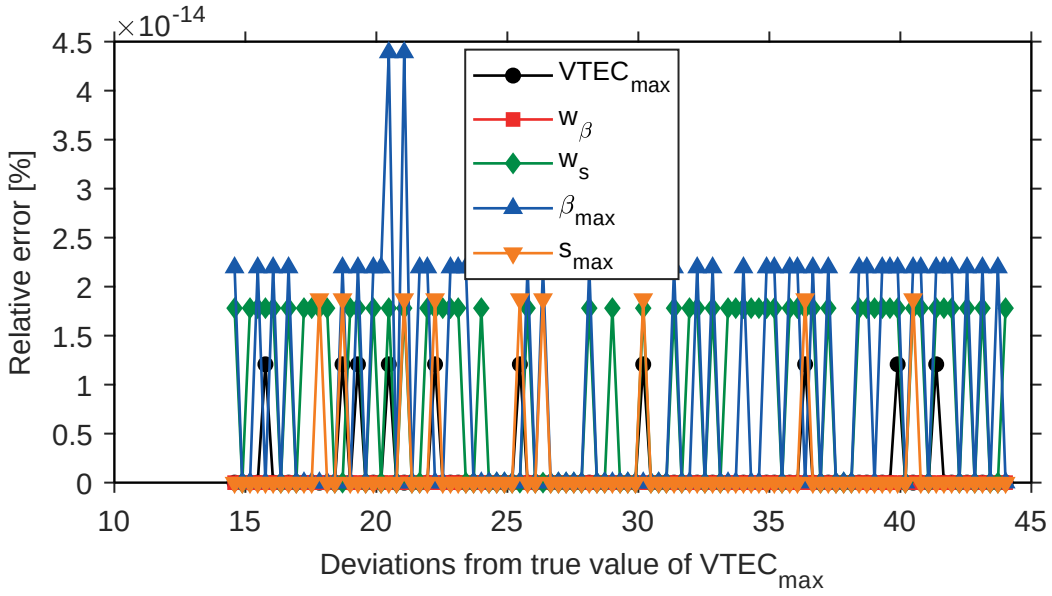

Figure 5.10: Estimated parameters derived from a range of a priori values for $VTEC_{max}$. The a priori values of all other parameters are set to the correct estimates.

which should be no problem as it is approximately equal to the declination of the Sun, which can be calculated. In a pessimistic scenario, $VTEC_{max}$, w_β, and w_s must be known with accuracies between -22 % and 34 %; s_{max} and β_{max} between -22° and 34°. However, these values are only valid for this test where $\beta_{max} = 7.2°$.

$VTEC_{max}$

Hourly processing of the Giomo Model for eight months showed, that about 1.5 % of the VTEC values calculated by building the geometry-free linear combination are higher than the final value for the parameter $VTEC_{max}$. So the approximate value for $VTEC_{max}$ is not exactly set equal to the highest VTEC value derived by the one-hour-calculation, but to the value at about 98.5 % (0.985 quantile).

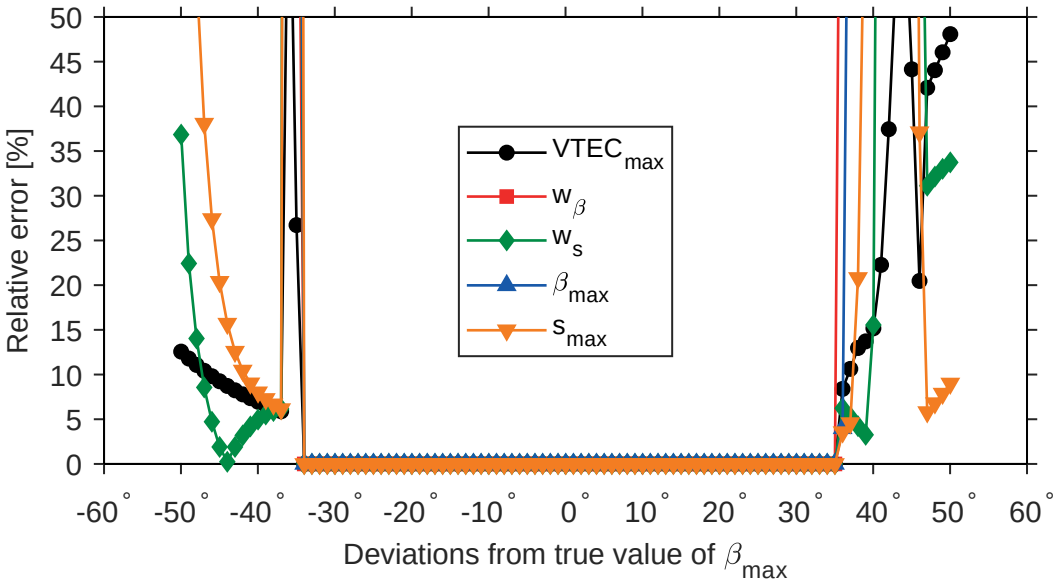

Figure 5.11: Estimated parameters derived from a range of a priori values for β_{max}. The a priori values of all other parameters are set to the correct estimates.

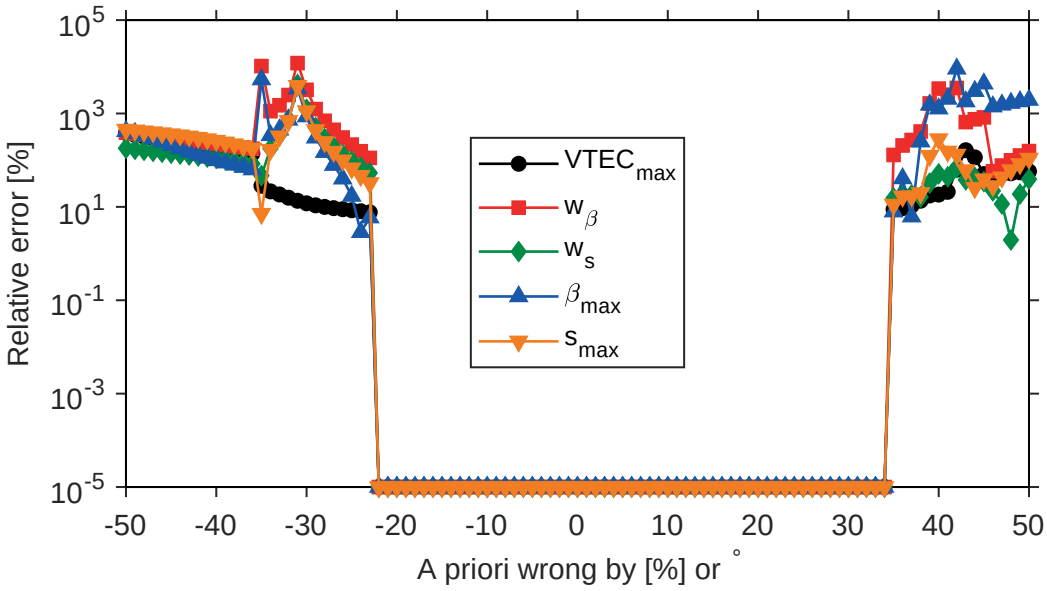

Figure 5.12: Estimated parameters derived from a range of a priori values. The a priori values for all parameters are modified by -50 % (-50° for β_{max} and s_{max}) to 50 % (50°) from the correct estimated values. All relative errors $<10^{-5}$ are set to 10^{-5} to allow visualization of small (or zero) errors (i.e., correct estimates).

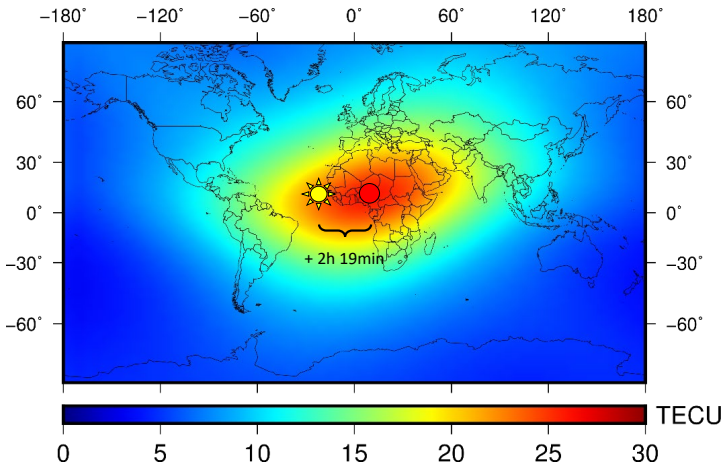

Figure 5.13: Approximately 2 hours and 19.4 minutes difference in longitude between the mean Sun and VTEC_{max}

$\mathbf{s}_{\text{max}}$ and β_{max}

To approximate s_{max} and β_{max} the coordinates of the Sun plus a two hour and 19.4 minutes delay in longitude was taken, because the maximum VTEC is located approximately in this range (see Figure 5.13). This behavior can also be deduced from Figure 6.6 in Chapter 6.

$\mathbf{w}_{\beta}$ and $\mathbf{w}_{s}$

The approximate values for w_β and w_s were gained as follows: First a band of ±0.3 rad next to the parallel or meridian of s_{max} or β_{max} is chosen. All coordinate differences in meters d_β or d_s and the corresponding VTEC-values of the IPPs located in this band computed for one hour are selected. Also the approximate value for VTEC_{max} was added with $d_\beta = 0$ or $d_s = 0$. After that $\text{VTEC}_{\text{max}}/2$ was calculated because this corresponds approximately to w_β (or w_s) (see Equation 5.1 and subsequent text). Finally the algorithm searches for all reference sites' observations with a VTEC-difference smaller than a certain marginal value to $\text{VTEC}_{\text{max}}/2$. The mean of all these observations' d_β or d_s is taken for the approximate value of w_β or w_s. The Figures 5.14 and 5.15 visualize the results for the approximation for June 3, 2018, 14:00. The blue dots show the VTEC-values for all IPPs located in the chosen band. The black curve is the moving average for all observations with equal distance to VTEC_{max}. The index 0 in $\text{VTEC}_{\text{max,0}}$ denotes the approximation value. The red curve is plotted with the approximate values for w_β (Figure 5.14) or w_s (Figure 5.15).

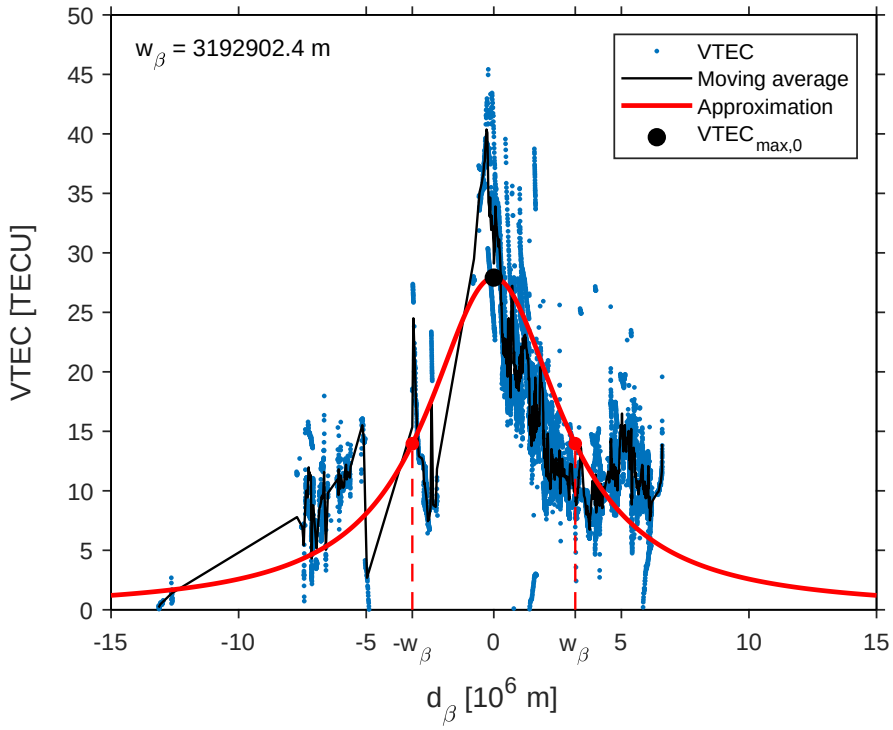

Figure 5.14: Approximate value for w_β ($\text{VTEC}_{\text{max,0}}$ denotes the approximation value)

5.7 IONEX Format

The Giomo software is able to write IONEX files based on the model parameters which are valid for predefined areas and periods. This file format provides VTEC values on a geographical grid (Schaer *et al.*, 1998). The arbitrary located user receiver can interpolate this grid information by e.g. bilinear splines.

By default IONEX files are named according to (Schaer *et al.*, 1998):

`ccceddd h.yyI`

where

- `ccc`: 3-character Analysis Center designator
- `e`: extension or region code (`G` ... Global Ionosphere Maps)
- `ddd`: day of year (DOY) of first record
- `h`: file sequence number (`1,2,...`) or hour (`A,B,...` within one day)
  `0`: file contains all existing data of the current day
- `yy`: 2-digit year
- `I`: file type (`I` ... Ionosphere map)

The Giomo Model has three different types of extensions or regional codes:
`G` ... Global Ionosphere Maps

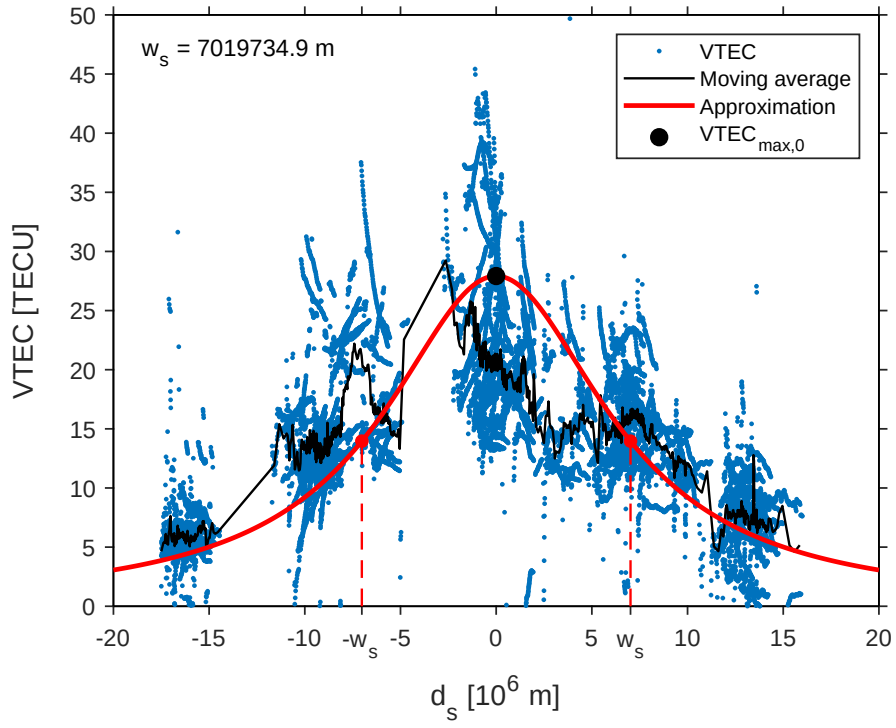

Figure 5.15: Approximate value for w_s ($\text{VTEC}_{\text{max},0}$ denotes the approximation value)

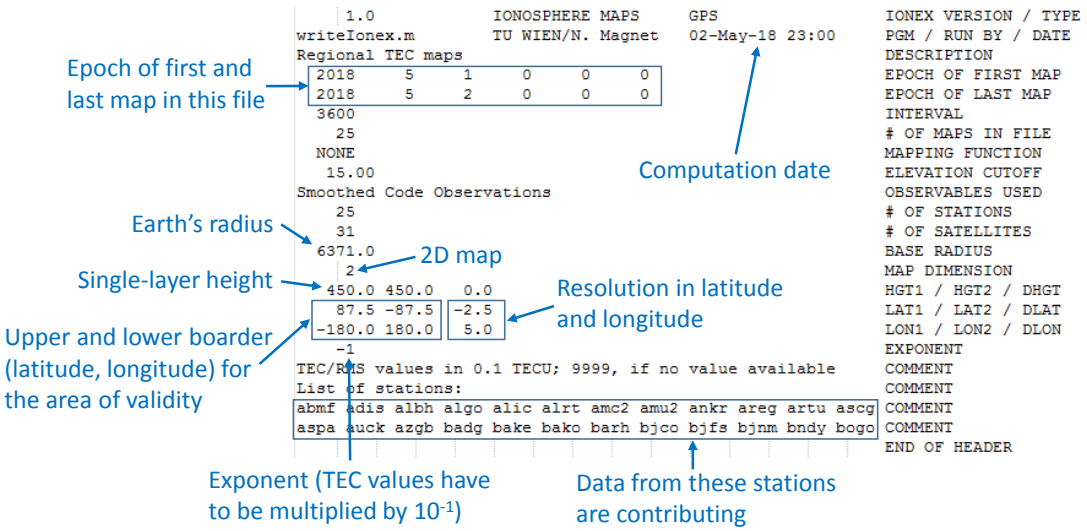

Figure 5.16: IONEX file header

`R` ... Regional Ionosphere Maps (= Maps of Europe)
`P` ... Predicted Ionosphere Maps

For example a file computed at Technische Universität Wien for DOY 145 in 2018 can be named `TUWG1450.18I`.

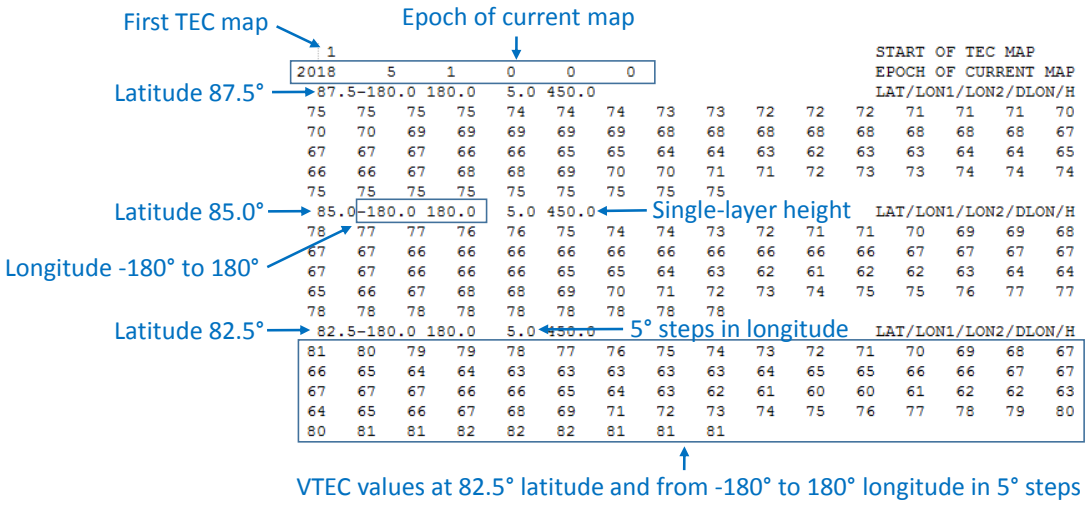

Figure 5.17: IONEX file data section

Each IONEX file consists of a header and a data part. The figures (5.16) and (5.17) explain the most important entries in the IONEX file. For further information and regulations see Schaer *et al.* (2015).

5.7.1 Spatial and temporal resolution

On the one hand the Giomo Model can be evaluated globally, on the other hand only for Europe. The global IONEX files have a spatial resolution of $2.5° \times 5°$. The IONEX maps for Europe have a resolution of $1° \times 1°$, although they have the same spectral resolution as the global maps. The temporal resolution is one hour, starting with 00:00 Universal Time Coordinated (UTC). An IONEX file with $\mathtt{h} = 0$ contains 25 TEC maps starting with 00:00 UTC of the current day and ending with 00:00 UTC of the following day.

Chapter 6

Giomo Model: Results

To evaluate the plausibility of the VTEC values calculated with the Giomo Model, each model parameter is analyzed. Then a comparison of the resulting TEC maps and VTEC values to established models is carried out. The evaluation also includes a comparison to the other ionosphere model calculated at TU Wien, the regional Regiomontan Model. Finally a quality analysis is carried out, including an analysis of pseudorange corrections with different ionosphere models. At the end of this chapter, the performance of the Giomo Model to predict the ionosphere state is described and evaluated.

6.1 Model parameter analysis

This section focuses on the five parameters of the Giomo Model. Each parameter was checked for its plausibility, using time lines, analysis or comparisons. Formal errors and correlations of the model parameters are given in Chapter 6.4.1.

6.1.1 $\mathbf{VTEC_{max}}$

The time series of $VTEC_{max}$ values between March 26 and July 1, 2018 is shown in Figure 6.1. The Giomo Model underestimates the $VTEC_{max}$ compared to the CODE model, but both models are consistent.

The corresponding frequency spectrum, computed after the removal of a linear trend, is presented in Figure 6.2. A detail screen can be seen in Figure 6.3. The peak at around 14 days possibly correlates with half the Sun rotation period.

6.1.2 Coordinates of $\mathbf{VTEC_{max}}$

The position of $VTEC_{max}$, β_{max} and s_{max} (see Equations (5.2) and (5.3)), is shown on a map in Figures 6.4 and 6.5. The former illustrates the change of $VTEC_{max}$ over a day, the latter the season-dependency of the geomagnetic latitude of $VTEC_{max}$. Whereas in March the position of the maximum is placed in the equatorial region, it moves in summer (at solstice) up to the obliquity

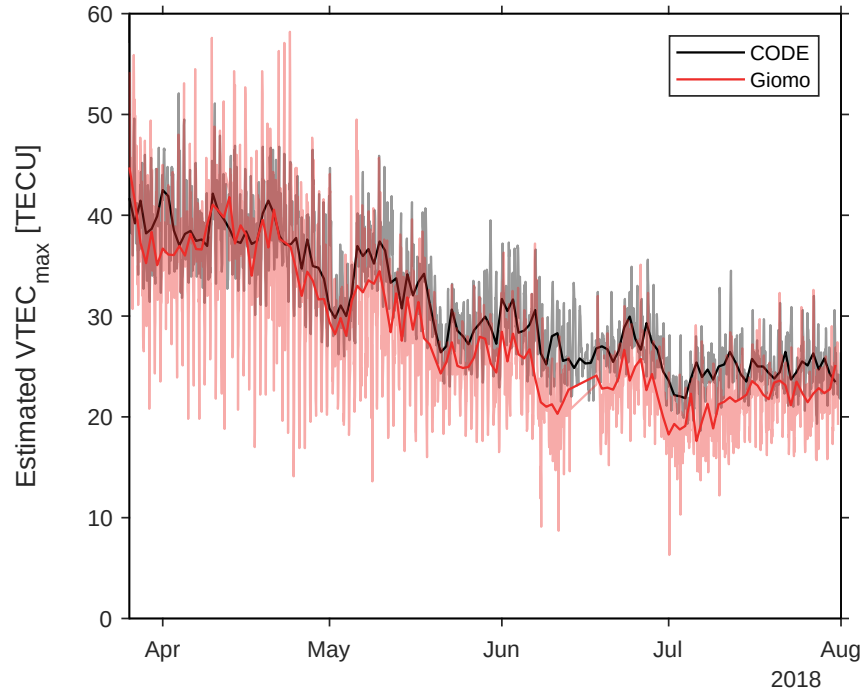

Figure 6.1: Time series of estimated $VTEC_{max}$ with hourly time resolution compared to the VTEC maximum values calculated by CODE between March 26 and July 31, 2018. The darker bold lines show daily median values.

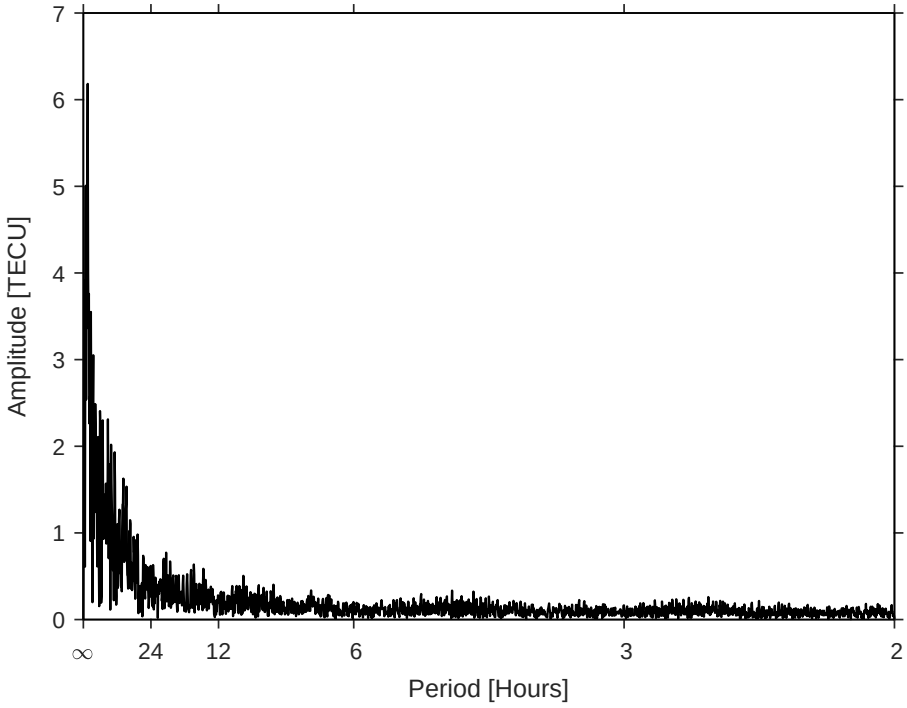

Figure 6.2: Frequency spectrum of estimated $VTEC_{max}$ between March 26 and July 1 2018. A linear trend has been removed prior to estimating the Fourier coefficients.

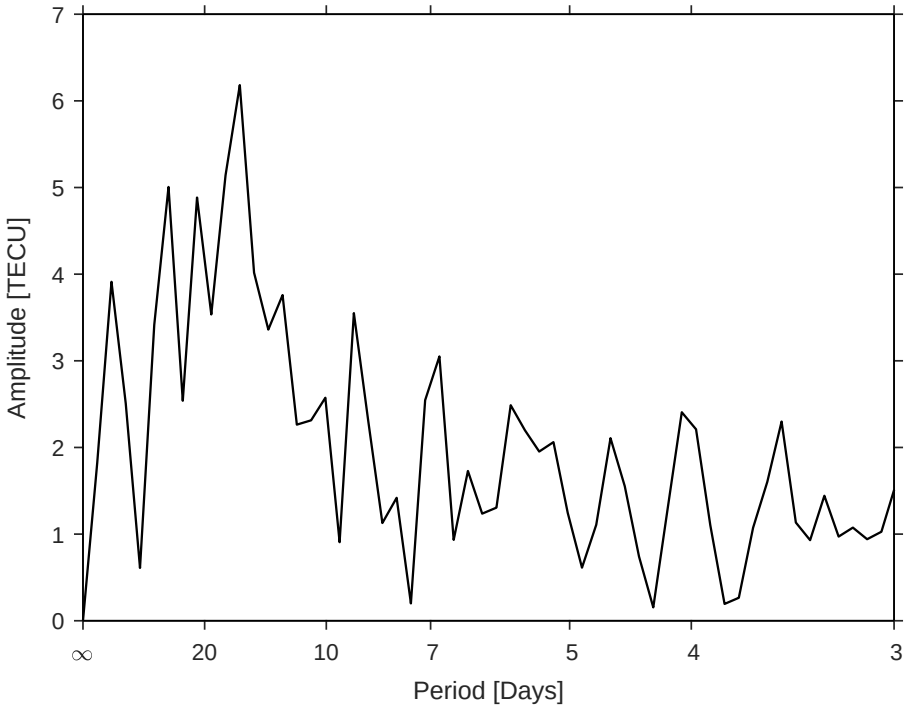

Figure 6.3: Frequency spectrum of estimated $VTEC_{max}$ between March 26 and July 1 2018. Detailed visualization of Figure 6.2.

of the ecliptic of about 23.5°, like the Sun. $VTEC_{max}$ is always clearly located along and parallel to the geomagnetic equator.

Figure 6.6 displays a histogram of the sun-fixed longitude s_{max} of the maximum VTEC. The mean sun-fixed longitude is 34.86°, indicating that the $VTEC_{max}$ follows the Sun's tracing point with a delay of about 2 hours and 19.4 minutes (± 31 minutes).

6.1.3 Weighting factors

The estimated weighting factors w_β and w_s from March 26 to July 1, 2018 are presented in Figure 6.7. The weighting factor in longitude is more than two times bigger than the one in latitude, indicating that the VTEC decreases faster in latitude direction. This is expected as also the VTEC maps show that the ionospheric bulge is stretched more in longitude direction, caused by the Earth's rotation.

6.2 TEC Maps

Hourly **global TEC maps** are produced with a resolution of 2.5° × 5°. Figure 6.8 shows an example for October, 2nd 2018.

Hourly **regional TEC maps** covering Europe are produced with a spatial resolution of 1° × 1° within the grid area $\varphi = 35°$ to 60° N and $\lambda = -10°$ to 35° E. An example is given in Figure 6.9.

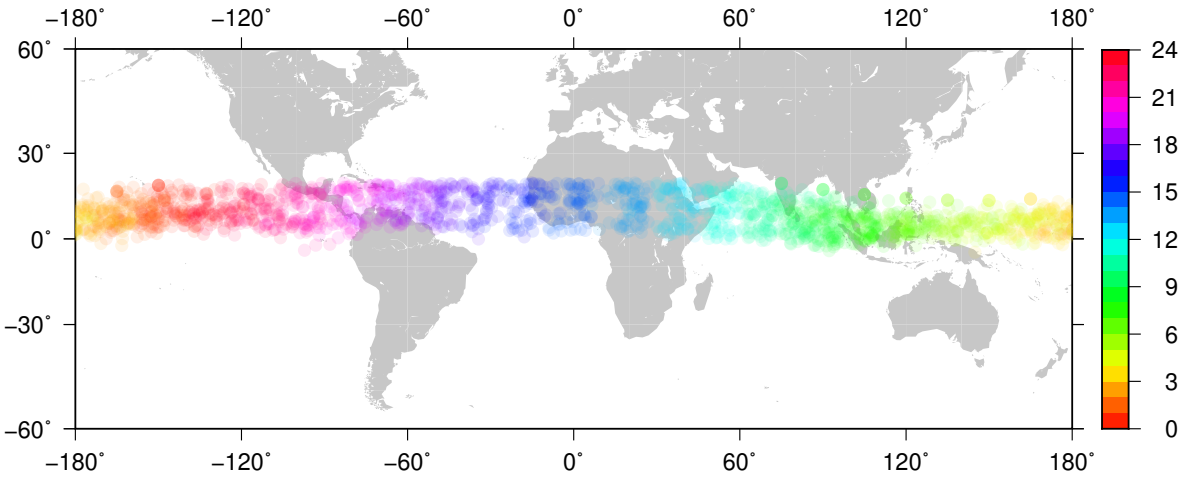

Figure 6.4: Hourly position of $VTEC_{max}$ between March 26 and July 1 2018. Colors represent the hour of the day (in UTC).

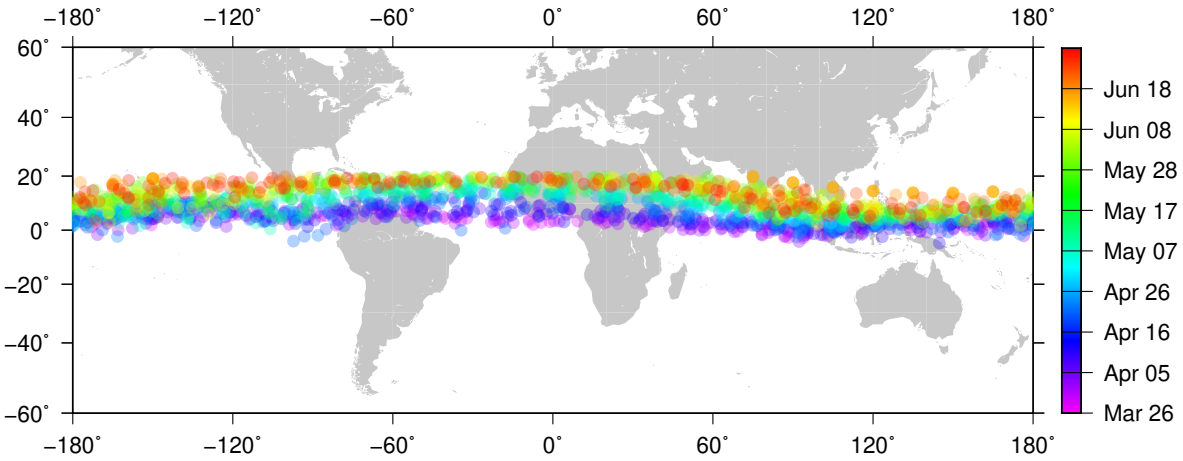

Figure 6.5: Hourly position of $VTEC_{max}$ between March 26 and July 1 2018. Colors represent the epoch.

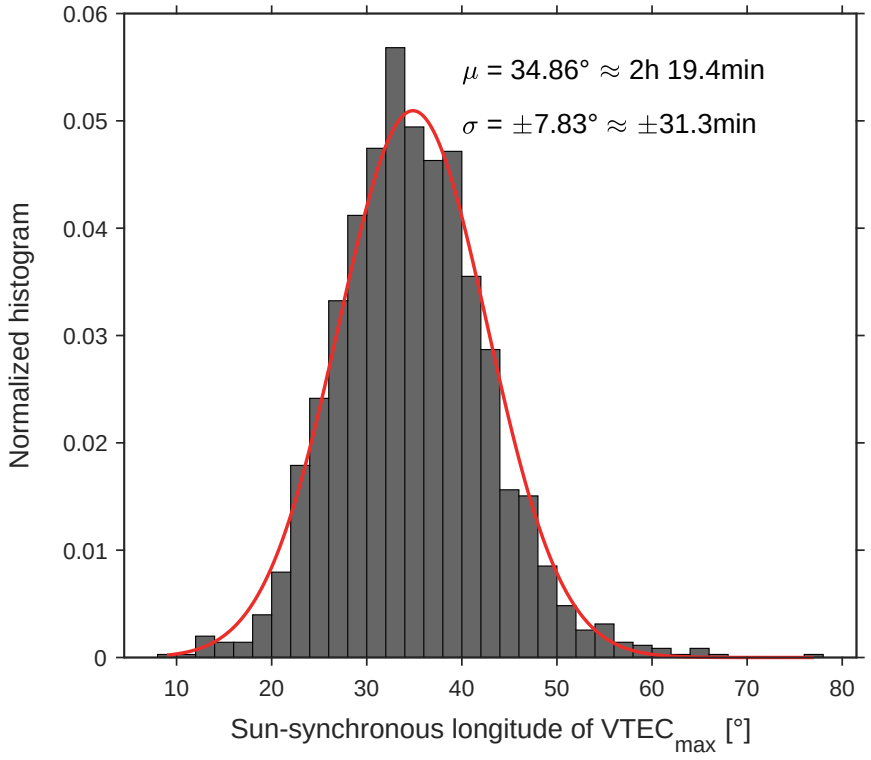

Figure 6.6: Position of $VTEC_{max}$ in a solar-fixed coordinate system between March 26 and July 1 2018

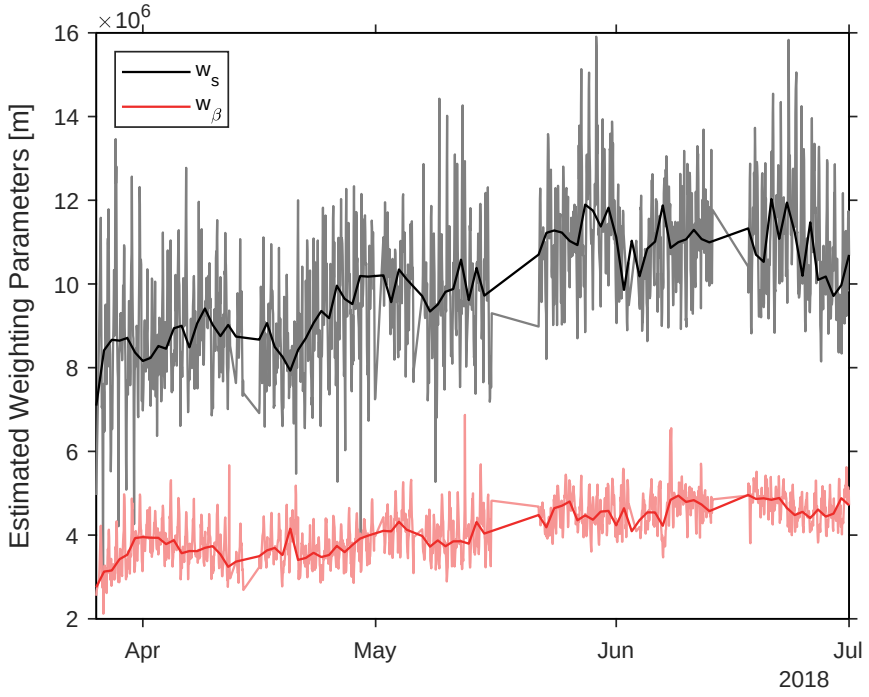

Figure 6.7: Time series of weighting factors between March 26 and July 1, 2018. The dark black and red lines show daily median values.

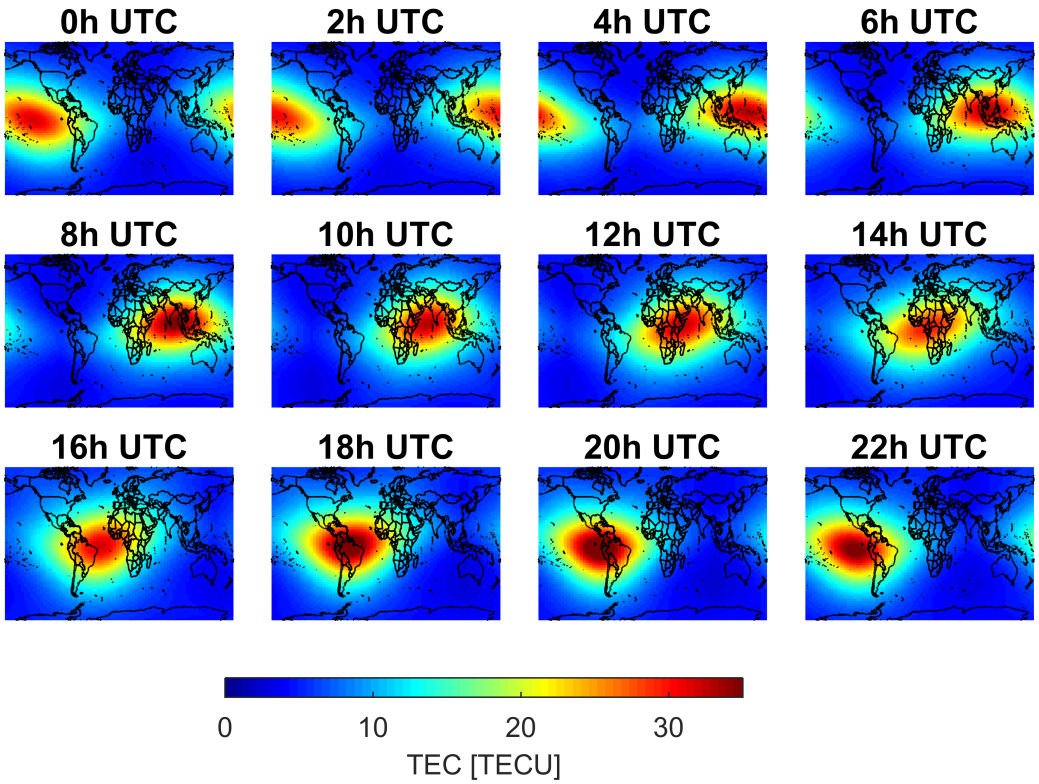

Figure 6.8: Global TEC map for October, 2nd 2018 calculated with the Giomo Model

Although they have a different spatial resolution, both the global and the regional maps have the same spectral resolution, as they are calculated only with the five parameters.

6.3 Comparison to established models

The Giomo Model gets compared to the established models of Klobuchar, CODE and IGS and additionally to the Regiomontan Model.

Table 6.1 shows a statistical comparison of the ionosphere models. Hourly VTEC differences between June 3rd and October 11th 2018 were calculated. From these differences, mean values, standard deviations and median values are derived, which are presented in Table 6.1.

The mean differences indicate a good general agreement between the Giomo Model and the IGS Model (mean difference of -0.12 TECU). However, the standard deviation (±2.75 TECU) shows that there exist larger differences between the two models which average out over longer time spans. The IGS Model and the CODE Model show a good agreement of 0.80 TECU mean difference. The Klobuchar Model clearly shows the largest discrepancies to all other models with mean differences between 2.59 TECU and 4.13 TECU. This is also graphically demonstrated in Figure 6.10.

Moreover, VTEC plots for specific locations at $\varphi = 0°$, 20°, 40°, 60°, 80° and 48° N (located in Austria) and $\lambda = 15°$ E (for all) were computed (Figure 6.11).

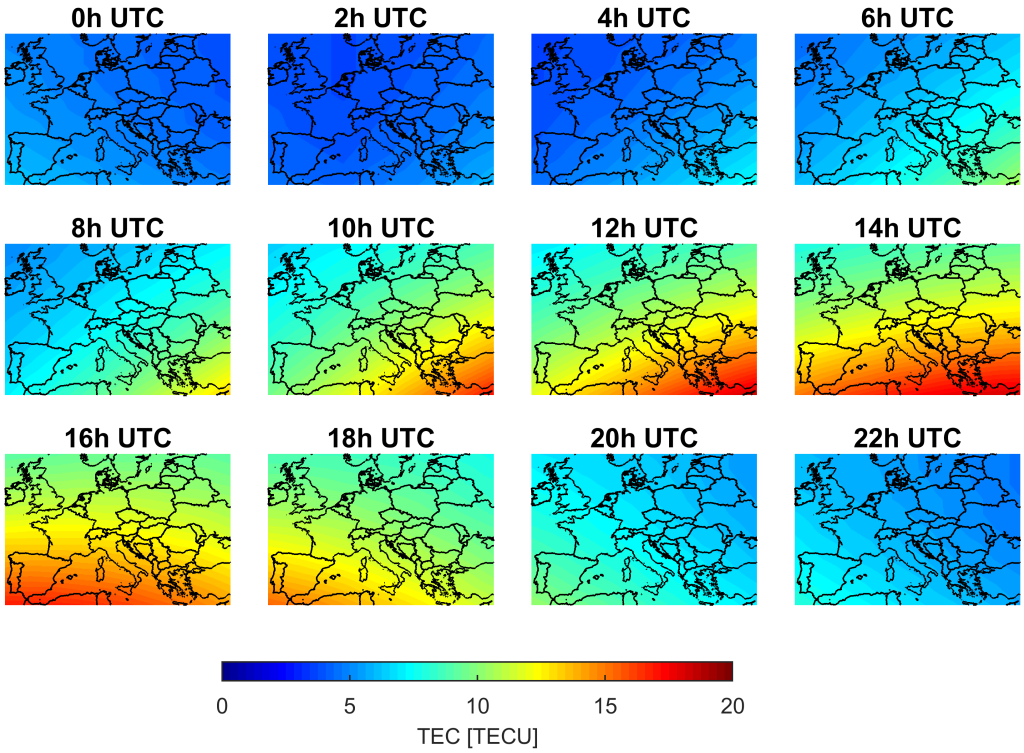

Figure 6.9: Regional TEC map for October, 2nd 2018 calculated with the Giomo Model

Table 6.1: Statistical comparison of the VTEC derived by various ionospheric models. Numbers are calculated over all epochs between June 3rd 2018 and October 11th 2018. First row for each model: Mean ± standard deviation; Second row: Median. Unit: TECU.

	Giomo	CODE	IGS	Klobuchar
Giomo		-0.80 ± 2.76	0.12 ± 2.75	2.71 ± 3.47
		-1.00	-0.10	3.30
CODE	0.80 ± 2.76		0.93 ± 0.52	3.51 ± 4.09
	1.00		0.90	4.09
IGS	-0.12 ± 2.75	-0.93 ± 0.52		2.59 ± 4.13
	0.10	-0.90		3.10
Klobuchar	-2.71 ± 3.47	-3.51 ± 4.09	-2.59 ± 4.13	
	-3.30	-4.09	-3.10	

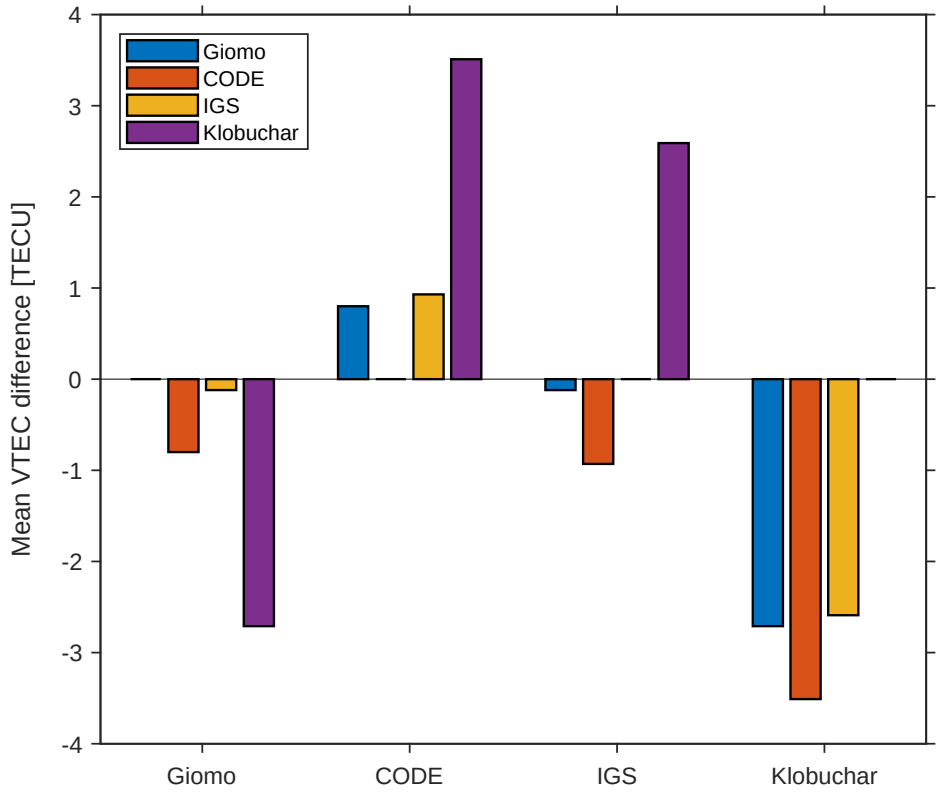

Figure 6.10: Comparison of different ionosphere models regarding their mean VTEC difference

In the figures (a) and (b), for points near the ionospheric maximum, all models show a good consistency, especially at $\varphi = 20°$ N. At the equator, the other models seem to underestimate the TEC compared to CODE and IGS. It can be clearly seen, that the Klobuchar Model only delivers a constant value at night, which appears to be too optimistic for some hours.

In the figures (c) and (d) Klobuchar is overestimating the VTEC up to 7 TECU. The other models show a good consistency again, although the Giomo Model underestimates the VTEC at nighttime by up to -3 TECU. This is not the case for $\varphi = 48°$ N, here the TEC gets slightly overestimated at noon. This can be explained by the fact, that the Giomo Model only consists of five parameters, so it cannot account for small regional changes of the TEC, but estimates the VTEC maximum very well. In figure (d), where the point of interest is located in Austria, also the Regiomontan Model takes part in the comparison. It fits very well to the model of CODE.

In figure (e) the Giomo Model again delivers higher values than CODE and IGS, which can be explained by the flat drop of the Giomo functional model towards the poles. In both figures (e) and (f) the IGS Model seems to underestimate the TEC for those high latitudes. Here Klobuchar overestimates the VTEC in general. For $\varphi = 80°$ N only a constant value is derived for the whole day, which is on average about 4 TECU above the real TEC.

In a further step the corresponding IONEX files and also their differences are plotted as VTEC maps. There is always a global map (except for the regional Regiomontan Model) and a European map shown, one for the whole day (composed of 12 maps every two hours) and one for

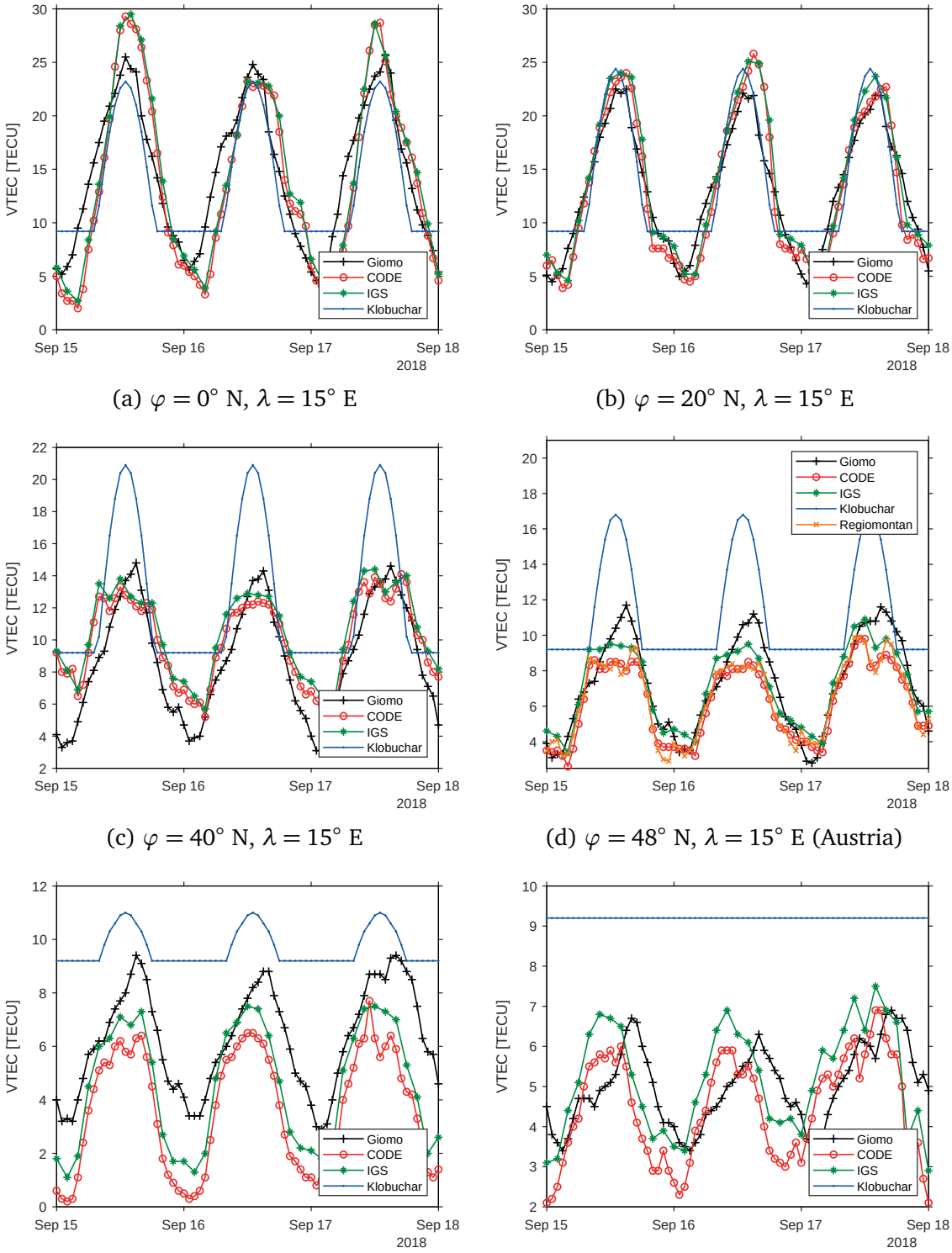

(a) $\varphi = 0°$ N, $\lambda = 15°$ E

(b) $\varphi = 20°$ N, $\lambda = 15°$ E

(c) $\varphi = 40°$ N, $\lambda = 15°$ E

(d) $\varphi = 48°$ N, $\lambda = 15°$ E (Austria)

(e) $\varphi = 60°$ N, $\lambda = 15°$ E

(f) $\varphi = 80°$ N, $\lambda = 15°$ E

Figure 6.11: Comparison of VTEC values of different ionosphere models for different latitudes

14:00 UTC. The plots can be seen in Chapters 6.3.1 (Klobuchar Model), 6.3.2 (CODE Model), 6.3.3 (IGS Model) and 6.3.4 (Regiomontan Model).

6.3.1 IONEX comparison: Giomo - Klobuchar

In order to visually compare the Klobuchar and the Giomo Model via TEC maps, daily global IONEX files were computed out of the Klobuchar parameters. Figure 6.12 visualizes a daily global map, Figure 6.13 a daily European map, Figure 6.14 a global map at 14:00 UTC and Figure 6.15 a European map at 14:00 UTC. The Klobuchar Model seems to underestimate the VTEC at daytime and overstimates it at night. This is why the plots show differences from -10 TECU to +10 TECU. This is also why for the European map the highest differences of about -10 TECU occur at noon and get smaller as time progresses. Figure 6.14 demonstrates, that the ionospheric bulges of the two models expand in different directions. The result is a kind of interference pattern at the difference plot.

6.3.2 IONEX comparison: Giomo - CODE

The Center for Orbit Determination in Europe (CODE) provides hourly global VTEC maps using a Spherical Harmonics Expansion up to degree 15 with a spatial resolution of 2.5° × 5°. Figure 6.16 visualizes the difference to the Giomo Model for a daily global map, Figure 6.17 for a daily European map, Figure 6.18 for a global map at 14:00 UTC and Figure 6.19 for a European map at 14:00 UTC. The Giomo Model and the CODE Model show a good consistency, although of course CODE accounts also for regional effects, which cannot be handled with Giomo. For Europe the differences are between -2 TECU and 5 TECU, at 14:00 UTC they are even smaller.

6.3.3 IONEX comparison: Giomo - IGS

The IGS delivers global VTEC maps with a spatial resolution of 2.5° × 5° and a temporal resolution of two hours. Figure 6.20 visualizes a daily global map, Figure 6.21 a daily European map, Figure 6.22 a global map at 14:00 UTC and Figure 6.23 a European map at 14:00 UTC. The Giomo Model and the IGS Model even show a better consistency than with CODE. In Europe the differences are only about -1 TECU to +3 TECU. At 14:00 UTC the Giomo Model seems to overestimate the VTEC in Europe by a mean of about 2 TECU.

6.3.4 IONEX comparison: Giomo - Regiomontan

Regiomontan is a regional model for Austria only delivering hourly VTEC values over Europe with a spatial resolution of $1° \times 1°$. This is why also the plots look a bit different, like the ionization would decrease again towards the equator, since only Austrian and surrounding stations were used for the calculation.

Figure 6.24 visualizes a daily European map and Figure 6.25 a European map at 14:00 UTC. Giomo Model and Regiomontan Model show larger differences at the model boundaries from

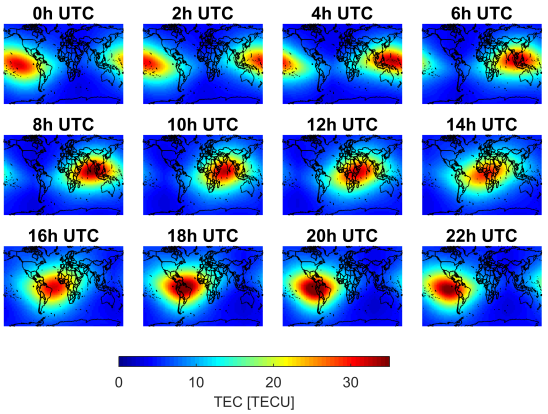

(a) Giomo

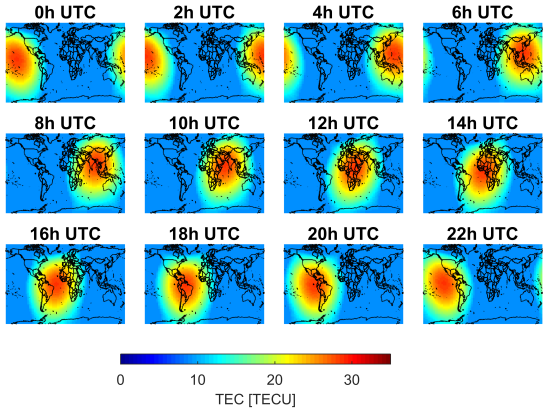

(b) Klobuchar

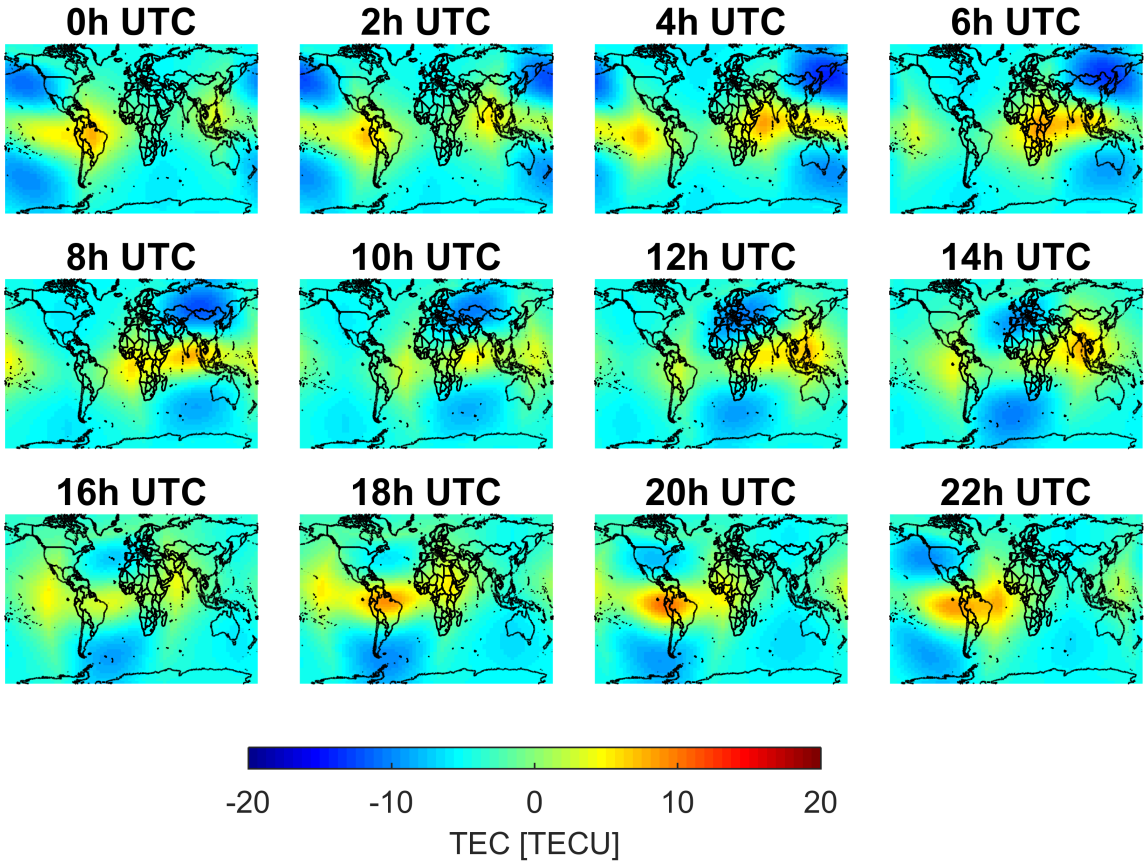

(c) Difference (Giomo - Klobuchar)

Figure 6.12: Global VTEC maps of Giomo and Klobuchar Model and their difference for October 2, 2018

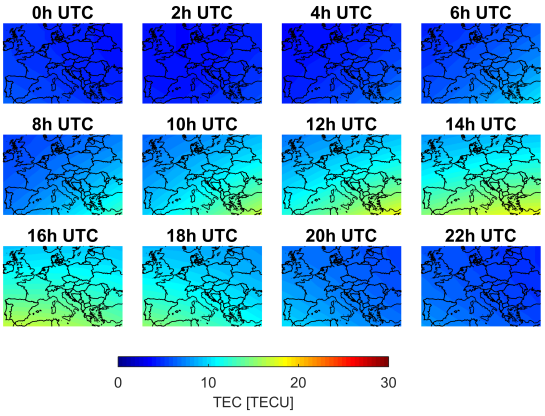

(a) Giomo

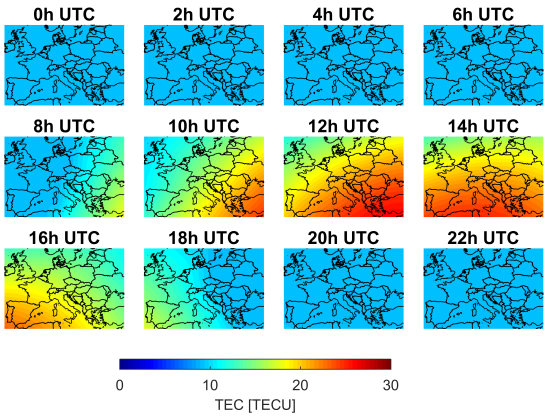

(b) Klobuchar

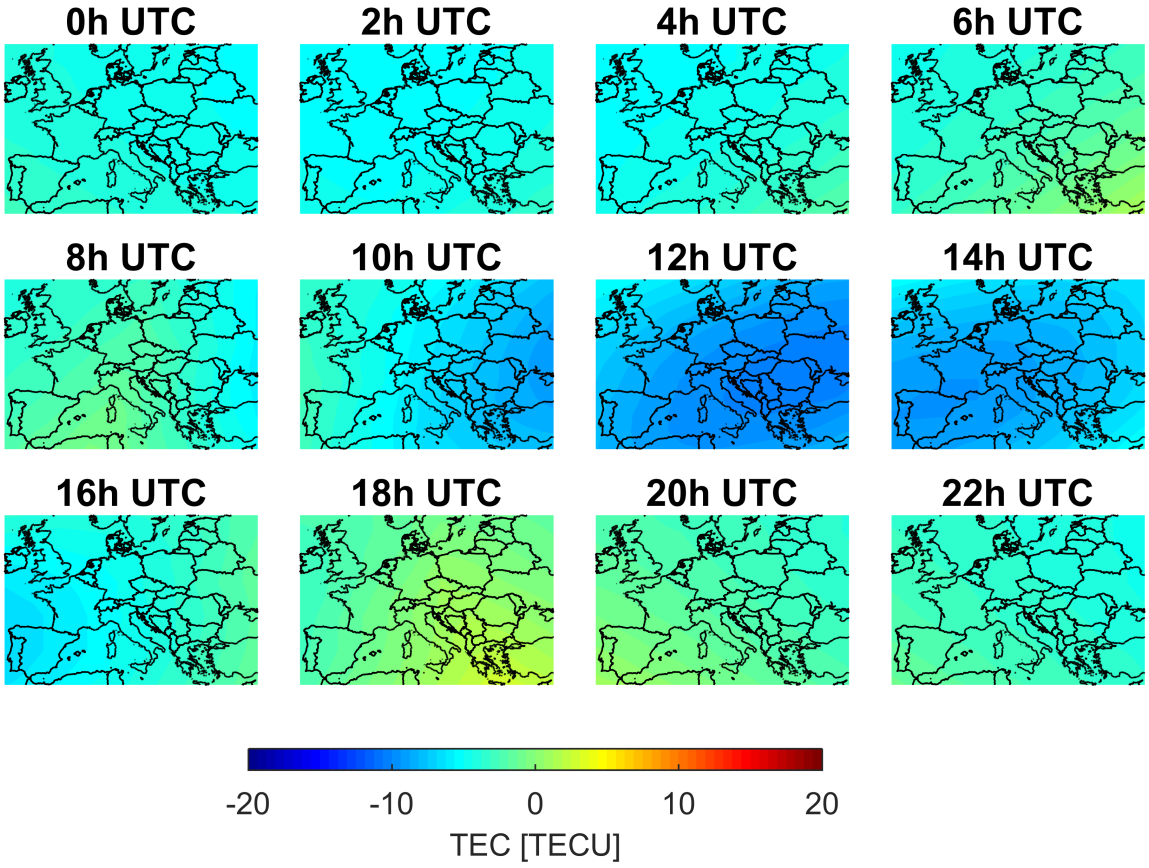

(c) Difference (Giomo - Klobuchar)

Figure 6.13: European VTEC maps of Giomo and Klobuchar Model and their difference for October 2, 2018

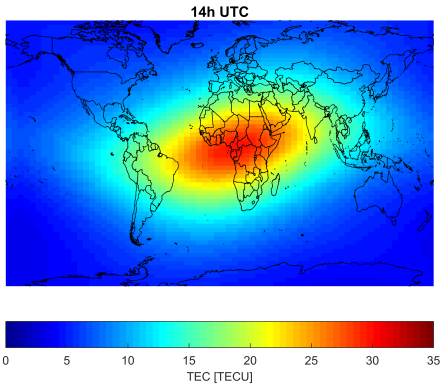

(a) Giomo

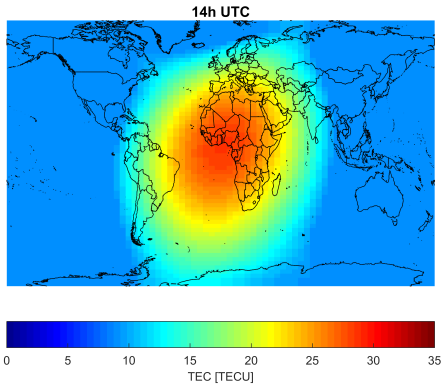

(b) Klobuchar

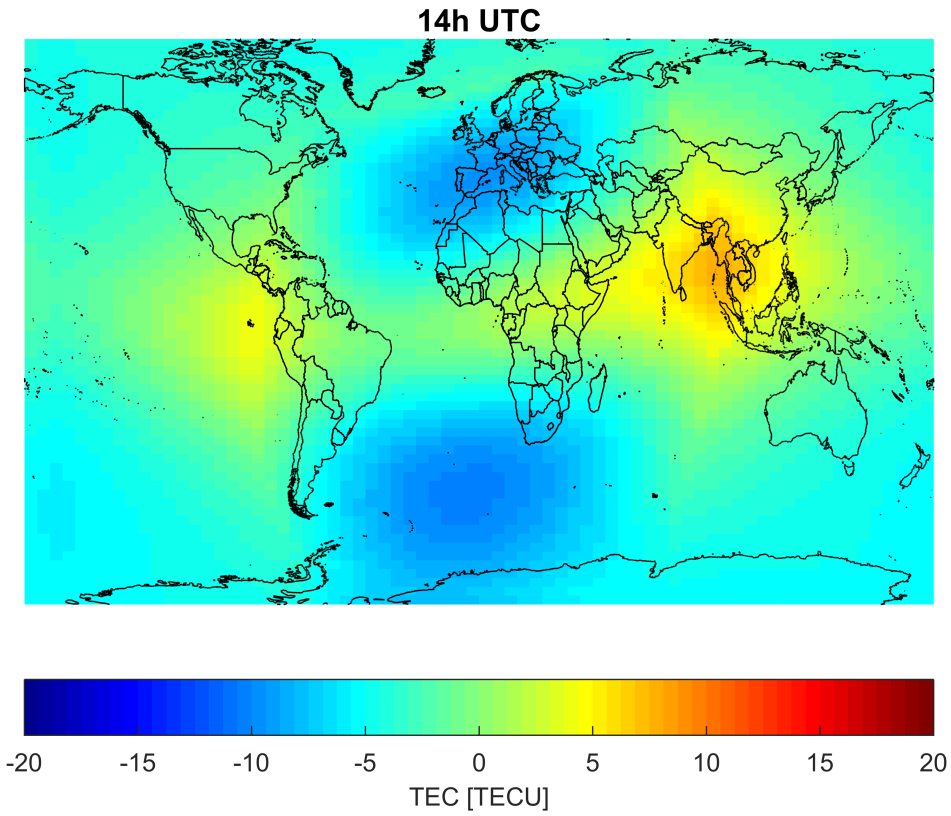

(c) Difference (Giomo - Klobuchar)

Figure 6.14: Global VTEC maps of Giomo and Klobuchar Model and their difference for October 2, 2018, 14:00 UTC

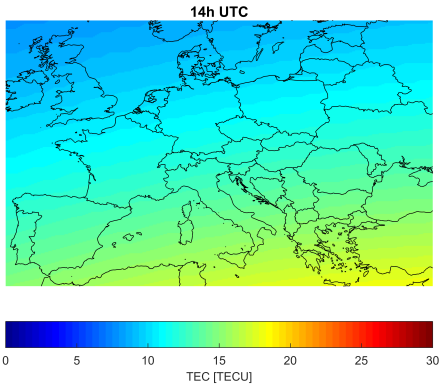

(a) Giomo

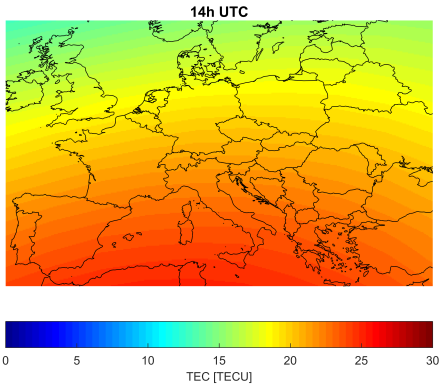

(b) Klobuchar

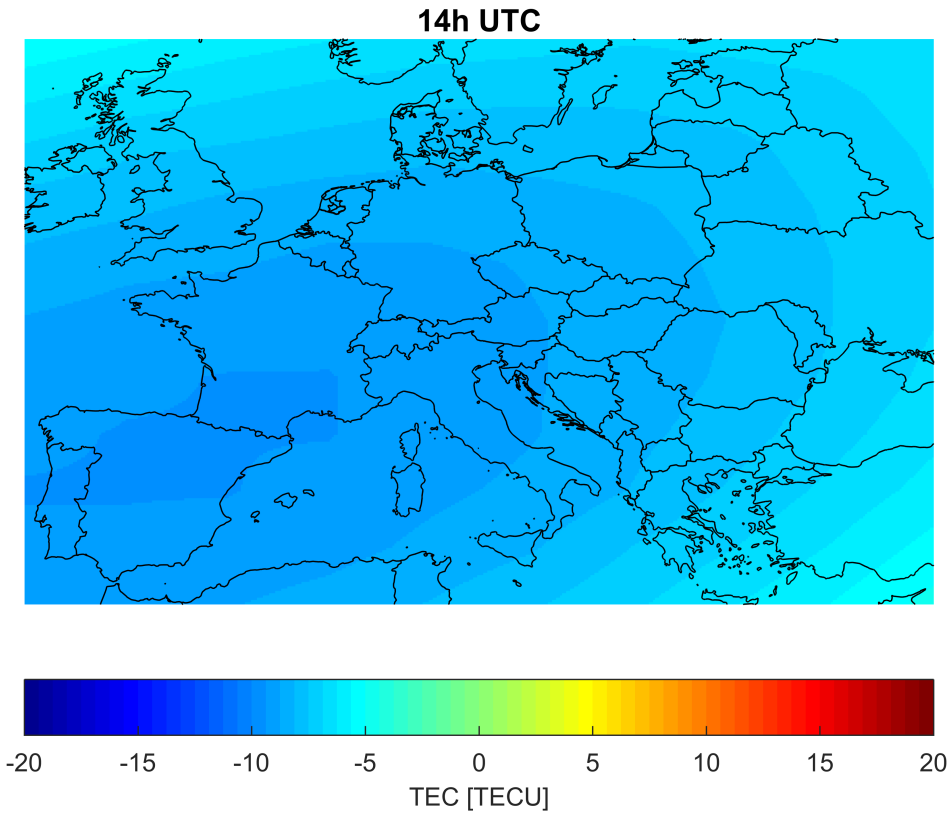

(c) Difference (Giomo - Klobuchar)

Figure 6.15: European VTEC maps of Giomo and Klobuchar Model and their difference for October 2, 2018, 14:00 UTC

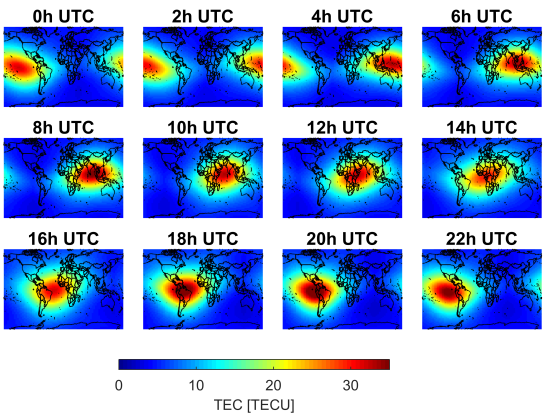

(a) Giomo

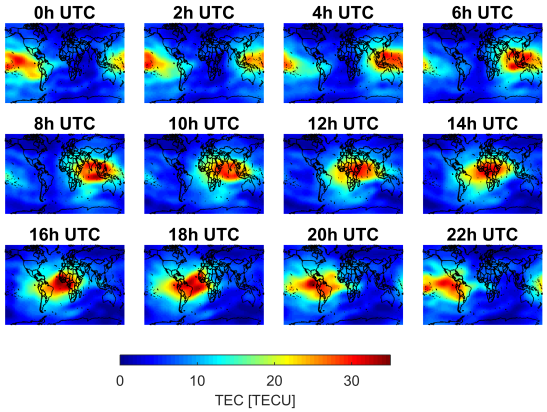

(b) CODE

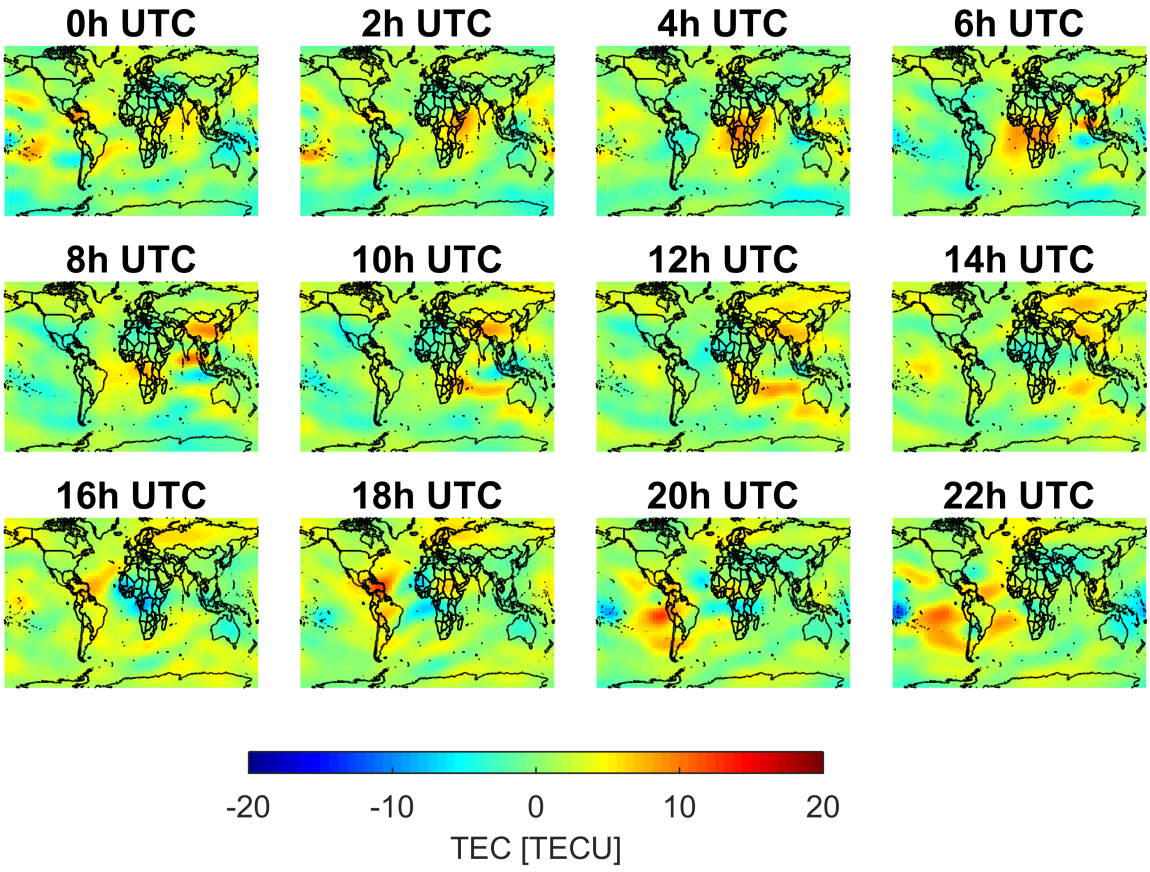

(c) Difference (Giomo - CODE)

Figure 6.16: Global VTEC maps of Giomo and CODE Model and their difference for October 2, 2018

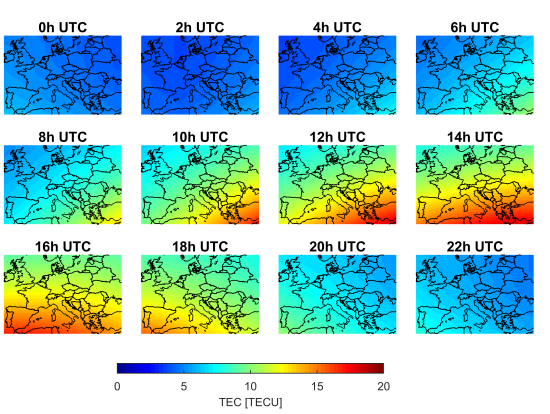

(a) Giomo

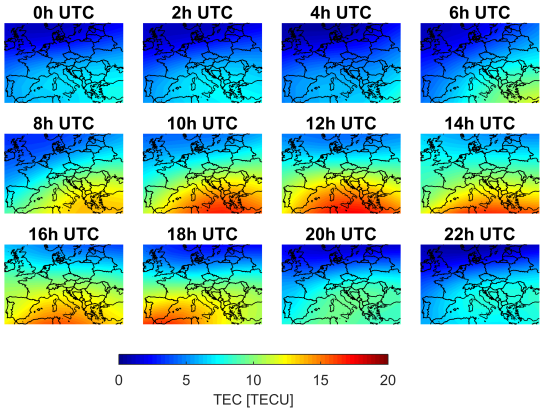

(b) CODE

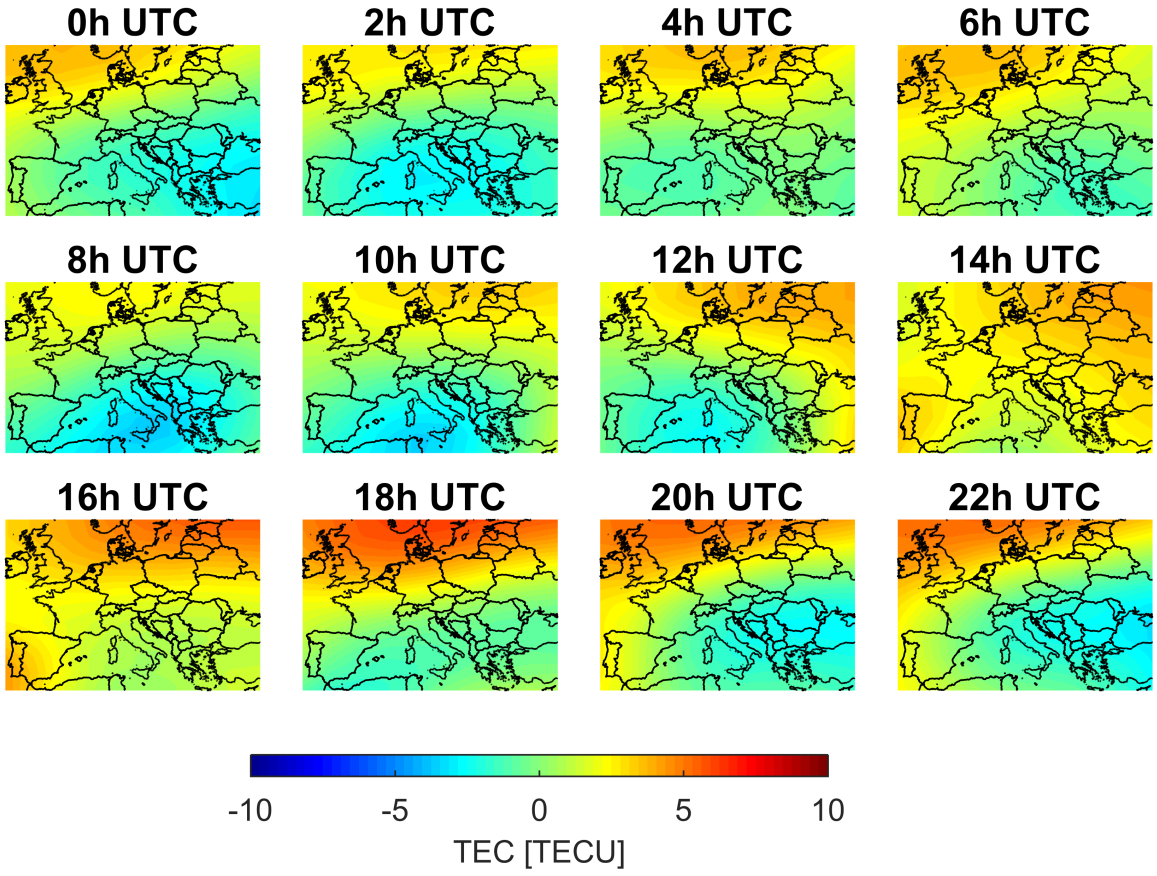

(c) Difference (Giomo - CODE)

Figure 6.17: European VTEC maps of Giomo and CODE Model and their difference for October 2, 2018

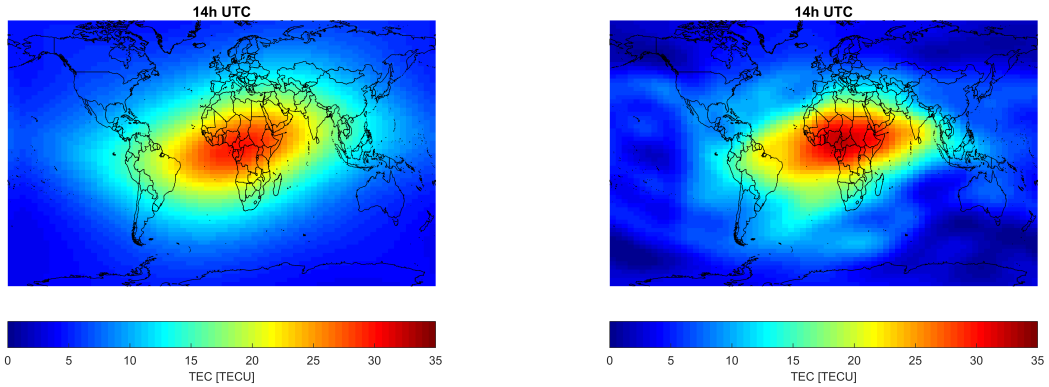

(a) Giomo

(b) CODE

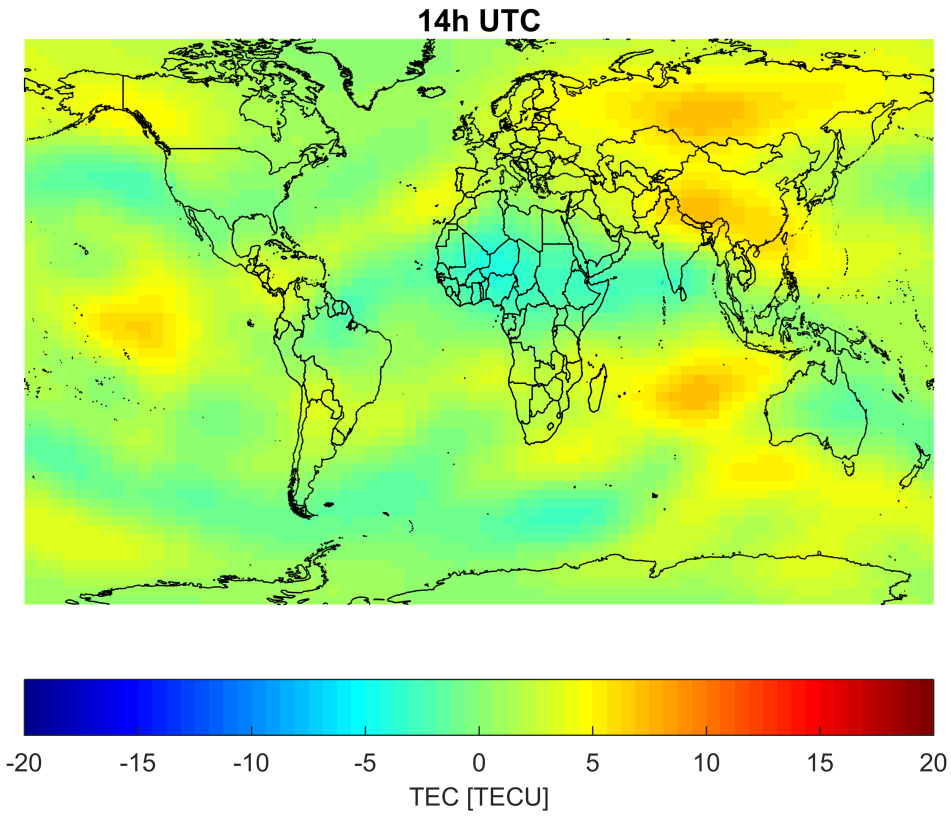

(c) Difference (Giomo - CODE)

Figure 6.18: Global VTEC maps of Giomo and CODE Model and their difference for October 2, 2018, 14:00 UTC

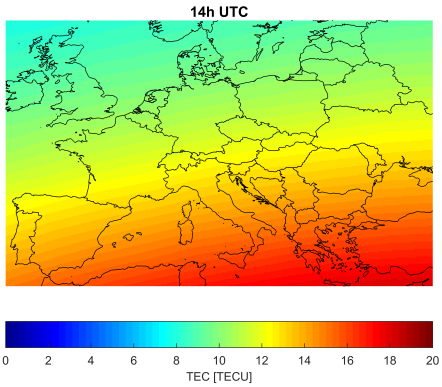

(a) Giomo

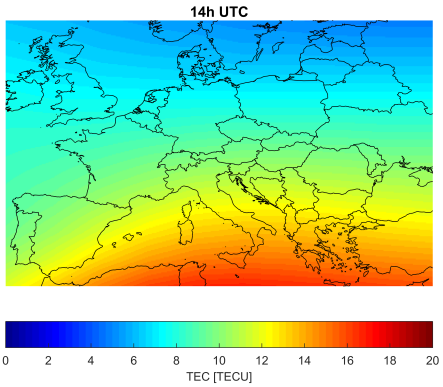

(b) CODE

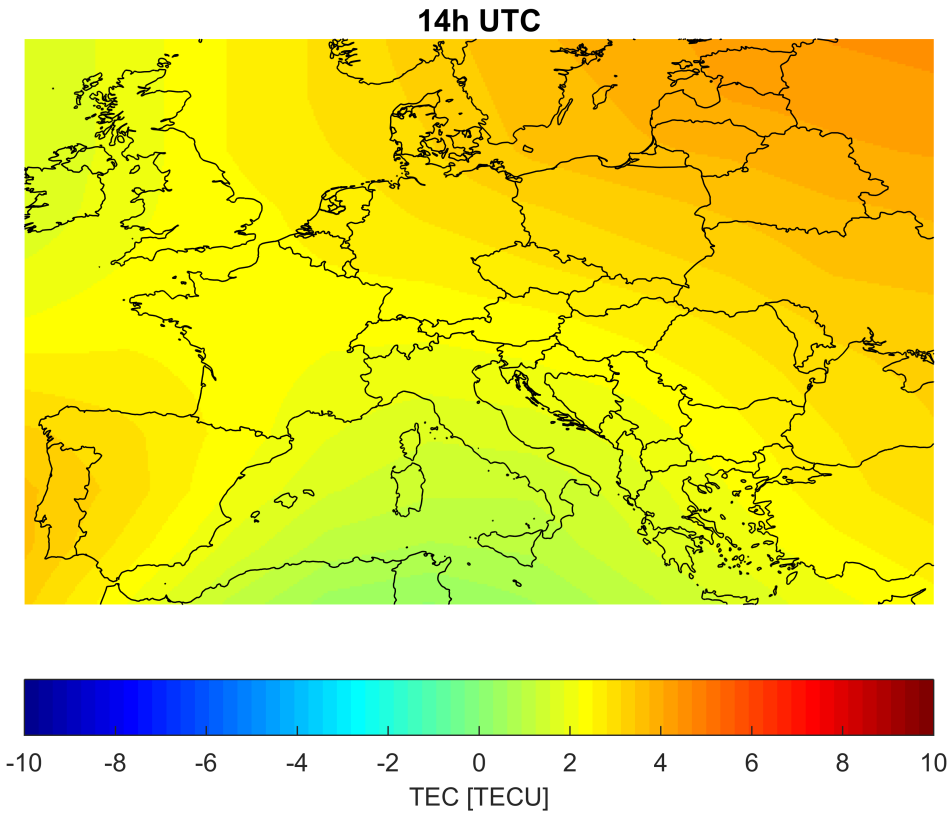

(c) Difference (Giomo - CODE)

Figure 6.19: European VTEC maps of Giomo and CODE Model and their difference for October 2, 2018, 14:00 UTC

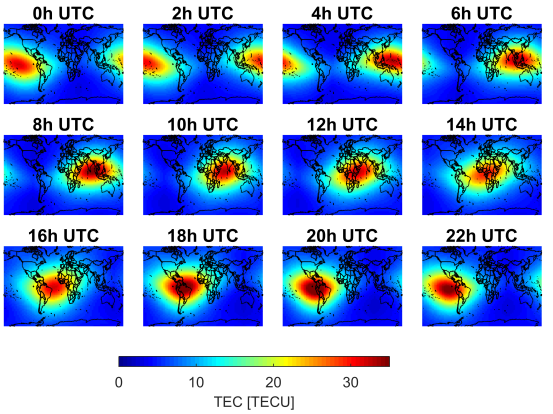

(a) Giomo

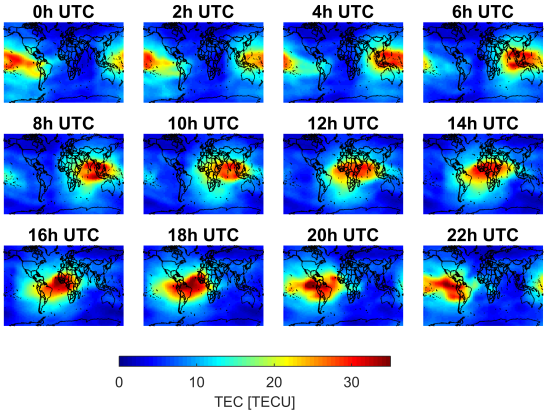

(b) IGS

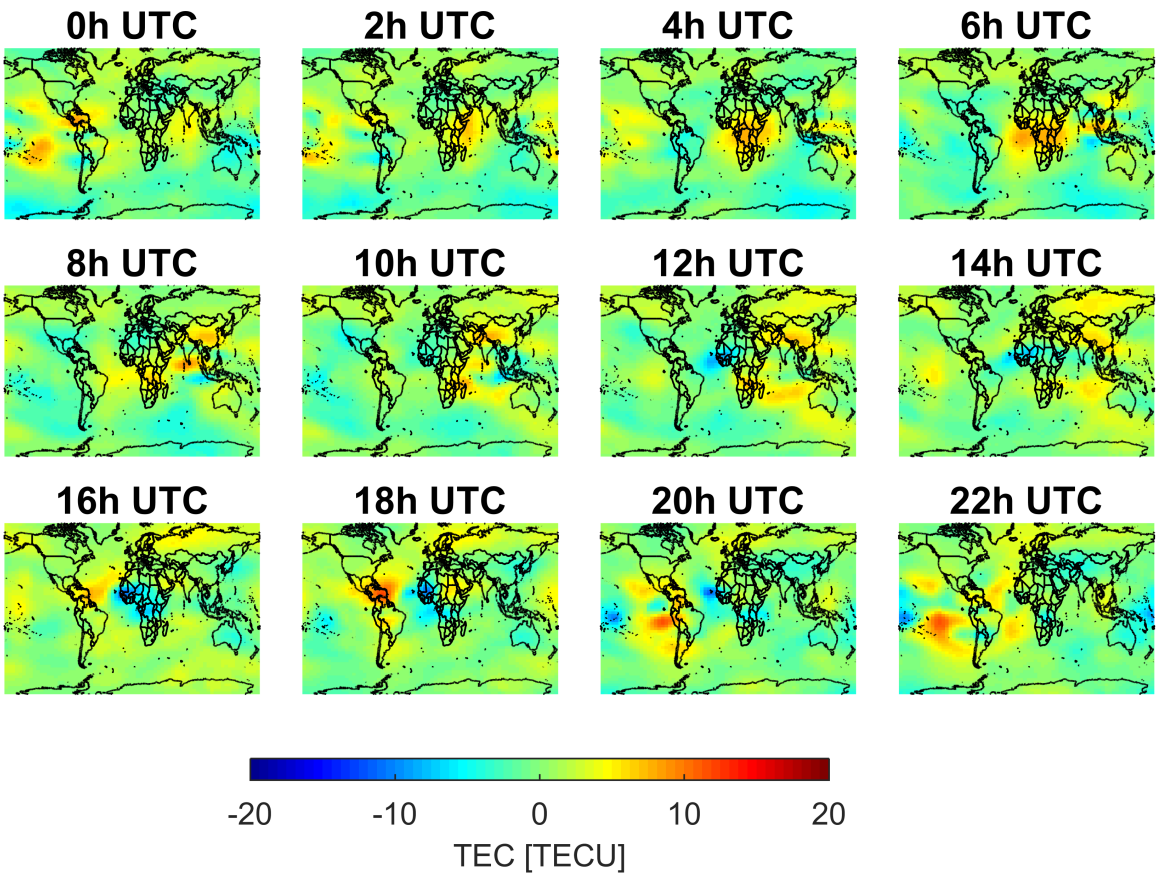

(c) Difference (Giomo - IGS)

Figure 6.20: Global VTEC maps of Giomo and IGS Model and their difference for October 2, 2018

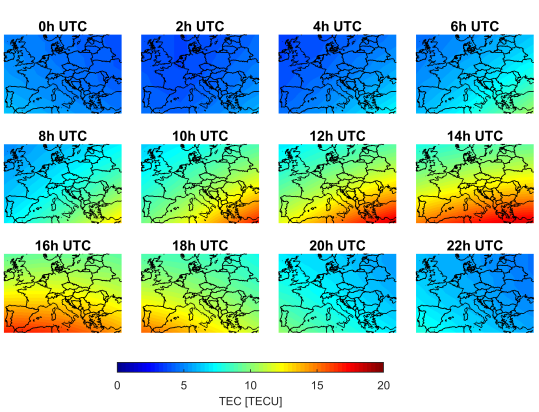

(a) Giomo

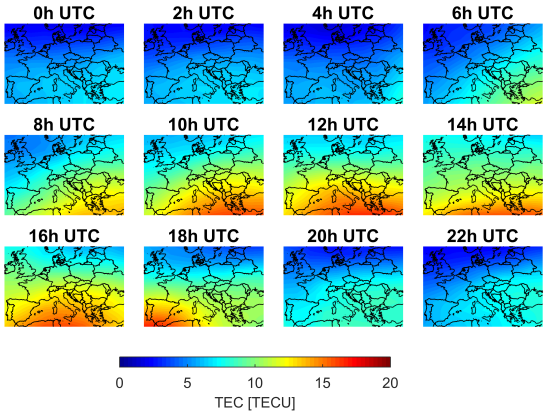

(b) IGS

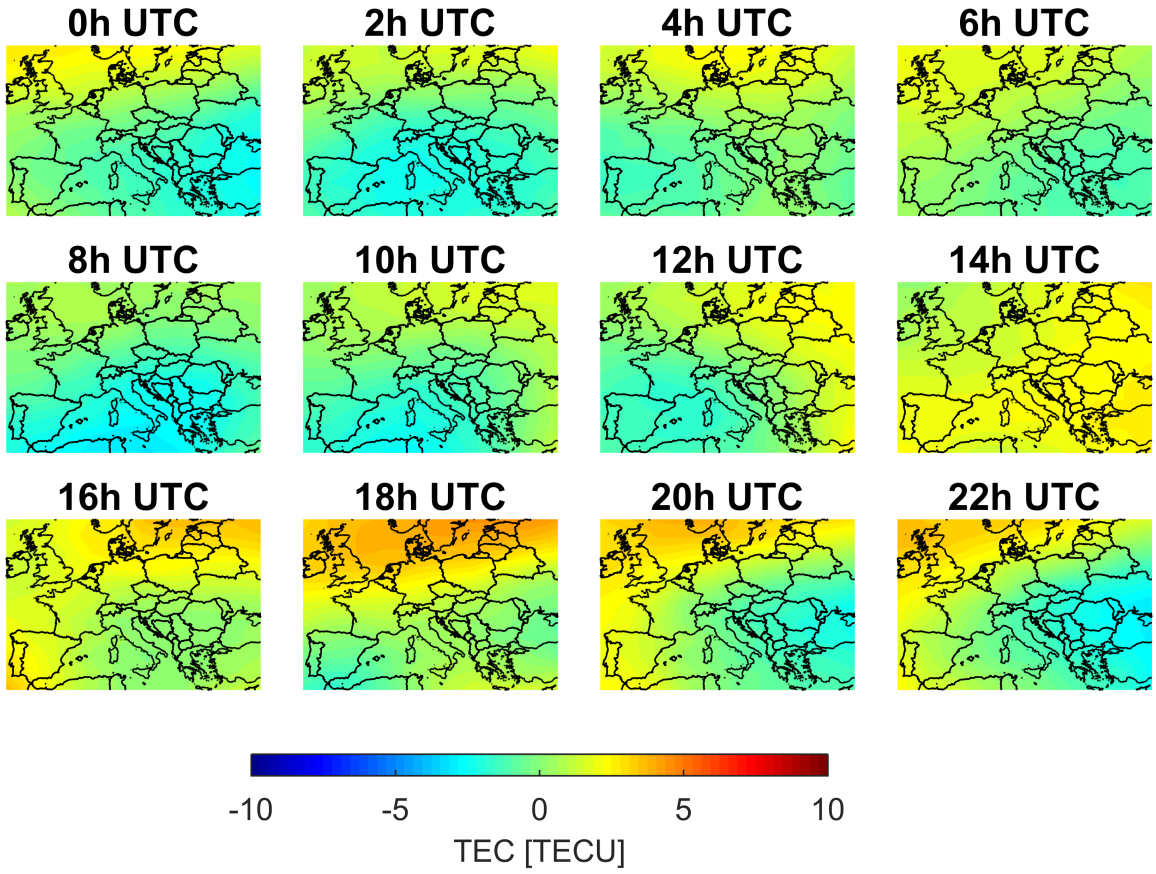

(c) Difference (Giomo - IGS)

Figure 6.21: European VTEC maps of Giomo and IGS Model and their difference for October 2, 2018

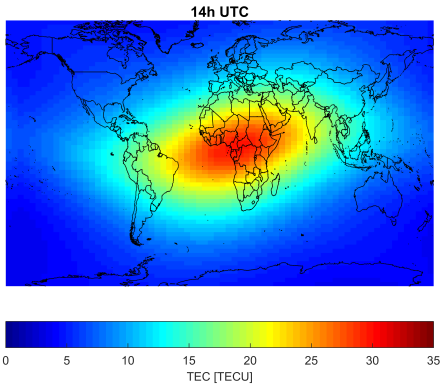

(a) Giomo

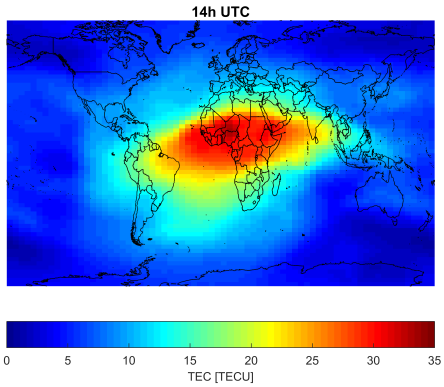

(b) IGS

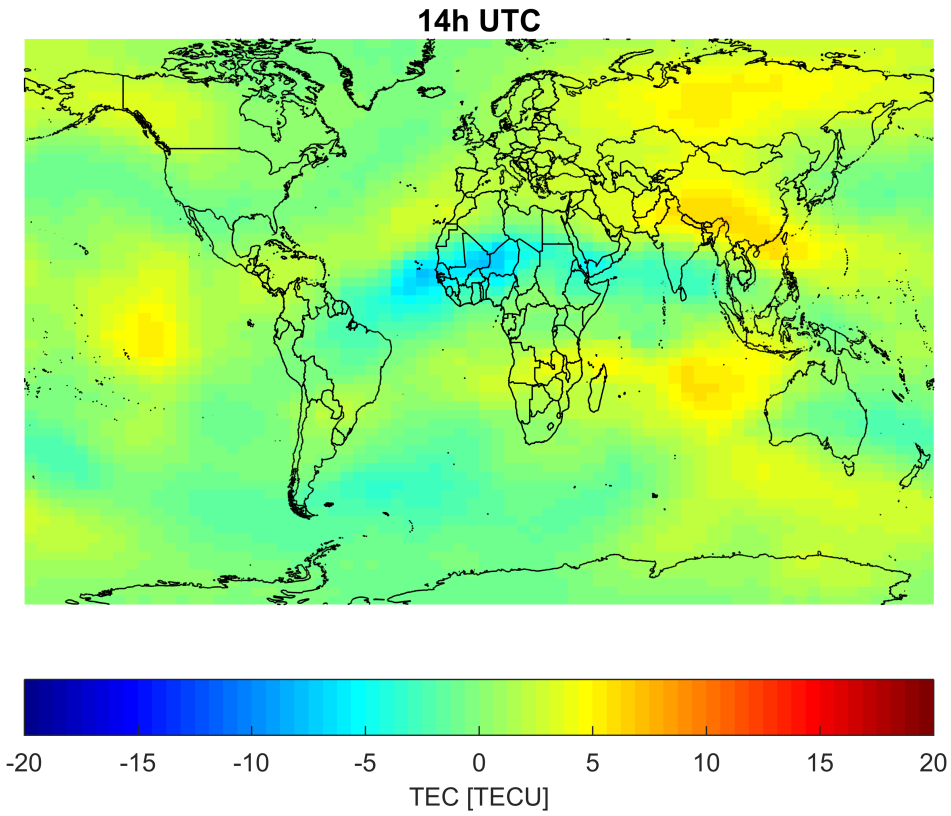

(c) Difference (Giomo - IGS)

Figure 6.22: Global VTEC maps of Giomo and IGS Model and their difference for October 2, 2018, 14:00 UTC

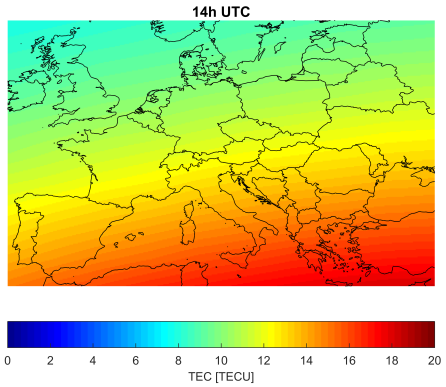

(a) Giomo

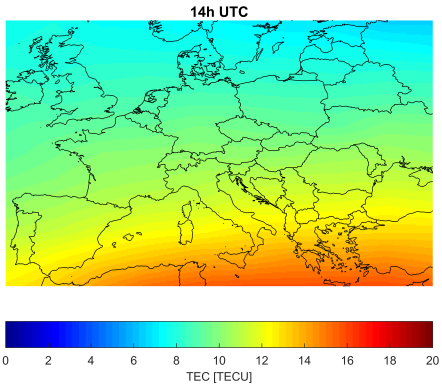

(b) IGS

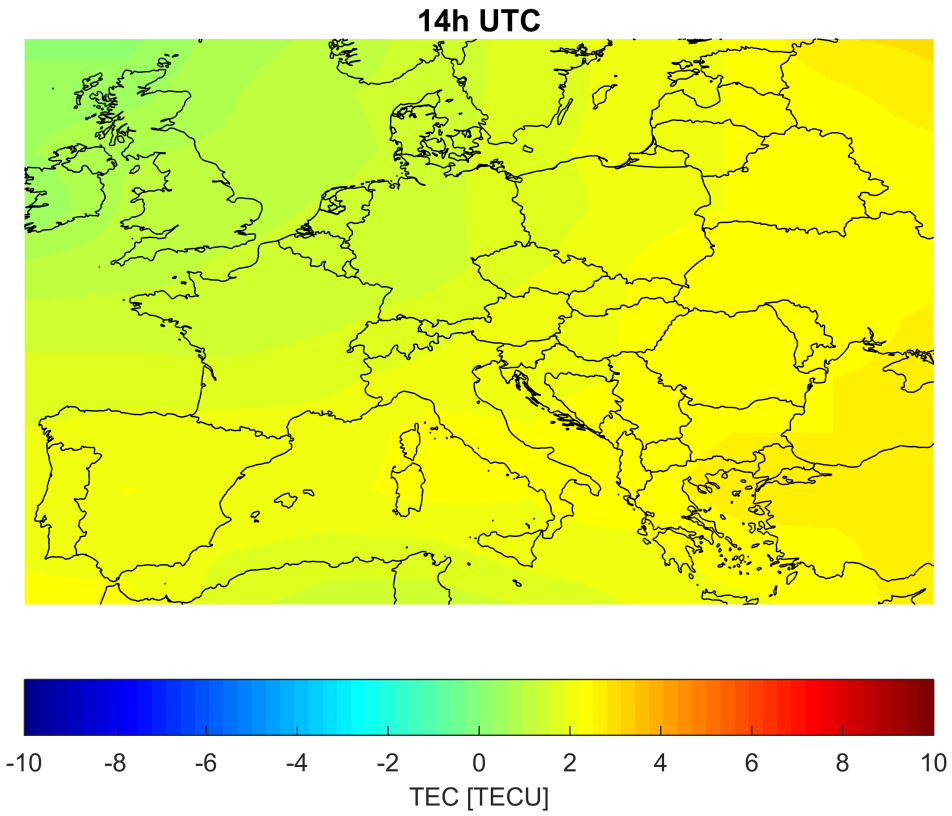

(c) Difference (Giomo - IGS)

Figure 6.23: European VTEC maps of Giomo and IGS Model and their difference for October 2, 2018, 14:00 UTC

time to time, reaching differences from -10 TECU up to +10 TECU. Nevertheless the consistency is better for central Europe, where Austria is located. The differences in this area are within ± 2 TECU. As the Regiomontan Model is primarily based on Austrian reference stations, peripheral areas of the raster cannot be modeled with the same accuracy than the center.

6.4 Quality analysis

6.4.1 Parameter estimation statistics

This section presents the quality analysis in terms of formal errors and correlations between the Giomo parameters.

The post-adjustment stochastic information can be derived from the variance-covariance matrix of the estimated parameters a posteriori,

$$\mathbf{\Sigma}\hat{x}\hat{x} = \sigma_0^2 \cdot \mathbf{Q}\hat{x}\hat{x} \tag{6.1}$$

$$= \sigma_0^2 \cdot \mathbf{N}^{-1} \tag{6.2}$$

with σ_0^2 as the variance of unit weight a posteriori (cf. Equation 5.10), empirically estimated using

$$\sigma_0^2 \approx s_0^2 = \frac{\mathbf{v}^T\mathbf{P}\mathbf{v}}{n-u}, \tag{6.3}$$

where n is the number of observations and u is the number of unknowns (Perović, 2005).

The variance-covariance matrix, $\mathbf{\Sigma}_{\hat{x}\hat{x}}$, contains the variances in the main diagonal as well as the co-variances (remaining elements). The variances give formal errors of the parameters, which, however, are too optimistic compared to a rigorous or external accuracy validation. This is due to the fact that the GNSS smoothed code observations are assumed to be independent of each other. The (existing) correlation of observations is, therefore, neglected in the estimation procedure. In addition, the observations are not scaled or individually weighted.

For the formal error assessment, 840 variance-covariance matrices for Epochs between September 5$^{\text{th}}$ and October 10$^{\text{th}}$ 2018 are analyzed. The mean formal errors are shown in Table 6.2. Figure 6.26 visualizes these formal errors of all Giomo parameters.

The mean formal error of VTEC_{max} over this time span of 0.33 TECU indicates a very accurate prediction of this parameter. Both for the weighting factors and for the coordinates of VTEC_{max}, the accuracy seems better for the latitude dependent parameters (w_β, β_{max}). This is likely due to the shape of the ionospheric bulge which is spread wider in longitude direction than in latitude direction. It is also in accordance with Figure 6.7, showing a larger scatter for w_s than for w_β.

Boxplots of the formal errors corresponding to the different Giomo parameters sorted by the hour of day can be seen in Figure 6.27. The central mark of each blue box indicates the median, the bottom and upper edges mark the 25$^{\text{th}}$ and 75$^{\text{th}}$ percentiles, respectively. The black dashed

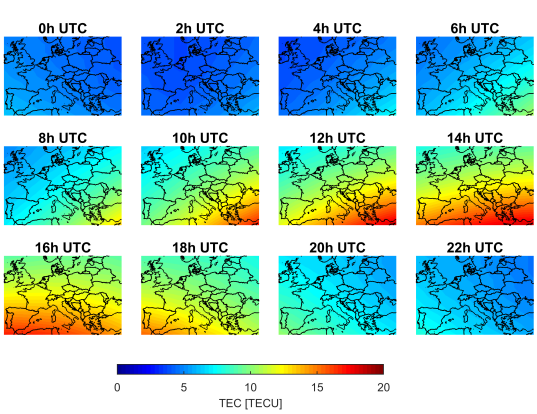

(a) Giomo

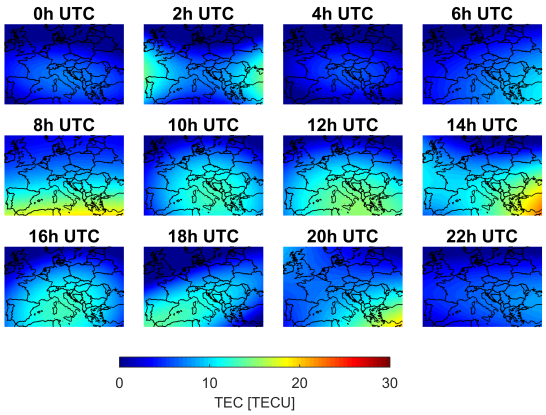

(b) Regiomontan

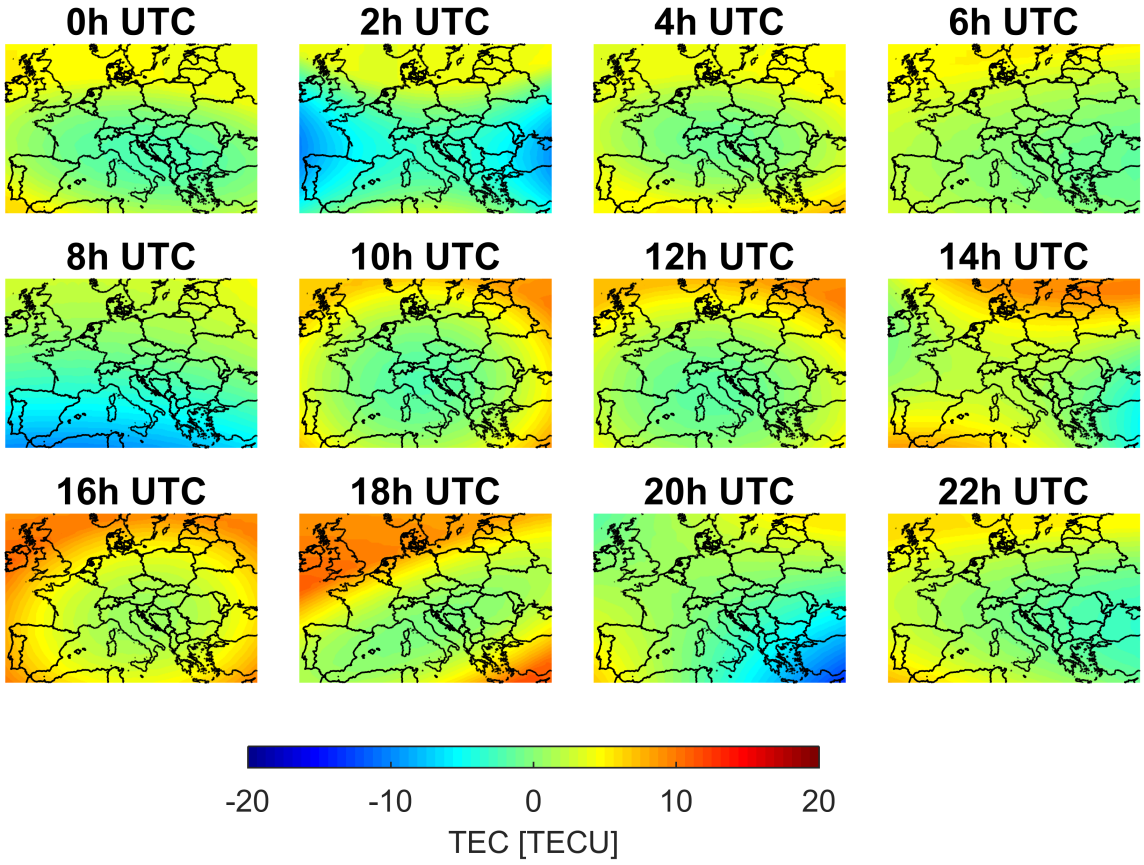

(c) Difference (Giomo - Regiomontan)

Figure 6.24: European VTEC maps of Giomo and Regiomontan Model and their difference for October 2, 2018

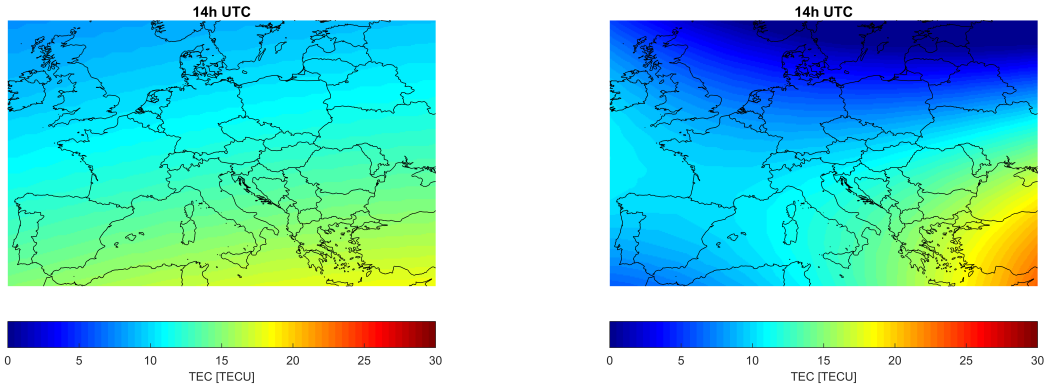

(a) Giomo

(b) Regiomontan

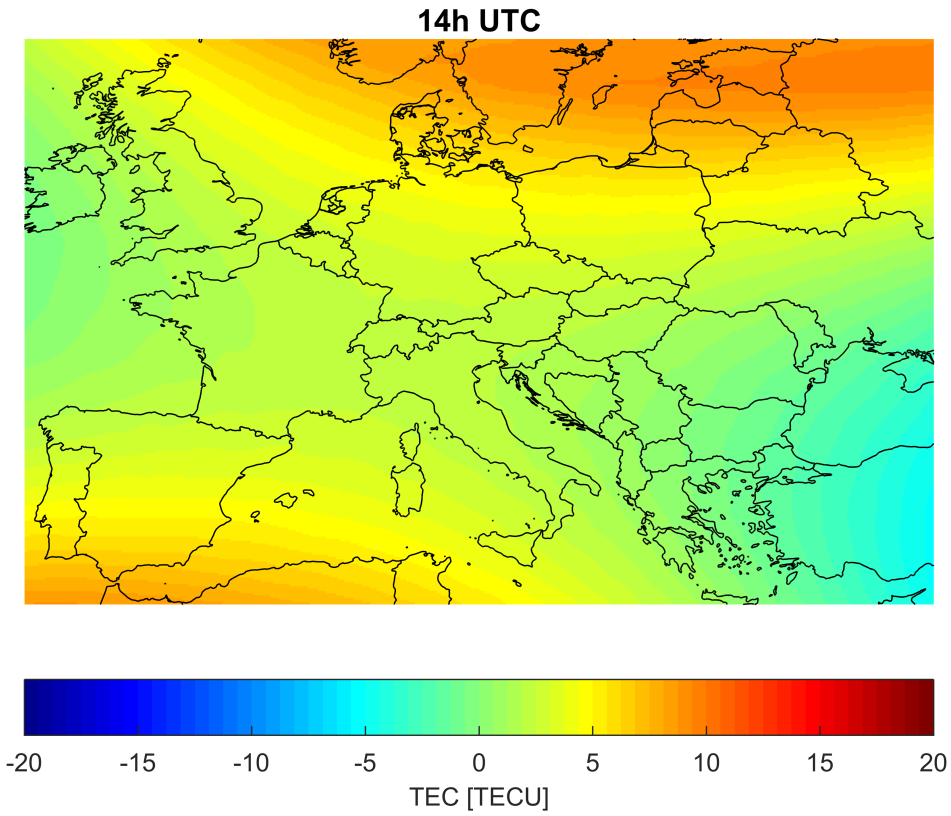

(c) Difference (Giomo - Regiomontan)

Figure 6.25: European VTEC maps of Giomo and Regiomontan Model and their difference for October 2, 2018, 14:00 UTC

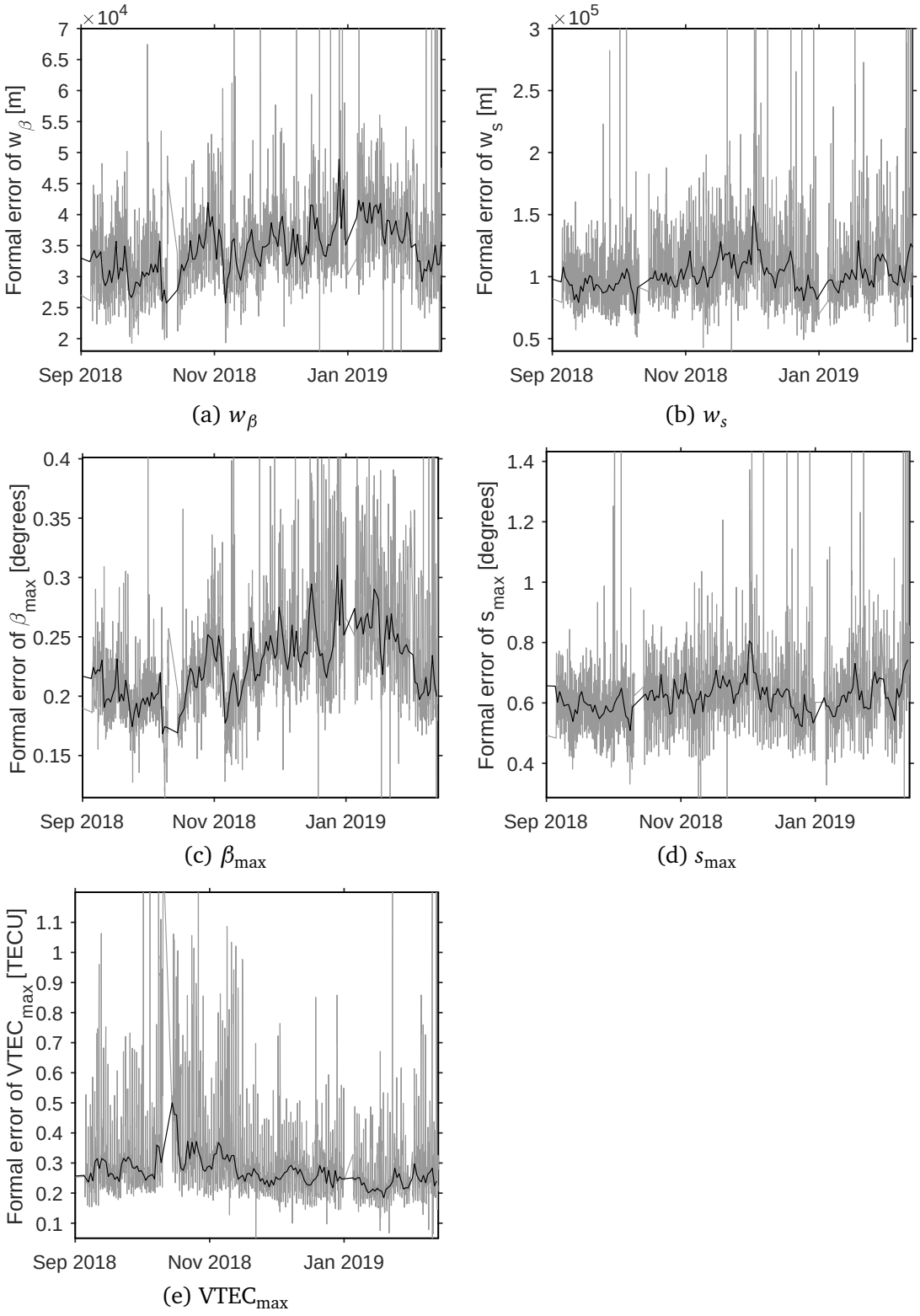

Figure 6.26: Time series of the formal errors (gray) and the daily median (black) of the Giomo parameters for September, 2018 to February, 2019.

Table 6.2: Formal error statistics for 840 Epochs between September 5 and October 10, 2018

Parameter	Mean ± Standard Deviation	Median
$VTEC_{max}$	0.33 TECU ± 0.93 TECU	0.27 TECU
w_β	0.92 % ± 0.16 %	0.90 %
w_s	1.10 % ± 0.17 %	1.08 %
β_{max}	0.24° ± 0.21°	0.22°
s_{max}	0.63° ± 0.30°	0.62°

lines (whiskers) extend to minimum and maximum values (not considering outliers), and the outliers are plotted individually as red crosses. Points as marked as outliers if they are greater than $q_3 + w \cdot (q_3 - q_1)$ or smaller than $q_1 - w \cdot (q_3 - q_1)$, where $w = 1.5$ is the maximum whisker length, and q_1 and q_3 are the 25th and 75th percentiles of the data.

For $VTEC_{max}$ the formal errors are small around noon, but reach their maximum at 21:00 UTC. This is due to the fact, that the ionospheric buldge at this time is located in the Pacific, where hardly any reference stations are available. The lack of stations of the ionospheric maximum also affects the parameters corresponding to latitude, so they cannot be estimated that precise. The formal errors slightly increase around 16 UTC, where the ionospheric maximum is close to the east part of South America, as there are hardly any stations north and south of the ionospheric maximum.

The opposite happens to the parameters in longitude: When the ionospheric maximum is located in the Pacific with few stations, the remaining area is covered with many stations, so the progression of the Function 5.3 along the parallels is well defined. The estimation of w_s and s_{max} gets worse around noon, if instead the ionospheric buldge is located over Europe/Africa with many stations, but few stations in east-west direction.

Correlations between estimated parameters can be derived from a variance-covariance matrix by scaling with the respective variances,

$$\mathrm{Corr}(X, Y) = \frac{\mathrm{Cov}(X, Y)}{\sqrt{\mathrm{Var}(X)\mathrm{Var}(Y)}} \tag{6.4}$$

where Corr is the correlation, Cov is the covariance and Var is the variance of a parameter (Weisstein, 2018). The statistics for the correlation of estimated parameters between September 5 and October 10, 2018, are presented in Table 6.3.

Statistically significant correlations can be found for $VTEC_{max}$ and the weighting parameters as well as for w_β and β_{max}. The former correlations are of the order of -0.6 or -60 %. A negative correlation between $VTEC_{max}$ and the weighting parameters is expected because a larger maximum value would produce a narrower weighting function (cf. Figure 5.14) and, thus, smaller weighting parameters. The noticeable correlation between w_β and β_{max} of -0.30 ± 0.09 cannot be

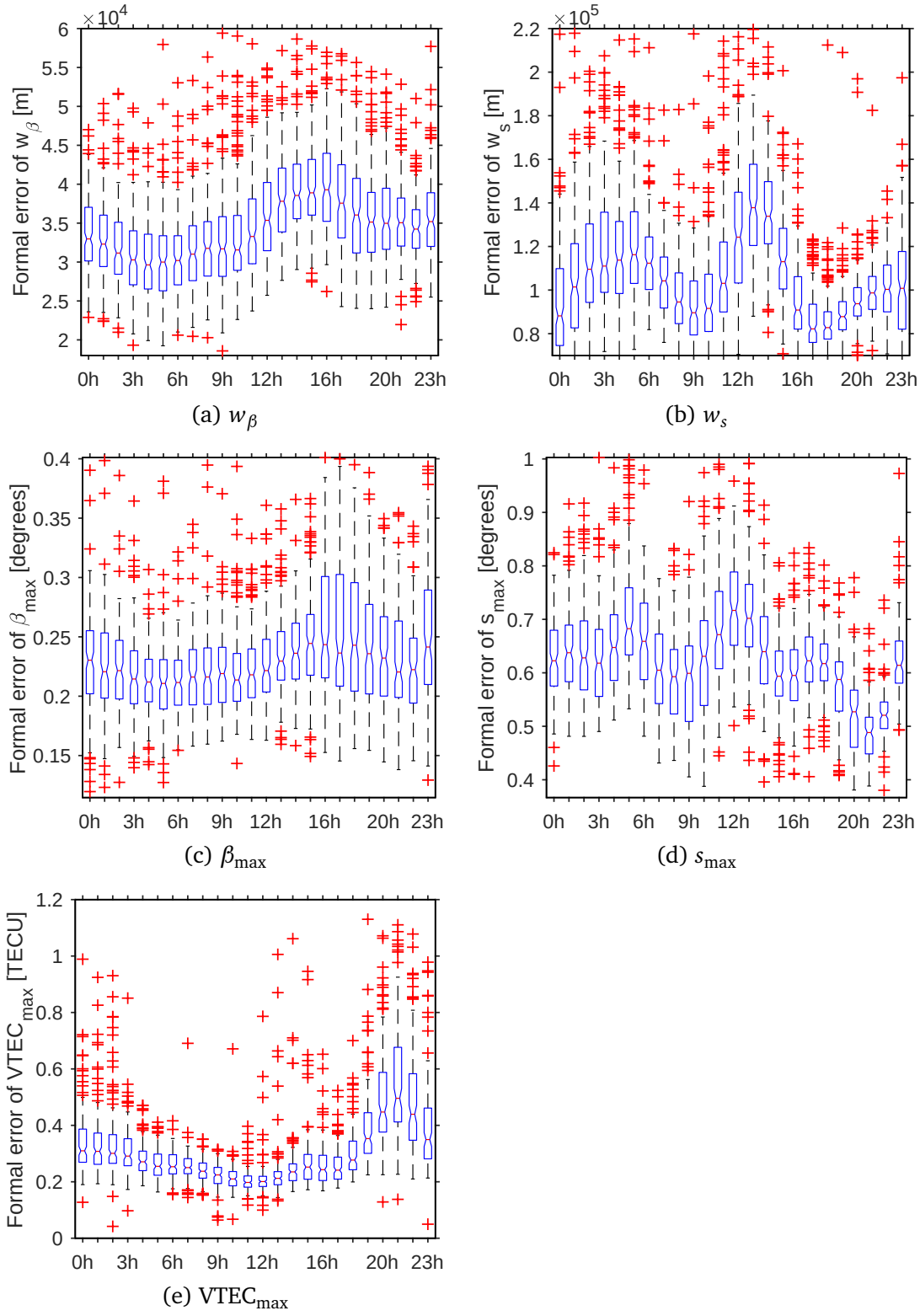

Figure 6.27: Formal errors per hour of day of the Giomo parameters (boxplots) for September, 2018 to February, 2019.

Table 6.3: Mean correlation and standard deviation for 840 Epochs between September 5 and October 10, 2018

	VTECmax	$w\beta$	w_s	β_{max}	s_{max}
$VTEC_{max}$	1				
w_β	**-0.65 ± 0.11**	1			
w_s	**-0.58 ± 0.09**	0.10 ± 0.18	1		
β_{max}	-0.04 ± 0.17	**-0.30 ± 0.09**	0.03 ± 0.15	1	
s_{max}	-0.03 ± 0.18	0.01 ± 0.18	0.11 ± 0.17	0.02 ± 0.17	1

explained easily, maybe it is due to the smaller extension of the ionospheric bulge in north-south direction. All other correlations are insignificant.

6.4.2 Pseudorange correction

To further investigate the quality of the Giomo Model, pseudorange corrections with different ionosphere models are compared. For this purpose VTEC values of the corresponding IONEX maps were first mapped to STEC values and then further converted to range corrections. These range corrections were then applied to phase-smoothed L1 pseudoranges. As "“true value"' for each measurement serves the ionosphere-free linear combination derived out of phase-smoothed code observations.

All following figures were calculated for September 7th, 2018 for the whole day for a single EPOSA reference station in Austria. Data was available every second, but for visibility reasons the graphics only show the results for every 30 minutes. This means, the figures show all observations to every visible satellite for every half an hour. In this chapter the results of only two representative stations (Figures 6.28 and 6.29) are shown, figures of all 22 computed stations can be found in Appendix A.

The first Figure 6.28 represents a station, where the residuals are small compared to other stations for all models, although the regional Regiomontan Model performs best. Nevertheless it is obvious, that the Klobuchar Model generally underestimates the ionospheric range correction and therefore performs worst. In order to explain some of the major residuals, one should have a look at an observation at 14:00 UTC with a residuum of around -4 m which is visible for Regiomontan, CODE and IGS. This observations belongs to satellite PRN28 with a low elevation of 10.3°. The VTEC values derived by the different models are mapped to the respective STEC by a mapping function (see Chapter 4.1.3), which is equal for all tested models. Table 6.4 shows the VTEC and the resulting STEC values for PRN28 at 14:00 UTC calculated with the different ionosphere models. The figures make one believe, that with Giomo and Klobuchar this specific observation gets corrected better, but unfortunately the residuum is even larger. Only the scale is limited to ± 5 m.

The second Figure 6.29 incorporates the station with the biggest residuals for all models, the

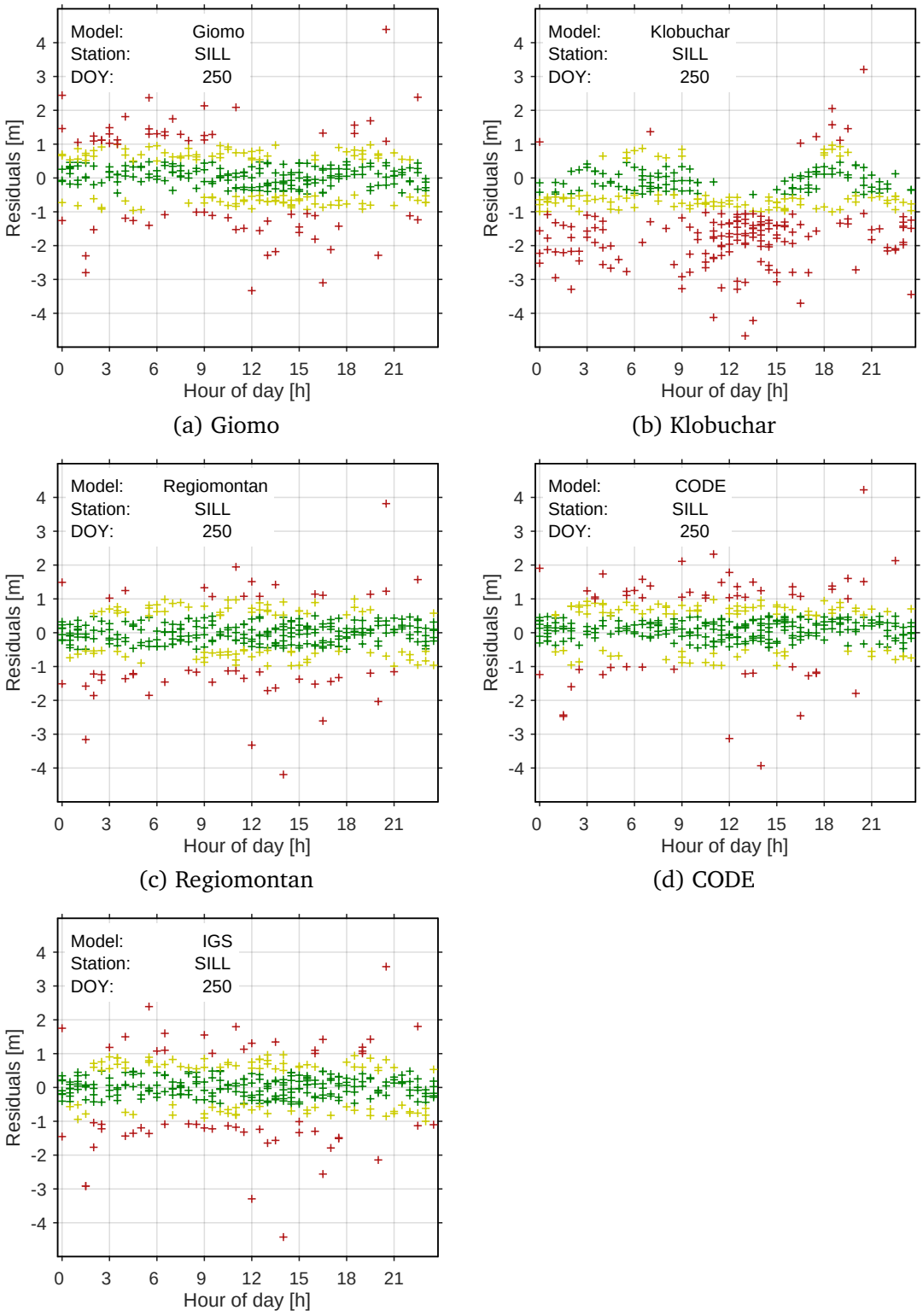

(a) Giomo (b) Klobuchar

(c) Regiomontan (d) CODE

(e) IGS

Figure 6.28: Differences between L1 pseudoranges corrected with different ionosphere models (a) - (e) and the ionosphere-free linear combination for station Sillian (SILL) for September 7, 2018)

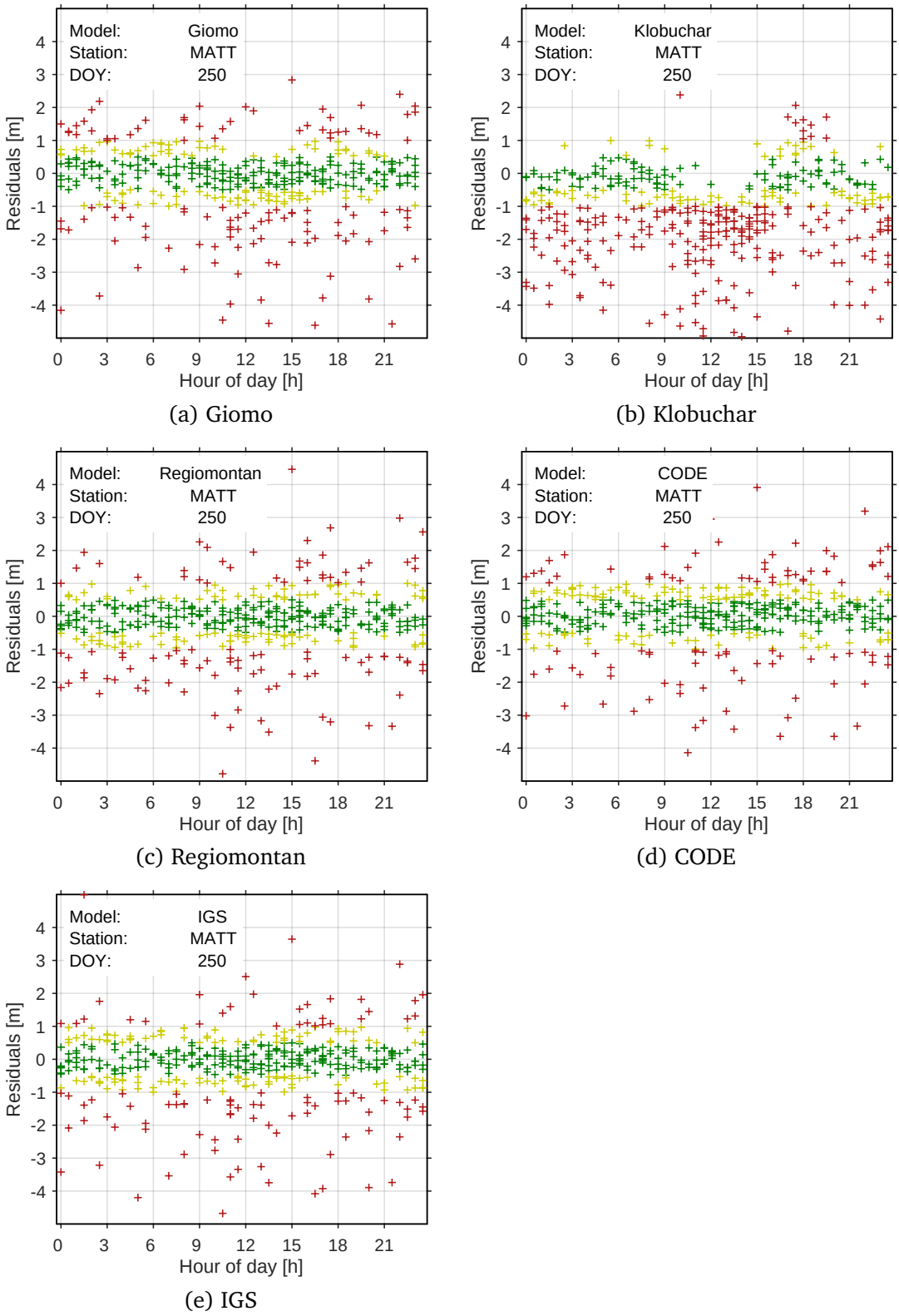

Figure 6.29: Differences between L1 pseudoranges corrected with different ionosphere models (a) - (e) and the ionosphere-free linear combination for station Mattersburg (MATT) for September 7, 2018)

Table 6.4: VTEC and resulting STEC values for PRN28 at 14:00 UTC calculated with different ionosphere models

Model	VTEC	STEC	Residuum
Giomo	10.7 TECU	-41.9 TECU	-5.021 m
Regiomontan	7.9 TECU	-34.0 TECU	-4.194 m
CODE	8.0 TECU	-31.5 TECU	-3.932 m
IGS	9.2 TECU	-36.2 TECU	-4.423 m
Klobuchar	15.5 TECU	-66.3 TECU	-7.587 m

Table 6.5: Differences between L1 pseudoranges corrected with different ionosphere models and the ionosphere-free linear combination for all stations (September 7, 2018)

Difference	Giomo	Klobuchar	Regiomontan	CODE	IGS
± 0.5 m	48.3 %	26.9 %	**56.2 %**	52.5 %	54.6 %
± 1.0 m	75.5 %	50.8 %	**80.5 %**	79.9 %	80.1 %
± 1.5 m	87.7 %	67.6 %	90.4 %	**90.6 %**	90.2 %

station Mattersburg, which has a very high code noise. Again the Klobuchar Model performs worst, the models of CODE and Regiomontan correct the data best. Giomo Model corrections are generally much better than those from Klobuchar Model, and only a little worse than the others (see Table 6.5).

An analysis of the output demonstrates the benefit of the different models when they are applied as range corrections to the pseudoranges. Table 6.5 presents in numbers, how many of the corrected values show a difference of >0.5 m, >1 m and >1.5 m to the true value.

According to these results the regional Regiomontan Model performs best, as expected when computing data from only Austrian stations. But CODE and IGS are really close. Also the Giomo Model, which is only based on five parameters, provides comparable results to the established models. 48.3 % (best performance: 56.2 % by Regiomontan) of the calculated pseudoranges only show a difference of 0.5 m from the true value, and 87.7 % (best performance: 90.6 % by CODE) of the observations are in the 1.5 m range. The Klobuchar Model delivers the worst results, only correcting 67.6 % of the measurements within 1.5 m difference.

6.4.3 EPOSA Service

The Austrian reference station provider EPOSA established a service for single-frequency users to improve their position accuracy using the VTEC maps (IONEX files) calculated at Technische Universität Wien. Both models, the regional Regiomontan and the global Giomo Model will be available for download via their webpage. The files for the previous day can be ordered from

04:05 CET (Regiomontan) or 03:15 CET (Giomo). For real-time applications, a predicted Giomo Model is calculated in addition (cf. Chapter 6.5), which is available from 03:15 CET for the respective day.

As GNSS raw data can be read from cell phones for about two years, smartphone users also benefit from the service. Using the IONEX file in combination with appropriate software or an application can improve the accuracy of their position.

6.5 Model prediction

For real-time and forecast applications, a prediction of VTEC values is required. In case of the Giomo Model only the five contributing parameters have to be predicted. This section presents the results of several prediction methods and gives recommendations about the preferred procedure based on the findings.

For the prediction also the solar-fixed coordinate system is used, so the coordinates of VTEC_{max} do not change rapidly over time and remain almost constant. The same holds for the other parameters, as the ionosphere in the solar-fixed system is not subject to any great fluctuations, except for solar storms or other sudden events.

As the ionosphere of consecutive days for the same time of day is usually very similar, the VTEC of the previous day(s) at the same location is already a good estimate for the predicted day. Therefore, a prediction based on previous-day values at the same hour of day may result in a better prediction than using the preceding VTEC values.

For the prediction of the coordinates of VTEC_{max}, β_{max} and s_{max}, also the coordinates of the Sun are taken into account, as the ionospheric buldge moves with the position of the Sun. β_{max} varies with the declination of the Sun, so this small change from one to the following day can be calculated. The declination $\delta_{\odot}$ of the Sun can be derived from Equation (6.5).

$$\delta_{\odot} = \sin\left(\frac{2\pi}{365}(\text{DOY} - \Upsilon)\right) \cdot \epsilon \tag{6.5}$$

where DOY is the day of the year, for which the declination is calculated, Υ is the day of the year of the vernal equinox and ϵ is the obliquity of the ecliptic.

The geographic longitude of the Sun's base point can be derived by

$$\lambda_{\odot} = \pi - \text{UTC} \tag{6.6}$$

where UTC has to be entered in radians.

As the ionospheric activity is mainly driven by the Sun, the time series of VTEC_{max} is overlaid with the 11-year solar cycle as well as with seasonal oscillations. Since the model parameters have been calculated over one year, these long periods cannot be well derived from the solutions so far.

Table 6.6: Overview of tested prediction methods for the Giomo Model

Name	Description
Previous	The last available value is taken as predicted value
Last day	The value of the last (available) day at the same time (e.g. 06:00) is taken as predicted value
Last 3 days	A weighted average (weight [a]: $1/\Delta t$) of the last three (available) days at the same time is used as predicted value
Last 5 days	A weighted average (weight [a]: $1/\Delta t$) of the last five (available) days at the same time is used as predicted value
Previous 3 hours	A weighted average (weight [a]: $1/\Delta t$) of the previous three values (usually the most recent three hours) is used as predicted value
Previous 5 hours	A weighted average (weight [a]: $1/\Delta t$) of the previous five values (usually the most recent five hours) is used as predicted value

[a] The weights are inversely proportional to the elapsed time, normalized to sum 1. Example: If the three latest estimations were done 1 hour, 2 hours and 4 hours ago, the weights $w_i = \frac{\Delta t_i^{-1}}{\sum_i \Delta t_i^{-1}}$ are 0.571, 0.286, 0.143.

The parameters w_β and w_s are negatively correlated to $\mathrm{VTEC}_{\max}$ (cf. Table 6.3), so a larger value for $\mathrm{VTEC}_{\max}$ produces a narrower curve of the weighting function. This correlation can also be used to predict the weighting parameters more precisely which could be a future enhancement of the current prediction procedure.

The different prediction methods, which are used in the following tests, are presented in Table 6.6. In addition to the mentioned six methods, linear interpolation methods have been studied as well. However, these show less accurate results and are, therefore, omitted in further discussions.

The prediction of the Giomo Model is done on a daily basis, always predicting the following day. Therefore, a VTEC map in IONEX Format is calculated every day at 23:59 for the next day (25 hourly maps from 00:00 to 24:00). In order to find the most accurate prediction method, all five parameters are predicted for all (hourly) Epochs between March 26th and August 1st 2018 between 0 and 48 hours in advance. These predicted values are then compared to the derived values from the classical parameter estimation process. Statistical parameters are calculated from more than 500 000 predictions per parameter. The medians of the differences are shown in Figure 6.30.

For the prediction methods that do not account for the hour of the day, i.e. "‘Previous"', "‘Previous 3 hours"', and "‘Previous 5 hours"', a large variation of the parameters with prediction time can be seen. This variation also comes with larger errors in terms of standard deviation and maximum deviation. The other methods shown in Figure 6.30 show a constant median for each time block of 24 hours. This is due to the fact that the prediction value for one epoch only changes every 24 hours when a newer value at the same time of day becomes available.

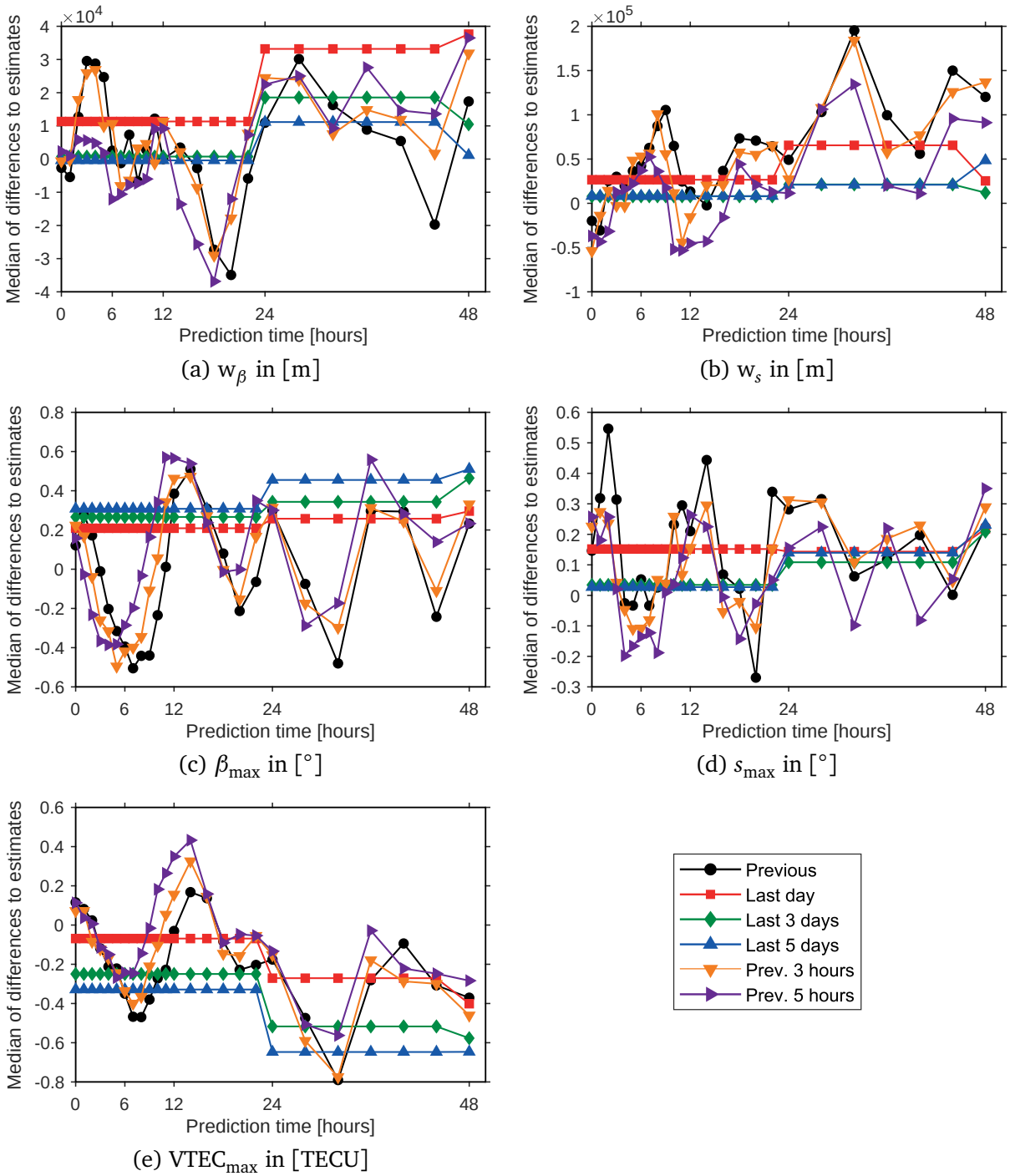

Figure 6.30: Comparison of various prediction methods for the Giomo model. Shown are median values of the differences between predicted and true (estimated) values. The predictions are performed between 0 (i.e. prediction using data up to one hour before the current epoch) and 48 hours. Data between March 26, 2018 and August 1, 2018 are used for the prediction tests.

As a more homogeneous prediction of the model parameters is preferred, prediction methods accounting for the time of day, i.e. "'Last day'", "'Last 3 days'", and "'Last 5 days'", are favored. Based on the results and due to the fact that the method "'Last day'" can be manipulated very easy because it relies only on a single value, following prediction methods are used for the Giomo parameters: "'Last 3 days'" for $VTEC_{max}$, β_{max}, s_{max} and w_s; and "'Last 5 days'" for w_β.

The predicted Giomo TEC maps compared to the post-processed ones of the same day deliver a mean difference of 0.0022 TECU ± 2.1 TECU (the numbers were calculated over a time span from June, 3rd to October, 11th), which shows a good agreement. The two Figures 6.31a and 6.31b show, that despite the good result in fact there appear bigger differences up to ±2 TECU, but they average out over the whole world.

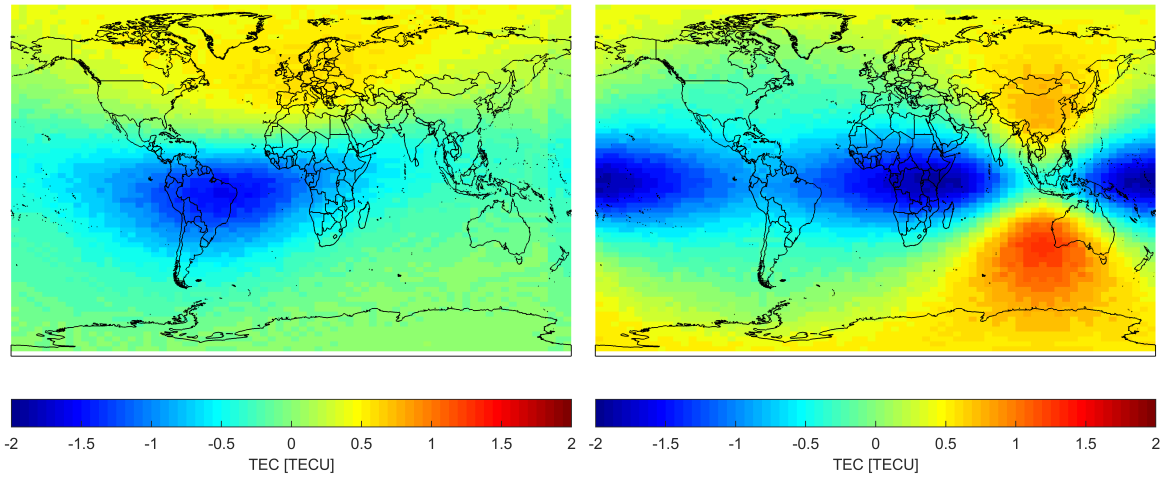

(a) August 19, 2018, 15:00 UTC

(b) March 14, 2018, 07:00 UTC

Figure 6.31: Differences between the predicted and the post-processed Giomo Model

Figures 6.32 and 6.33 visualize an example for the differences between the predicted and the actual IONEX file for August 24th, 2018. For Europe, they differ only up to ±2 TECU. Globally there are higher differences at 14:00 UTC of about 4 TECU, but in general the predicted maps match the post-processed ones quite good.

Table 6.7 presents the mean differences ΔVTEC between the post processed and the predicted Giomo Model for the same day. On the one hand the models were evaluated globally and on the other hand stations in the north, at mid-latitudes and at the equator were picked for comparison. Also the ΔVTEC at daytime and nighttime were computed separately. Overall they show a good agreement, although differences increase at daytime. Nearly all values are negative, which leads to the conclusion that the prediction underestimates the VTEC to a small extent.

Table 6.8 shows the equivalent to Table 6.7 for the mean differences ΔVTEC between the CODE final Global Ionosphere Map (GIM)s and the predicted Giomo Model. The models only differ up to ±1.88 TECU, in most cases the prediction performs even better.

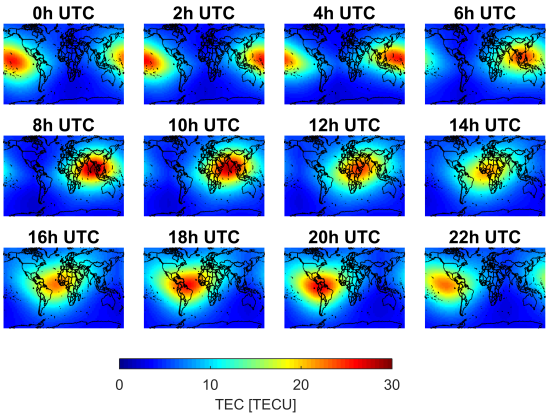

(a) Giomo

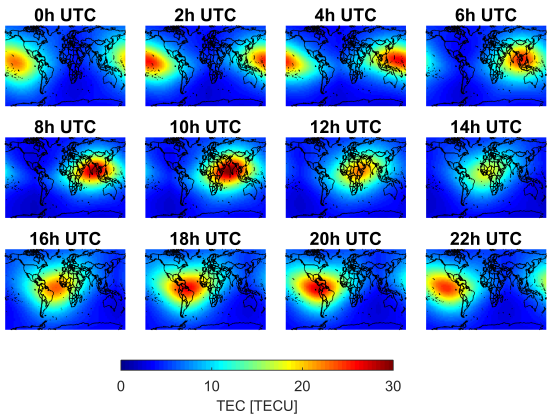

(b) IGS

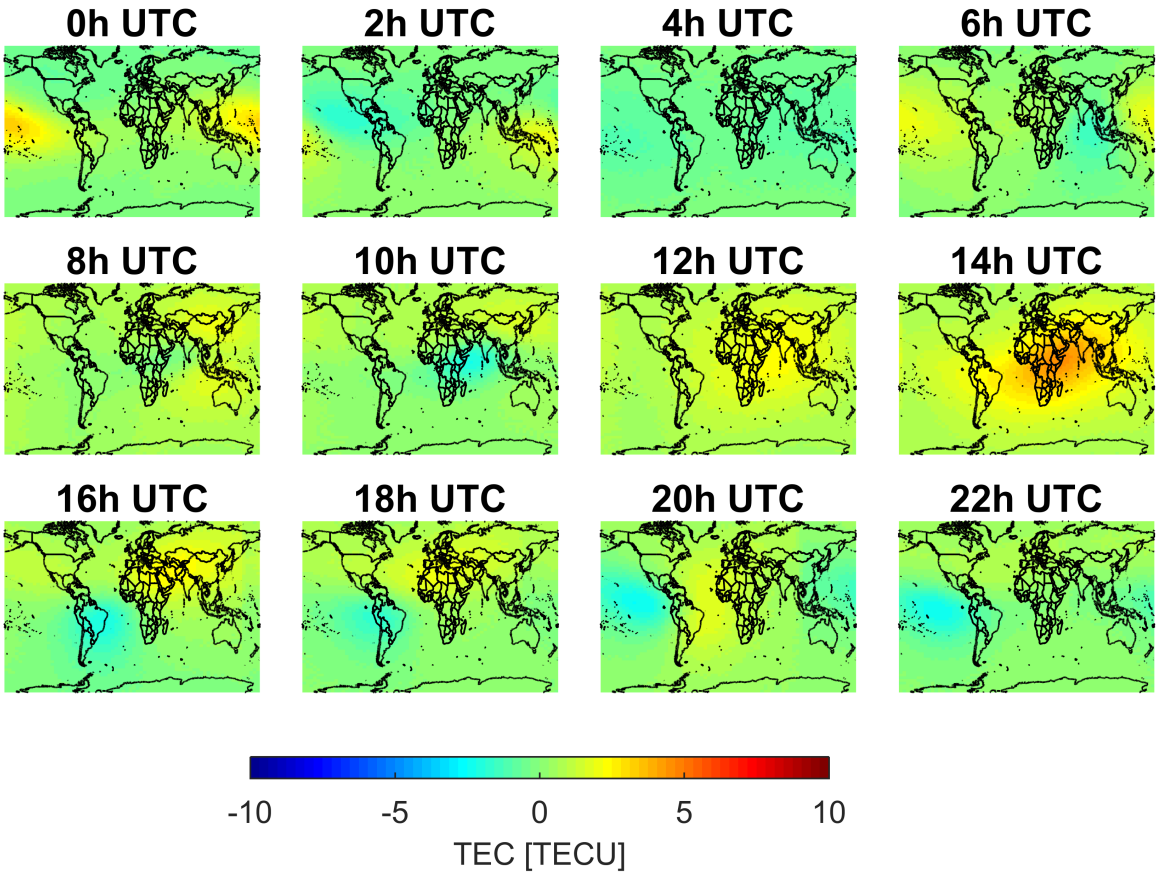

(c) Difference (Giomo - IGS)

Figure 6.32: Difference between the post-processed and the predicted Giomo global TEC map for August 24, 2018

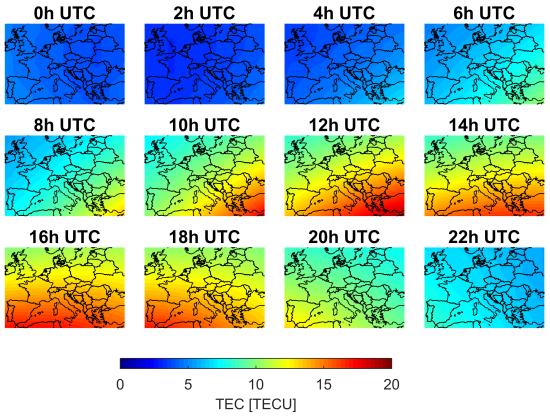

(a) Giomo

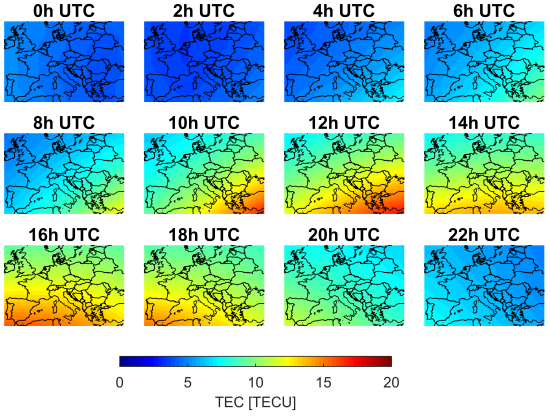

(b) IGS

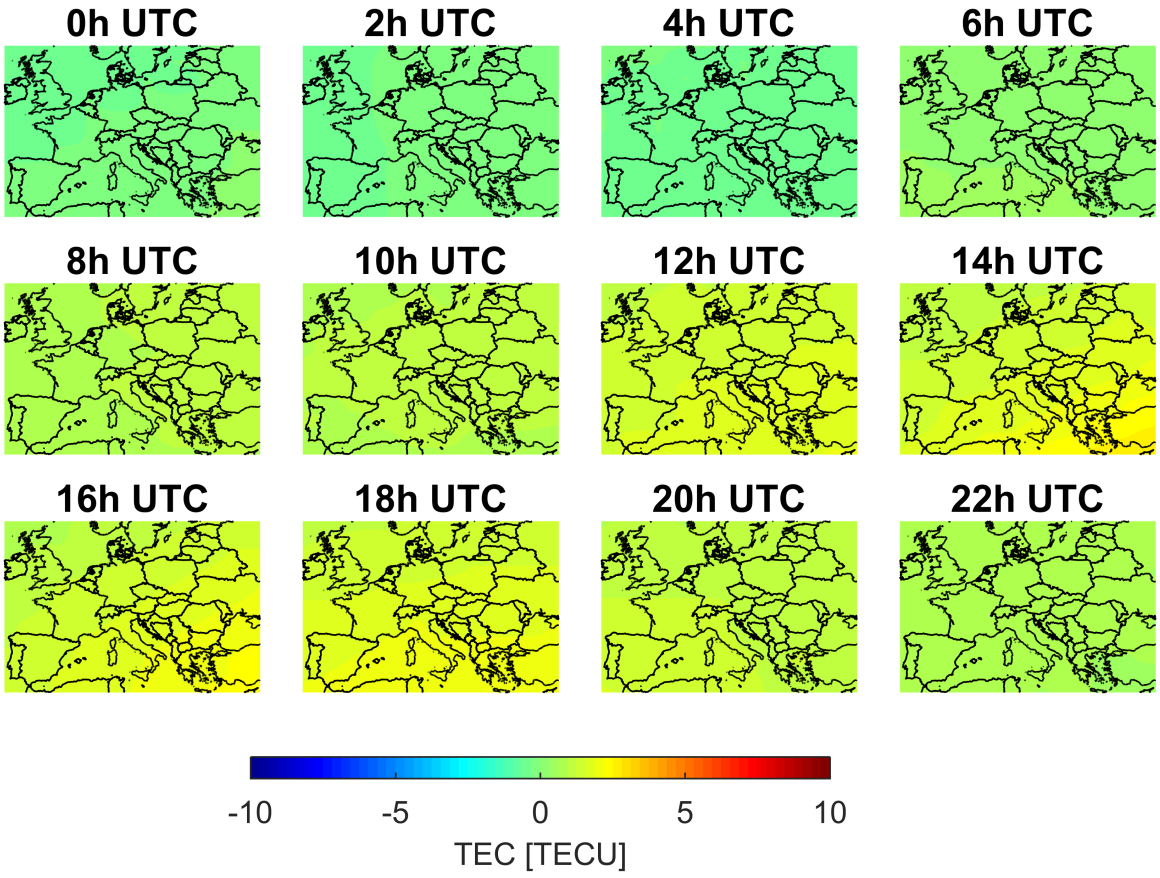

(c) Difference (Giomo - IGS)

Figure 6.33: Difference between the post-processed and the predicted Giomo regional TEC map (Europe) for August 24, 2018

Table 6.7: Mean ΔVTEC (predicted - post processed) of the Giomo Model for August 24, 2018 (day = 11:00 - 18:00 UTC, night = 21:00 - 04:00 UTC)

Stations	ΔVTEC	$\Delta VTEC_{day}$	$\Delta VTEC_{night}$
All	-0.36 TECU	-0.98 TECU	0.06 TECU
Northern (80°N, 15°E)	-0.41 TECU	-0.80 TECU	-0.10 TECU
Mid latitude (47.5°N, 15°E)	-0.84 TECU	-1.23 TECU	-0.43 TECU
Equatorial (0°N, 15°E)	-0.49 TECU	-0.45 TECU	-0.35 TECU

Table 6.8: Mean ΔVTEC (Giomo Model predicted - CODE final GIMs) for August 24, 2018 (day = 11:00 - 18:00 UTC, night = 21:00 - 04:00 UTC)

Stations	ΔVTEC	$\Delta VTEC_{day}$	$\Delta VTEC_{night}$
All	0.54 TECU	0.04 TECU	1.33 TECU
Northern (80°N, 15°E)	-0.90 TECU	-1.88 TECU	0.43 TECU
Mid latitude (47.5°N, 15°E)	-0.17 TECU	-0.55 TECU	-1.00 TECU
Equatorial (0°N, 15°E)	1.17 TECU	0.10 TECU	1.73 TECU

6.5.1 Availability of different ionosphere models

Nowadays a lot of different ionosphere models exist, like they were shown in Chapter 4.4 or Chapter 6.3. The following Table 6.9 shows their different products and availabilities. The availability is based on the time the file is normally uploaded. Sometimes, however, the upload is delayed. The 1-, 2- and 5-day predicted GIMs (in IONEX format) of CODE get substituted with temporally closer versions, when they are available. So the 5-day predicted file of DOY275 gets substituted by the 2-day predicted file after 3 days, and this gets substituted by the 1-day predicted file after another day.

As the service for downloading CODE predictions in IONEX format was just recently established, these ionosphere maps were not taken into account in this thesis.

Table 6.9: Availability of different ionosphere models (as of October 2018)

Product	File name	Availability
CODE		
Final GIMs (IONEX)	CODGddd0.yyI	4 to 8 days later (time varies)
Rapid GIMs (IONEX)	CORGddd0.yyI	2 days later (6:55 UTC)
1-day predicted (IONEX)	COPGddd0.yyI	same day (6:55 UTC)
2-day predicted (IONEX)	COPGddd0.yyI	previous day (6:55 UTC)
5-day predicted (IONEX)	COPGddd0.yyI	4 days prior (6:55 UTC)
Final GIMs (SH)	CODwwwwd.ION	4 days later (time varies)
Rapid GIMs (SH)	CODwwwwd.ION_R	2 days later (6:55 UTC)
1-day predicted (SH)	CODwwwwd.ION_P	same day (6:55 UTC)
2-day predicted (SH)	CODwwwwd.ION_P2	previous day (6:55 UTC)
5-day predicted (SH)	CODwwwwd.ION_P5	4 days prior (6:55 UTC)
Klobuchar [a] final	CGIMddd0.yyN	4 days later (time varies)
Klobuchar [a] rapid	CGIMddd0.yyN_R	next day (6:55 UTC)
Klobuchar [a] 1-day predicted	CGIMddd0.yyN_P	same day (6:55 UTC)
Klobuchar [a] 2-day predicted	CGIMddd0.yyN_P2	previous day (6:55 UTC)
Klobuchar [a] 5-day predicted	CGIMddd0.yyN_P5	4 days prior (6:55 UTC)
IGS		
Final GIMs	igsgddd0.yyI	11 to 25 days later (time varies)
Rapid GIMs	igrgddd0.yyI	1 day later (time varies)
Regiomontan		
Final GIMs	REGRddd0.yyI	next day (04:10 UTC)
Giomo		
Final GIMs	TUWGddd0.yyI	next day (03:15 UTC)
1-day predicted GIMs	TUWPddd0.yyI	previous day (23:00 UTC)

[a] Klobuchar-style ionospheric coefficients (alphas and betas) best fitting CODE's IONEX data are computed on a regular basis (`http://www.aiub.unibe.ch/research/code___analysis_center/klobuchar_style_ionospheric_coefficients/index_eng.html`, accessed: 28.01.2019, 13:23)

Chapter 7

Summary and Conclusions

This thesis deals with modeling approaches of the ionospheric influence on GNSS measurements and their applications. Within this work a simple model of global ionospheric delays has been developed.

The ionosphere depicts the upper part of the atmosphere, from about 50 km to 1000 km height above Earth surface. Due to its ionization, mainly depending on the Sun's activity and the electromagnetic field, electromagnetic waves are affected when traveling through this part of the atmosphere. Global Navigation Satellite Systems (GNSS) are based on the transmission of microwaves, i.e. waves that are affected by the ionosphere. This means that on the one hand, microwave signals transmitted from satellites measured at the Earth's surface can be used to derive information about the ionosphere; for navigation and positioning applications, however, this effects denote a signal error source which has to be taken into account.

As the ionosphere is a dispersive medium, the ionospheric delay can be derived by measuring on two frequencies. The use of more than one frequency allows to build linear combinations which have advantages such as a lower noise level, a greater wavelength or a removed (first order) ionospheric effect. However, most GNSS receivers, in particular those in mass market productions, are single-frequency devices. In this case, the signal distortion due to the ionosphere needs to be corrected differently. This is mostly done using a priori knowledge of the state of the ionosphere from an ionosphere model.

Present ionosphere models for positioning and navigation applications represent the Total Electron Content (TEC), which is the integral electron density along the signal path with a cross section of one meter squared. The knowledge of the TEC allows for the correction of satellite signals due to the ionosphere. Typically, ionosphere models distribute the vertical TEC (VTEC, in zenith direction) which needs to be projected to the desired elevation using proper mapping functions.

Common mathematical formulations of the VTEC field are Taylor Series Expansions, Spherical Harmonics Expansions and B-Spline formulations. But there also exist empirical models, such as Klobuchar, NeQuick or IRI. In order to correct for the ionospheric delay, the global VTEC information is distributed to the users via a set of parameters or via a standardized format (IONEX).

As part of this dissertation, a new ionosphere model has been developed. The goal was to establish a real-time service for the correction of ionospheric delays with a simple model consisting of only five parameters. This Giomo Model uses a single infinitesimal layer at 450 km height above the Earth's surface. The VTEC at any IPP of interest is obtained from the location and magnitude of the current electron maximum multiplied by two distance dependent weighting functions, which account for the spherical distance to the IPP. Therefore, the model parameters are the electron maximum (amplitude), its location in latitude and longitude and two weighting parameters describing the decrease of electron density with increasing distance to this point.

All parameters are calculated in an iterative least-squares adjustment with an hourly time resolution from global observation data. GPS measurements from all IGS stations which provide L1, L2, P1 and P2 signals are used. For the processing the code observations were smoothed with phase observations. Because of the non-linearity of the equation system approximate values were required, so several tests concerning the accuracy requirements of a priori values are performed. In a best-case scenario where all but one parameter have perfect a priori values, this one approximate value may be wrong by up to ±50 %. Only β_{max}, the latitude coordinate of the ionospheric maximum, requires ±35°, but such a big difference to the approximate value is quite unrealistic.

A second and more realistic scenario was tested by modifying all a priori values prior to the estimation process of the least-squares algorithm. This test yielded to a very conservative accuracy requirement for the parameters, because all parameters are assumed to differ by a similar amount. Additionally also a greater difference to the true value of one parameter could still yield proper results if the others are closer to their correct values.

The results from the Giomo Model were validated by analyzing the post-adjustment statistics and comparing the VTEC values with existing, independent ionosphere models. The internal validation yielded very optimistic results because the correlation between GNSS observations is neglected. The mean formal error of $VTEC_{max}$ between September 5th and October 10th of 0.33 TECU indicates a very accurate prediction of this parameter. Both for the weighting factors and for the coordinates of $VTEC_{max}$, the accuracy is better for the latitude dependent parameters (w_β, β_{max}). This is due to the shape of the ionospheric bulge which is spread wider in longitude direction than in latitude direction. The mean formal errors for the weighting factors correspond approximately to 1 % of the estimated value.

Statistically significant correlations can be found for $VTEC_{max}$ and the weighting parameters as well as for w_β and β_{max}. The former correlations are of the order of -0.6. A negative correlation between $VTEC_{max}$ and the weighting parameters is expected because a larger maximum value would produce a "'narrower"' VTEC function and, thus, smaller weighting parameters.

An external validation was performed by comparing the Giomo Model results to those from Klobuchar, CODE, IGS and the regional model Regiomontan. Time series of the models at various latitudes (0°, 20°, 40°, 48°, 60°, 80°) at the 15° meridian are derived and compared. For locations close to the ionospheric maximum, all models show a good consistency, especially at $\varphi = 20°$. At the equator, CODE and IGS seem to overestimate the TEC compared to the other models. In mid-latitudes at 40° and 48°, the Klobuchar Model overestimates the VTEC up to 7 TECU, the other

models show a good agreement. Some discrepancies of the Giomo Model (e.g. underestimating the TEC at nighttime to a maximum of -3 TECU at $\varphi = 40°$ or slightly overestimating the TEC at noon) can be explained by the fact that the Giomo Model only consists of five parameters, so it cannot account for small regional changes of the TEC, but rather estimates the VTEC maximum well. At the location in Austria (48°), also the regional Regiomontan Model participates in this comparison. It shows a very good agreement to the CODE model. At high latitudes (60° and 80°) the Giomo Model seems to derive higher values than CODE and IGS, which can be explained by the flat drop of the Giomo functional model towards the poles. IGS Model, however, seems to underestimate the TEC for those high latitudes. Here, Klobuchar produces too high results for all epochs. For $\varphi = 80°$ only the constant value is given for the whole day, which is on average about 4 TECU above the real TEC.

For all hourly TEC maps between June 3rd and October 11th 2018, differences to all other given models were calculated. From these differences, the statistical parameters mean, standard deviation and median were calculated. The mean differences indicate a good general agreement and no systematic deviation between the Giomo Model and the IGS Model (mean difference of -0.12 TECU). However, the standard deviation (±2.75 TECU) shows that there exist larger differences between the two models which average out over longer time spans. The IGS Model and the CODE Model show a good agreement of 0.80 TECU mean difference. The Klobuchar Model clearly shows the largest discrepancies to all other models with mean differences between 2.59 TECU and 4.13 TECU. The median values show in general the same behavior.

Another validation procedure was performed by converting the TEC values from different models to pseudorange corrections and applying them to L1. The corrected pseudoranges are then compared to the correspondent ranges obtained by the ionosphere-free linear combination. Although the models of IGS and CODE perform better, the close to real-time Giomo Model can compete: 79.9 % of the corrections of CODE are within a difference of ±1 m, 80.1 % of IGS and 75.5 % of Giomo.

For real-time and forecast applications, a prediction of VTEC values is required. In case of the Giomo Model only the five contributing parameters have to be predicted. Several forecast methods have been tested for epochs between March 26th and August 1st 2018. For the parameter w_β, a weighted average (weight: $1/\Delta t$) of the last five (available) days at the same time is used as predicted value. For the remaining four parameters a weighted average of only three previous values at the same time gives the most accurate predictions.

The Austrian reference station provider EPOSA established a service for single-frequency users to improve their position accuracy using ionospheric corrections calculated with the Giomo Model. IONEX files for the previous day as well as predicted files for the current day will be available for download via the EPOSA webpage. In combination with an appropriate application also smartphone users can benefit from the service.

Some adaptions in prediction could expand the model and increase its accuracy even further. As the ionospheric activity is mainly driven by the Sun, the time series of $VTEC_{max}$ contains the 11-years period of the solar cycle as well as seasonal oscillations. These effects can be empirically

estimated, if Giomo calculations are available for a longer time span. Alternatively the effect can be derived from existing models. Also the accuracy of the prediction of the parametersw_β and w_s can be improved if the correlation to $\mathrm{VTEC}_{\max}$ is exploited for the estimate.

Another improvement for users might be a higher temporal resolution of the model. Instead of an hourly computation of the VTEC values, the calculation interval could be decreased, e.g. to 15 minutes.

Appendix A

Pseudorange correction

For an extended explanation according the Figures A.2 - A.23 and their calculation see Chapter 6.4.2. Figure A.1 visualizes, where the stations used for the validation are located.

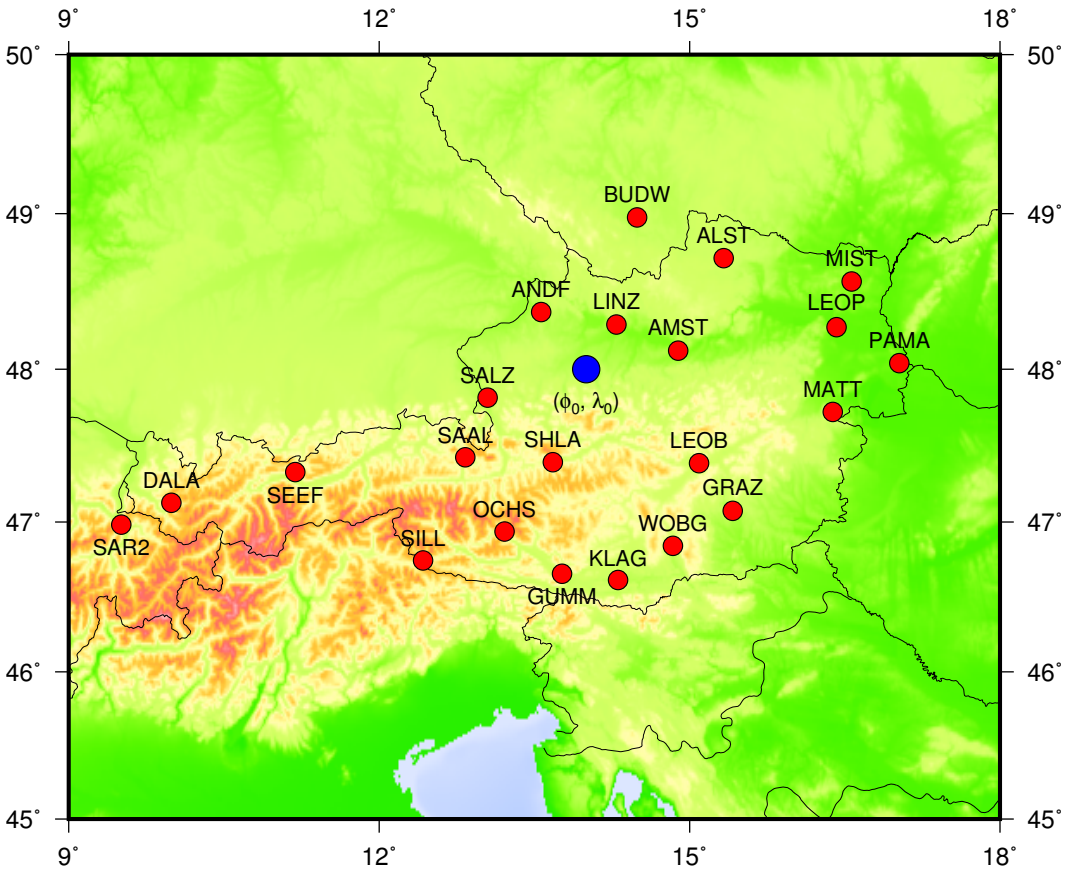

Figure A.1: EPOSA stations in Austria and nearby used to calculate the pseudorange corrections

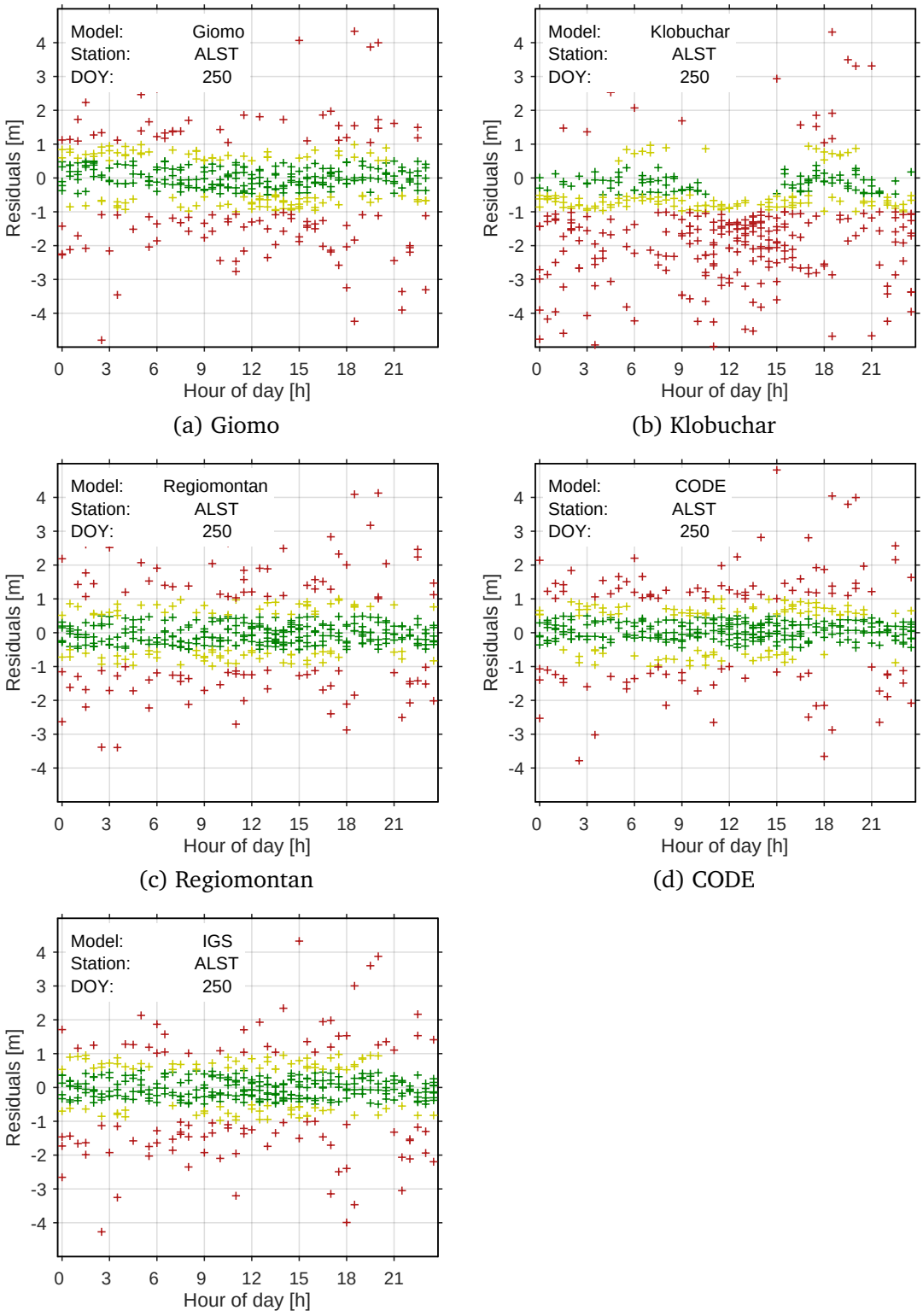

Figure A.2: Differences between L1 pseudoranges corrected with different ionosphere models (a) - (e) and the ionosphere-free linear combination for station Allentsteig (ALST) for September 7, 2018)

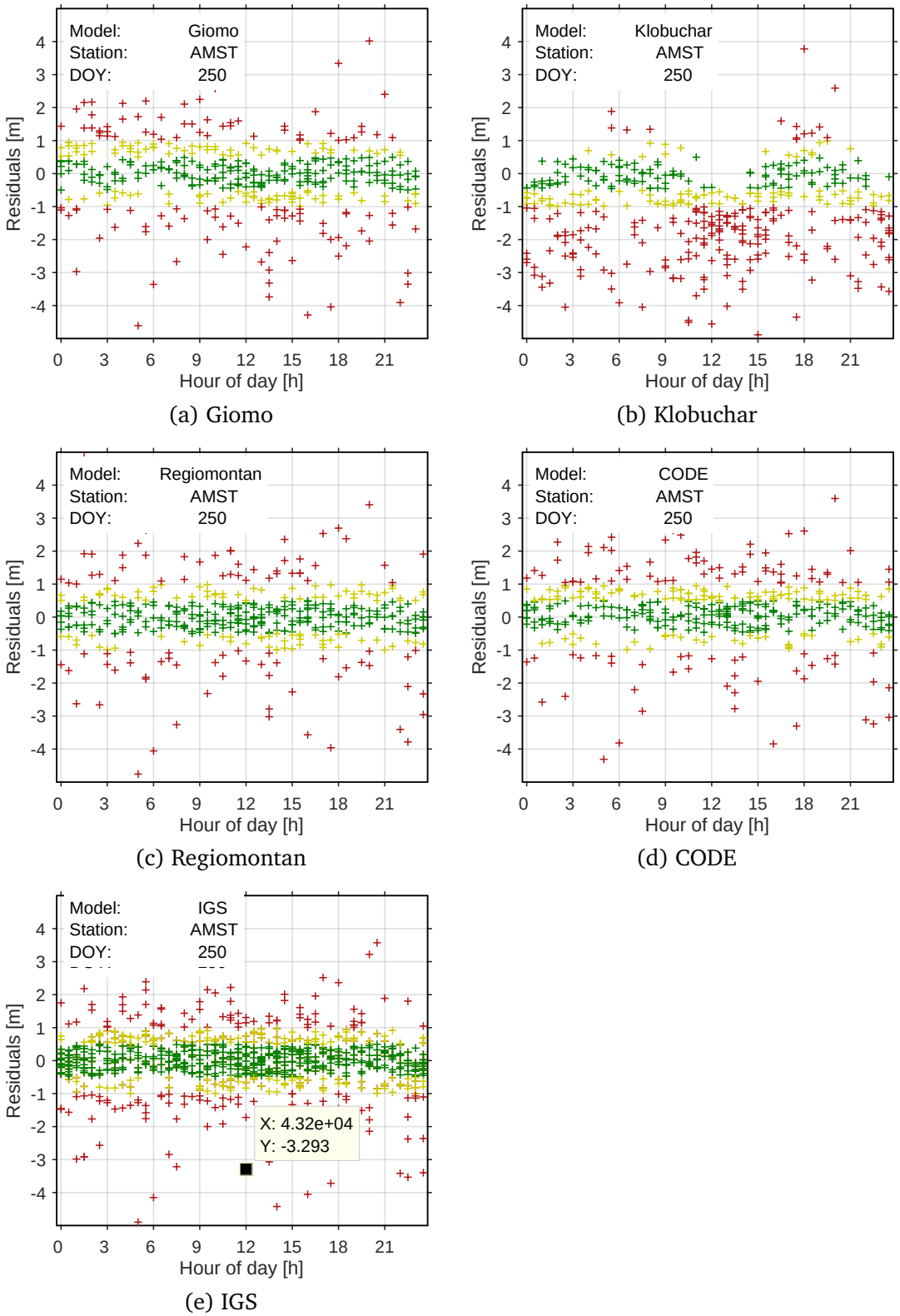

Figure A.3: Differences between L1 pseudoranges corrected with different ionosphere models (a) - (e) and the ionosphere-free linear combination for station Amstetten (AMST) for September 7, 2018)

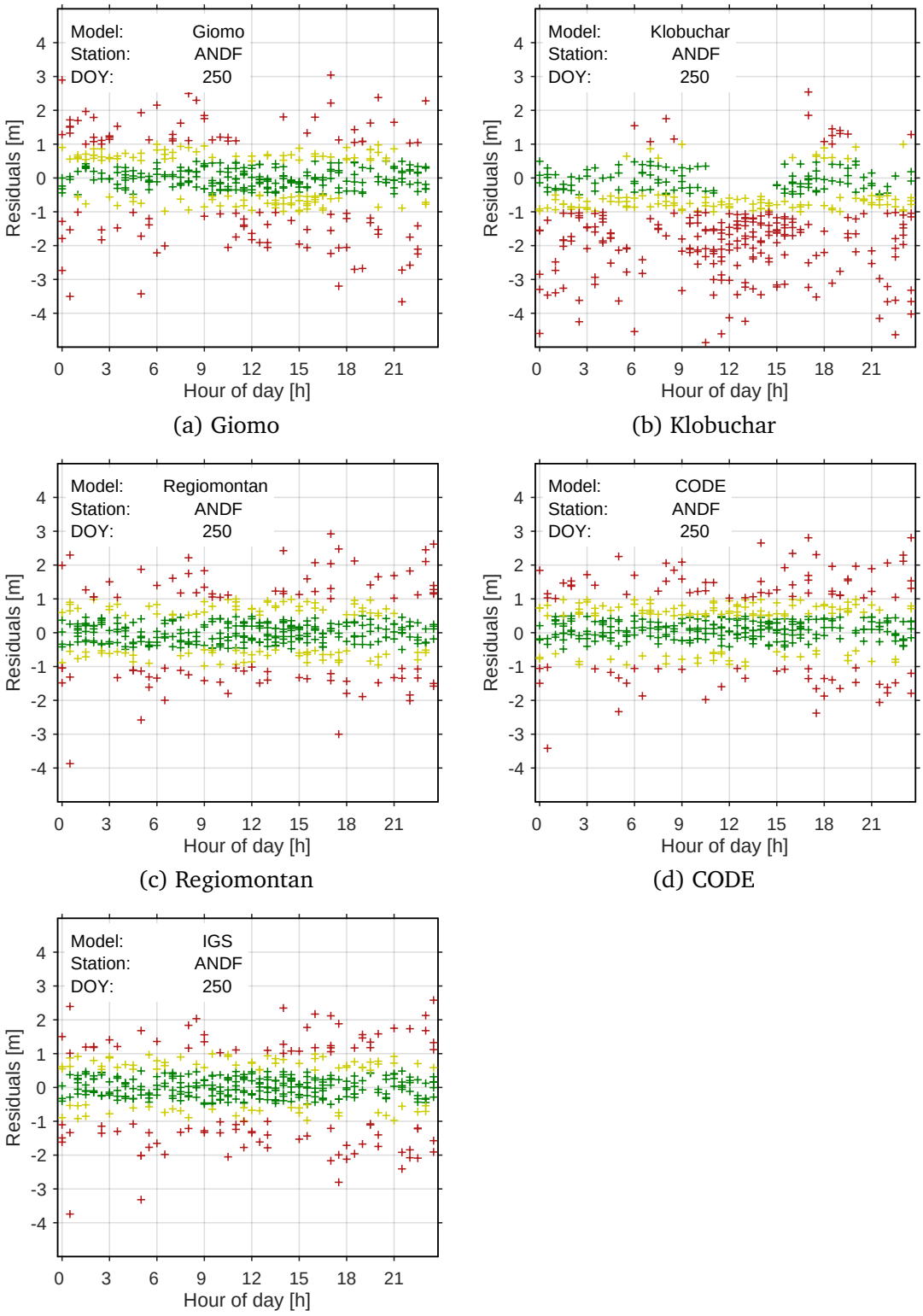

Figure A.4: Differences between L1 pseudoranges corrected with different ionosphere models (a) - (e) and the ionosphere-free linear combination for station Andorf (ANDF) for September 7, 2018)

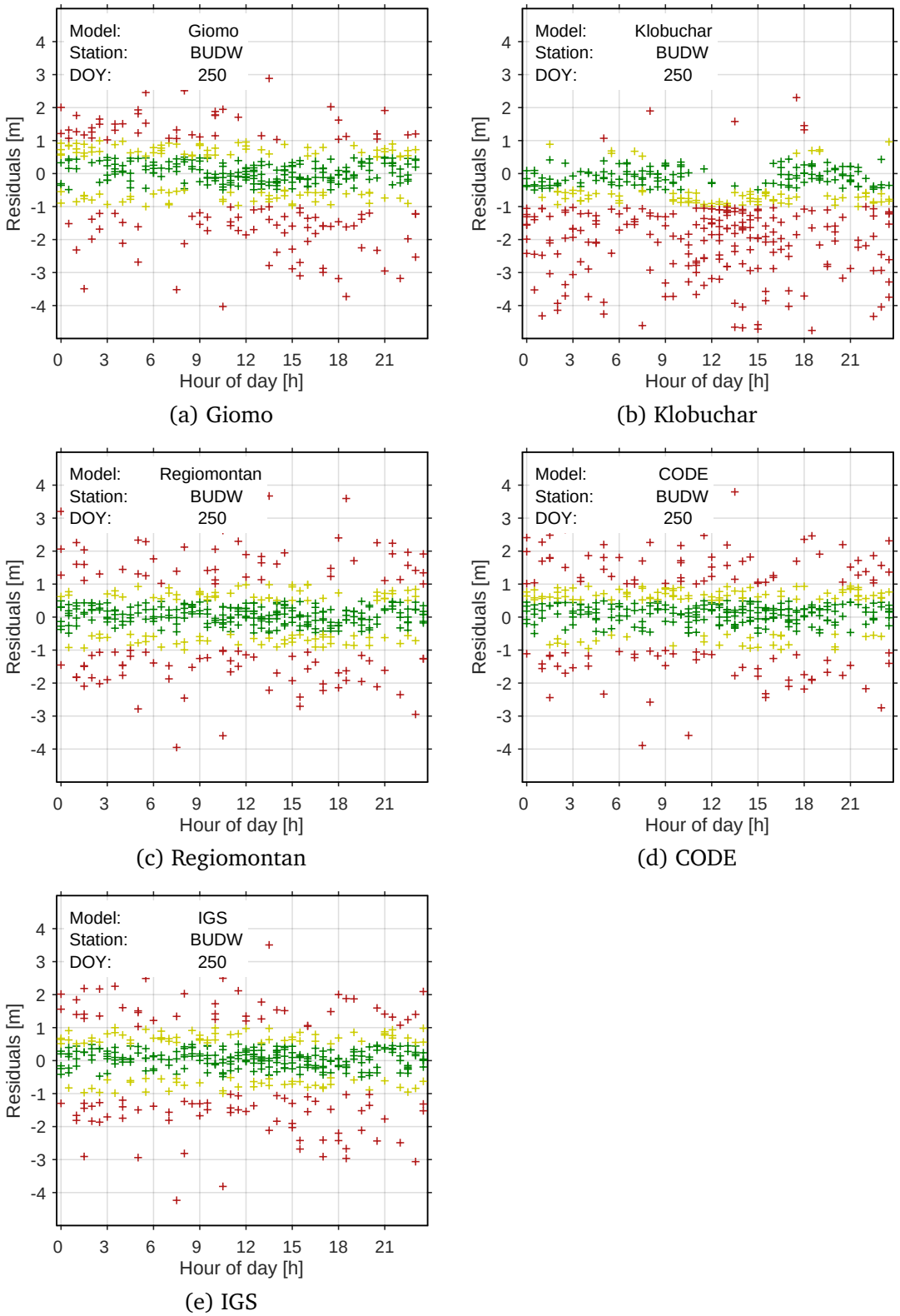

Figure A.5: Differences between L1 pseudoranges corrected with different ionosphere models (a) - (e) and the ionosphere-free linear combination for station Budweis (BUDW) for September 7, 2018)

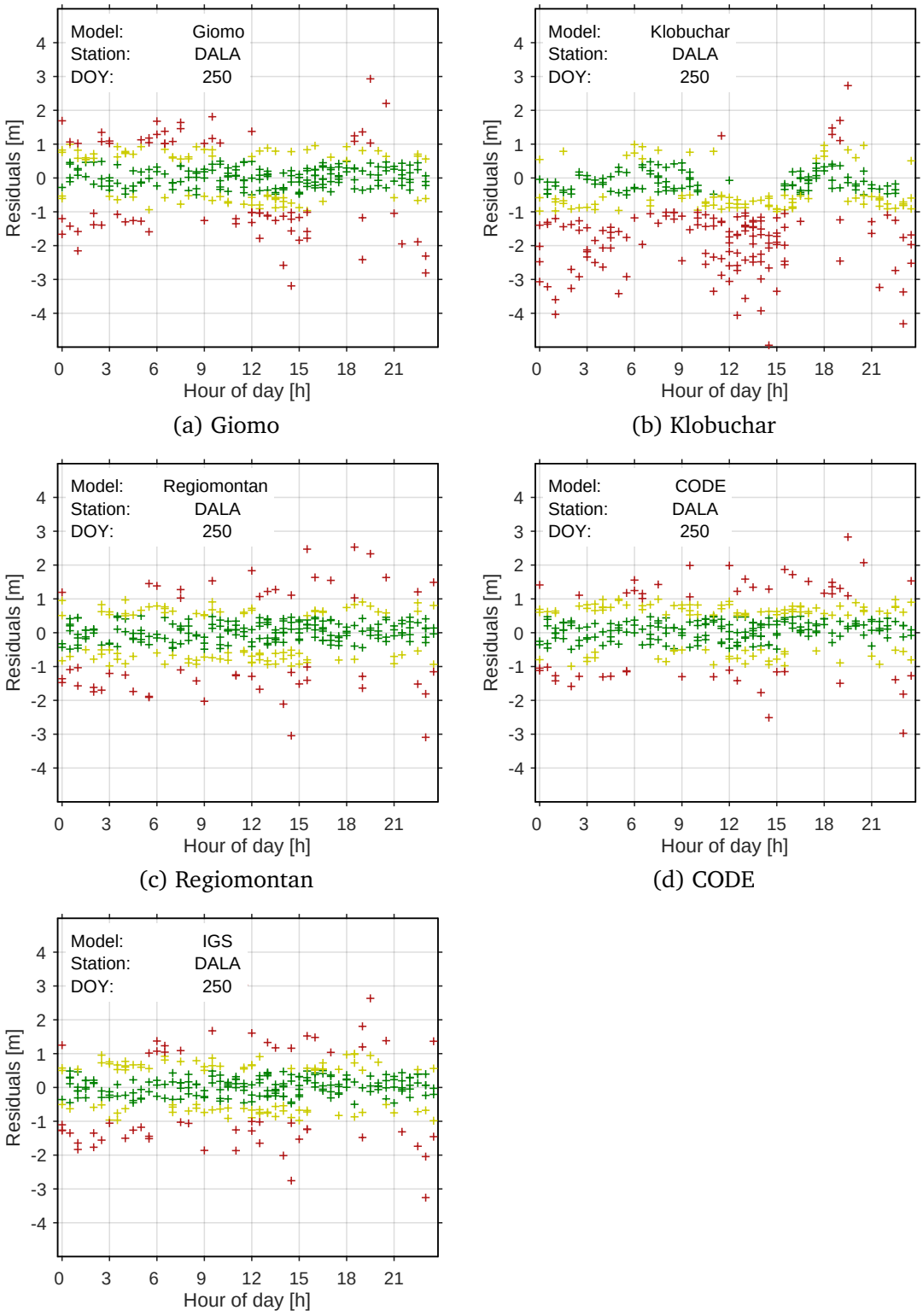

Figure A.6: Differences between L1 pseudoranges corrected with different ionosphere models (a) - (e) and the ionosphere-free linear combination for station Dalaas (DALA) for September 7, 2018)

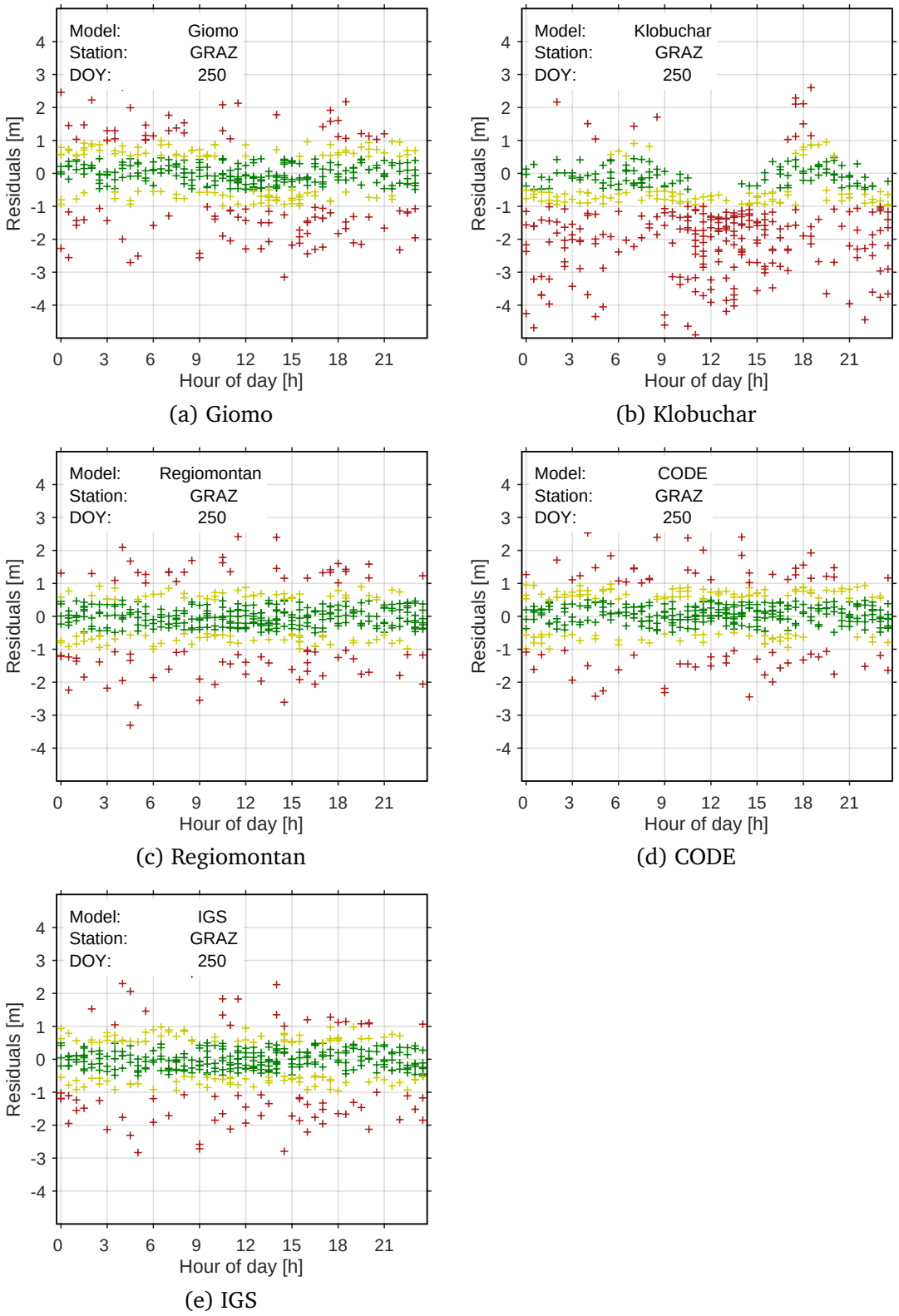

Figure A.7: Differences between L1 pseudoranges corrected with different ionosphere models (a) - (e) and the ionosphere-free linear combination for station Graz (GRAZ) for September 7, 2018)

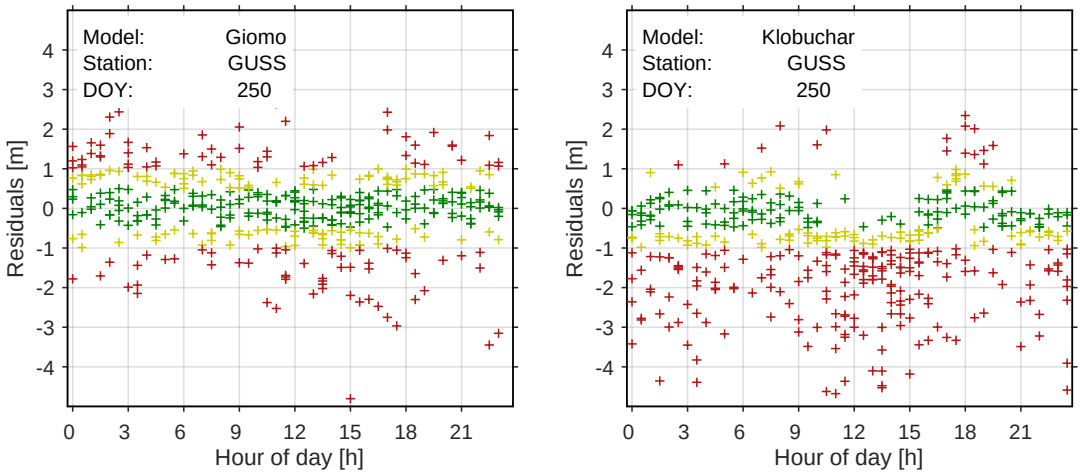

(a) Giomo

(b) Klobuchar

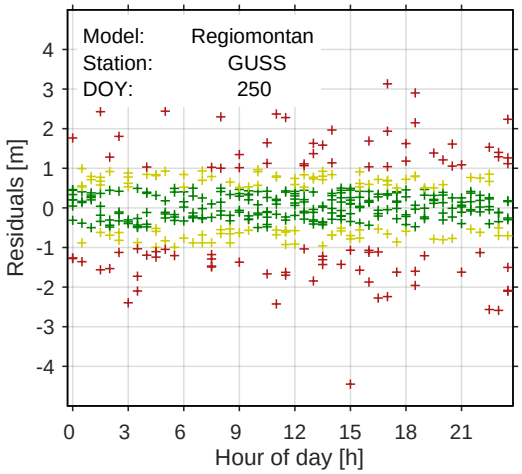

(c) Regiomontan

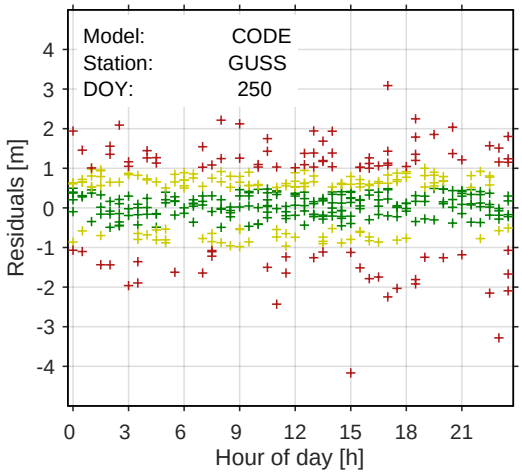

(d) CODE

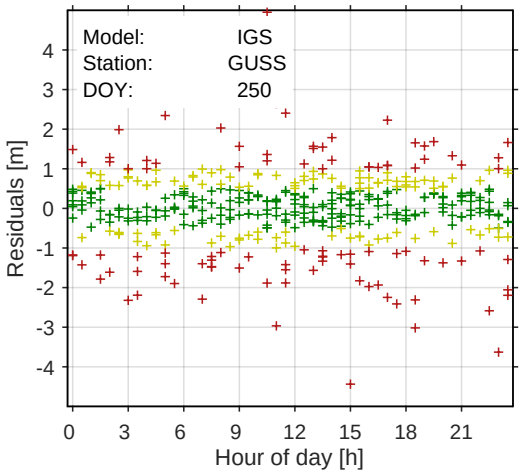

(e) IGS

Figure A.8: Differences between L1 pseudoranges corrected with different ionosphere models (a) - (e) and the ionosphere-free linear combination for station Güssing (GUSS) for September 7, 2018)

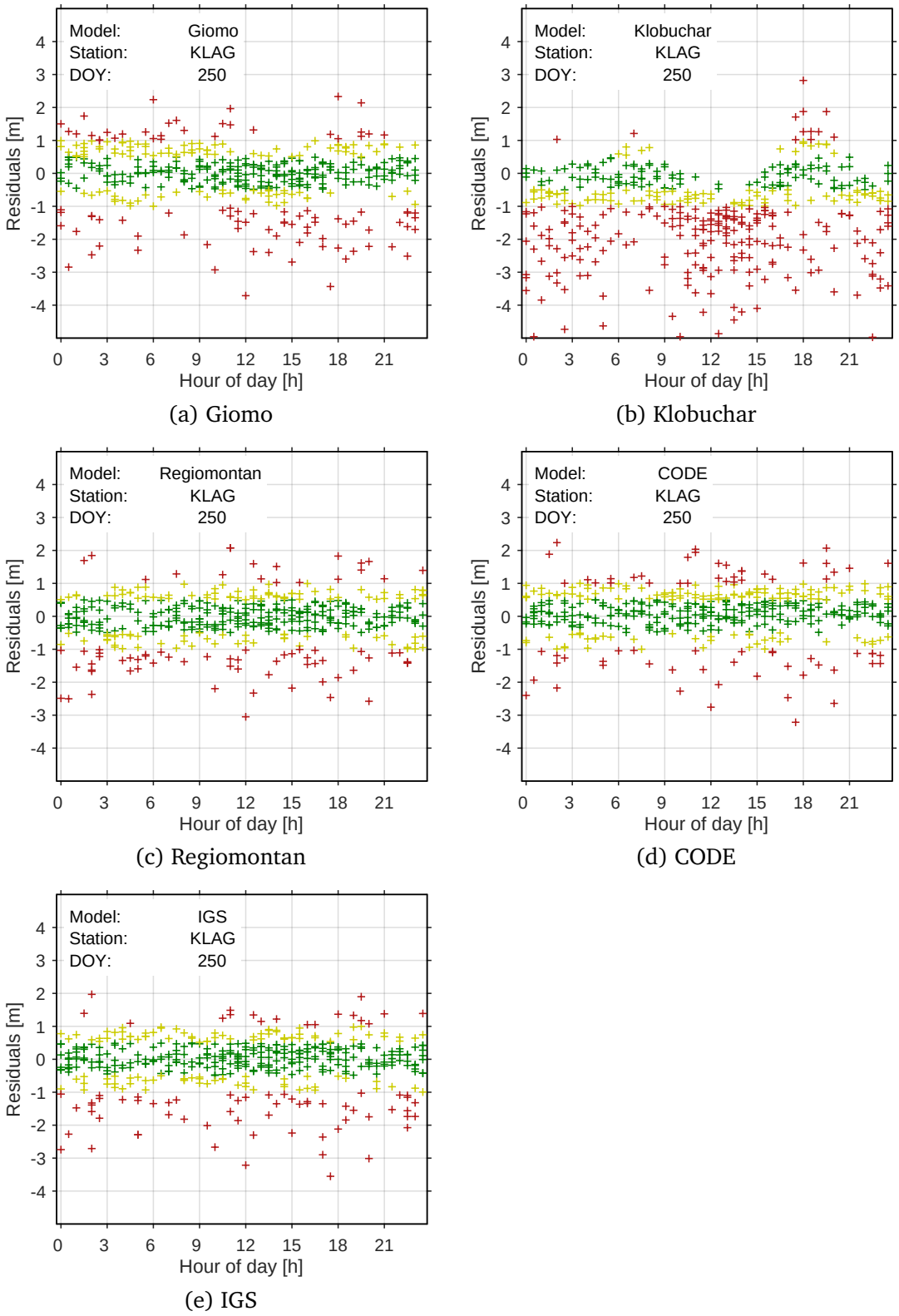

Figure A.9: Differences between L1 pseudoranges corrected with different ionosphere models (a) - (e) and the ionosphere-free linear combination for station Klagenfurt (KLAG) for September 7, 2018)

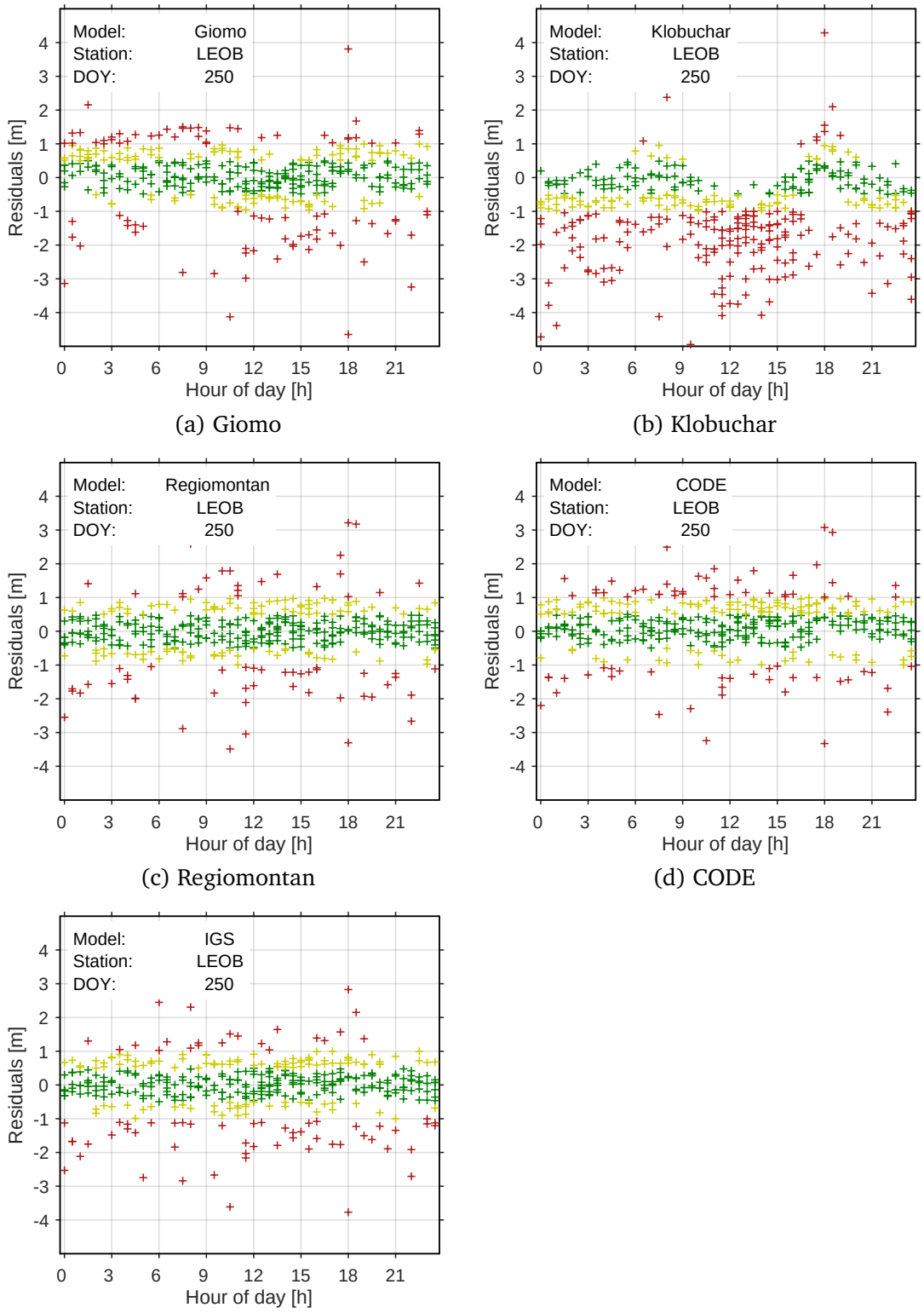

Figure A.10: Differences between L1 pseudoranges corrected with different ionosphere models (a) - (e) and the ionosphere-free linear combination for station Leoben (LEOB) for September 7, 2018)

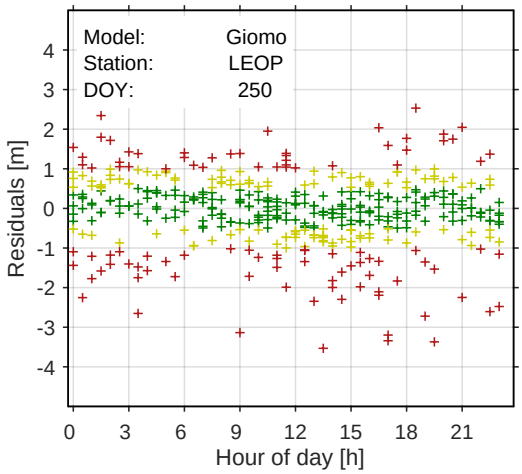

(a) Giomo

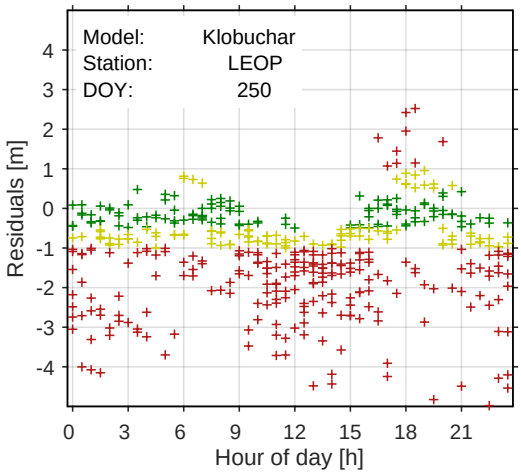

(b) Klobuchar

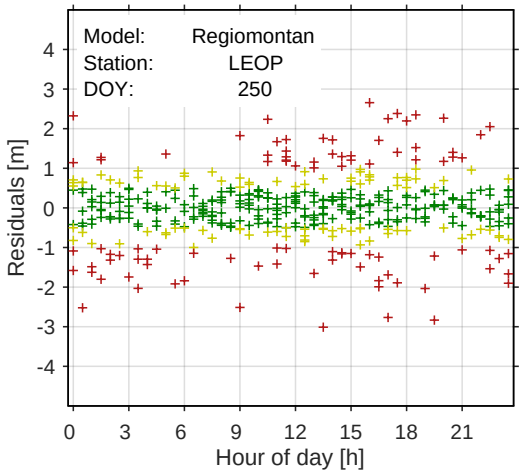

(c) Regiomontan

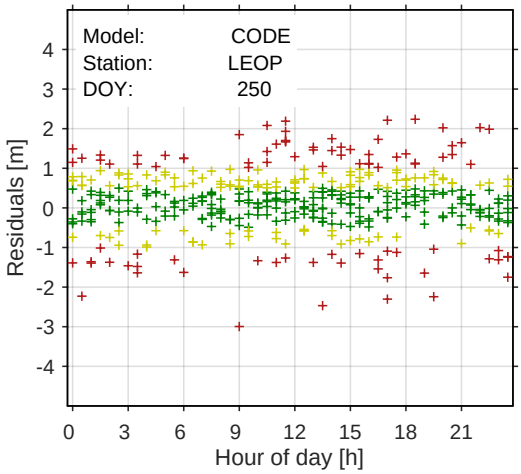

(d) CODE

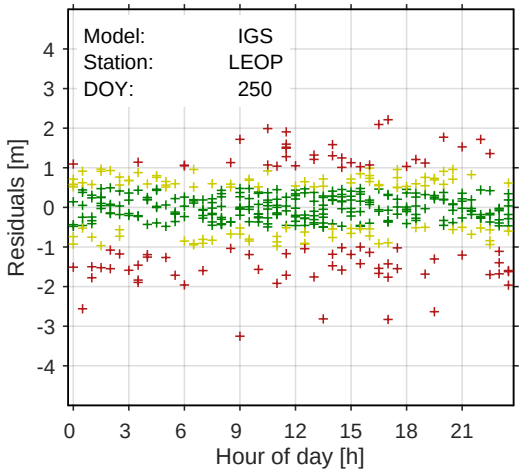

(e) IGS

Figure A.11: Differences between L1 pseudoranges corrected with different ionosphere models (a) - (e) and the ionosphere-free linear combination for station Leopoldau (LEOP) for September 7, 2018)

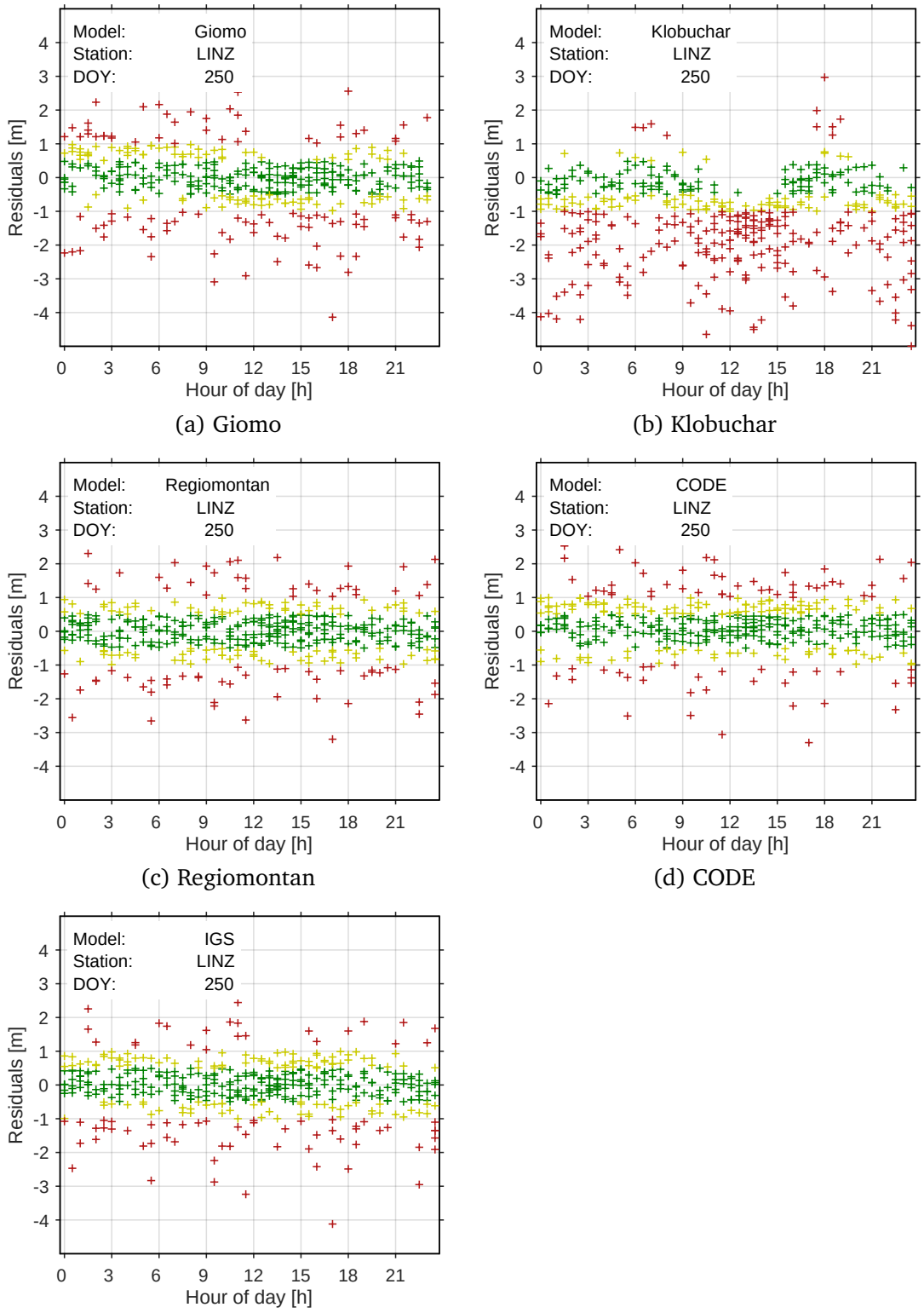

Figure A.12: Differences between L1 pseudoranges corrected with different ionosphere models (a) - (e) and the ionosphere-free linear combination for station Linz (LINZ) for September 7, 2018)

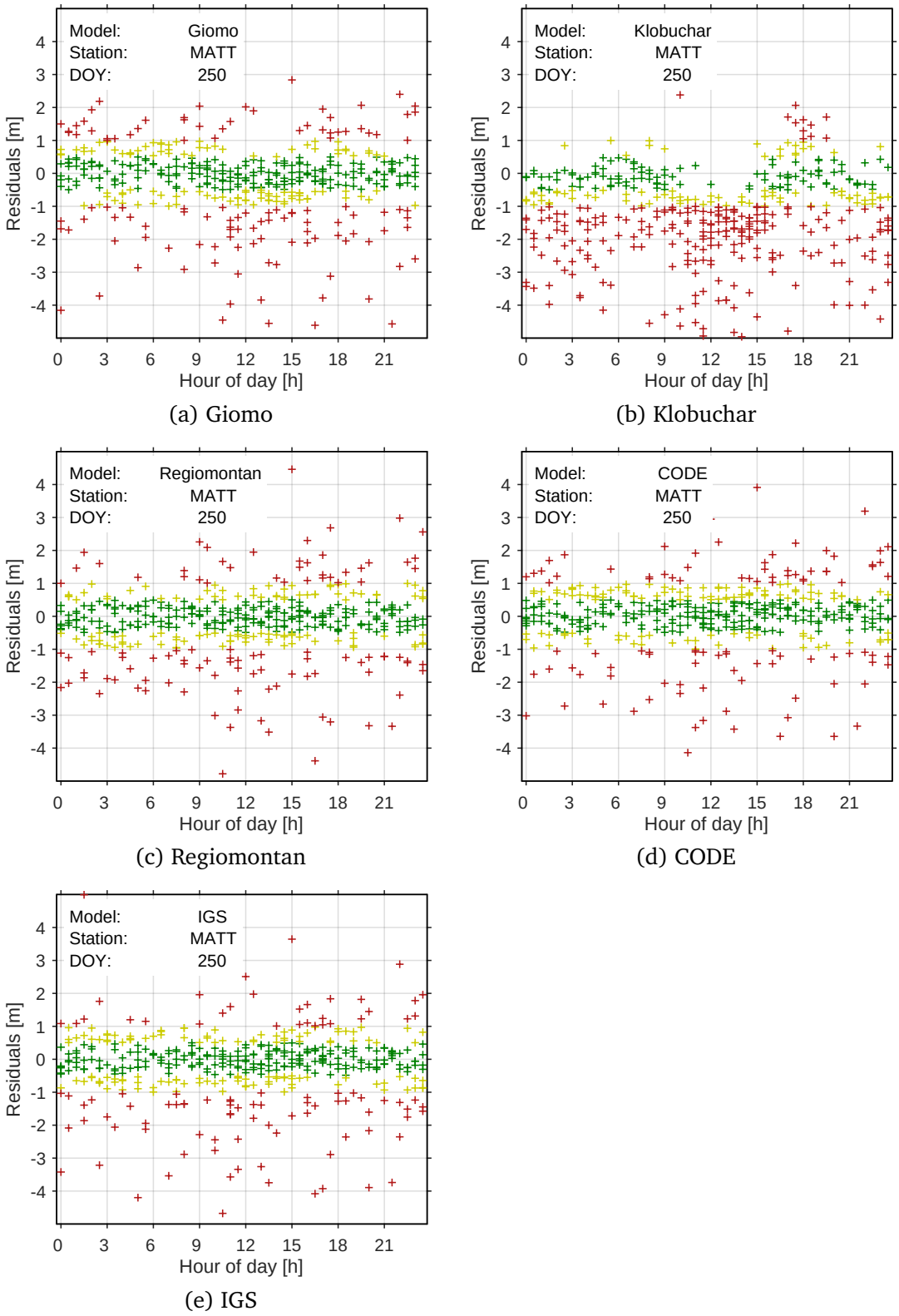

Figure A.13: Differences between L1 pseudoranges corrected with different ionosphere models (a) - (e) and the ionosphere-free linear combination for station Mattersburg (MATT) for September 7, 2018)

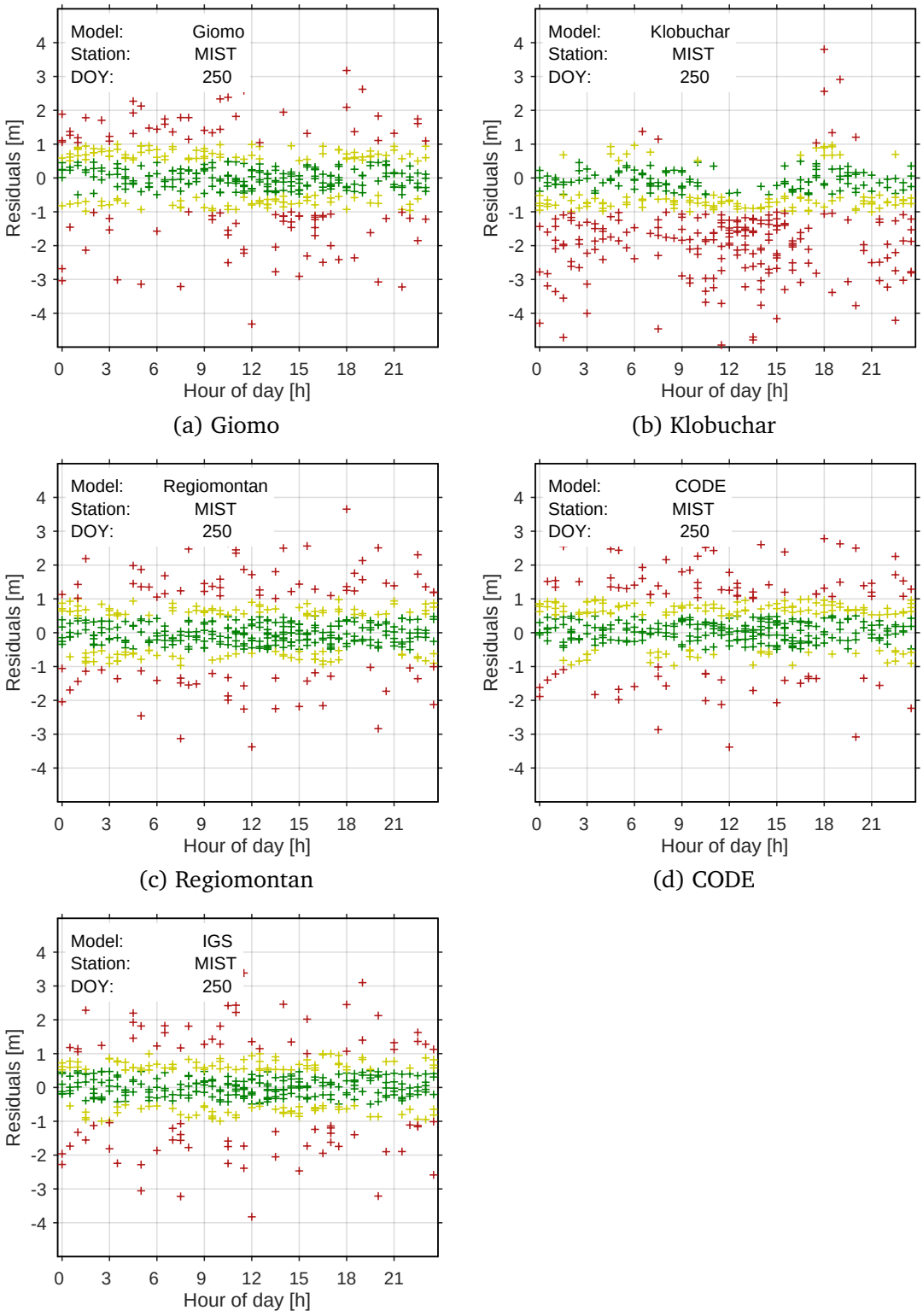

Figure A.14: Differences between L1 pseudoranges corrected with different ionosphere models (a) - (e) and the ionosphere-free linear combination for station Mistelbach (MIST) for September 7, 2018)

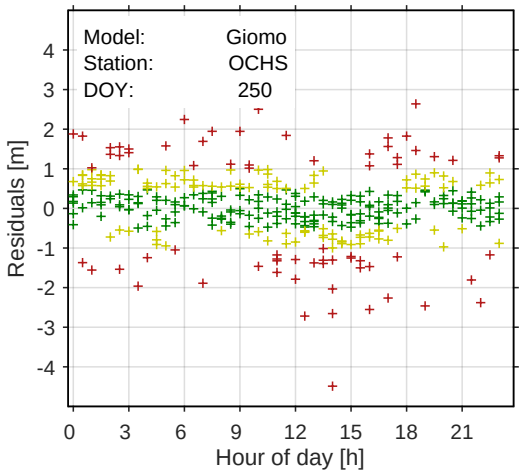

(a) Giomo

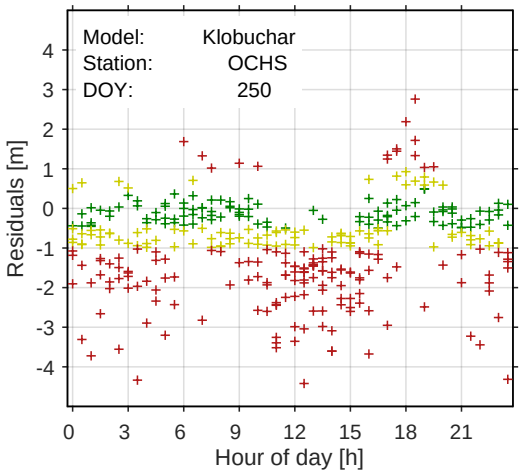

(b) Klobuchar

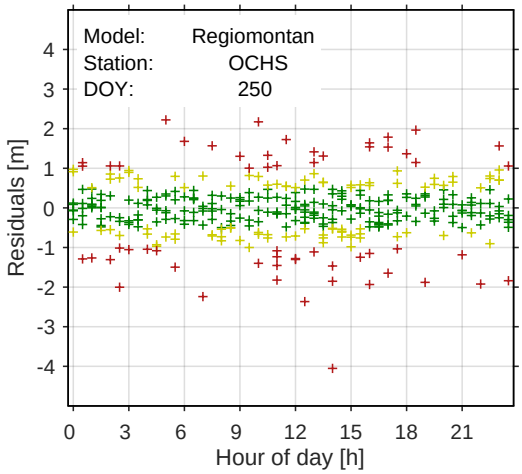

(c) Regiomontan

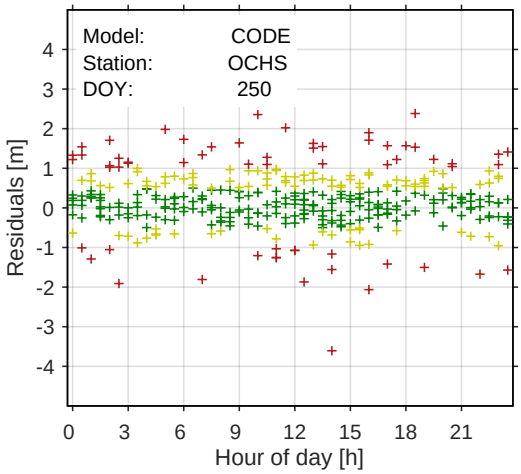

(d) CODE

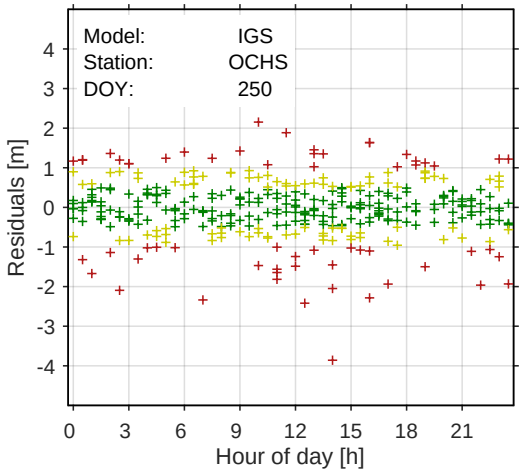

(e) IGS

Figure A.15: Differences between L1 pseudoranges corrected with different ionosphere models (a) - (e) and the ionosphere-free linear combination for station Ochenig Süd (OCHS) for September 7, 2018)

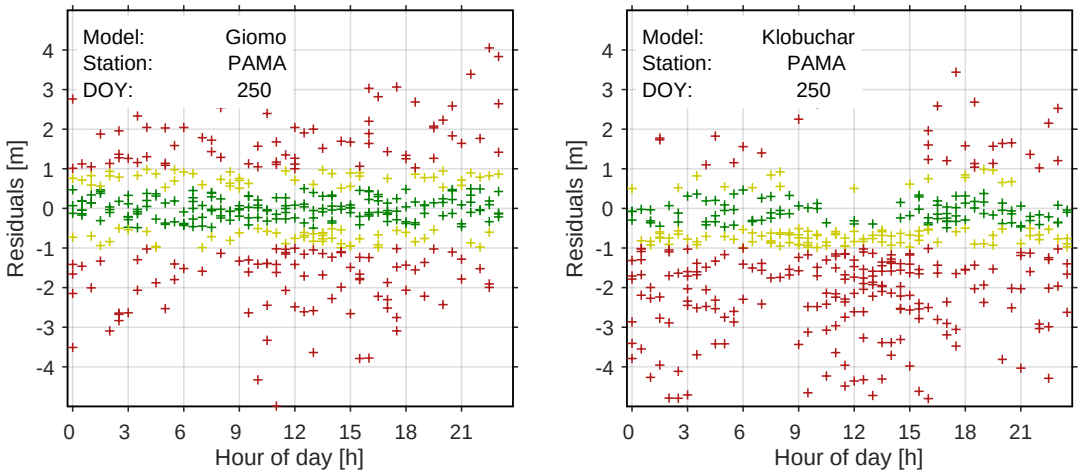

(a) Giomo

(b) Klobuchar

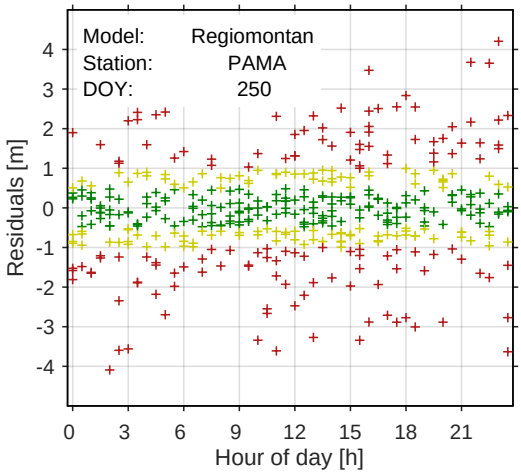

(c) Regiomontan

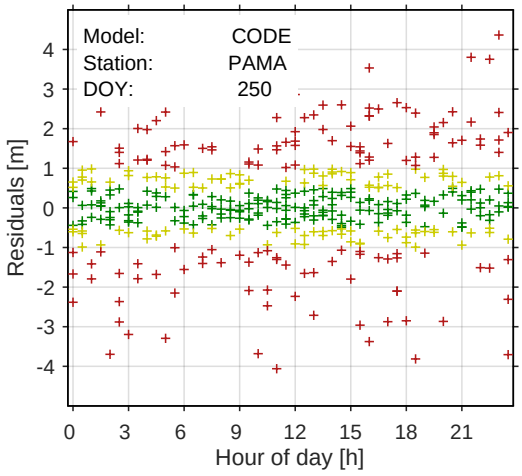

(d) CODE

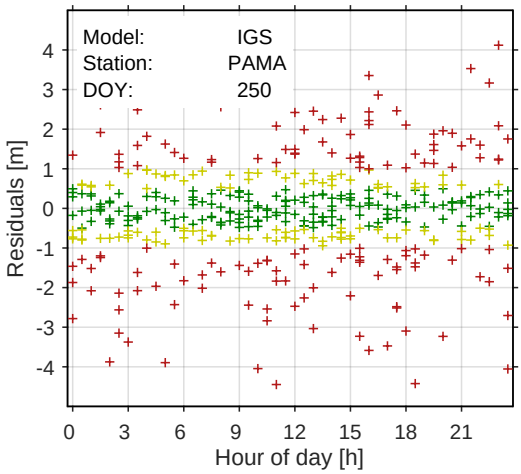

(e) IGS

Figure A.16: Differences between L1 pseudoranges corrected with different ionosphere models (a) - (e) and the ionosphere-free linear combination for station Pama (PAMA) for September 7, 2018)

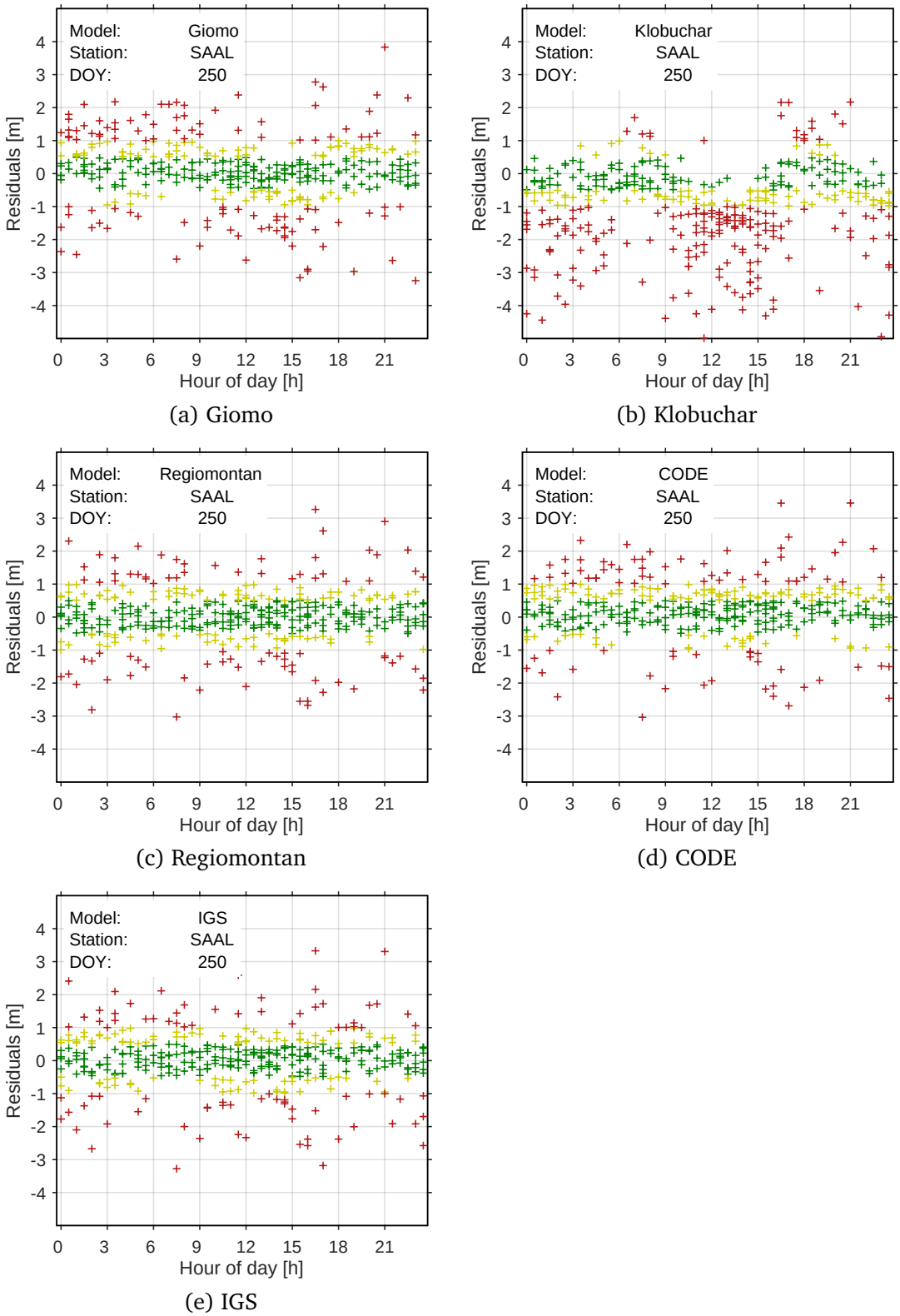

(a) Giomo (b) Klobuchar

(c) Regiomontan (d) CODE

(e) IGS

Figure A.17: Differences between L1 pseudoranges corrected with different ionosphere models (a) - (e) and the ionosphere-free linear combination for station Saalfelden (SAAL) for September 7, 2018)

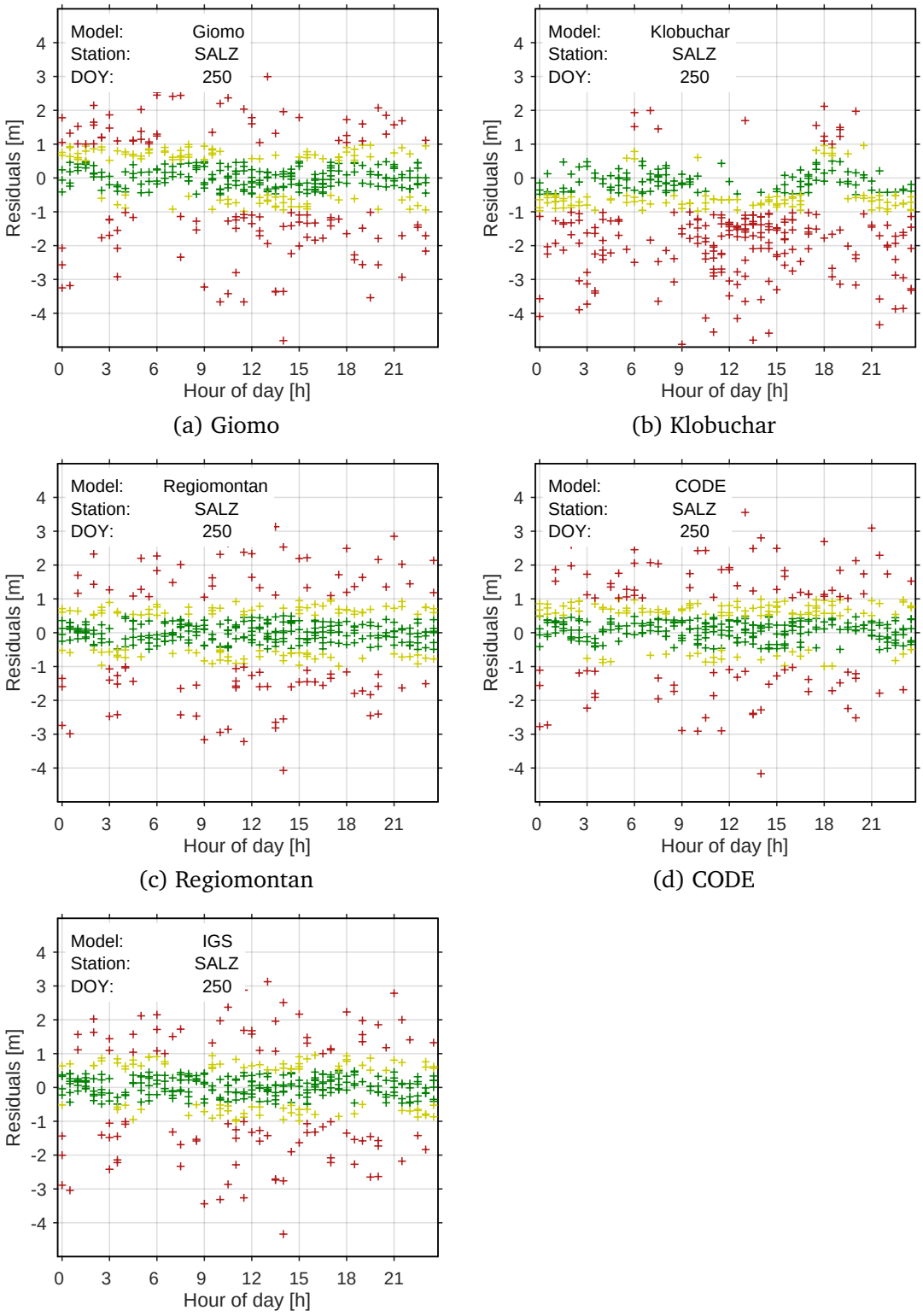

Figure A.18: Differences between L1 pseudoranges corrected with different ionosphere models (a) - (e) and the ionosphere-free linear combination for station Salzburg (SALZ) for September 7, 2018)

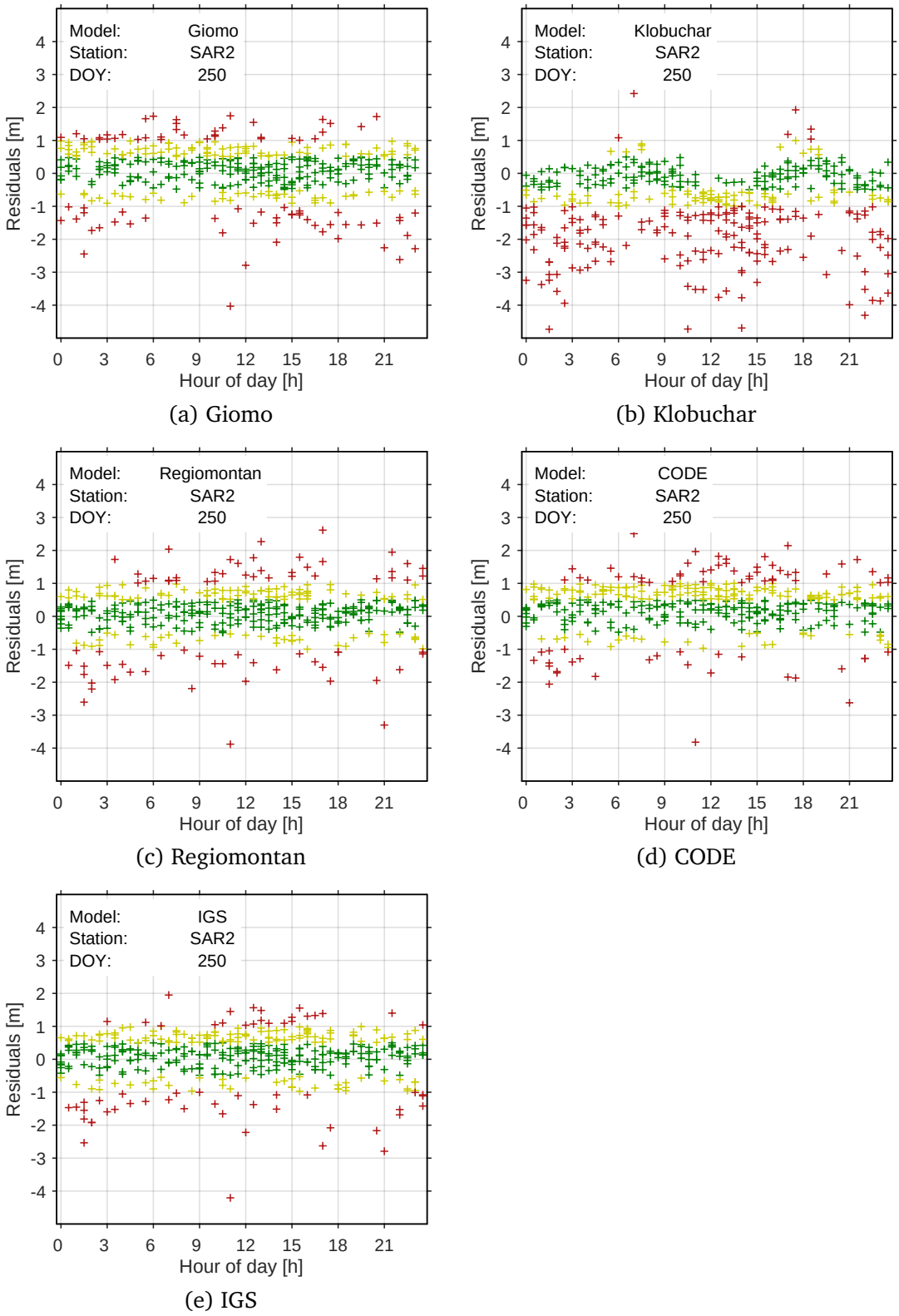

Figure A.19: Differences between L1 pseudoranges corrected with different ionosphere models (a) - (e) and the ionosphere-free linear combination for station Sargans 2 (SAR2) for September 7, 2018)

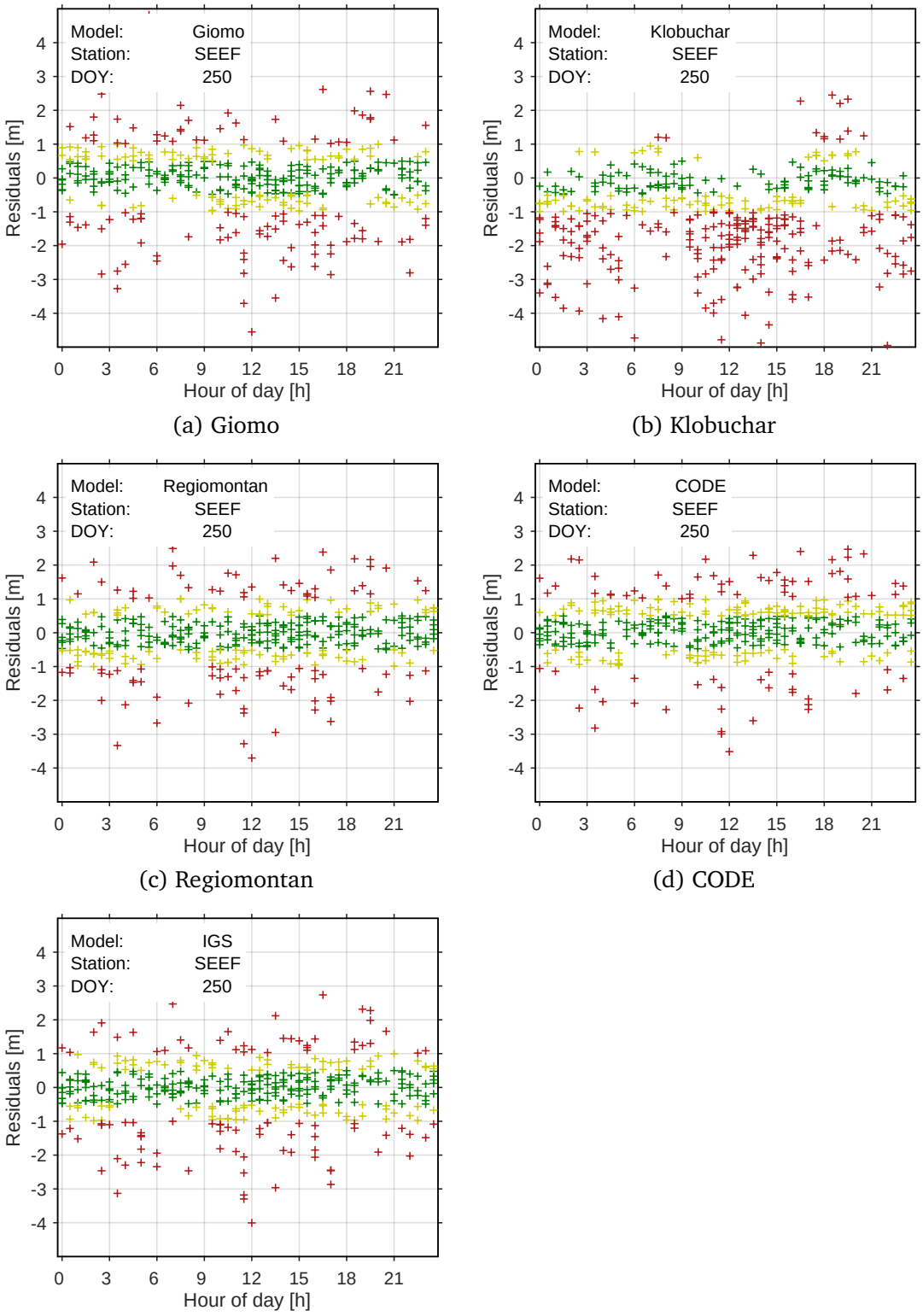

Figure A.20: Differences between L1 pseudoranges corrected with different ionosphere models (a) - (e) and the ionosphere-free linear combination for station Seefeld (SEEF) for September 7, 2018)

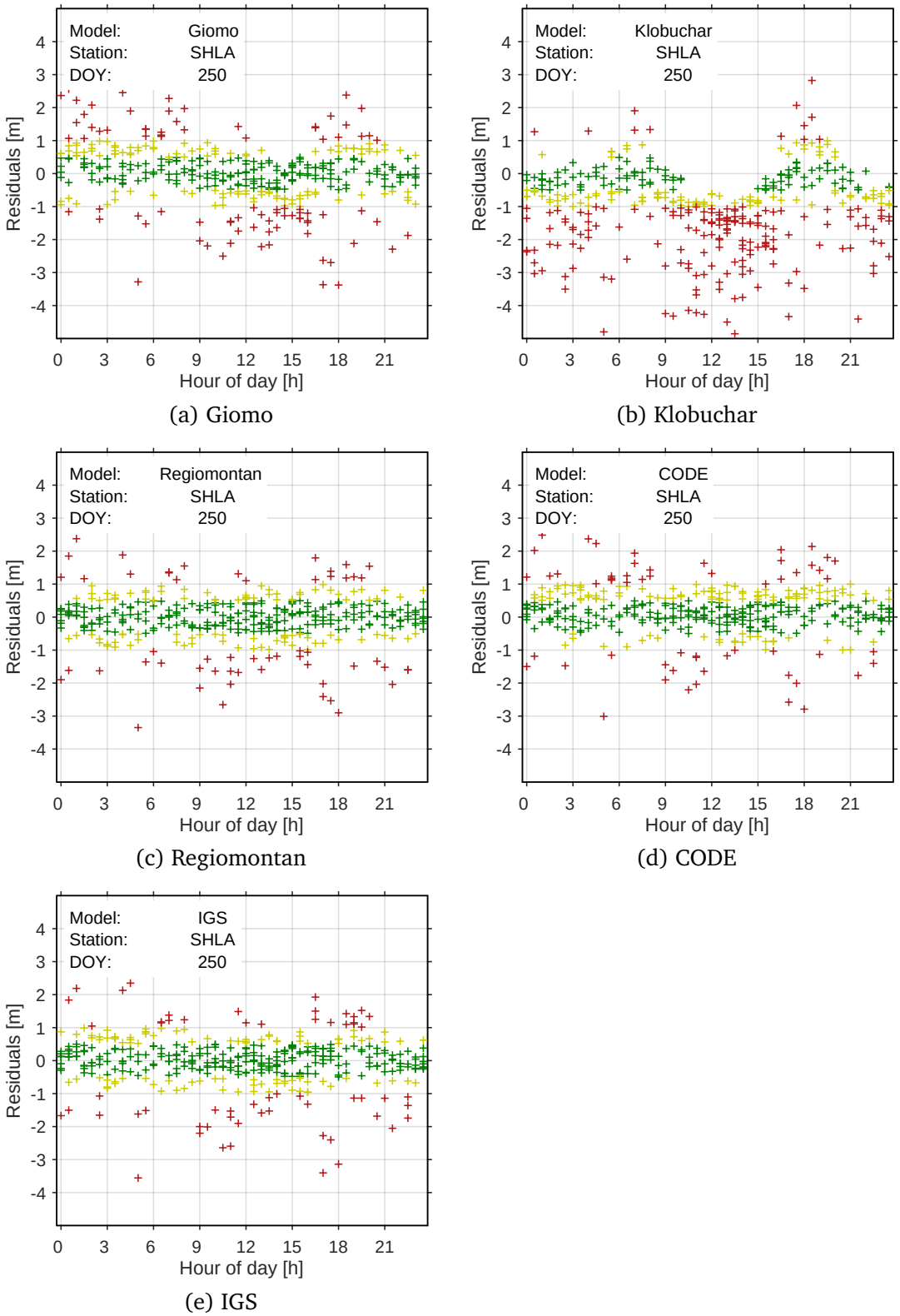

(a) Giomo (b) Klobuchar

(c) Regiomontan (d) CODE

(e) IGS

Figure A.21: Differences between L1 pseudoranges corrected with different ionosphere models (a) - (e) and the ionosphere-free linear combination for station Schladming (SHLA) for September 7, 2018)

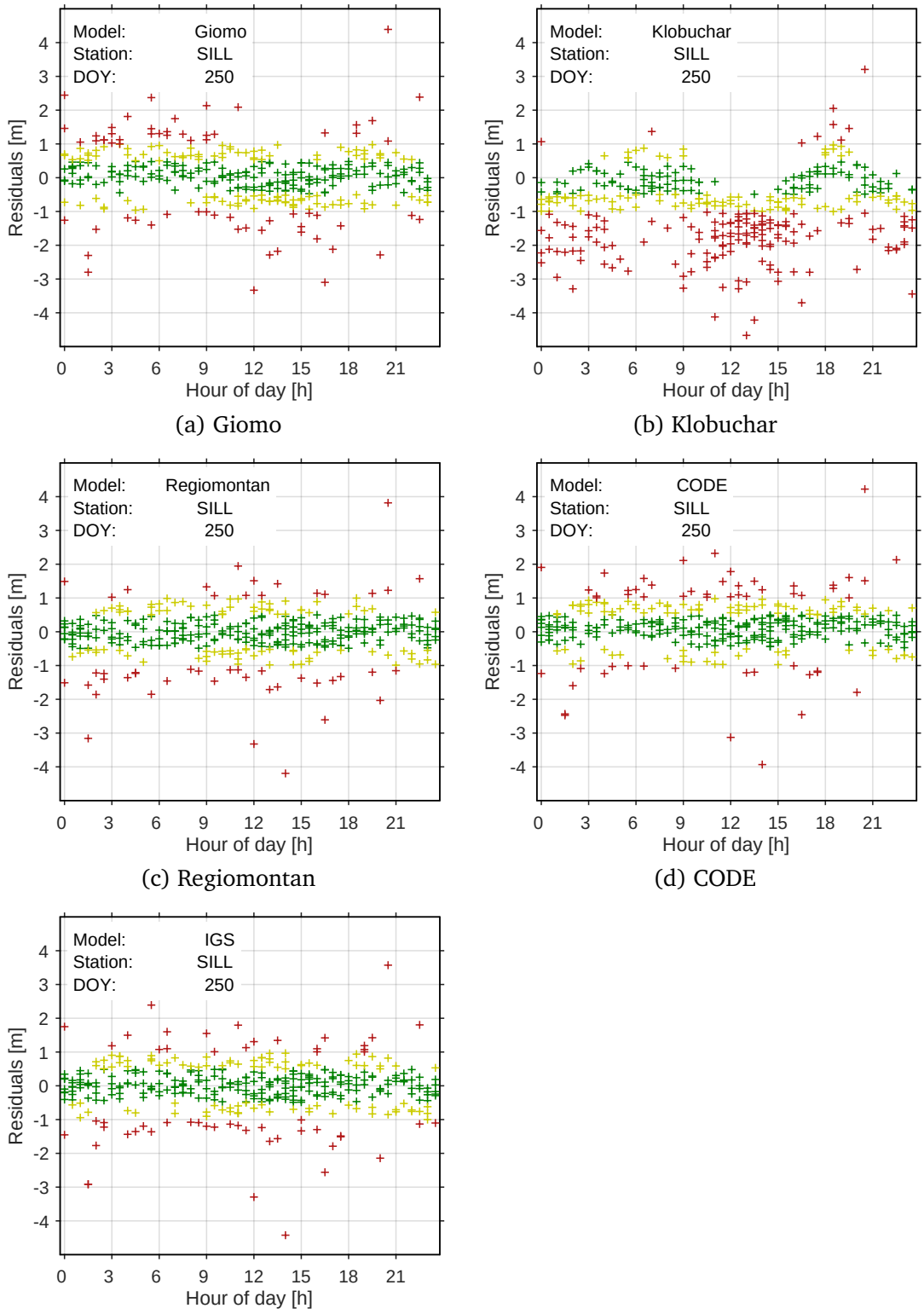

Figure A.22: Differences between L1 pseudoranges corrected with different ionosphere models (a) - (e) and the ionosphere-free linear combination for station Sillian (SILL) for September 7, 2018)

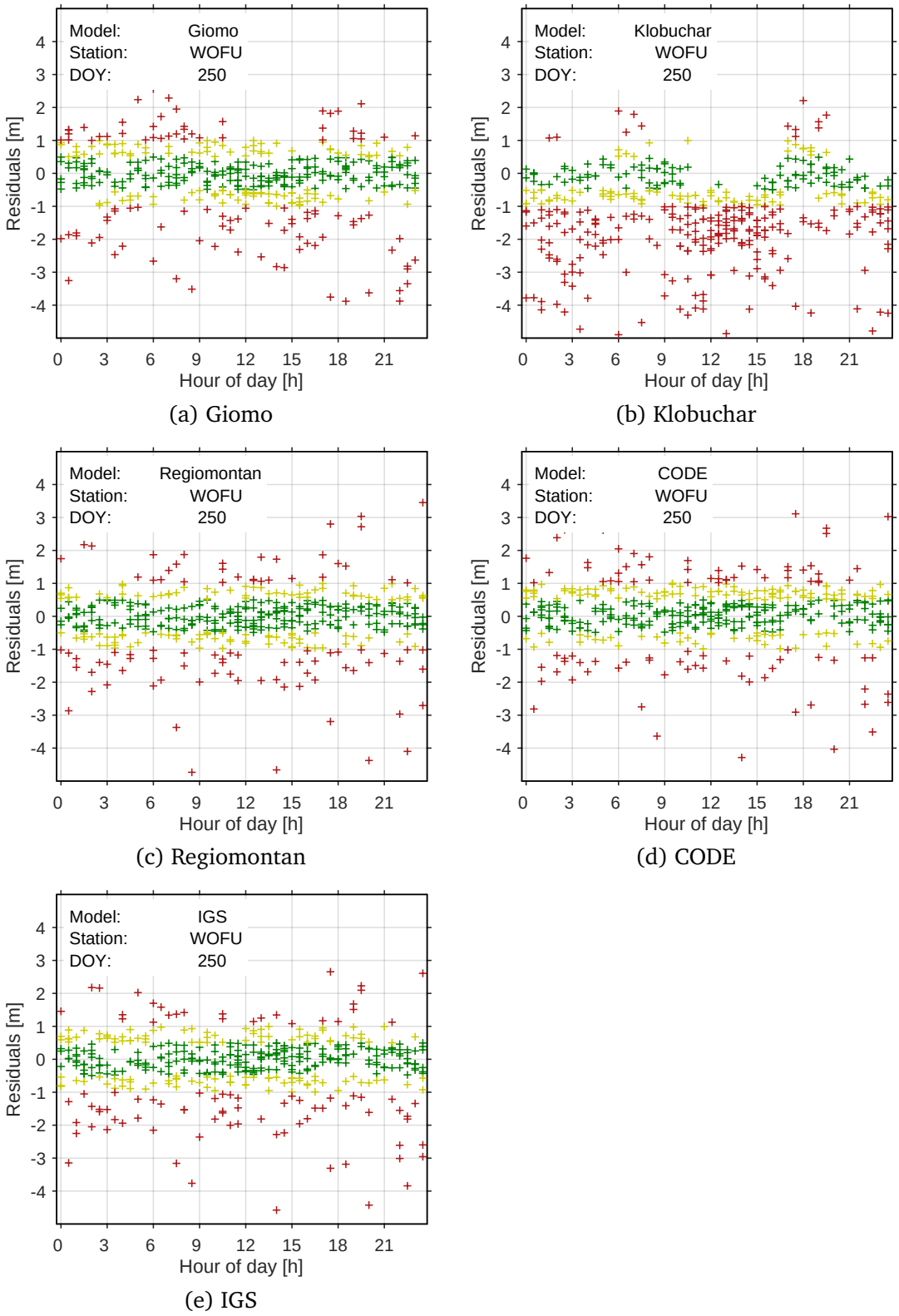

Figure A.23: Differences between L1 pseudoranges corrected with different ionosphere models (a) - (e) and the ionosphere-free linear combination for station Wolfurt (WOFU) for September 7, 2018)

List of Figures

List of Tables

Bibliography

ALIZADEH, M. (2013). *Multi-Dimensional modeling of the ionospheric parameters, using space geodetic techniques*. Ph.D. thesis, Technische Universität Wien, Institut für Geodäsie und Geophysik.

ARBESSER-RASTBURG, B. (2006). The GALILEO single frequency ionospheric correction algorithm. In *Proceedings of the 3rd European Space Weather Week, Brussels*.

BANVILLE, S., ZHANG, W. AND LANGLEY, R.B. (2013). A Better Way – Monitoring the Ionosphere with Integer-Leveled GPS Measurements. *GPS World*.

BILITZA, D. (1990). International reference ionosphere 1990. *NSSDC 90-22, Greenbelt, Maryland*, 157.

BILITZA, D., MCKINNELL, L., REINISCH, B. AND FULLER-ROWELL, T. (2011). The international reference ionosphere today and in the future. *Journal of Geodesy*, 85, 909–920.

BILITZA, D., ALTADILL, D., ZHANG, Y., MERTENS, C., TRUHLIK, V., RICHARDS, P., MCKINNELL, L.A. AND REINISCH, B. (2014). The international reference ionosphere 2012 – a model of international collaboration? *J. Space Weather Space Clim.*, 4, A07.

BILITZA, D., ALTADILL, D., TRUHLIK, V., SHUBIN, V., GALKIN, I., REINISCH, B. AND HUANG, X. (2017). International Reference Ionosphere 2016: From ionospheric climate to real-time weather predictions. *Space Weather*, 15, 418–429.

BLEWITT, G. (2007). GPS and Space-Based Geodetic Methods. In T. Herring, ed., *Treatise on Geophysics, Volume 3*, 351–390, Elsevier.

BÖHM, J. AND SCHUH, H. (2006). Troposphere Mapping Functions for GPS and Very Long Baseline Interferometry from European Centre for Medium-Range Weather Forecasts Operational Analysis Data. *Journal of Geophysical Research*, 111.

BÖHM, J. AND SCHUH, H., eds. (2013). *Atmospheric Effects in Space Geodesy*. Springer Verlag.

BOISITS, J. AND WEBER, R. (2016). REGIOMONTAN (REGionale IOnosphärenMOdellierung für Einfrequenz-NuTzerANwendungen). Tech. rep., Technische Universität Wien, Austria, Department of Geodesy and Geoinformation.

BOISITS, J., JOLDZIC, N. AND WEBER, R. (2016). Regional ionospheric modelling for single-frequency users. EGU Poster.

BORIO, D. AND LO PRESTI, L. (2008). Data and Pilot Combining for Composite GNSS Signal Acquisition. *International Journal of Navigation and Observation*, 2008.

BRUNINI, C. (1997). *Global ionospheric models from GPS measurements*. Ph.D. thesis, Universidad Nacional de La Plata.

COSTER, A.J., GAPOSCHKIN, E.M. AND THORNTON, L.E. (1992). Real-Time Ionospheric Monitoring System Using GPS. *Navigation, Journal of the Institute of Navigation*, 39, 191 – 204.

DACH, R., LUTZ, S., WALSER, P. AND FRIDEZ, P. (1998). Bernese GNSS Software Version 5.2.

DAVIES, K., ed. (1990). *Ionospheric Radio*. IEE Electromagnetic Waves Series.

DETTMERING, D., SCHMIDT, M., HEINKELMANN, R. AND SEITZ, M. (2011). Combination of different space-geodetic observations for regional ionosphere modeling. *Journal of Geodesy*, 85, 989–998.

DI GIOVANNI, G. AND RADICELLA, S.M. (1990). An analytical model of the electron density profile in the ionosphere. *Advances in Space Research*, 10, 27–30.

EUROPEAN GNSS (GALILEO) OPEN SERVICE (2016). Ionospheric Correction Algorithm for Galileo Single Frequency Users.

EUROPEAN UNION (December 2016). European GNSS (Galileo) Open Service Signal In Space Interface Control Document, OS SIS ICD.

EZQUER, G.R., MOSERT, M. AND HEREDIA, T. (1996). Combination of different space-geodetic observations for regional ionosphere modeling. *Annali Di Geofisica*, XXXIX, 539–542.

FELTENS, J. (2003). The activities of the Ionosphere Working Group of the International GPS Service (IGS). *GPS Solutions*, 7, 41–46.

FRIEDLI, TH. K. (2016). *Sunspot Observations of Rudolf Wolf from 1849 - 1893*, Vol. 291. Solar Physics, Springer.

GLANER, M.F. (2017). *Eigenschaften und Einsatzmöglichkeiten von GPS und Galileo Signal-Linearkombinationen*. Master's thesis, Department für Geodäsie und Geoinformation, Technische Universität Wien.

GOSS, A., ERDOGAN, E., SCHMIDT, M., GARCIA-RIGO, A., HERNANDEZ-PAJARES, M., LYU, H. AND NOHUTCU, M. (2017). Advanced algorithms for ionosphere modelling in GNSS applications within the AUDITOR project.

GPS NAVSTAR GLOBAL POSITIONING SYSTEM (2007). *Global Positioning System Precision Positioning Service Performance Standard*. United States Department of Defense, 1^{st} edn.

GPS NAVSTAR GLOBAL POSITIONING SYSTEM (2008). *Global Positioning System Standard Positioning Service Performance Standard*. United States Department of Defense, 4^{th} edn.

HARGREAVES, J. K. (1992). *The solar-terrestrial environment*. Cambridge University Press.

HAUSCHILD, A., MONTENBRUCK, O., SLEEWAEGEN, J.M., HUISMAN, L. AND TEUNISSEN, P.J.G. (2012). Characterization of compass m-1 signals. *GPS Solutions*, 16, 117–126.

HERNÁNDEZ-PAJARES, M., JUAN, J.M., SANZ, J., ORUS, R., GARCIA-RIGO, A., FELTENS, J., KOMJATHY, A., SCHAER, S.C. AND KRANKOWSKI, A. (2009). The IGS VTEC maps: a reliable source of ionospheric information since 1998. *Journal of Geodesy*, 83.

HOBIGER, T. (2006). *VLBI as a tool to probe the ionosphere*. Ph.D. thesis, Technische Universität Wien, Institut für Geodäsie und Geophysik.

HOFMANN-WELLENHOF, B., LICHTENEGGER, H. AND WASLE, E. (2008). *GNSS - Global Navigation Satellite Systems (GPS, GLONASS, Galileo, and more)*. Springer Verlag Wien New York.

HOQUE, M.M. AND JAKOWSKI, N. (2011). Ionospheric bending correction for GNSS radio occultation signals. *Radio Science*, 46.

JIN, R., JIN, S. AND FENG, G. (2012). M_DCB: Matlab code for estimating GNSS satellite and receiver differential code biases. *GPS Solutions*, 16, 541–548.

KINTNER JR., P.M., COSTER, A.J., FULLER-ROWELL, T., MANNUCCI, A.J., MENDILLO, M. AND HEELIS, R. (2013). *Midlatitude ionospheric dynamics and disturbances*. Geophysical Monograph Series, American Geophysical Union.

KUMAR, P.N., SWAMY, K.C.T., SWETHA, A. AND SARMA, A.D. (2012). VTEC estimation with Taylor Series Expansion model using GPS data for low latitude region. In *2012 Annual IEEE India Conference (INDICON)*, 395–398.

LI, Z., YUAN, Y., LI, H., OU, J. AND HUO, X. (2012). Two-step method for the determination of the differential code biases of COMPASS satellites. *Journal of Geodesy*, 86.

LIMBERGER, M. (2015). *Ionosphere modeling from GPS radio occultations and complementary data based on B-splines*. Ph.D. thesis, Technische Universität München.

LIMBERGER, M., LIANG, W., SCHMIDT, M., DETTMERING, D. AND HUGENTOBLER, U. (2013). Regional representation of F2 Chapman parameters based on electron density profiles. *Annales Geophysicae*, 31, 2215–2227.

LIU, Z., YUAN, Y., LI, H., OU, J. AND HUO, X. (2011). Solar activity effects of the ionosphere: A brief review. *Chinese Science Bulletin*, 56, 1202–1211.

LYU, H., HERNANDEZ-PAJARES, M., NOHUTCU, M., GARCIA-RIGO, A., ZHANG, H. AND LIU, J. (2018). The Barcelona ionospheric mapping function (BIMF) and its application to northern mid-latitudes. *GPS Solutions*, 22.

MAGNET, N. AND WEBER, R. (2012a). Investigating the quality of a new regional model of the ionospheric electron content. IGS Workshop Poster, Olzstyn, Poland.

MAGNET, N. AND WEBER, R. (2012b). Multilayer model: A new regional ionospheric model for near real-time applications. AGU Poster, San Francisco, CA, USA.

MAGNET, N. AND WEBER, R. (2013). Positioning Accuracy Within a Single-Frequency GNSS Network Using a New Ionospheric Model. *European Navigation Conference Proceedings*.

MCCARTHY, D. AND SEIDELMANN, P. (2018). *Time: From Earth Rotation to Atomic Physics*. Cambridge University Press, 2nd edn.

MITCH, R. AND PSIAKI, M. (2010). Local Ionosphere Model Estimation From Dual-Frequency GNSS Observables. *Preprint from ION GNSS 2010*.

MONTENBRUCK, O., RIZOS, C., WEBER, R., WEBER, G., NEILAN, R. AND HUGENTOBLER, U. (2013). Getting a grip on multi-GNSS - the international GNSS service MGEX campaign. *GPS World*, 24, 44–49.

MONTENBRUCK, O., HAUSCHILD, A. AND STEIGENBERGER, P. (2014a). Differential Code Bias Estimation using Multi-GNSS Observations and Global Ionosphere Maps. *Navigation, Journal of the Institute of Navigation*, 61, 191–201.

MONTENBRUCK, O., STEIGENBERGER, P., KHACHIKYAN, R., WEBER, G., LANGLEY, R.B., MERVART, L. AND HUGENTOBLER, U. (2014b). IGS-MGEX: Preparing the Ground for Multi-Constellation GNSS Science. *Inside GNSS*, 9, 42–49.

MONTENBRUCK, O., STEIGENBERGER, P., PRANGE, L., DENG, Z., ZHAO, Q., PEROSANZ, F., ROMERO, I., NOLL, C., STÜRZE, A., WEBER, G., SCHMID, R. AND MACLEOD, K. (2017). The Multi-GNSS Experiment (MGEX) of the International GNSS Service (IGS) – Achievements, Prospects and Challenges. *Advances in Space Research*, 59, 1671–1697.

NAVA, B., RADICELLA, S.M., LEITINGER, R. AND COISSON, P. (2006). A near-real-time model-assisted ionosphere electron density retrieval method. *Radio Science*, 41.

PARKINSON, B.W. AND SPILKER JR., J.J. (1996). *Global Positioning System: Theory and Applications, Volume 1*, Vol. 163. American Institute of Aeronautics and Astronautics, Washington DC.

PEROVIĆ, G. (2005). *Least Squares (Monograph)*. TON, Belgrade, ISBN: 86-907409-0-2.

RADICELLA, S.M. (2009). The NeQuick model genesis, uses and evolution. *Annals of Geophysics*, 52.

RAWER, K. (1963). Propagation of decameter waves (HF-band). *Meteorological and Astronomical Inuences on Radio Wave Propagation*.

RISHBETH, H. AND GARRIOTT, O.K. (1969). *Introduction to Ionospheric Physics*, Vol. 14. International Geophysics Series.

SANZ SUBIRANA, J., JUAN ZORNOZA, J.M. AND HERNANDEZ-PAJARES, M., eds. (2013). *GNSS Data Processing, Vol. I: Fundamentals and Algorithms*. ESA Communications.

SCHAER, S. (1999). *Mapping and predicting the Earth's ionosphere using the Global Positioning System*. Ph.D. thesis, Bern University.

SCHAER, S., GURTNER, W. AND FELTENS, J. (1998). IONEX: The IONosphere Map EXchange Format Version 1.

SCHAER, S., GURTNER, W. AND FELTENS, J. (2015). IONEX: The IONosphere Map EXchange Format Version 1.1.

SCHMIDT, M., DETTMERING, D., MÖSSMER, M., WANG, Y. AND ZHANG, J. (2011). Comparison of spherical harmonic and B-spline models for the vertical total electron content. *Radio Science*, 46.

SCHMIDT, M., DETTMERING, D. AND SEITZ, F. (2013). Using b-spline expansions for ionosphere modeling. In W. Freeden, Z.M. Nashed and T. Sonar, eds., *Handbook of Geomathematics*, Springer Berlin Heidelberg, Berlin, Heidelberg.

SEEBER, G. (2003). *Satellite Geodesy, 2nd Edition*. Walter de Gruyter GmbH & Co. KG.

TEUNISSEN, P. AND MONTENBRUCK, O. (2017). *Springer Handbook of Global Navigation Satellite Systems*. Springer International Publishung AG 2017.

TODOROVA, S. (2009). *Kombination geodätischer Weltraumverfahren für globale Karten der Ionosphäre*. Ph.D. thesis, Technische Universität Wien, Institut für Geodäsie und Geophysik.

URQUHART, L. (2009). An Analysis of Multi-Frequency Carrier Phase Linear Combinations for GNSS. Senior technical report 263, Department of Geodesy and Geomatics Engineering, University of New Brunswick, Fredericton, New Brunswick, Canada, 71 pp.

WANG, N., YUAN, Y., LI, Z., MONTENBRUCK, O. AND TAN, B. (2016). Determination of differential code biases with multi-GNSS observations. *Journal of Geodesy*, 90, 209–228.

WANNINGER, L. (2012). Carrier-phase inter-frequency biases of GLONASS receivers. *Journal of Geodesy*, 86, 139–148.

WANNINGER, L. AND BEER, S. (2015). BeiDou satellite-induced code pseudorange variations: diagnosis and therapy. *GPS Solutions*, 19, 639–648.

WEISSTEIN, E.W. (2018). Statistical Correlation. MathWorld - A Wolfram Web Resource (accessed: 2018-10-01), http://mathworld.wolfram.com/StatisticalCorrelation.html.

WILSON, T., ROHLFS, K. AND HUETTEMEISTER, S. (2014). *Tools of Radio Astronomy*. Springer-Verlag Berlin Heidelberg.

WINKLER, W. (2006). *Validierung des EGNOS - Bahn- und Ionosphärenmodells*. Master's thesis, Institut für Geodäsie und Geophysik, Technische Universität Wien.

WÜBBENA, G. (1989). The GPS Adjustment Software Package -GEONAP- Concepts and Models. In *Proceedings of the Fifth International Symposium on Satellite Positioning*, Vol. 1: 452–461, Las Cruces.

ZOLESI, B. AND CANDER, L.R. (2014). *Ionospheric Prediction and Forecasting*. Springer-Verlag Berlin Heidelberg.